# NGAURUHOE INNER CRATER VOLCANIC PROCESSES OF THE 1954-1955 AND 1974-1975 ERUPTIONS

A thesis
submitted in partial fulfilment
of the requirements for the degree
of

**Master of Science in Earth and Ocean Sciences**

at
**The University of Waikato**
by

**JANINE BARBARA KRIPPNER**

---

The University of Waikato
2009

# *Abstract*

Ngauruhoe is an active basaltic andesite to andesite composite cone volcano at the southern end of the Tongariro volcanic complex, and most recently erupted in 1954-55 and 1974-75. These eruptions constructed the inner crater of Ngauruhoe, largely composed of 1954-55 deposits, which are the basis of this study.

The inner crater stratigraphy, exposed on the southern wall, is divided into seven lithostratigraphic units (A to G), while the northern stratigraphy is obscured by the inward collapse of the crater rim. The units are, from oldest to youngest: Unit A, (17.5 m thick), a densely agglutinated spatter deposit with sharp clast outlines; Unit B, (11.2 m) a thick scoria lapilli deposit with local agglutination and scattered spatter bombs up to 1 m in length; Unit C, (6.4 m thick) a clastogenic lava deposit with lateral variations in agglutination; and Unit D, (10 m thick) a scoria lapilli with varying local agglutination. The overlying Unit E (15 cm thick) is a fine ash fallout bed that represents the final vulcanian phase of the 1954-55 eruption. Unit F is a series of six lapilli and ash beds that represent the early vulcanian episode of the 1974-75 eruption. The uppermost Unit G (averaging 10 m thick) is a densely agglutinated spatter deposit that represents the later strombolian phase of the 1974-75 eruption. Units A-D juvenile clasts are porphyritic, with phenocrysts of plagioclase, orthopyroxene, clinopyroxene, minor olivine, within a microlitic glassy groundmass. Quartzose and greywacke xenoliths are common in most units, and are derived from the underlying basement.

The 1954-55 and 1974-75 eruptions are a product of a short-lived, continental arc medium-K calc-alkaline magma. The magma originated from the mantle, then filtered through the crust, undergoing assimilation and fractionation, and evolving to basaltic andesite and andesite compositions. The magma body stagnated in shallow reservoirs where it underwent further crustal assimilation and fractionation of plagioclase and olivine, and homogenisation through magma mixing. Prior to the 1954-55 eruption a more primitive magma body was incorporated into the melt. The melt homogenised and fed both the 1954-55 and 1974-75 eruptions, with a residence time of at least 20 years.

The 1954-55 eruption produced alternating basaltic andesite and andesite strombolian activity and more intense fire fountaining, erupting scoria and spatter that built up the bulk of the inner crater. A period of relative quiescence allowed the formation of a cooled, solid cap rock that resulted in the accumulation of pressure due to volatile exsolution and bubble coalescence. The fracturing of the cap rock then resulted in a vulcanian eruption, depositing a thin layer of fine ash and ballistic blocks. The 1974-75 eruption commenced with the rupturing of the near-solid cap rock from the 1954-55 eruption in an explosive vulcanian blast, the result of decompressional volatile exsolution and bubble coalescence, and possible magma-water interaction. The eruption later changed to strombolian style, producing a clastogenic lava that partially flowed back into the crater.

# *Acknowledgements*

It takes a village to raise a child, it takes a much larger village to help a Masters student complete her degree! To all my helpers, those who physically hauled field gear and rocks up and down Ngauruhoe Volcano, and those who have offered much needed scientific and moral support, thank you from the bottom of my heart.

This thesis would not have been possible without the invaluable help and support of my supervisors. Associate Professor Roger Briggs, Dr. Adrian Pittari, and Geoff Kilgour have provided lifetimes of knowledge and expertise to get me through my research and writing. The Department of Earth and Ocean Sciences has offered great support and encouragement throughout the two year process, and previous three years of a Bachelors degree.

Thank you to the Broad Memorial Fund, and the Masters Research Scholarship for the vital financial assistance. It was well used and I would not have managed to eat without it! Thank you to GNS for my first helicopter rides, they were a lot of fun and definitely helped with field work.

There is no way I would have made it up and down the steep and slippery slopes of ‘my’ volcano, Ngauruhoe, carrying many exciting rocks without my fit and strong field helpers. Thank you to Roger, Adrian, Geoff, Fernando, Steve, Chris, Bryna, Craig, Anja and Duck. Your help in the field, whether it be advice or acting as a pack horse, made field work fun and productive.

Lab work and analyses just wouldn’t have made sense without the help of Renat, Xu, Roger, Adrian, Steve (all from University of Waikato), and Richie (The University of Auckland).

I may not have survived the two year Masters process without my family and friends. Thank you Mum, Dad, Ian, Caleb, Alison, Fiona, all of the EOS MSc students, and every other wonderful person who has given me kind and positive words through this journey. You are my rocks and I am forever grateful to you all.

To the next step

Thank you.

# *Table of Contents*

## Chapter One – Introduction

## Chapter Two - Inner Crater Stratigraphic Architecture and Facies

**Chapter Three – Clast Componentry and Morphology**

**Chapter Four – Petrography, Mineralogy and Geochemistry**

PART 1: PETROGRAPHY AND MINERALOGY

PART 2: GEOCHEMISTRY

**Chapter Five – Discussion**

**Chapter Six – Conclusions**

# *List of Figures*

### Chapter One - Introduction

### Chapter Two - Inner Crater Stratigraphic Architecture and Facies

### Chapter Three – Clast Componentry and Morphology

**Chapter Four – Petrography, Mineralogy, and Geochemistry**

**Chapter Five – Discussion**

# *List of Tables*

# Chapter One

# Introduction

## 1.1 Introduction

Eruption behaviour is significantly influenced by magma dynamics controlling not only the resulting deposits, but landforms and hazards. Understanding the relationships between magma geochemical and physical processes, and eruption dynamics provide an insight into the overall development of an open-system composite volcano. Various studies have been conducted on the Tongariro Volcanic Complex and Ngauruhoe Volcano, and this study of inner crater near-vent eruption processes of the 1954-1955 to 1974-1975 eruptions will add further detail to the record of andesitic volcanism in the Taupo Volcanic Zone, New Zealand.

The inner crater of Ngauruhoe volcano offers a direct investigation of the internal structure of a young composite cone crater. The cone has undergone little erosion and is relatively accessible for anyone with a reasonable level of fitness. The exposed inner crater stratigraphy provides excellent outcrops to study the deposits, and interpret magma development and eruption processes throughout the eruption sequence. This study describes the stratigraphy, componentry, petrography, and geochemistry of the two recent (1954-55 and 1974-75) eruptions of Ngauruhoe Volcano. The two eruptions were extensively documented through photographs, video footage, and eye witness accounts that illustrate the chronology of the inner crater formation.

## 1.2 Research Objectives

This study has three primary aims: (1) To reconstruct the physical near-vent emplacement processes that formed the inner crater deposits, through stratigraphic descriptions, and hand specimen and petrographic studies, as well as special focus on welding and agglutination features; (2) to explore the eruption dynamics within the conduit and vent system during strombolian, vulcanian, and fire fountain-style eruptions from studies of vesicularity, grain size and morphology; and (3) to understand the pre-eruptive magma evolution through geochemical and petrological analyses, and to assess the possible role of processes such as magma mixing and mingling, assimilation, recharge, and fractional crystallisation.

## 1.3 Geological Setting

New Zealand is positioned within the Pacific Ring of Fire and provides a good example of diverse eruption styles, ranging from caldera-producing rhyolitic eruptions (central TVZ) and composite cone building andesitic eruptions (central North Island) to monogenetic basaltic fields (such as the Auckland and Northland volcanic fields). The basaltic andesite, andesite, and rhyolite volcanism in the North Island of New Zealand is related to the subduction of the Pacific Plate under the Australian Plate at a rate of approximately 50 mm per year (Bibby et al., 1995; Ballance et al., 1999).

### *1.3.1 Taupo Volcanic Zone*

The Taupo Volcanic Zone (TVZ) is a NE-trending arc of volcanic activity that has been the focus of over 90% of volcanism in New Zealand during the late Pliocene to Quaternary (Graham et al., 1995; Wilson et al., 1995), and contains the most frequently active rhyolitic centre on Earth (Wilson et al., 1995; Allan et al., 2008). The TVZ has an average magma production rate over the last 2 Ma of 0.3 $m^3s^{-1}$, and an estimated total of $\geq$ 15,000 $km^3$ rhyolitic eruptive products over the Quaternary (Bibby et al., 2002; Allan et al., 2008). The TVZ NE-trending continental back-arc system stretches c. 300 km long and up to c. 60 km, wide as a southern extension of the 3000 km Tonga-Kermadec subduction system (Wilson et al., 1995; Ballance et al., 1999; Price et al., 2005; Cassidy et al., 2008). Volcanism within the TVZ continues today with recent andesitic eruptions from the Ruapehu and Tongariro volcanic centres. The central TVZ is a relatively thin area of crust with a thickness of c. 15 km owing to active faulting and extension at rates between 7 and 18 mm per year along the Taupo Fault Belt (Wilson et al., 1995; Bibby et al., 2002) with a high heat flux producing over 4000 MW of heat from 20 geothermal systems (Davy and Caldwell, 1998; Rowland and Sibson, 2001; Bibby et al., 2002).

The rocks of the TVZ can be partitioned into four significant compositional groups: rhyolites, andesites, high-alumina basalts, and minor dacite as a consequence of magma mixing between andesites and rhyolites (Graham et al., 1995). The TVZ andesites are generated through interactions in a complex storage and transportation system within the crust by the interaction of mantle-derived arc magmas and the lower crust, and the remelting and recycling of andesites and rhyolites due to the high heat flux (Wilson et al., 1995). As one of the most productive rhyolite centres on Earth, more than 90% of the eruption products are of rhyolite composition and c. 2.5% are andesite (Wilson et al., 1995). The two main andesite centres within the TVZ are the Tongariro Volcanic Centre, comprising over 95% total andesites, and the remaining 5% in the Bay of Plenty (Cole, 1981; Graham et al., 1995; Rowland and Sibson, 2001).

### *1.3.2 Tongariro Volcanic Centre*

The most recent activity in the TVZ has been concentrated within the Tongariro Volcanic Centre (TgVC) (Figure 1.1) which comprises two significant composite andesitic volcanoes, Tongariro (the Tongariro Volcanic Complex including Ngauruhoe volcano) and Ruapehu, and minor associated cones: Ohakune, Hauhungatahi, Pihanga, Kakaramea, Pukeonaki, and Maungakatoetoe.

Mesozoic metagreywacke basement underlies the TgVC (Cole, 1978; Graham et al., 1995) outcropping to the east and west of the TVZ, down faulting at the margins to form a large, 40 km wide NNE-trending graben filled with low-density volcanic material (Nairn et al., 1998; Bibby et al., 2002; Cassidy et al., 2008). Tertiary sediments from a few 10s to 100s of metres thickness overlie the basement, and underlie 800 m of TgVC deposits and dyke systems, as shown by gravity surveys of the Tama Lakes Saddle, south of Ngauruhoe (Cassidy et al., 2008).

As there is no confirmed date for the onset of activity in the TgVC, the oldest dated lavas 250-275 ka are inferred to represent the earliest activity within the volcanic centre (Graham et al., 1995; Hobden et al., 1996). Volcanic activity at Tongariro can be grouped into older (> 20,000 years) and younger (< 20,000 years) eruptives (Cole and Nairn, 1975). Older vents including Kakaramea and Pihanga were erupted from a NW-SE lineament, while recent lava producing vents (including Ngauruhoe) lie in a NNE-SSW lineament at 027° (Cole, 1978; Rowland and Sibson, 2001). The Tongariro composite volcano contains at least 12 volcanic cones, the youngest being the Upper Te Maari Crater, Red Crater, and the most recently active Ngauruhoe, that has produced over 73 eruptive episodes since 1839 (Bebbington and Lai, 1996). The cones of Tongariro overlap and merge to form the Tongariro Volcanic Complex, and have been eroded heavily by glaciations to produce the large Mangatepopo, Waihohonu, and Oturere valleys. The volcanic complex covers an approximate area of 200 km$^2$ and the post-glacial volume is c. 60 km$^3$ with an additional c. 15 km$^2$ surrounding ring plain (Hobden, 1997).

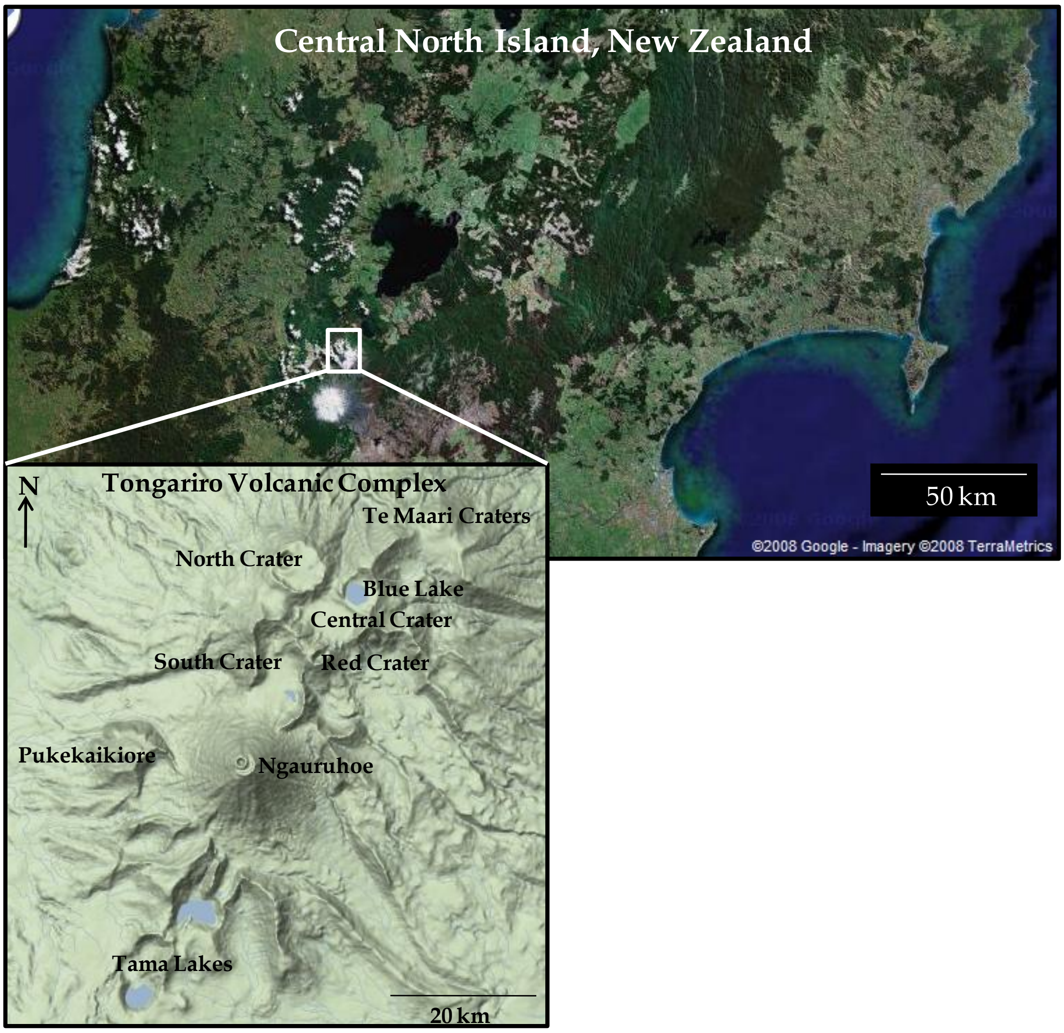

**Figure 1.1:** Overview of the Tongariro Volcanic Centre with major craters and cones including Ngauruhoe in the southern sector (Google Maps New Zealand, 2008).

The first significant cone-forming episode occurred from 275 to 215 ka at the southern end of Tongariro (Hobden et al., 1996). A major cone was then constructed at the southern end of the complex during an active period from 210 to 200 ka, the summit of which is estimated to have been located where Ngauruhoe is today, and was subsequently eroded and buried by the younger cone (Topping, 1973; Hobden et al., 1996). From 180 to 70 ka a third major cone building period produced over 30 lava flows and flank scoria cones to the north-eastern side of TgVC, and Pukekaikiore grew to the west. Tongariro Trig and Oturere were active from 110 to 65 ka, producing extensive lavas. The volcanic complex underwent a period of relative quiescence from 65 ka to 25 ka that was broken by the recent productive phase forming Te Maari Craters, Tama Lakes, Red Crater, Emerald Lakes, North Crater, young Pukekaikiore, and Blue Lake Crater (Topping, 1973; Hobden et al., 1996). Recent eruptions have been relatively small, only reaching VEI 3 (Volcanic Explosivity Index), but one VEI 4 (subplinian) eruption was produced between 11 – 12 cal. ky BP from a vent close to where Ngauruhoe is now located (Hitchcock and Cole, 2007). Since 3.47 ka activity in the complex has been dominated by the formation of Ngauruhoe Volcano (Hobden et al., 1996). Underlying the TgVC vents is an area of NNE-trending relatively young normal faults that control vent location (Cole, 1978; Hagerty and Benites, 2003), and an extensive geothermal system that is apparent through numerous active geothermal sites throughout Tongariro and on the summit of Ngauruhoe.

Studies on the TgVC have been carried out by University of Waikato Graduate students including Chizmar (2003) on the nature and dynamics of explosive eruptions and associated crater formation at Tama Lakes, Bardsley (2004) on the physical volcanology of Red Crater, Basher (2005) on the physical volcanology and hazards at Te Maari Craters, and Griffin (2007) on the products and processes of cone-building eruptions of North Crater.

## 1.4 Ngauruhoe Volcano

Ngauruhoe is the youngest and one of the currently active vents of the TgVC alongside the Te Maari craters, Emerald Lakes, North and Red craters. The Ngauruhoe eruptions have been fed from a series of small, complex interconnected magma chambers that are part of a larger system underlying the TgVC that also drives the active geothermal system (Rowlands et al., 2005).

Ngauruhoe is a relatively small, symmetrical cone with steep 30˚ flanks, with the symmetrical profile due to the sectoral focus of aá lava flows and pyroclastic material controlled by summit morphology (Figure 1.2). These lavas have been subdivided into five main groups (Figure 1.3) that correlate with eruption episodes contributing to cone growth, with Group 1 being the oldest exposed flows from 2.5-1.85 ka (Hobden et al., 2002). The five groups show abrupt changes in magma and isotope compositions due to the interconnected, open magma system producing small and short lived eruptions throughout its history (Hobden et al., 2002).

The summit of Ngauruhoe is currently composed of two craters, an older outer crater with a diameter of c. 450 m (Hobden et al., 2002), and a younger inner crater formed in the NW sector of the outer crater that is approximately 220 m in diameter. Prior to the 1954 eruption, a single vent was active in the NW sector of the main crater that remained active throughout the two most recent eruptions. A previous eruption had blanketed the summit in ash and lapilli that levelled off the previous sub-craters (Figure 1.2d), resulting in an overall dip to the west (Allen, 1949). Until recently, the age of Ngauruhoe was thought to be c. 2500 (Gregg, 1960; Hobden et al., 2002) as dated by the Mangatawai Tephra, but recent carbon dating of leaves found within the Mangatawai Tephra bed suggest a radiocarbon age of 3470 ± 40 BP (A. Moebis Pers. Comm.). Ngauruhoe has grown to 2,287 m above sea level, or c. 900 m above the Tongariro saddle, covering an area of 15 $km^2$ (Hobden et al., 2002). An updated growth rate of c. 0.6 $km^3$ per 1000 years is calculated from the new carbon age calculated by Moebis and previous cone volume of 2.2 $km^3$ given by Hobden et al. (2002).

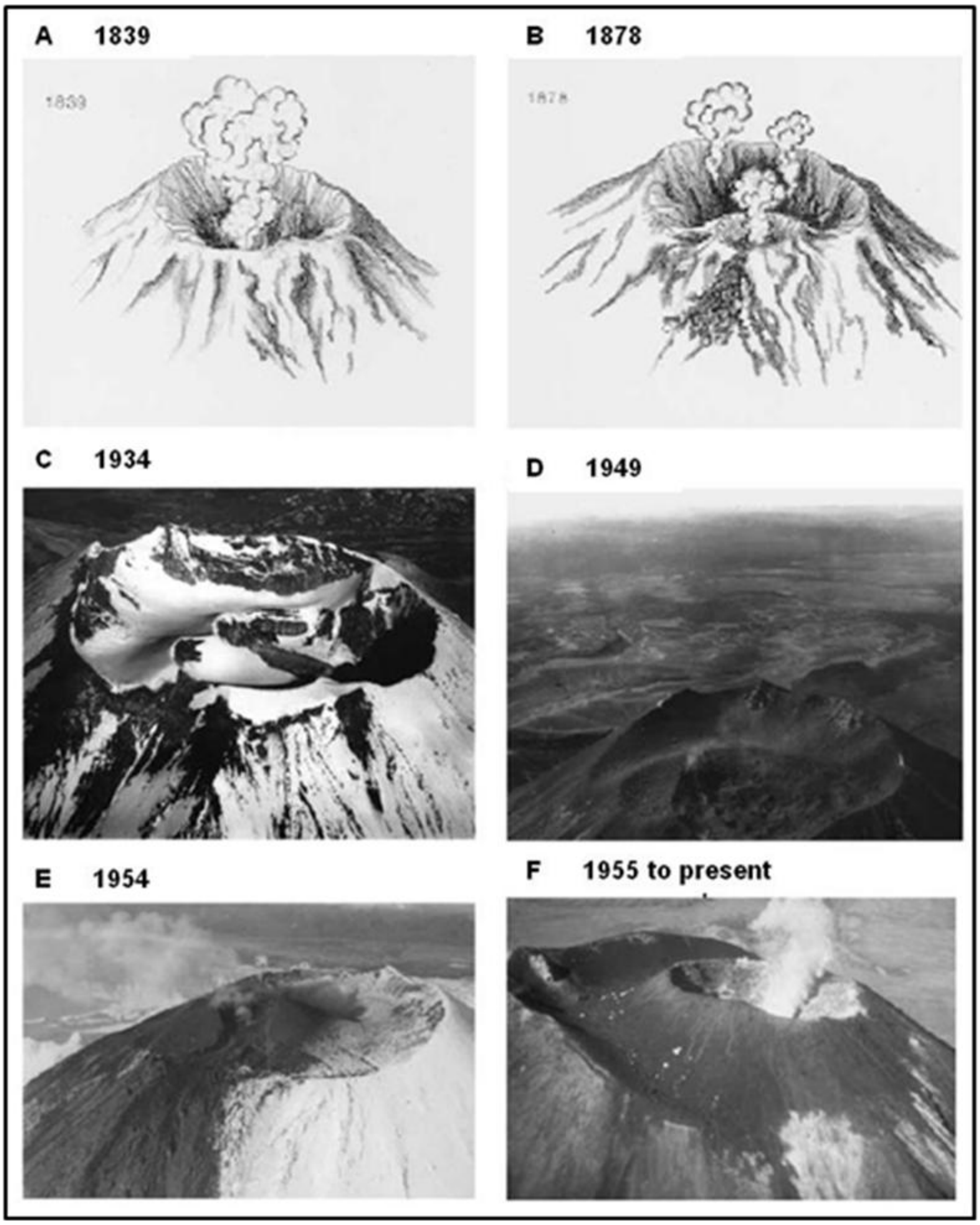

**Figure 1.2:** Morphological evolution of Ngauruhoe summit crater(s) as viewed from the SW, from oldest (A) to present day (F). Compiled by Hobden et al. (2002) from collections from GNS Wairakei Research Centre, and sketches from Williams (1989).

Ngauruhoe has produced 73 eruptions, ejecting $\geq 10^5$ $m^3$ eruptive material since 1839 (Bebbington and Lai, 1996), characterised by explosive strombolian, vulcanian, and sub-plinian eruptions that have produced lava flows, block and ash flows, ash columns, pyroclastic flows, and scoria and spatter deposits.

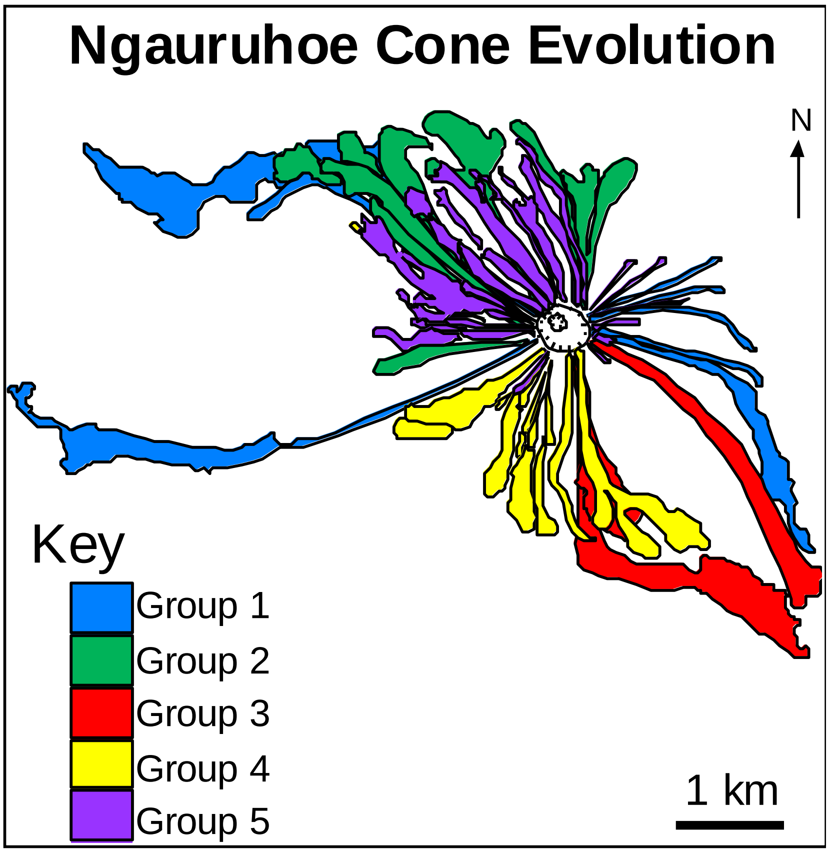

**Figure 1.3:** Evolution of Ngauruhoe volcano through exposed lava flows that have contributed to the symmetry of the cone, modified from Hobden et al. (2002).

The 1954 to 1955 eruption was dominantly strombolian in nature, producing numerous ash explosions and at least 11 lava flows down the NW flanks of Ngauruhoe, with a total flow volume of c. 3,030,750 $m^3$ (Sanders, Unpublished data). The 1974 to 1975 eruption was of a more explosive vulcanian to sub-plinian nature, producing at least five block and ash flows down the NW flanks (Hobden et al., 2002) and adding an average of 10 m of ash fallout and welded spatter to the top of the inner crater rim.

Ngauruhoe eruptives are principally basaltic andesite (with secondary andesite) in composition. The typical phenocryst assemblage of Ngauruhoe lavas is dominated by plagioclase and two pyroxenes: orthopyroxene and lesser amounts of clinopyroxene, within a microlite rich glassy groundmass (Hobden, 1997). Phenocryst compositions and morphologies suggest disequilibrium within the magma through assimilation, recharge, and magma mixing processes. The

January to March 1974 eruptive products are petrographically and chemically indistinguishable from the previous 1954-55 eruption products, suggesting no new magma input (Nairn et al., 1976). Ngauruhoe eruption deposits contain varying concentrations of buchitic metagreywacke and quartzose xenoliths derived from the underlying Mesozoic Torlesse argillite and greywacke basement (Graham et al., 1988; Hobden, 1997). Sharp boundaries between the xenoliths and lava are characteristic in 1954 deposits (Steiner, 1958; Graham, 1988) and evidence of partial melting of some of the xenoliths was recorded by Hobden (1997). Hobden (1997) went on to describe the quartzose xenoliths within andesites of the TgVC as typically composed of 60-100% quartz, and 5-40% calc-silicates including wollastonite, anorthite, minor diopside, and sanidine.

A summary of all Ngauruhoe eruption records, eye witnesses accounts, and authors up to 1959 has been given by Gregg (1960) and is reviewed in section 1.6. More recent eruptions and their deposits have been described by Gregg (1956), Steiner (1958), Self (1975), Nairn et al. (1976), Nairn and Self (1978), Hobden et al. (1999), and Lube et al. (2007), with more in depth petrographical, geochemical and stratigraphic work carried out on Ngauruhoe by Cole (1978), Graham et al. (1988), Hobden (1997) and. Hobden et al. (1996, 1999, 2001, 2002)

## 1.5 Pre-1954 Ngauruhoe Eruption Activity

Ngauruhoe has been recognised to be an active volcano since pre-European times in the early 1800's where legends tell of the Gods sending fire to the Maori people, and many witnessed eruptions were seen as signs of war (Gregg, 1956, 1960). The morphology of the cone was first described by Missionary John Carne Bidwill (1841) after his ascent to the summit in March 1841. Gregg (1960) compiled a series of sketch maps and crater descriptions depicting the various stages of the crater evolution based on Bidwill's report, and others by Collie (1880), Ross (1898), Girdlestone (1909), Marshall (1909), Duncan (1918), and various aerial photographs.

Historical European eruption records begin on 3 March 1839 when Bidwill (1841) was one of the very first to ascend Ngauruhoe. Since then, eruptions have been near-continuous to sporadic and have ranged from small steam eruptions to explosive eruptions producing large quantities of ash, such as February 1907 (Cole and Nairn, 1975), with the most common activity being ash emission (Gregg, 1960). Since 1839 eruptions have occurred on average every 4.5 years, with the largest eruptions in 1870, 1948-49, 1954-55, and 1974-75 (Allen, 1949; Hobden et al., 2002). The outer crater of Ngauruhoe was the sole crater before the 1954-55 inner crater-forming eruptions, although the dynamic summit has produced multiple vents over the historical record (Figure 1.2).

Bidwill described the eruption of 3 March 1839 as a loud eruption accompanied by a thick black mushroom cloud, lasting for half an hour, and large continuous steam emissions (Bidwill, 1841). An eruption in 1870 produced large steam explosions, scoria deposits, and the first three documented lava flows on Ngauruhoe (Hector, 1887, cited in Gregg, 1960; Cole and Nairn, 1975). Various ash eruptions occurred over the following years and are summarised in Gregg (1960).

After almost 8 years of little to no activity the next significant eruption commenced on April 30 1948, with a brief strombolian eruption that ejected blocks and bombs up to the size of a small house, and produced hot block and ash flows, ash columns reaching over 3000 m above the crater (Figure 1.4), and one lava flow that resulted from the breach of a lava lake over the NW rim of the crater (Allen, 1948; Cloud, 1951; Cole and Nairn, 1975). Emission of small quantities of ash continued after May 1948, until the 1949 eruption began with a vent-clearing explosion on February 9, with eruptive activity occurring over a three week period. Ash explosions occurred throughout the three weeks, with columns reaching heights of 6000 m above the crater rim (Allen, 1949).

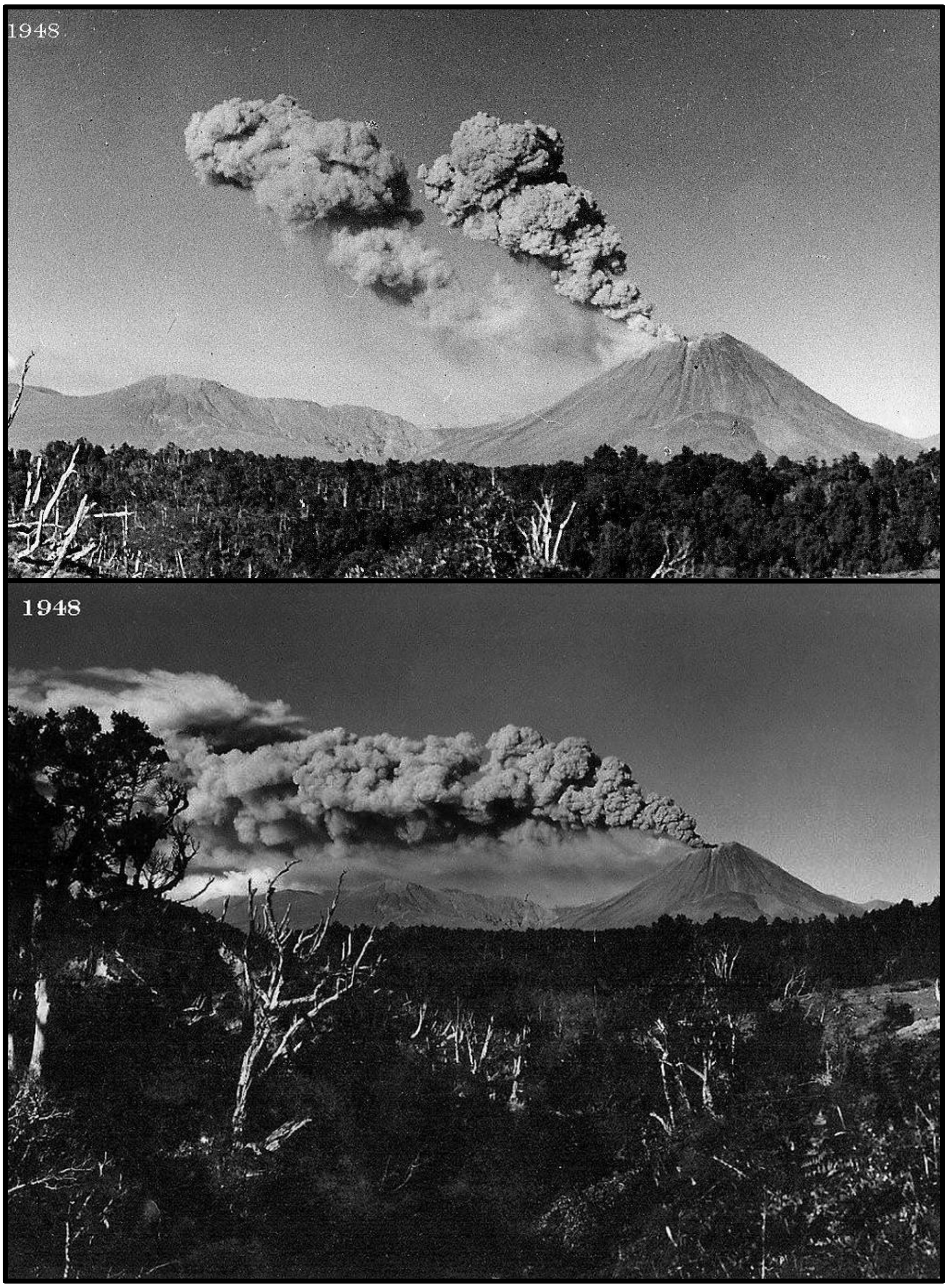

**Figure 1.4:** Top: Ash clouds of the 1948 eruption at Ngauruhoe detaching and drifting north, Bottom: voluminous ash cloud produced in the 1948 eruption. Photos courtesy of John A. Krippner.

## 1.6 1954-1955 Eruption Chronology

The following summary of the 1954-55 eruption is a review of the report given by Gregg (1956). The 1954-55 eruption spanned from June 1954 to July 1955, although lava was seen in the crater in February 1954 prior to any eruptive activity. Activity ranged from effusive lava production to explosive vulcanian-style eruptions (Figure 1.5).

### *June 1954*

The eruption commenced on June 2, 1954 when lava fountaining was observed. Two days later, near-continuous lava fountaining recommenced, reaching c. 300 m Above the Crater Rim (a.c.r.) and producing two lava flows down the northwestern sector by 11 am, covering a dry hot avalanche that had occurred earlier that day, that actively flowed through to the next day. Explosivity increased on the 6th when loud, sharp explosions produced light brown ash clouds reaching heights of c. 600 m a.c.r.. Sporadic explosions continued through to the end of the month. Activity declined on the 12th - 13th and increased again when lava fountaining and ash emissions commenced on the 20th. Lava emission reached a maximum for the 1954-55 eruption period on the 30th, with near-continuous lava fountaining until 11 pm reaching heights of 300 m above the crater, and overtopping the crater rim to produce the largest lava flow that came to rest alongside the June 4th flow.

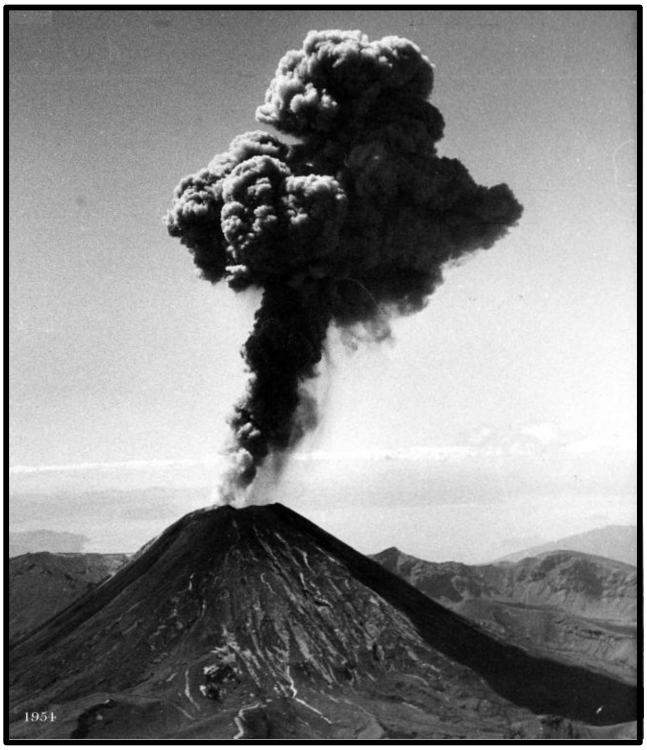

**Figure 1.5:** 1954-55 vulcanian eruption producing an ash column and recent lava flow situated on the NW flanks of Ngauruhoe. Photo courtesy of John A. Krippner.

### *July 1954*

The June 30th flow halted on the 2nd of July. Fire fountaining and ash emission continued throughout July. On July 8th and 9th two more lava flows descended down the western slopes, continuing to flow through to the 13th. The near continuous emission of black ash occurred on the 11th, but lessened after 1 pm when lava fountaining threw incandescent blocks onto the northern slopes of Ngauruhoe. Three more lava flows were witnessed from the Chateau on the evening of the 14th before visibility declined through to the 29th obscuring visibility of lava flows and fountaining. On the 29th a new lava flow was accompanied by sharp explosions that produced visible shock waves (seen as rising arcs of bright light) and vortex rings (annular puffs of ash). The next day another incandescent lava flow was reported.

### *August 1954*

The first two weeks of August saw quiet ash emission from the crater. Three lava flows were produced, the first reaching Pukekaikiore on the 15th, and the second on the 18th, measured moving 15 cm per minute with dimensions of 15 m high and 183 m wide. The third lava flow travelled at the same speed, advanced 300 m down the western slopes and around the southern side of Pukekaikiore.

### *September 1954*

Ash emission intensified, accompanied by loud explosions throughout September. Fire fountaining resumed on the 15th and breached the crater rim the next day to generate a lava flow and hot avalanche that caused large clouds of ash and steam to rise from the Pukekaikiore saddle. Multiple loud explosions produced visible shock waves and dark ash clouds that rose above the crater to about 1.2 km, ejecting lapilli up to 12 mm in size that fell near the Pukekaikiore saddle and coated the chateau in a fine layer of ash. On the 18th a lava flow travelled 240 m down the western slopes of Ngauruhoe. On the 19th the Chateau was shaken by loud explosions, while lava continued to flow from the crater. Lava fountaining and ash emission were accompanied by loud explosions that continued throughout the following week. On the 26th large dense black ash clouds were large enough to deposit ash at Taupo township, and the last lava flow of the 1954-55 eruption episode was produced.

***October to November 1954***

Activity declined through the next two months with sporadic steam and ash emission throughout October, and one ash explosion in November.

***December 1954***

Activity increased with intermittent lava fountaining and ash emission accompanied by loud explosions through to the 30th, before activity again declined to rumbling steam emission.

***January 1955***

An increase in activity was marked by numerous sharp explosions and ash emission that reached a peak on the 28th. During this time several episodes of fire fountaining were reported.

***February to July 1955***

Ash explosions continued through to the end of February, decreasing toward March. On February 13, it was reported that incandescent rock and small ejecta surrounded the vent and were being carried up within a blue gas discharge that continued into March. The last ash explosion occurred on the 10th at 12.22 pm, although incandescent lava was reported to be present around the vent on several occasions up to the 25th of June.

## 1.7 1974-1975 Eruption Chronology

The 1975 eruption was dominantly vulcanian in style, and many spectacular photos document the eruption plumes and pyroclastic surges travelling down the flanks of Ngauruhoe (Figure 1.6). The eruptions of January to March 1974 (Nairn and Self, 1978), and February 19, 1975 (Nairn et al., 1976) have been recorded in detail to produce an accurate chronology, summarised here.

Activity began on December 29, 1972, that then peaked on January 2, 1973, with ash emission and ejection of incandescent material containing fresh volcanic glass. More effusive activity occurred in September and October that year, and upon inspection in November the crater had near vertical walls down to a depth of

**Figure 1.6:** February 19, 1975, vulcanian eruption with Pukekaikiore in the foreground. Partial collapse of the large eruption column produced pyroclastic flows down the flanks of the volcano. Photo courtesy of GNS Lower Hutt, taken by I.A. Nairn.

at least 180 m, with a secondary crater at the bottom. A seismically active period during July to October 1973 preceded minor eruptive activity in the following December (Nairn et al., 1976).

### *January 1974*

The first activity of the 1974-75 eruption was reported on January 22, 1974, when a black convoluting cloud rose to 600 m a.c.r. with activity continuing through the day, producing small amounts of incandescent ejecta. Explosive activity produced a large black cloud early on the 23rd, ejecting incandescent bombs that lit up the summit flanks, with ash emission continuing throughout the morning.

At midday a large explosive eruption followed a regional earthquake. After the initial explosion, cyclic activity followed, consisting of periods of relative quiescence and low seismic activity, that were interrupted by violent explosions ejecting bombs that rolled down to the foot of the cone, followed by vigorous ash emission (Nairn et al., 1976). This cyclic activity, although less explosive, continued through to January 24. Ash emission continued through to the morning of the 26th, when the largest eruption since 1955 produced a densely convoluting ash column rising to 1500 m a.c.r. that eventually underwent partial collapse to produce pyroclastic flows (Nairn et al,. 1976).

### *March 1974*

After a lull in activity the eruption commenced on March 27, producing a large ash column rising to 1700 m a.c.r.. Near-continuous explosive ash emission continued throughout the afternoon, depositing dense ash fallout over Tongariro. Cyclic activity followed with a decline in seismic energy, before increasing again prior the onset of ash emission. The 28th produced violent activity that amplified into the most rapid and voluminous degassing of Ngauruhoe since 1954 (Nairn et al., 1976). Partially collapsing ash columns and resulting pyroclastic flows occurred that morning with shock waves shaking the Chateau at the base of neighbouring Ruapehu. Large blocks and bombs reaching 5 m diameter were ejected, some of which impacted half way down the flanks of Ngauruhoe. Inward collapse of the NW sector of the inner crater rim occurred before another violent explosion, producing a visible atmospheric shock wave (Nairn et al., 1976). The most explosive eruptions occurred over March 28-29, more explosive than those in January, throwing ejecta up to 40 m above the crater rim with some near-horizontal ejecta. Dark ash columns followed, rising to 2500 m a.c.r. with internal lightning. These columns then separated from the summit and drifted NW (Nairn et al., 1976).

### *February 1975*

Activity increased on February 12, 1975 with ash emission after an 11 month lull in activity, followed by intermittent ash eruptions occurring through to February 17. Activity reached a climax on February 19, with the largest explosions of the 1974-75 eruption episode (Nairn and Self, 1978). Intermittent eruptions generated pyroclastic avalanches down the flanks of Ngauruhoe, accompanied by continuous gas emission and intense tremor, producing an ash column that rose to 6000 m a.c.r.. The accumulation of large blocks and bombs within the fosse between the inner and outer crater collapsed to produce a hot block and ash flow, with ash clouds rising 500 m from the avalanche. An eruption column producing lightning followed visible shock waves, and ejected scoriaceous material up to 15 cm in diameter (Sidwell and Spannagl personal communication in Nairn and Self, 1978). By the afternoon the eruption column had risen to 10,000 m a.c.r., and produced a flattened top in the tropopause that deposited fine ash as far as Rotorua, Hamilton and Tauranga (Nairn and Self, 1978). Pyroclastic avalanches and steam emission continued through the day and explosivity increased in the afternoon with intermittent eruptions and visible shock waves, before declining to a 4000 m high ash column (Nairn and Self, 1978). The eruption ended late that night.

## 1.8 Thesis Layout

The remaining chapters of this thesis outline the volcanic products and processes associated with the Ngauruhoe inner crater. Chapter two is a discussion of the internal crater stratigraphy. Chapter three contains the smaller scale description of these units including clast morphology and componentry. Chapter four contains petrographic and geochemical data. These results are discussed in Chapter five, outlining an interpretation of magma genesis and chronology of physical and geochemical processes leading to the 1954-55 and 1974-75 eruptions, and conclusions are presented in Chapter six.

# *Chapter Two*

# *Inner Crater Stratigraphic Architecture and Facies*

## 2.1 Introduction

### *2.1.1 Ngauruhoe summit overview*

The summit of Ngauruhoe consists of two craters, an older c. 450 m wide outer crater and a younger c. 220 m wide inner crater (Figure 2.1a-b). The outer crater, constructed prior to 1954, still has active geothermal vents occurring around the rim. The outer crater rim is higher than the inner crater to the SE toward the peak of the volcano, but is discontinuous on the N to NW side of the summit where the rim declines towards the base of the inner crater (Figure 2.1a). There is a fosse between the outer crater and the flanks of the inner crater (Figure 2.1b). The outer flanks of the inner crater are covered by loose lapilli to blocky scoriaceous material and large clots of agglutinated spatter. The rim surface of the inner crater reaches widths of up to 6 m and has a depression to the NW where the uppermost unit collapsed into the crater on March 28, 1974 (Figure 2.2a). Several large ballistic blocks up to 4 m in diameter, ejected during the later stages of the 1974-75 eruption, lie on the inner crater rim but the majority of loose clasts along the rim are variably agglutinated grey to red scoriaceous lapilli and bombs.

An in situ stratigraphic succession is exposed on the SE wall of the crater, which has been divided into seven units based on physical characteristics, from the lowermost Unit A to the uppermost Unit G. Units A to E are considered to be products of the 1954-1955 eruption, while units F and G are considered to represent the 1974-1975 eruption. The eruption sequence is discussed further in Chapters One and Five. Unit G partially flowed back down the inner crater walls and has obscured the stratigraphy on the northern, southern (Figure 2.2b), and western walls. The inner crater outcrop is portrayed on composite stratigraphic logs in Figure 2.3. The internal walls of the inner crater are steep and near-vertical in places. The bottom of the crater is infilled with scoriaceous scree and dense angular blocks. Active geothermal vents are seen on the north to northwestern inner crater wall and are dynamically altering the deposits to a light yellow colour, and crystallising secondary minerals.

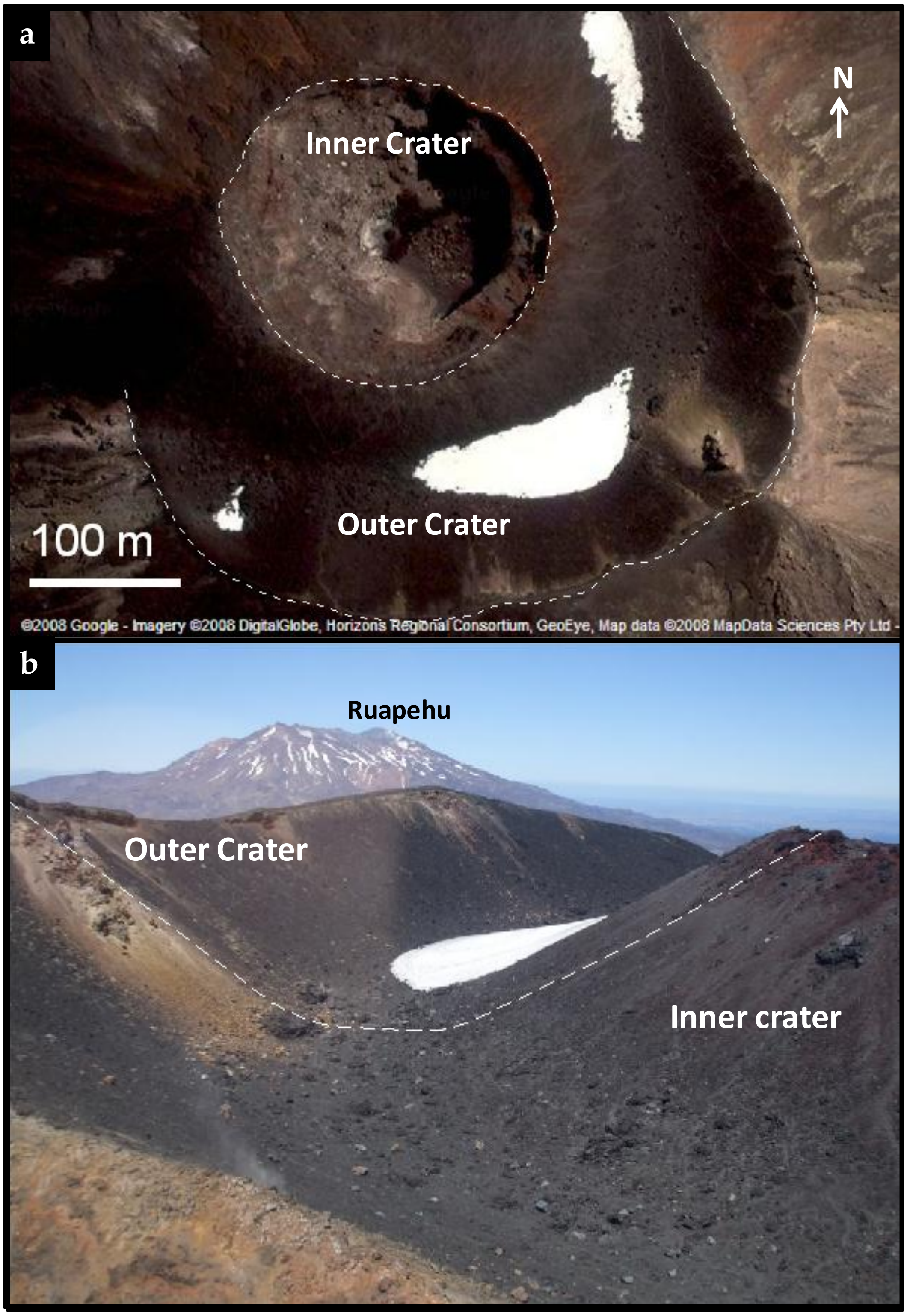

**Figure 2.1:** (a) Aerial view of the summit of Ngauruhoe showing the outer and inner craters. White patches are snow (Google maps New Zealand, 2008). (b) Ngauruhoe inner crater flanks and fosse between the inner and outer craters, view looking south towards Ruapehu Volcano (2797 m). Height from base of fosse to top of the inner crater rim is c. 40 m.

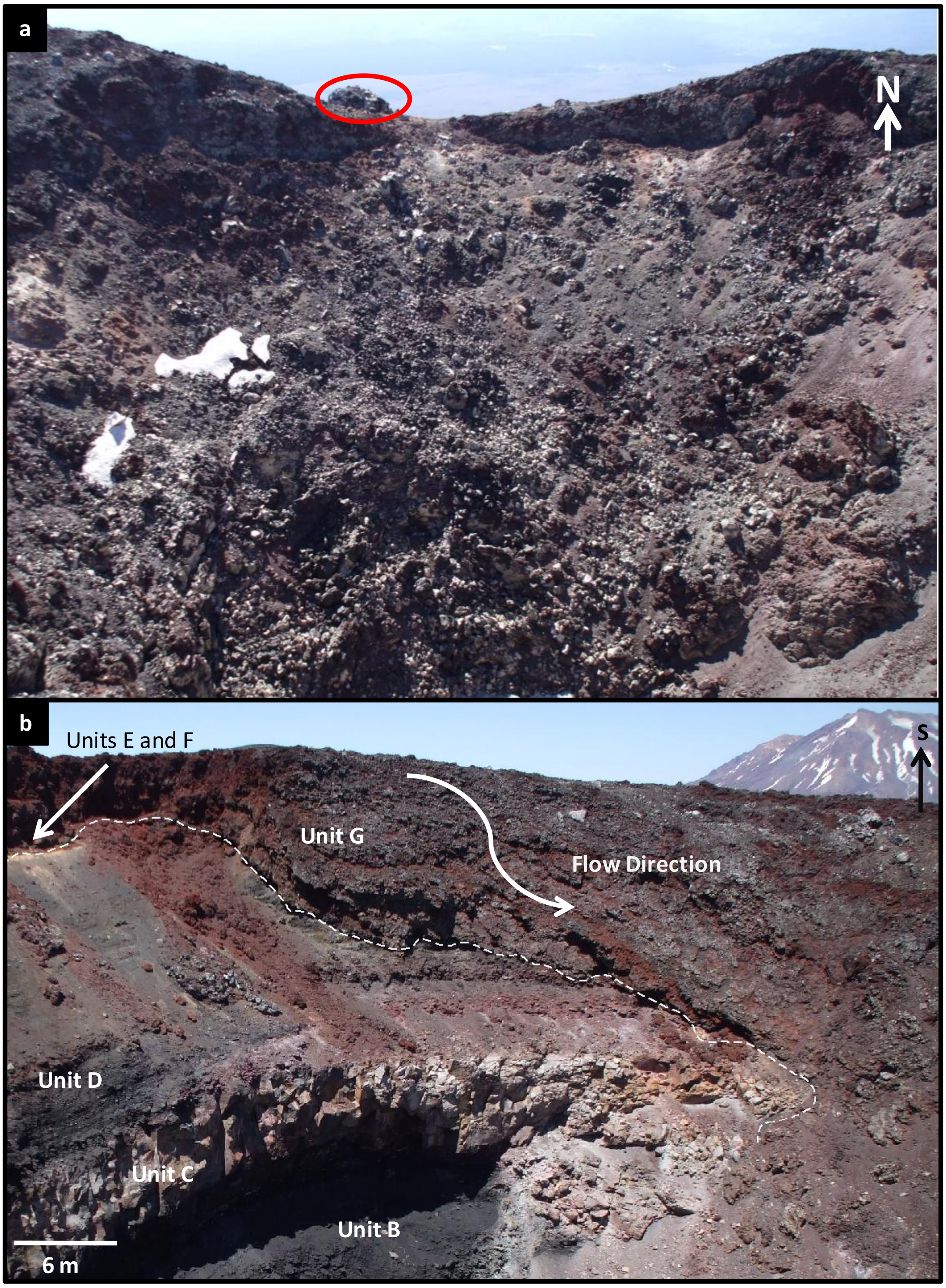

**Figure 2.2:** (a) Depression in the NW rim of the inner crater and resulting slump deposit that collapsed into the inner crater on March 28, 1975. Boulder in red circle is 4 m across. (b) Southern face of the inner crater with Unit G showing lava flow direction into the crater over lower southern stratigraphic units.

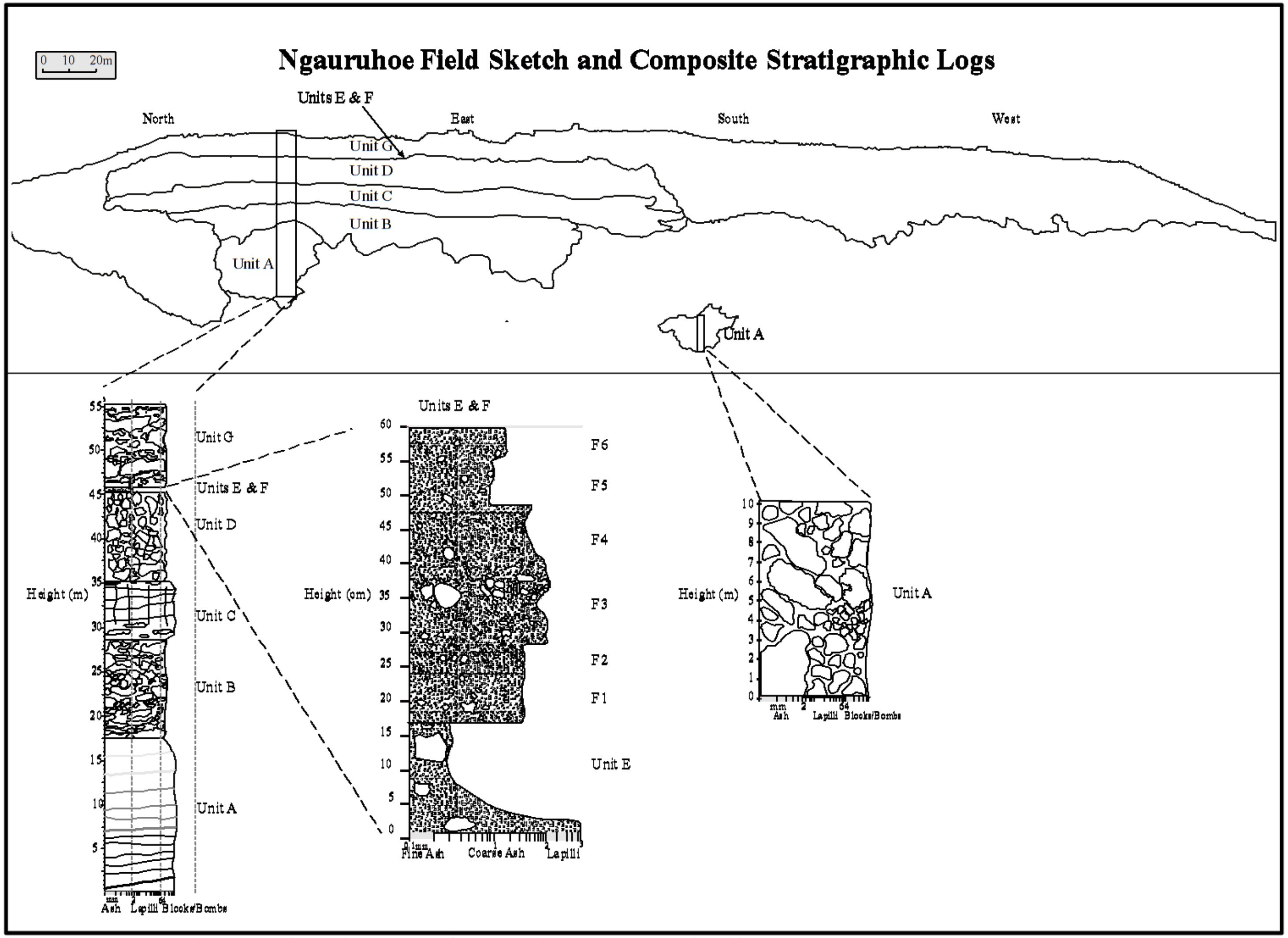

**Figure 2.3**: Crater sketch and composite stratigraphic logs of the Ngauruhoe Inner Crater Stratigraphic Succession

### 2.1.2 *Clast types*

Clast varieties composing the inner crater stratigraphic succession are categorised into three types: (1) scoriaceous juvenile clasts, (2) dense, poorly vesicular, sub-angular to angular basaltic andesite to andesite clasts, and (3) xenoliths. Type (1) juvenile clasts are primary basaltic andesite to andesite lapilli, blocks, and bombs directly related to the eruption, and are highly to poorly vesicular and generally sub-rounded. It is uncertain whether the type (2) basaltic andesite to andesite angular clasts are accessory and originate from pre-1954 or if they are primary and derived from the 1954-55 and 1974-75 eruptions. Type (3) xenoliths within the 1954-55 and 1974-75 eruptive products are accessory inclusions derived from underlying contact metamorphosed argillite greywacke basement and resulting quartz veins (Graham et al., 1988; Hobden, 1997).

### 2.1.3 *Terminology*

The term ‘bomb’ refers to sub-rounded to rounded clasts greater than 64 mm in size that were erupted in a fluidal state. Different morphologies within the inner crater stratigraphic units include spindle bombs – bombs with twisting occurring at the ends, and bread-crust bombs – bombs with a fractured, rounded surface, and many are deformed and elongate due to deposition and compaction.

The term ‘block’ is used to describe angular to sub-rounded clasts greater than 64 mm in size and generally poorly-vesicular, that were erupted in a solid state. It is uncertain whether these clasts originate from recycled pre-1954 eruptive materials and are thus accessory clasts, or whether they are juvenile and derived from either the 1954-55 or 1974-75 eruptions. Therefore, the term lithic, which is used to describe a clast with an origin different to the erupted host magma, is not used in this study.

## 2.2 Unit Descriptions

### *2.1.1 Unit A*

Unit A is the first unit to be deposited during the 1954-55 eruption, and discontinuously outcrops on the northern and southern walls of the inner crater (Figure 2.4). The northern deposit is a densely agglutinated basaltic andesite spatter deposit resulting from strombolian to fire fountaining activity that coalesced into a clastogenic lava (Figure 2.4a-b). Although the exposure of Unit A is incomplete, the spatter deposit interpretation (as opposed to homogenous lava emission) is based on the morphology of the unit, reflecting a post-depositional flow into the crater, and the dominance of fire fountaining and spatter in cone development.

The Unit A northern deposit has a thickness of 17.5 m, is blocky and fractured, and ranges from light pink to dark yellow-red in colour from post-depositional hydrothermal alteration, with a dark grey porphyritic interior. No individual clast outlines are present, and the clastogenic lava shows banding of variable thickness, interpreted to be the result of coalescence of spatter clasts, a process that masks original clast outlines (Sumner et al., 2005) (Figure 2.4b). Unit A lava has rounded lobe-like structures at the base and surface that appear to be flow-related, suggesting the partial flow back down the inner crater wall (Figure 2.4a). The lava has a low vesicularity with a smooth exterior. Coalescence of stil-molten clasts made it difficult to sample with a rock hammer. Unit A is directly overlain by Unit B, the base and eastern edge of the outcrop are obscured by scree, and the northern edge is overlapped by Unit G clastogenic lava.

The entirety of the 9.8 m thick Unit A southern outcrop (Figure 2.4c-d) is a spatter deposit largely covered in scree, and is also partly overlapped by the inward clastogenic lava flow of Unit G (Figure 2.6e). Draping over the basal portion of the southern deposit is a dense homogenous lava (the upper, smaller portion of Unit A), the same as that described in the northern outcrop of Unit A (Figure

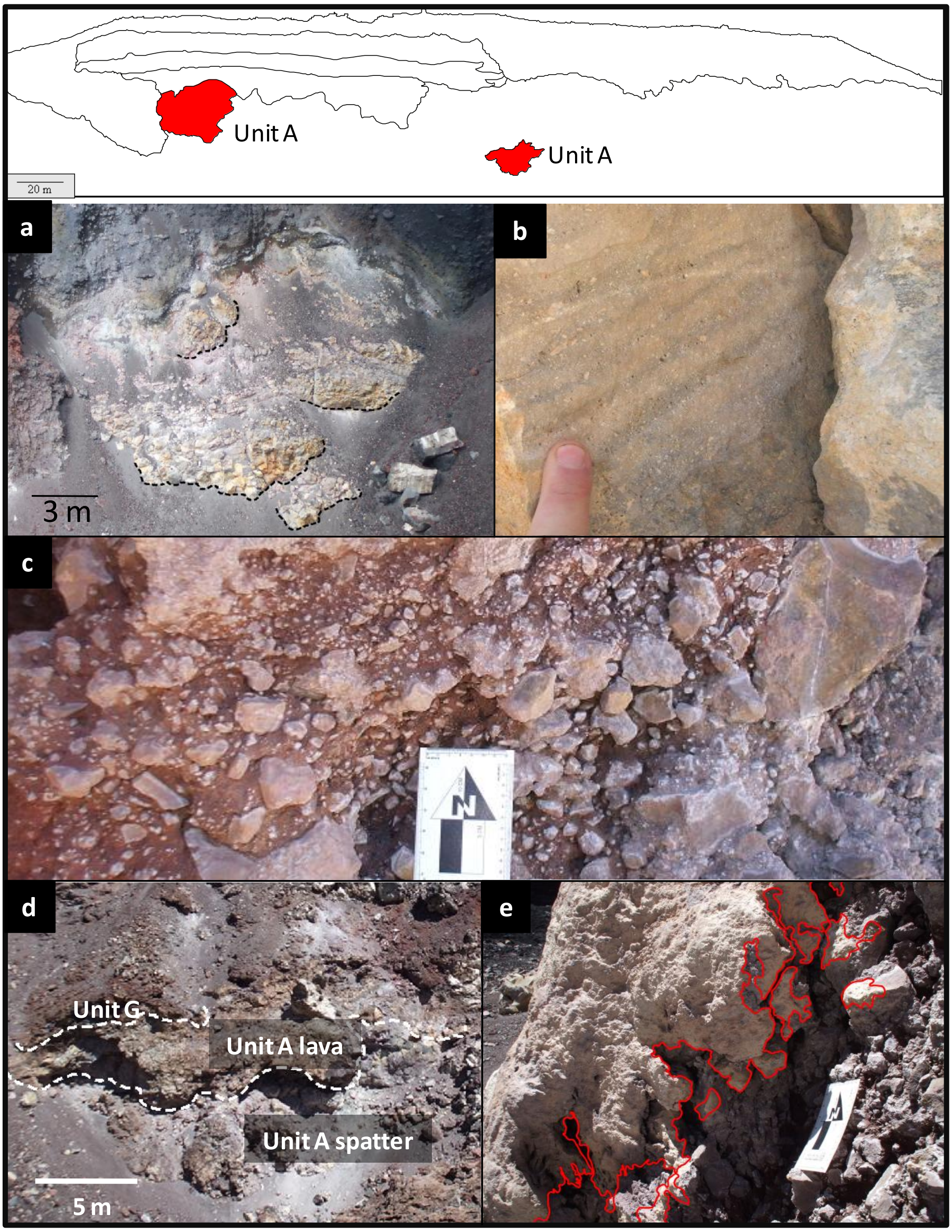

**Figure 2.4:** (a) 17.5 m thick Unit A northern outcrop with flow lobes indicated by dashed lines. (b) Unit A northern outcrop showing banding with finger for scale (photo courtesy of A. Pittari). (c) The southern outcrop of Unit A is a poorly agglutinated spatter deposit (Scale card 15.3 cm long). (d) Southern outcrop with overlapping of Unit A lava and Unit G lava. (e) The upper Unit A (southern deposit) lava (outlined in red) draped over the lower Unit A poorly agglutinated spatter deposit, (Scale card 15.3 cm long).

2.4f). The lava is a relatively thin layer (thinning to c. 1 cm thick at the flow edges) that drapes over the deposit with detached clots that have dripped onto underlying rocks (Figure 2.4f).

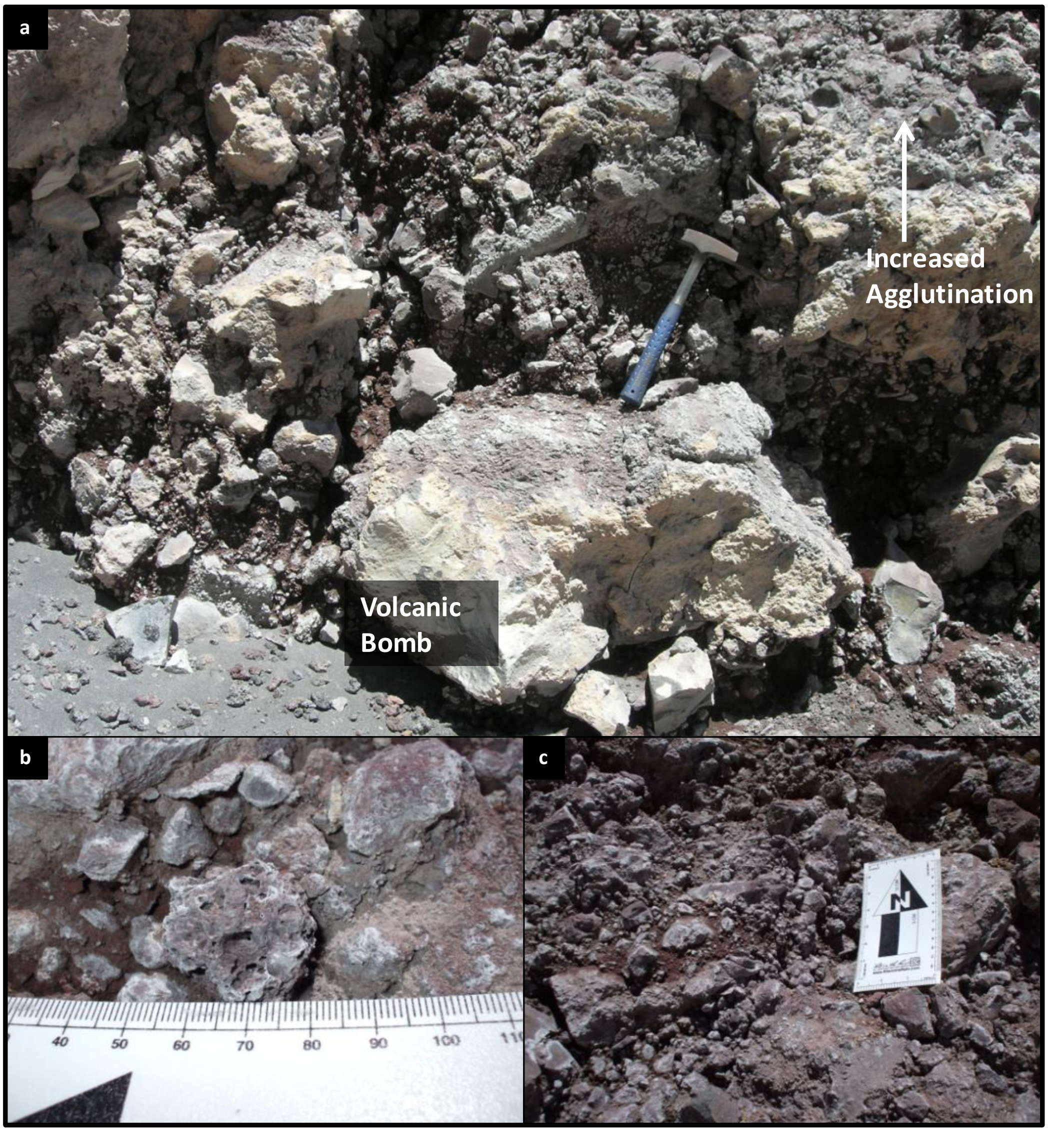

**Figure 2.5:** (a) View of the southern outcrop of Unit A with a larger volcanic bomb in the foreground, and variations in agglutination, rock hammer for scale (Photo courtesy of A. Pittari). (b) In situ dense, vesicular clast from southern deposit, scale in mm. (c) The range in clast sizes from lapilli to block and bomb, scale card is 15.3 cm in length.

This lava is then partly overlain by the southern portion of the Unit G lava flow, and loose scree. The deposit is poorly sorted, variably weakly to highly agglutinated with clear clast outlines and morphologies (Figure 2.5a-c). The deposit contains a red, coarse ash matrix between clasts (Figure 2.4c), and scattered (< 1% abundance) granular quartzofeldspathic xenoliths up to 2 cm in length. The clasts range in size from lapilli to bomb, and have a low vesicularity similar to that of the Unit A northern outcrop.

### *2.2.2 Unit B*

Unit B is exposed on the southern crater wall and was the second unit to be deposited during the strombolian phase of the 1954-55 eruption. It is an 11.2 m thick, poorly sorted, massive scoria deposit with a high abundance of fluidal,

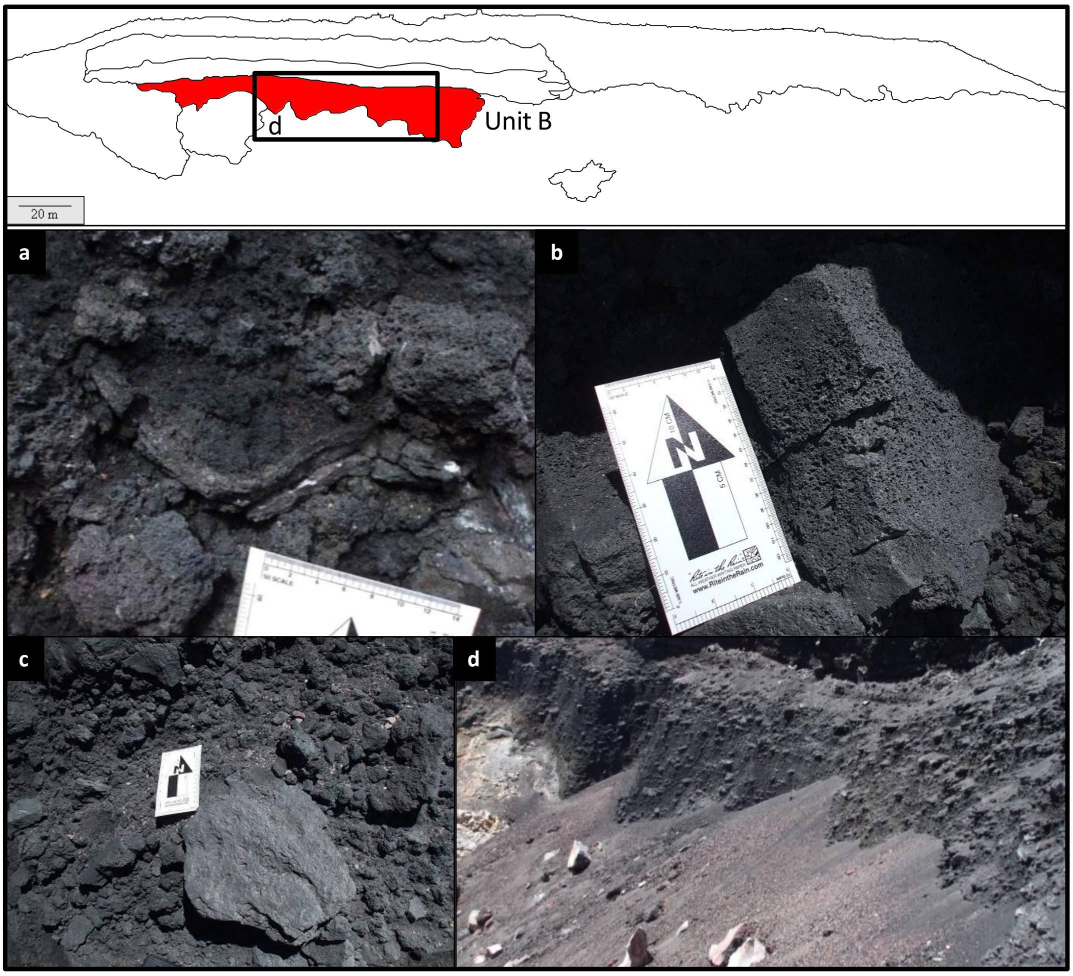

**Figure 2.6:** Unit B (a) fluidal bomb draping over scoriaceous lapilli and bombs, and small white xenolith inclusions, scale card is 8.4 cm wide. (b) Internal variation of vesicularity within a larger clast containing higher vesicularity in the centre, and a decrease in vesicularity to the rim. (c) Higher degree of agglutination of clasts on the northern side of the deposit. (d) Lateral photograph of Unit B showing larger, flattened bombs and lower contact with scree.

deformed bread-crust bombs draping over vesicular scoriaceous lapilli within a coarse ash–lapilli matrix (Figure 2.6a). Juvenile scoria clasts vary from moderately to highly vesicular, some clasts having zones of both (Figure 2.6b), with rare (< 2%) dense, angular, basaltic andesite lapilli and blocks up to 12 cm in diameter. Clasts are dominantly very-angular with minor sub-rounded morphologies. Some clasts (< 3%) appear quite glassy while most are dull black. The deposit is weakly agglutinated with a slight increase in agglutination towards the western side of the unit where the clasts are more welded and coherent (Figure 2.6c). White granular quartzofeldspathic xenoliths up to 5 cm in length are scattered through the deposit, with < 1% abundance (Figure 2.6a). The larger, flattened scoriaceous clasts have a horizontal alignment giving the deposit a sub-stratified appearance (Figure 2.6d). The Unit B outcrop is 32 m long with the northern end interrupted by the northern portion of the Unit G lava flow. The southern end of the outcrop is overlapped by the partial flow of Unit C, and the base of the deposit is obscured by black scoriaceous scree, with a gradational upper contact into Unit C.

### *2.2.3 Unit C*

Unit C (Figure 2.7a-d) is a 6.4 m thick variably banded to massive, columnar jointed, densely welded to coalesced basaltic andesite to andesite clastogenic lava that was produced during the 1954-55 eruption. It has lateral and vertical variation in both the degree of agglutination and welding, and vesicularity of spatter clasts. Due to the columnar jointing throughout the majority of Unit C, and undercutting of the underlying scoria deposit, large blocks have fallen into the crater (Figure 2.7b), allowing a closer inspection and sample collection. A moderately sharp upper boundary exists with the overlying Unit D and both the northern and southern ends of the outcrop are overlain by the Unit G lava flow. The southern end of the deposit has partially flowed downwards, obscuring the southern end of Unit B. The outcrop ranges in colour from black, to white, pink, and yellow from hydrothermal alteration. Towards the eastern termination of the outcrop, where the underlying Unit B overlies the southern outcrop of Unit A, there is a c. 15 m long zone with a decrease in agglutination resulting in a change to a more vesicular, black, scoria lapilli and bomb deposit, with dense white elongate bombs up to 2 m in length (Figure 2.7d). This then horizontally grades

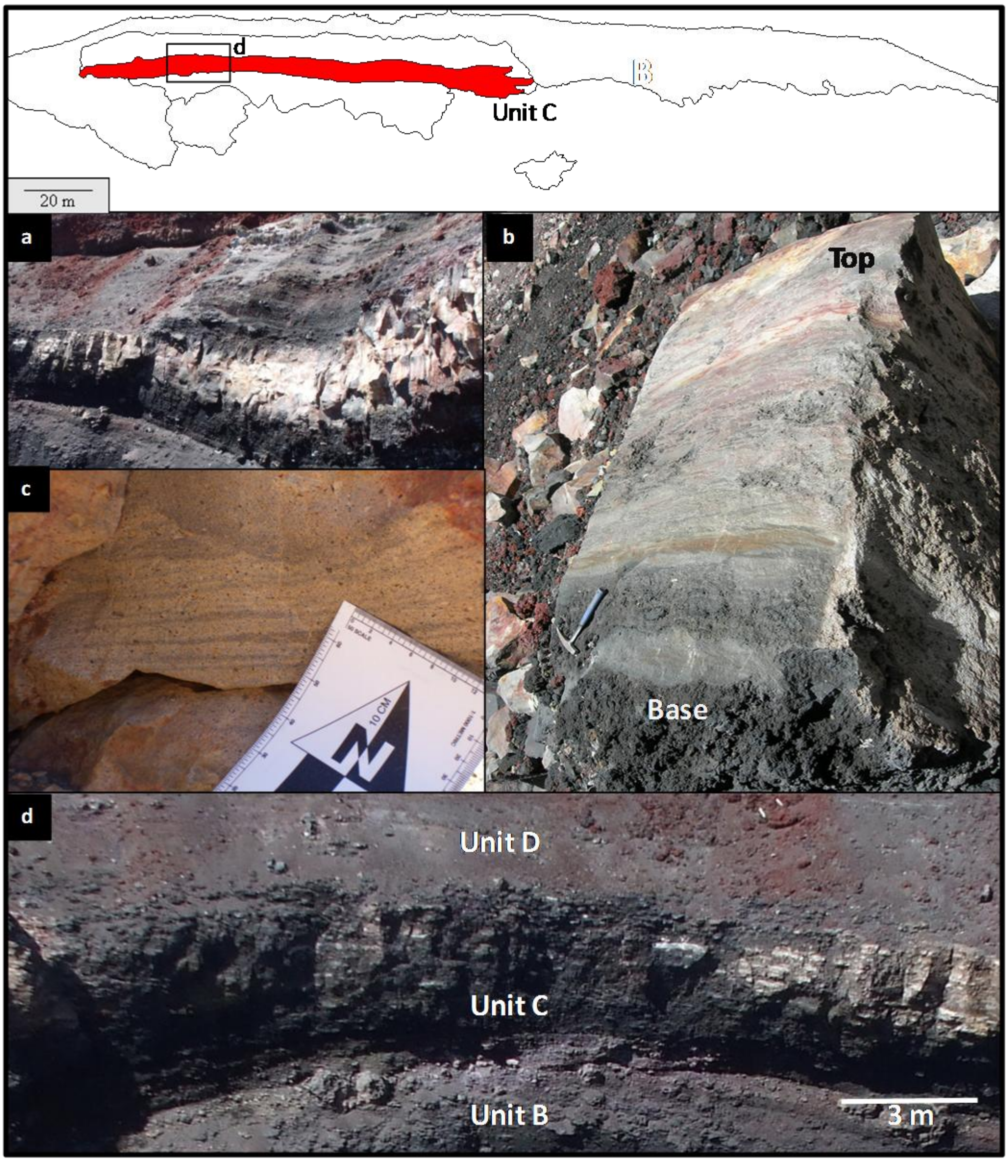

**Figure 2.7:** (a) North to south view of columnar jointed Unit C (average 6.4 m thick) with lower agglutination in the east. (b) Block of Unit C that had fallen into the crater, with hammer for scale. (c) Southern Unit C showing banding. (d) Close up of the eastern area (indicated in the upper map) of lower agglutination with dense flattened bombs, scale card 8.4 cm wide.

back into the dense, columnar jointed clastogenic lava seen at the southern end of the deposit.

The Unit C outcrop is c. 46 m long with a 1-2 m gradual vertical transition from the underlying Unit B, changing from the moderately (locally) agglutinated black scoriaceous lapilli and bombs of Unit B to the dense regionally agglutinated, light grey to yellow deposit centre that makes up the majority of Unit C. This broad transition zone is composed of highly agglutinated vesicular scoriaceous clasts and large flattened dense clasts up to 1 m long (Figure 2.7b). A thin (< 50 cm) layer at the top of the deposit is composed of black scoriaceous material. The rest of the deposit displays banding, with vesicular lenses at the base of the dense lava (Figure 2.7c), although no vesicular clasts are present in centre of the deposit. No quartzite xenoliths were seen in hand specimen but are described in thin section in Chapter Four.

### *2.2.4 Unit D*

Unit D is a discontinuous, parallel bedded, moderately sorted, basaltic andesite scoria lapilli to coarse ash (ash proportions given in Chapter 3, Figure 3.9) strombolian fallout deposit from the 1954-55 eruption (Figure 2.8a). The deposit contains beds up to 50 cm thick that alternate in degree of agglutination and dip c. 30°, parallel to the flanks of Ngauruhoe. The Unit D outcrop averages 10 m thick and 46 m in length. There is a sharp boundary with the overlying Unit E, and the ends of the outcrop are terminated by the Unit G clastogenic lava flow. Parallel bedding is more distinct in areas of increased agglutination, such as at the eastern end of the outcrop, but agglutination is generally weak to moderate across the outcrop. Little to no agglutination occurs at the top 2 m of the deposit (Figure 2.8b).

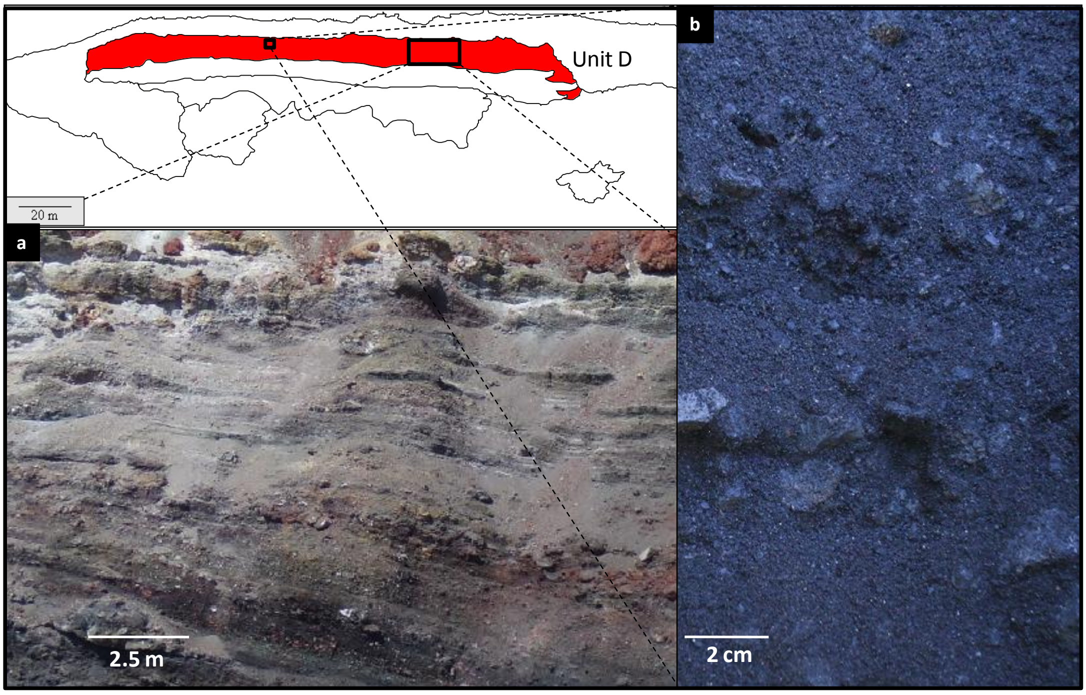

**Figure 2.8:** Unit D, (a) discontinuous parallel bedding in Unit D. (b) Upper portion of Unit D with weak bedding defined by concentrations in dense angular lithics.

Block and lapilli-sized basaltic andesite clasts are sub-angular to sub-rounded, ranging from dense to scoriaceous, and the deposit is moderately well sorted with a coarse ash to fine lapilli matrix. The outcrop has experienced varying degrees of hydrothermal alteration, with the more altered areas containing abundant crystals of gypsum (up to 7 mm) and sulfur (up to 2 mm). The top c. 2 m of the deposit is dominantly coarse ash to lapilli, with weak stratification developed by varying concentrations of angular dense basaltic andesite clasts (Figure 2.8b). Quartzofeldspathic xenoliths average 0.3 mm in length and are described in thin section in Chapter Four.

### *2.2.5 Unit E*

Unit E (Figure 2.9a-b) is a well sorted, pink-brown fine ash fallout bed interpreted to represent the final vulcanian phase of the 1954-55 eruption. Unit E contains minor dense angular basaltic andesite clasts reaching lengths of 10 cm, and lenses of grey coarse ash up to 2 cm thick (Figure 2.9a). Unit E is the thinnest unit in the crater with a thickness of 15 cm and with sharp upper and lower boundaries. No quartzose xenoliths were seen in outcrop or thin section.

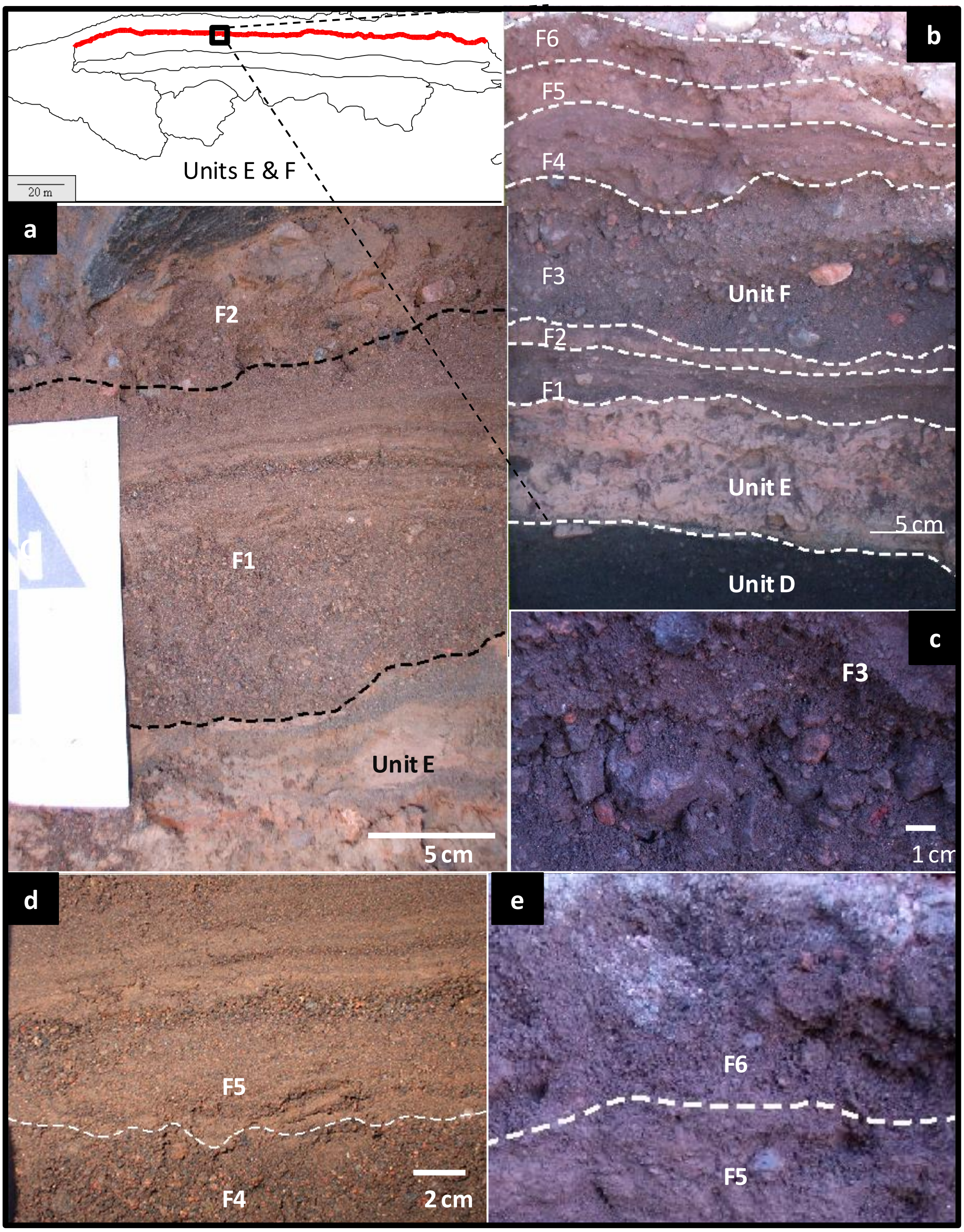

**Figure 2.9:** (a) Unit E and beds F1 (with laminations) and F2 containing angular dense clasts. (b) Units D, fine ash Unit E, and six defined coarse ash-lapilli beds within Unit F. (c) Coarse ash bed F3 containing dense basaltic andesite clasts. (d) Coarse ash bed F4 and coarse and fine ash laminations within bed F5. (e) Beds F5 and the uppermost coarse ash bed F6.

### 2.2.6 Unit F

Unit F is composed of a package of six coarse ash-lapilli fallout beds interpreted to mark the commencement of the 1974-75 vulcanian eruption. The unit has a total thickness of 45 cm, and sharp lower and upper boundaries with Units E and G, respectively (Figure 2.10). The six beds, F1 to F6, are distinguished by colour variation, grain size, and concentrations of dense angular lapilli and block content. Quartzose xenoliths are described in Chapter Four.

F1 (Figure 2.9a-b) is a c. 7 cm thick, well sorted, finely laminated (laminations up to 5 mm thick), brown/light brown coarse ash bed containing dense angular lapilli clasts up to 1.5 cm in length. The dense lapilli clasts average 5-10 mm in length and the majority of the clasts display rounding, with < 30% angular morphologies.

F2 (Figure 2.9a-b) is a c. 3 cm thick, well sorted light brown bed consisting of coarse ash (finer than Bed F1) with < 1% dense angular coarse ash clasts reaching 1.5 mm. A sharp boundary separates F2 from the underlying F1, and a gradual boundary exists with the overlying F3.

F3 (Figure 2.9b-c) is a light pink-brown, poorly sorted bed composed of subangular to subrounded lapilli in a coarse ash matrix with c. 48% dense angular lapilli and blocks, and is the thickest ash bed within Unit F at 13 cm. Approximately 90% of the dense clasts are < 1 cm in length, with the remaining 10% reaching lengths of 3 cm, and are sub-angular to angular. A gradual, undulating upper boundary is evident between F3 and the overlying F4.

F4 (Figure 2.9b-d) is a c. 8 cm thick dark brown coarse ash bed with medium brown laminations. F4 is well to moderately sorted, with < 5% rounded to sub-rounded dense lapilli clasts and rare angular lapilli clasts.

F5 (Figure 2.9b,d,e) is a c. 7 cm thick medium brown (lighter than F4) well sorted, coarse ash-lapilli bed with thin laminations (up to 7 mm thick), and a sharp upper boundary with the overlying F6. It contains < 1% dense sub-rounded to sub-angular blocks that are less than 1 cm in size.

F6 (Figure 2.9b-e) is the uppermost bed in Unit F. It averages c. 7 cm thick and is a moderately sorted, dark brown coarse ash and lapilli bed, containing reverse grading with increasing lapilli content towards the top. The very top of this bed is thinly laminated (< 5 mm thick laminations), with near-horizontal cross bedding of fine ash.

### *2.2.7 Unit G*

Unit G is a massive, oxidised red-brown densely welded, poorly sorted, strombolian spatter deposit averaging 10 m thick, that was deposited during the 1974-75 eruption. It is composed of dense, deformed and flattened juvenile spatter clasts with both diffuse and sharp clast boundaries, dense sub-rounded to rounded lithic clasts, and ≤ 5% granular quartzofeldspathic xenoliths, supported by a red coarse ash matrix (Figure 2.10a). Towards the base of the deposit there is a high proportion of dense, grey, basaltic andesite to andesite clasts, and to the south of the deposit the base contains a lower degree of agglutination (pers. comm. G. Kilgour). The quartzofeldspathic xenoliths are angular to very angular and range in size from < 1 cm to 10 cm. Unit G is the uppermost unit that mantles the inner crater rim. On the northern, southern, and western sides of the inner crater the deposit has partially flown down the inner walls, covering the lower stratigraphic units, and demonstrating flow morphologies with sub-rounded lobes at the foot of the deposit (Figure 2.10a-b).

The northern outcrop of Unit G has exposed the inner structure of the lava flow which is glassy and smooth, massive, poorly vesicular, dense, and fractured, with large (up to 5 cm length) granular quartzite xenoliths. There is a short, 10-15 cm transition into the red, scoriaceous outer rim of the deposit like that of the southern portion described above.

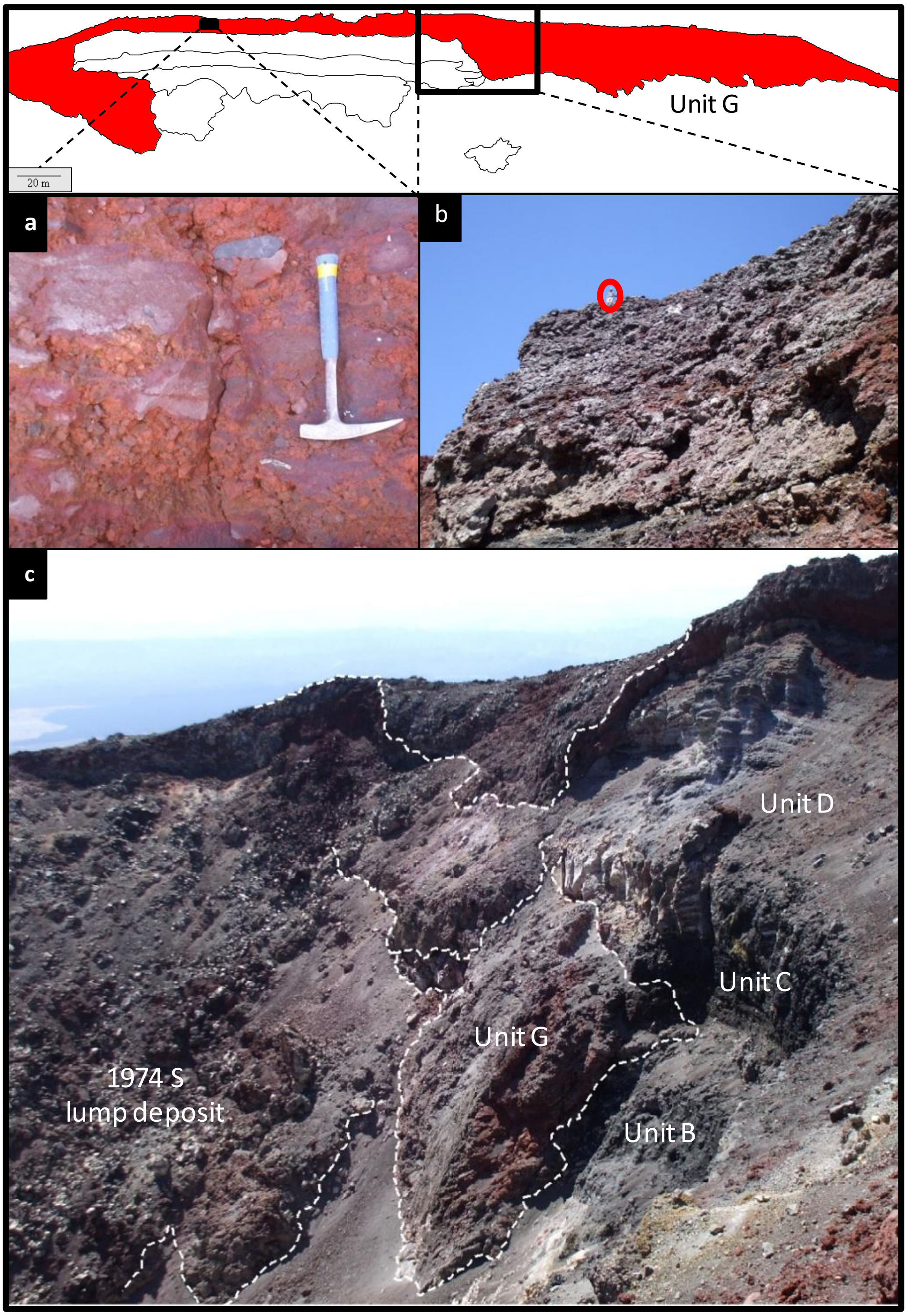

**Figure 2.10:** (a) Flattened basaltic andesite to andesite bombs of Unit G with scattered dense blocks (grey) and quartzofeldspathic xenoliths (white). (b) Flow direction of the southern portion of Unit G that flowed back into the crater and covered the underlying stratigraphy. Photo taken looking up from southern end of Unit C with person in red circle for scale. (c) Flow of Unit G into the northern sector of the inner crater, height of photo c. 50 m.

## 2.3 Inner Crater Rim Features

On the southern inner crater rim there is a pahoehoe-type flow with a ropy morphology, approximately 2 m wide by 5 m long and 15-30 cm thick, that partially flowed down the outer flanks of the inner crater cone (Figure 2.11a-b). There are no clast outlines or evidence of a clastogenic origin.

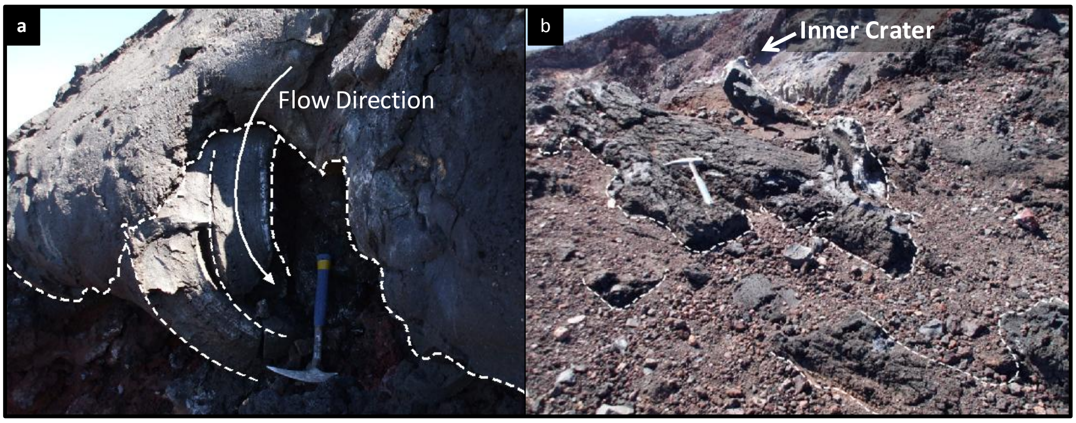

**Figure 2.11:** (a) Lava that flowed away from the southern Inner Crater rim over Unit G. (b) The surface of the lava on top of Unit G, with the inside of the inner crater in top right, and rock hammer for scale.

The later stages of the 1974-75 eruption ejected ballistic blocks and bombs that were deposited up to 2.4 km away. Fractured, smooth ballistic lava bombs with breadcrust textures up to 2 m in length are present around the crater rim on top of

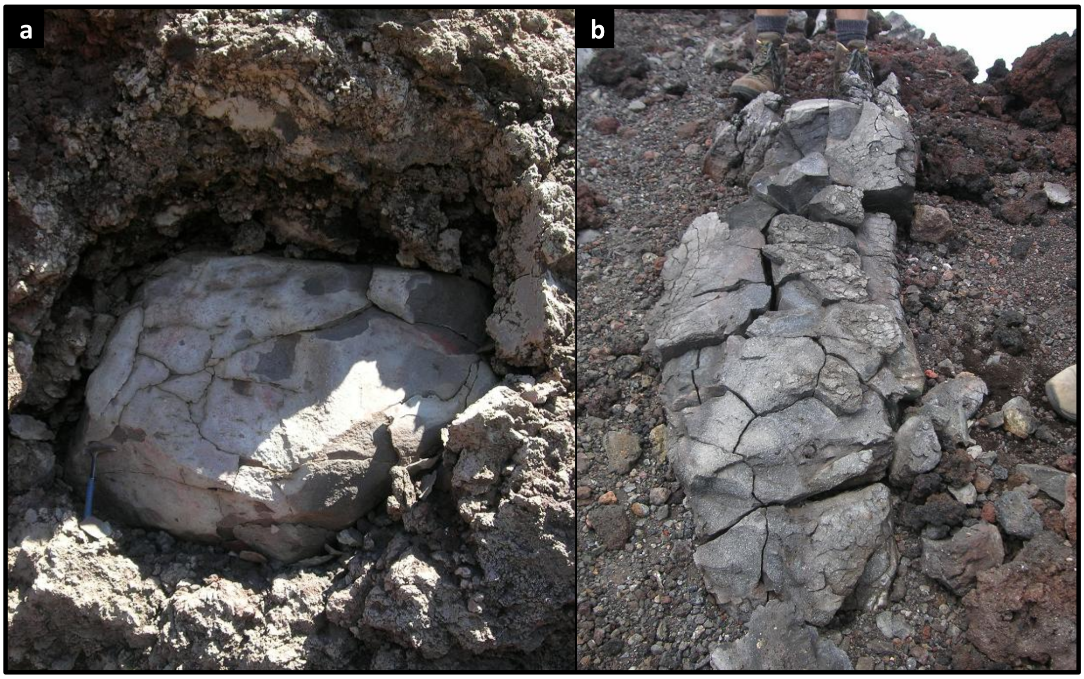

**Figure 2.12:** (a) Impacted dense bomb into the Unit G deposit on the southern inner crater wall, rock hammer for scale. (b) Fractured bread-crusted bomb on the northern rim of the inner crater, feet for scale above the clast, (photo courtesy of C. McKinnon).

Unit G (Figure 2.12a-b). Within the southern portion of the Unit G clastogenic lava flow deposit is a large, dense rounded bomb (1.7 m in diameter) that has impacted about 1 m into the flow (Figure 2.12a), indicating the viscous state of Unit G as it flowed down the southern wall of the inner crater. Large blocks up to 4 m in diameter have been deposited on the crater rim, and one particular bomb on the western rim with a diameter of c. 1.5 m has a high concentration of angular quartzose xenoliths (Figure 2.13) up to 3 cm in length (7-10% abundance). Blocks and bombs up to 15 cm in diameter were noted to have deposited in the Tongariro South Crater, 2.4 km away from Ngauruhoe, and the larger blocks were erupted in near-vertical parabolic trajectories, landing on the upper crater rim and in the fosse between the inner and outer craters (Nairn and Self, 1978). The largest recorded block to be ejected during the 1974-75 eruption was 27 x 15 x 3-4 m, weighing approximately 3000 tonnes, and was thrown into the summit fosse 100 m from the inner crater rim (Nairn and Self, 1978).

**Figure 2.53:** High xenolith concentration (white and yellow clasts) in a bomb deposited on the western inner crater rim, ejected during the 1974-75 eruption.

## 2.4 Summary

The Ngauruhoe inner crater stratigraphic succession was formed during the 1954-55 and 1974-75 eruptions, and has been divided into seven units based on field characteristics. Units A to E were constructed during the 1954-55 eruption, and

Units F and G represent the more recent 1974-75 eruption. The eruption experienced alternating vulcanian, strombolian, and possible fire fountaining phases. The seven units contain varying degrees of scoriaceous lapilli and bombs, dense basaltic andesite lapilli and blocks, ash, and xenoliths. Units A, B, C, D, and G are a result of strombolian to fire fountaining eruption phases, and Units E and F are products of vulcanian eruptions at the termination (Unit E) and commencement (Unit F) of the 1954-55 and 1974-75 eruptions, respectively.

# Chapter Three

# Clast Componentry and Morphology

## 3.1 Introduction

This chapter describes the characteristics of the clasts in each stratigraphic unit through clast componentry, morphology, deformation, and degree of agglutination. The characteristics are later interpreted and discussed in Chapter Five, and are used to determine the physical near-vent, depositional, and eruption processes. Vesicle characteristics including size, morphology, degree of coalescence, and vesicle content are indications of degassing and fragmentation processes occurring prior to, and during the eruption.

## 3.2 Methodology

Bulk and single clast samples of each unit were collected in the field, then described and photographed in the laboratory. Representative samples of each clast type were slabbed using a diamond tip saw to describe the inner clast textures. Thin sections were made and scanned to obtain a vesicle cross section for morphological description. Sieve and laser sizer analyses give proportions of block and bomb (> 64 mm), lapilli (64 – 2 mm), coarse ash (2 – 0.063 mm), and fine ash (< 0.063 mm) constituents.

Due to the degree of welding of Units A, C, and G in the inner crater, only samples from Units B, D, and F could be sieved. These bulk samples were sieved in the laboratory using whole phi intervals from -6 to 1. Bed F3 was the only ash bed of sufficient thickness to sieve.

The ash beds of Units E and F, and a sample from the upper 2 m zone of Unit D underwent particle size analysis using a Malvern Mastersizer ‘S’ laser diffraction particle size analyser. Laser sizer analysis gives an accurate volume percentage of coarse and fine ash, whereas sieve data gives a weight percentage of larger clasts. Representative samples were prepared by dry-sieving out the < 2 mm ash fraction.

Three-dimensional small scale images were obtained using a Scanning Electron Microscope/Energy Dispersive X-ray Analyser (SEM). Representative samples were adhered to a carbon-coated strip on an SEM stage before platinum coating for analysis. SEM images were taken at multiple magnifications from µm to mm scales to determine clast and vesicle morphologies and textures, and the identification of surface features such as secondary minerals and fine material adhered to clast surfaces. The high magnification through the SEM allowed for detailed descriptions of vesicle shapes and the degree of coalescence. The absence of quenching textures was confirmed.

## 3.3 Unit Componentry

### *3.3.1 Unit A*

***Northern Outcrop***

The yellow to red surface alteration in the northern outcrop of Unit A (Figure 2.4a-b) made it difficult to see any outcrop clast textures, but when a sample was removed, the fresh core is porphyritic and fractured with yellow discolouration along the fractures. No xenoliths are visible in hand specimen.

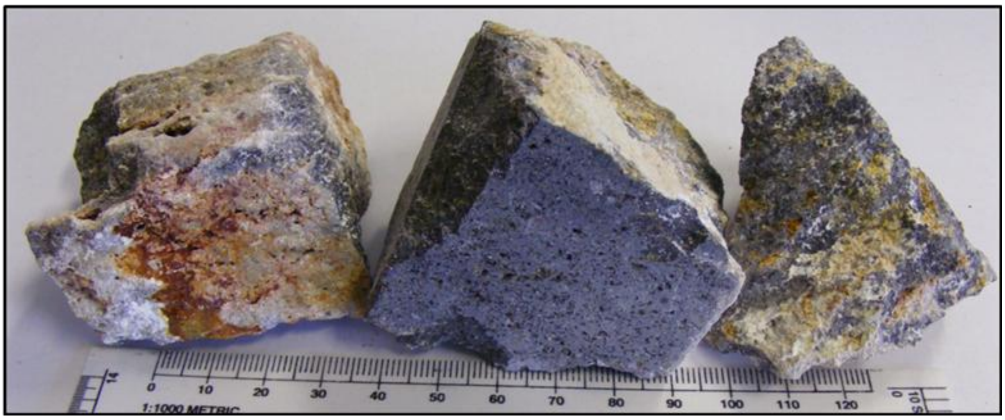

**Figure 3.1:** Slabbed poorly vesicular sub-angular blocks from the Unit A southern deposit, scale in mm.

***Southern Outcrop***

The southern outcrop is a poorly sorted, weakly to highly agglutinated (occurring when molten clasts fuse upon impact) basaltic andesite strombolian fallout deposit, with lapilli- to block-sized clasts (Figure 3.1) supported by a red ash matrix. The deposit is composed of c. 79% dense angular, poorly vesicular (< 10% vesicularity) juvenile lapilli and block clasts reaching ≥ 30 cm lengths with clear clast outlines (Figure 2.7c), an ash matrix comprising c. 20% of the deposit (Figure 2.7c), and < 1% granular quartzite xenoliths. Component proportions of Unit A, and other strombolian to fire fountain spatter and fallout deposits (Units B, D, and G) are summarised in Figure 3.2.

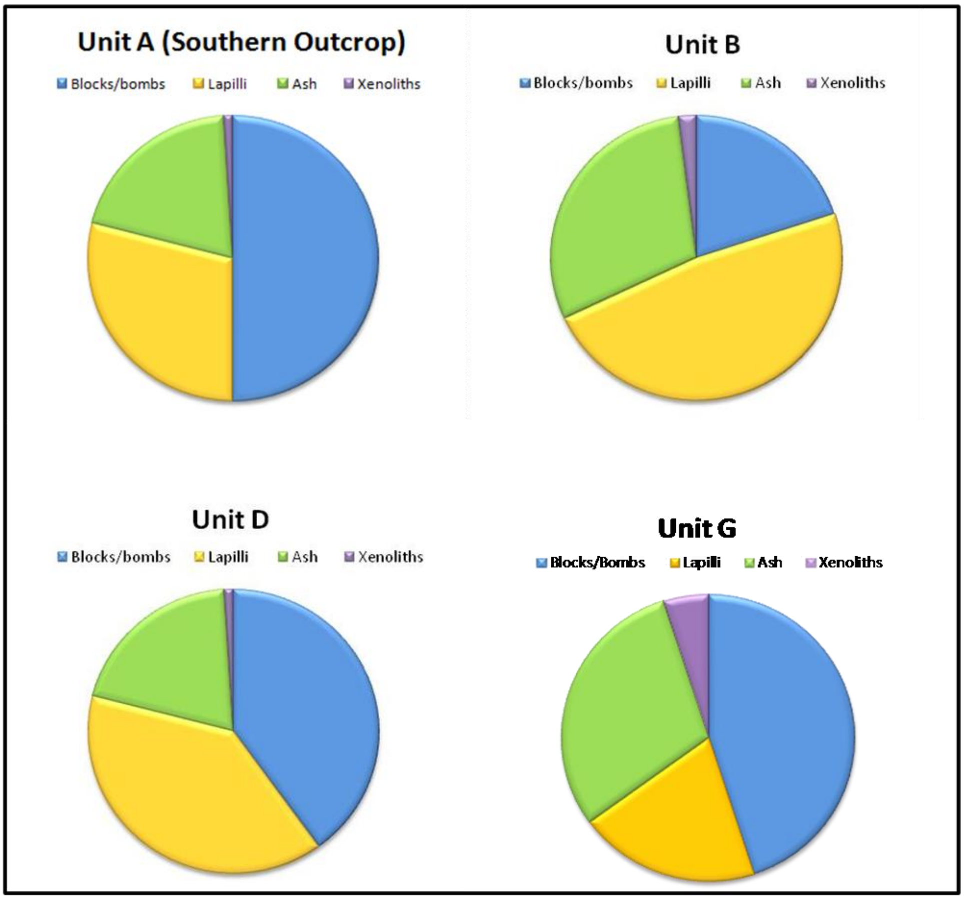

**Figure 3.2:** Grain size graphs (with xenolith proportions included) for strombolian spatter deposits, Units A (southern outcrop), B, D, and G. Block and bomb, lapilli, and ash proportions for Units B and D were obtained through sieving in the laboratory while xenolith percentages are estimated in the field. Units A and G grain size proportions were estimated in the field

The dense clasts range in shape and size, from sub-rounded lapilli to sub-rounded elongate bombs > 60 cm long. The deposit exhibits varying degrees of agglutination from low (clasts easily plucked from deposit by hand) to high (clasts cannot be sampled without a rock hammer) (Figure 2.5a). Clasts containing higher vesicularities are rare within the deposit (Figure 2.5b), and coalesced vesicles up to 8 mm across with partially-relaxed vesicle walls still intact. Many vesicles > 1 mm in diameter are elongate either due to pre-eruption distortion, flattening upon impact, or from overlying pressures, while smaller vesicles < 1 mm are more spherical, likely due to late formation during eruption. The dense lapilli and block clast surfaces are hydrothermally altered to colours from white to reddish-brown, with crystals of sulfur (up to 5 cm long) scattered around the clasts. The clasts are porphyritic with feldspar phenocrysts up to 1 mm long.

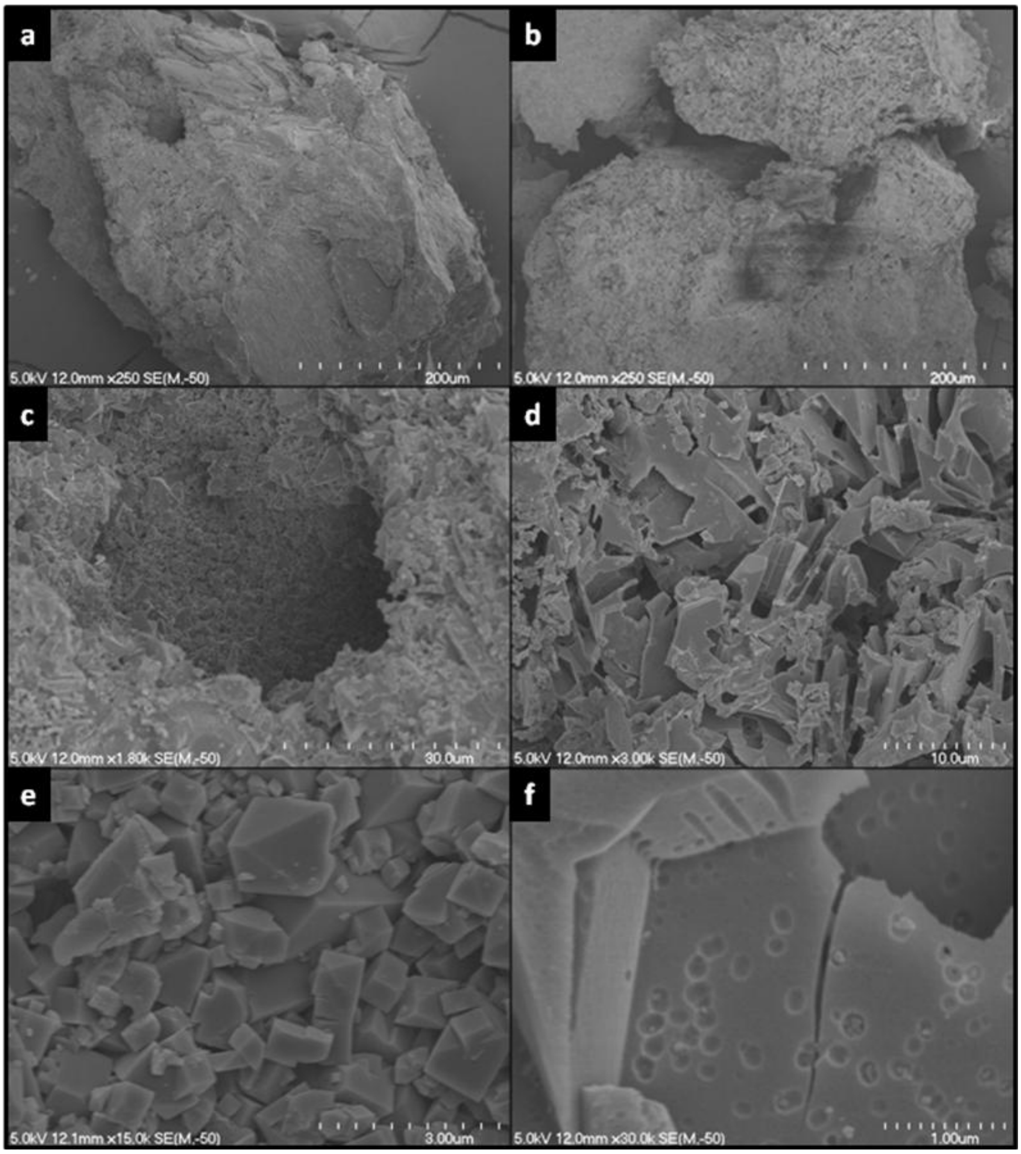

**Figure 3.3:** SEM images of ash-sized samples of Unit A. (a) Ash-sized clast showing surface and vesicle textures. (b) Surface textures of two ash-sized clasts. (c) Magnified view of vesicle textures. (d) Surface texture showing groundmass with dissolved microlite remnants. (e) Adhered crystals on clast surface. (f) Weathering texture on glassy material.

Scanning Electron Microscope (SEM) images of Unit A matrix grains show blocky to sub-rounded, poorly vesicular grains with irregular surfaces. Fine crystals and ash (< 3 µm) are adhered to the clast surfaces and within vesicle cavities (Figure 3.3a-c). The surfaces have sharp, elongate circular cavities (Figure 3.3d) that likely represent remnant microlites that were dissolved during hydrothermal vapour-phase alteration. Vapour-phase mineralisation and secondary alteration mineral growth of metastable cristobalite has occurred within vesicle cavities, with smooth, cubic morphologies (Figure 3.3e). Some glass surfaces have pock-marks indicative of weathering and/or hydrothermal or vapour-phase dissolution (Figure 3.3f).

### *3.3.2 Unit B*

Unit B is a poorly sorted, massive strombolian scoria and spatter deposit. The deposit grain size proportions are approximately 20% blocks, 47% lapilli, and 30% ash, (Appendix One) with < 1% quartzofeldspathic xenolith component. Two major juvenile clast morphologies are present within Unit B: fluidal, deformed scoriaceous bombs, and irregular scoriaceous blocks with variable vesicularities (Figure 3.4), ranging in colour from dull dark grey to glassy black. All clasts are coarsely porphyritic with phenocrysts reaching ≥ 1 mm in diameter. Vesicular spindle bombs containing elongate vesicles drape over the underlying clasts (Figure 3.4b-d).

Quartzofeldspathic xenoliths up to 5 cm in length are scattered throughout the deposit. Smaller quartzofeldspathic xenoliths (up to 7 mm in length) occur as inclusions within clasts, while the larger xenoliths are generally loose within the deposit (i.e. not contained within a juvenile clast). The intra-clast xenoliths have sugary or granular textures and are colourless with small granules breaking off around the main clast (Figure 3.4e-f), while the larger loose xenoliths are either granular, or angular non-granular clasts (xenolith characteristics discussed further in Section 3.4).

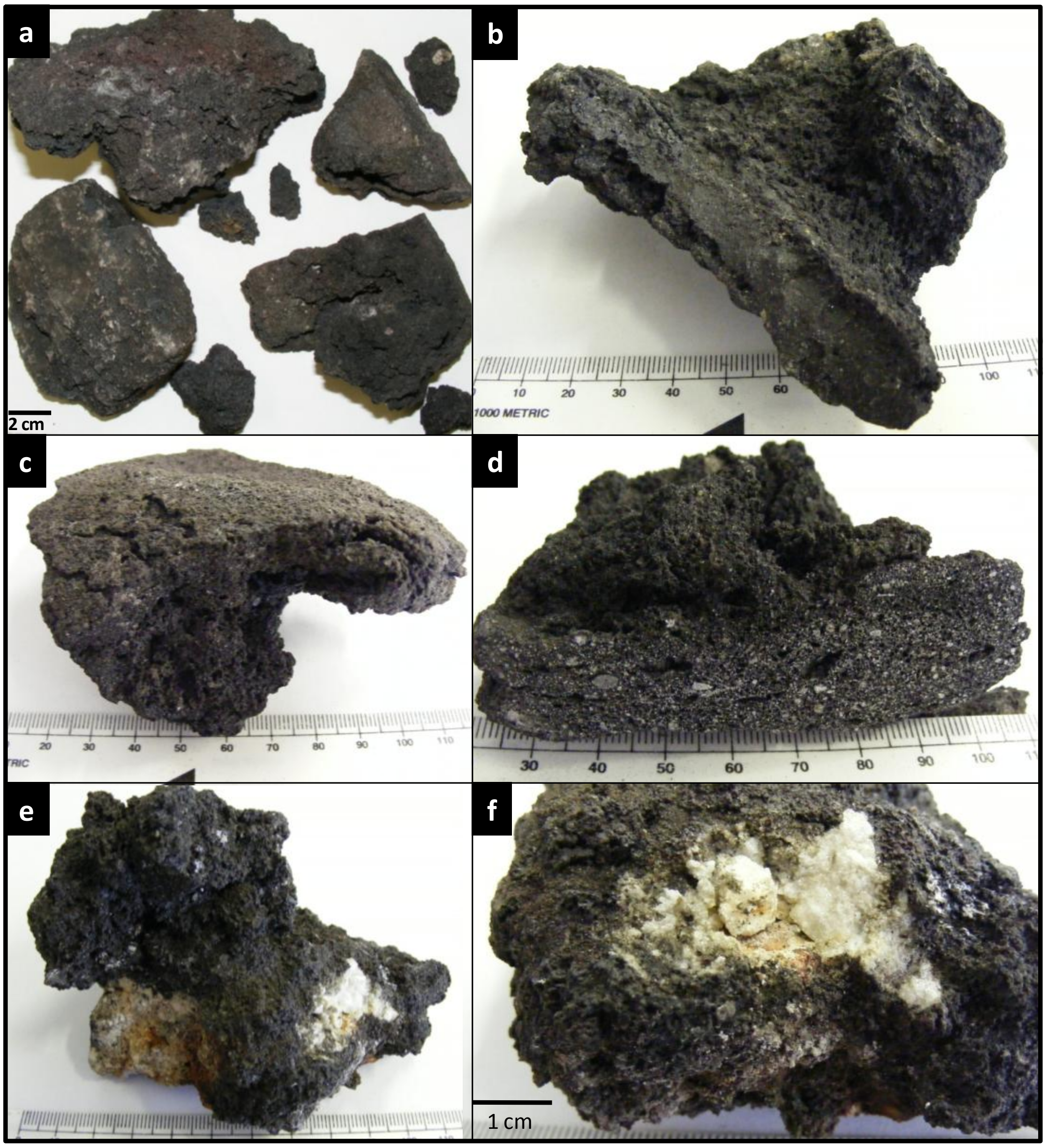

**Figure 3.4:** Scoriaceous clasts from Unit B. (a) Fluidal, deformed scoriaceous bomb morphologies. (b) Fluidal bomb with a scoriaceous crust and less vesicular core. (c) Fluidal scoriaceous bomb that experienced deformation upon deposition. (d) Porphyritic interior of fluidal clast with large coalesced elongate vesicles. (e) Very-angular scoriaceous bomb containing a large quartzofeldspathic xenolith inclusion. (f) Enlarged view granular quartzite inclusion from (e) illustrating the granular, fragile texture. (a) to (e) scale bar increments in mm.

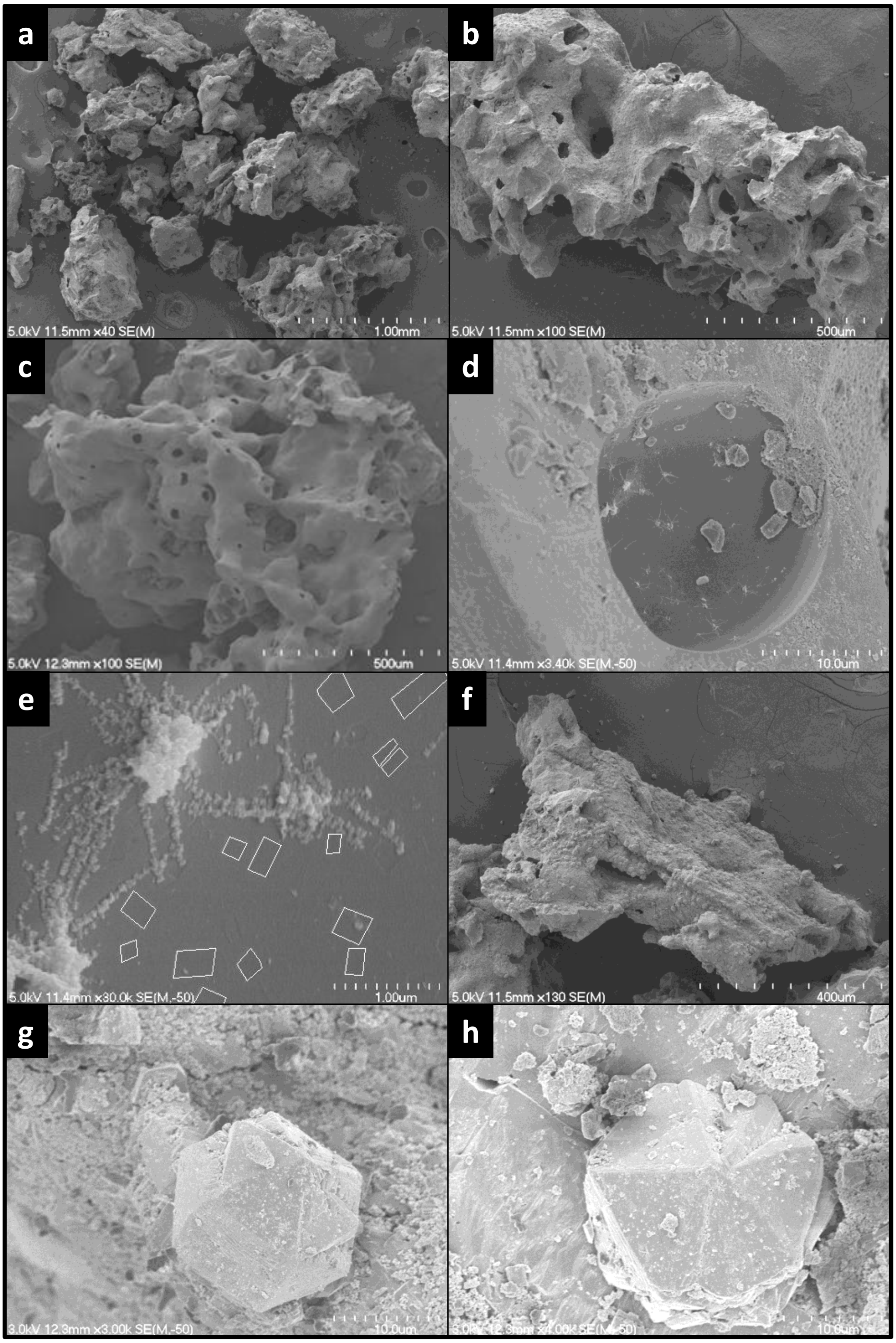

**Figure 3.5:** SEM images of Unit B, (a) irregular, vesicular ash particle morphologies. (b) An ash clast with abundant ruptured vesicle walls. (c) Smooth-surfaced ash particle with ruptured vesicle cavity walls visible on the surface, outlined in white. (d) A relatively smooth ash particle with ruptured vesicle walls. (e) Opaline growth within a smooth ash particle vesicle with remnant outlines of dissolved crystals. (f) Abundant cryptocrystalline material adhered to an ash clast surface. (g and h) Bipyrimidal quartz crystals that have grown on the clast surface.

SEM images of the Unit B ash fraction show a range in clast morphologies from rounded with high vesicle coalescence, to blocky with elongate vesicles, and blocky, poorly vesicular clasts (Figure 3.5a). Unit B has the highest degree of bubble coalescence of the inner crater deposits, seen in Figure 3.5b-c, with a large degree of ruptured vesicle walls. The vesicle cavity walls are smooth and rounded with a spider-web-like growth of amorphous opaline material (hydrated silica) (Figure 3.5d-e), and relict crystal imprints where vapour-phase dissolution may have dissolved minerals adhered to the surface (Figure 3.5e). Some dense blocky clasts have abundant cryptocrystalline material adhered to the clast surface and within vesicle cavities (Figure 3.5f), with some crystallisation of secondary metastable minerals (Figure 3.5g-h).

### *3.3.3 Unit C*

Unit C is a densely agglutinated strombolian to fire fountain spatter deposit with the characteristics of coalesced, clastogenic lava, such as columnar jointing and banding. The deposit is composed of approximately 80% dense spatter agglutinate, and up to 20% vesicular scoriaceous material (Figure 3.6a-f). Some individual agglutinated scoriaceous clasts (at the base and top of the deposit) contain an increasing vesicularity towards the rim (Figure 3.6b), and the majority of vesicles have irregular morphologies due to bubble coalescence. Clasts in the upper scoriaceous portion of the deposit have a more uniform vesicle size and distribution than those at the base of the deposit (Figure 3.6f). Vesicle walls are generally irregular, with smaller vesicles (≤ 1 mm in diameter) exhibiting more spherical shapes.

A 15 m long zone of decreased agglutination occurs to the north (Figure 2.7d) containing scoriaceous clasts similar to Unit B, and large, flattened dense bombs reaching up to 2 m in length. The section was inaccessible preventing a more detailed description. The upper (Figure 3.6a-b) and lower (Figure 3.6e-f) boundaries of Unit C are both composed of highly agglutinated, angular to very-angular scoriaceous bombs, with variable vesicularities from moderately to highly vesicular. The centre and majority of the deposit is dense, coalesced spatter containing a lower vesicularity (Figure 3.6c-d).

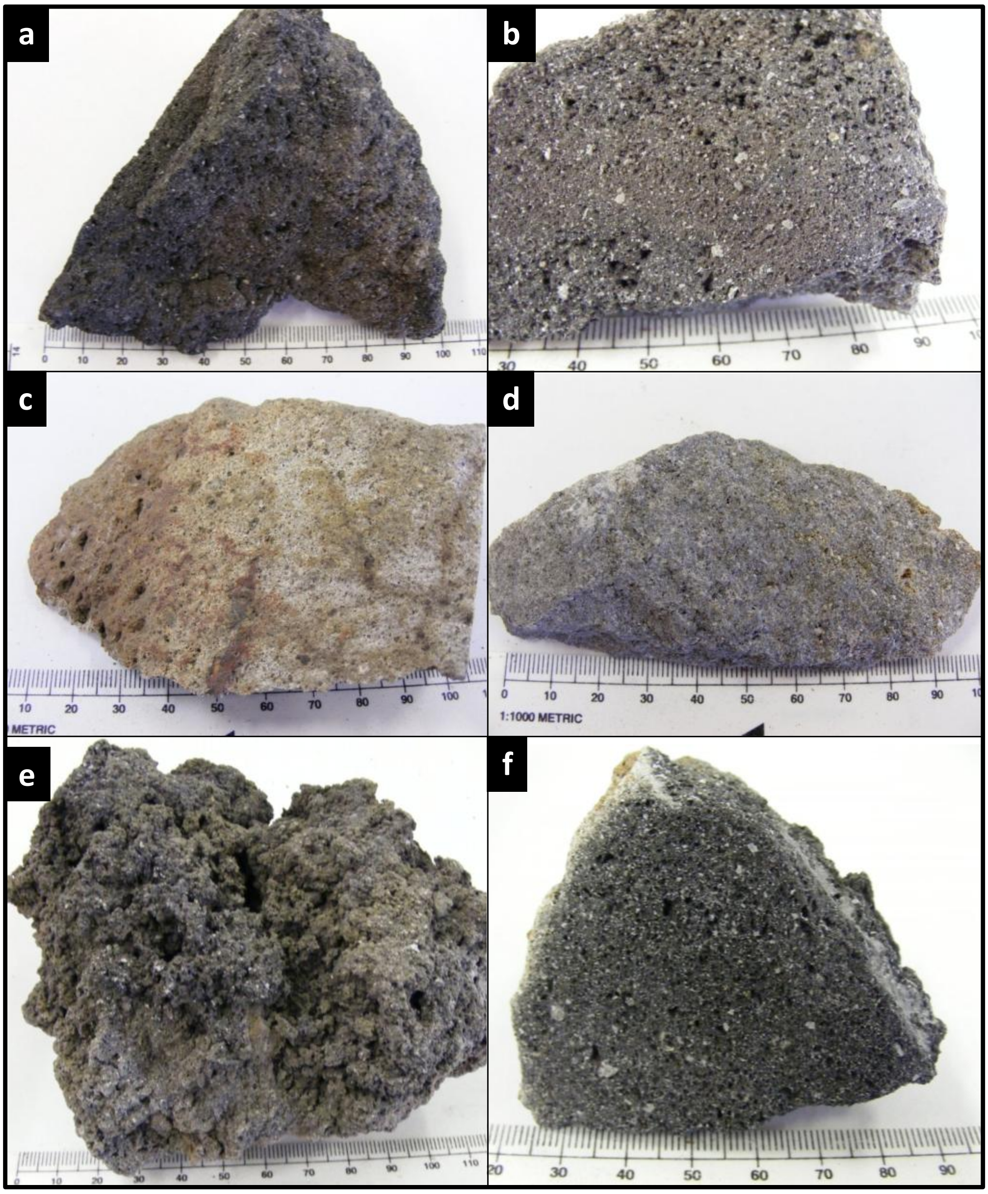

**Figure 3.6:** Samples from Unit C collected from a detached block within the crater, with a-b from the base of the deposit, c-d from the centre, and e-f from the top of the deposit. (a) Angular scoriaceous bomb. (b) Variation in vesicularity from core to rim of clast. (c) Dense, clastogenic lava sample from the surface of the deposit. (d) Grey, porphyritic interior of the centre of the deposit. (e) Very angular scoriaceous bomb. (f) Vesicular, porphyritic centre of scoriaceous bomb. All scale bar increments in mm.

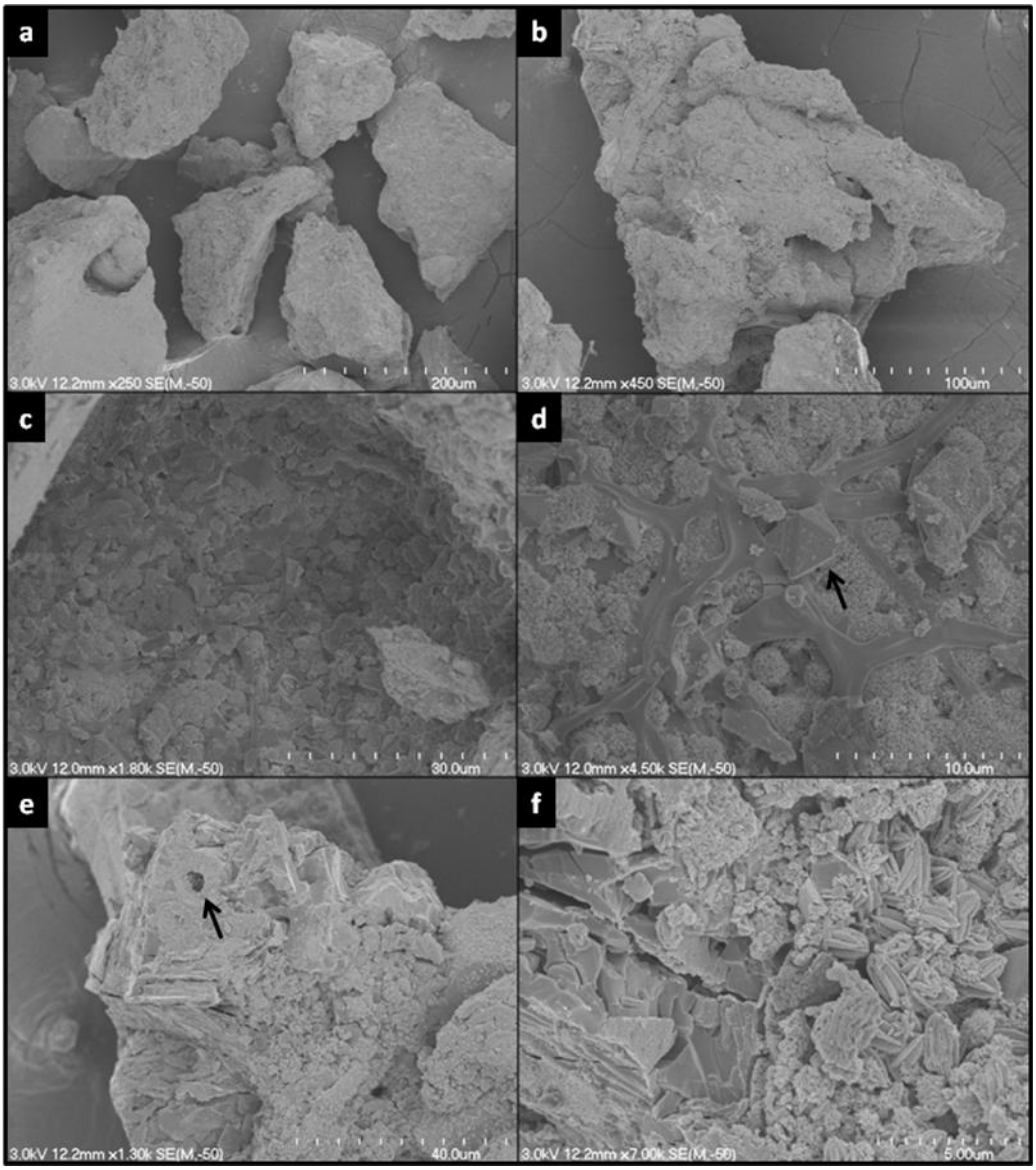

**Figure 3.7:** SEM images of samples from the upper portion of Unit C. (a) Sub-angular, non-vesicular ash-sized clast morphologies. (b) Sub-angular ash-sized particle with an irregular surface and a vesicle at the base of the clast. (c) Magnified view of the vesicle shown in (b), with fine cryptocrystalline material. (d) Greater magnification of the vesicle surface, showing a glassy web-like structure and crystals (black arrow), see text for crystal identification. (e) Irregular surface of an ash-sized particle with cryptocrystalline material adhered to the surface, and an elongate vesicle indicated by the arrow. (f) Magnified cryptocrystalline material adhered to a clast surface (see text for description).

Representative SEM images from the upper scoriaceous portion of the deposit are presented in Figure 3.7. Clasts are generally angular to sub-angular and poorly vesicular, with irregular surfaces (Figure 3.7a-b). The clast surfaces and vesicle cavities have abundant vapour-phase mineralisation products (Figure 3.7c), such as cristobalite (Figure 3.7d), with some adhered crystals and fine ash, and clusters of quartz polymorphs between a web of basaltic andesite glass. Cryptocrystalline material is illustrated in Figure 3.7e on a sub-angular ash particle, and magnified in Figure 3.7f, demonstrating gypsum crystals.

### *3.3.4 Unit D*

Unit D is a moderately sorted, basaltic andesite scoria lapilli to coarse ash strombolian fallout deposit, with discontinuous-parallel bedding due to varying degrees of agglutination. Grain size proportions from the poorly agglutinated subunit are approximately 40% ash (99.6% coarse ash and 0.4% fine ash, see Appendix Two), 40% lapilli, and 20% blocks and bombs (Figure 3.2). The blocks and bombs are sub-angular to sub-rounded clasts (Figure 3.8a) and vary in vesicle size from < 1 mm diameter to coalesced vesicles up to 10 mm in length (Figure 3.8b-f).

Unit D has undergone a large degree of hydrothermal alteration resulting in secondary mineral growth of sulfur and gypsum (identified through XRD analysis) visible in hand specimen (Figure 3.8a,c,d,f). Crystals of gypsum and sulfur have grown to c. 7 mm and c. 2 mm in length, respectively. SEM images of Unit D ash particles are illustrated and described in Figure 3.9a-f.

### *3.3.5 Unit E*

Unit E is the first unit within a series of ash beds underlying Unit G. The grain size proportions of these beds (Units E and F) are summarised in Figure 3.10. Unit E is a fine ash bed containing ≤ 5% dense lapilli and blocks, with the remaining 95% ash portion composed of 32% coarse ash and 68% fine ash (Figure 3.10). Angular, dense lapilli and blocks (Figure 3.11) reach 10 cm in diameter, although only one clast of this size was recorded.

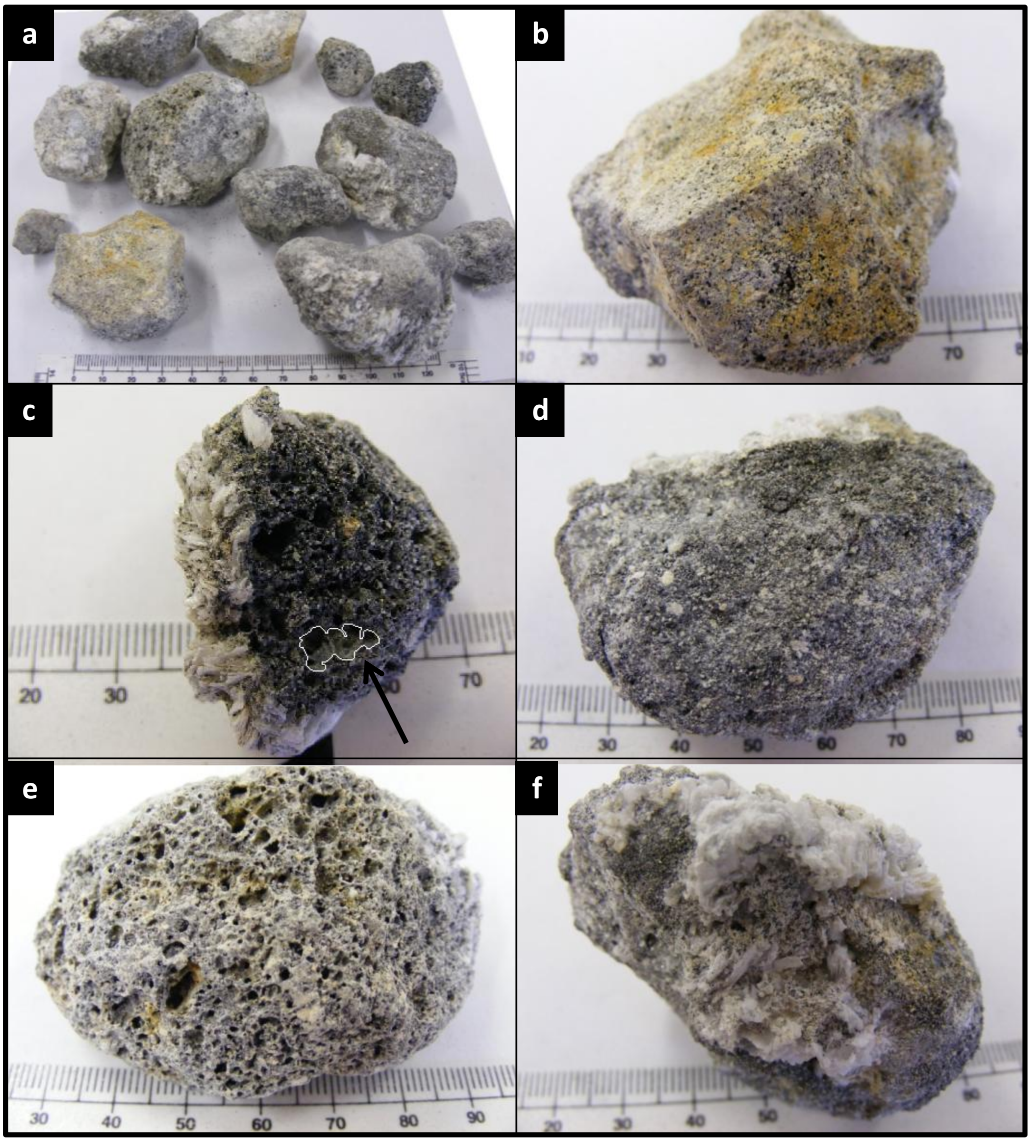

**Figure 3.8:** Lapilli and block clasts from Unit D. (a) Sub-rounded, poorly to moderately vesicular lapilli-blocks from Unit D. (b) Less vesicular, angular clast that has undergone hydrothermal alteration resulting in discolouration. (c) Sub-rounded vesicular lapilli clast showing vesicle coalescence, indicated by the arrow. (d) Less vesicular, sub-rounded lapilli clast. (e) Higher vesicularity, rounded lapilli clast. (f) Dense lapilli clast with crystals of gypsum and minor sulfur adhered to the surface. All scale bar increments in mm.

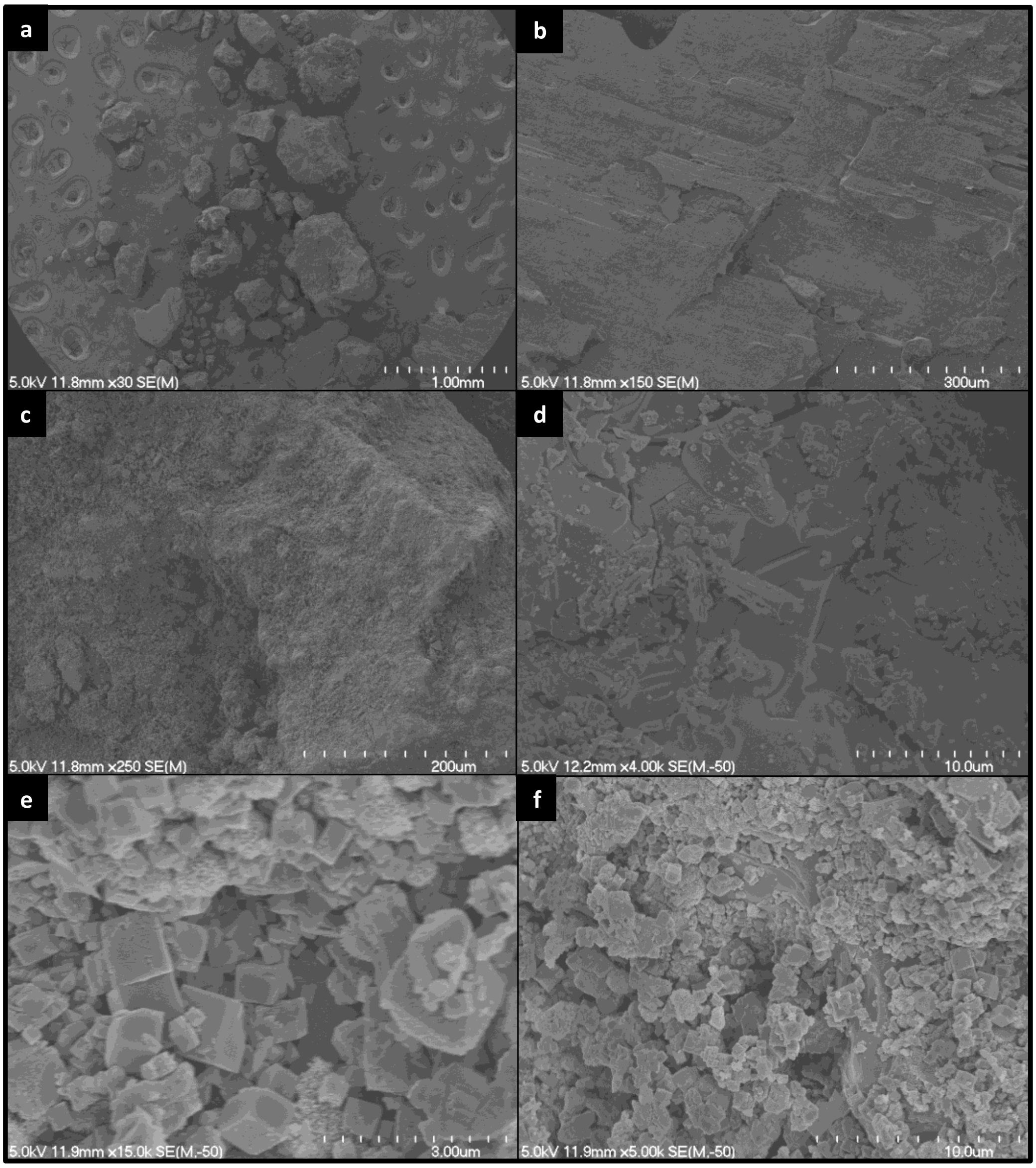

**Figure 3.9:** SEM images of a sample of the ash fraction from the top of Unit D. (a) A range in poorly vesicular sub-rounded to sub-angular ash-sized particles. (b) Planar, flaky surface of an ash particle. (c) Cryptocrystalline material adhered to the irregular surface of an ash particle. (d) Magnified view of cryptocrystalline material on a relatively smooth, glassy surface. (e) Cubic cristobalite crystals on the surface of an ash particle. (f) Crystals of cristobalite and tridymite (?) with irregular basaltic-andesite material.

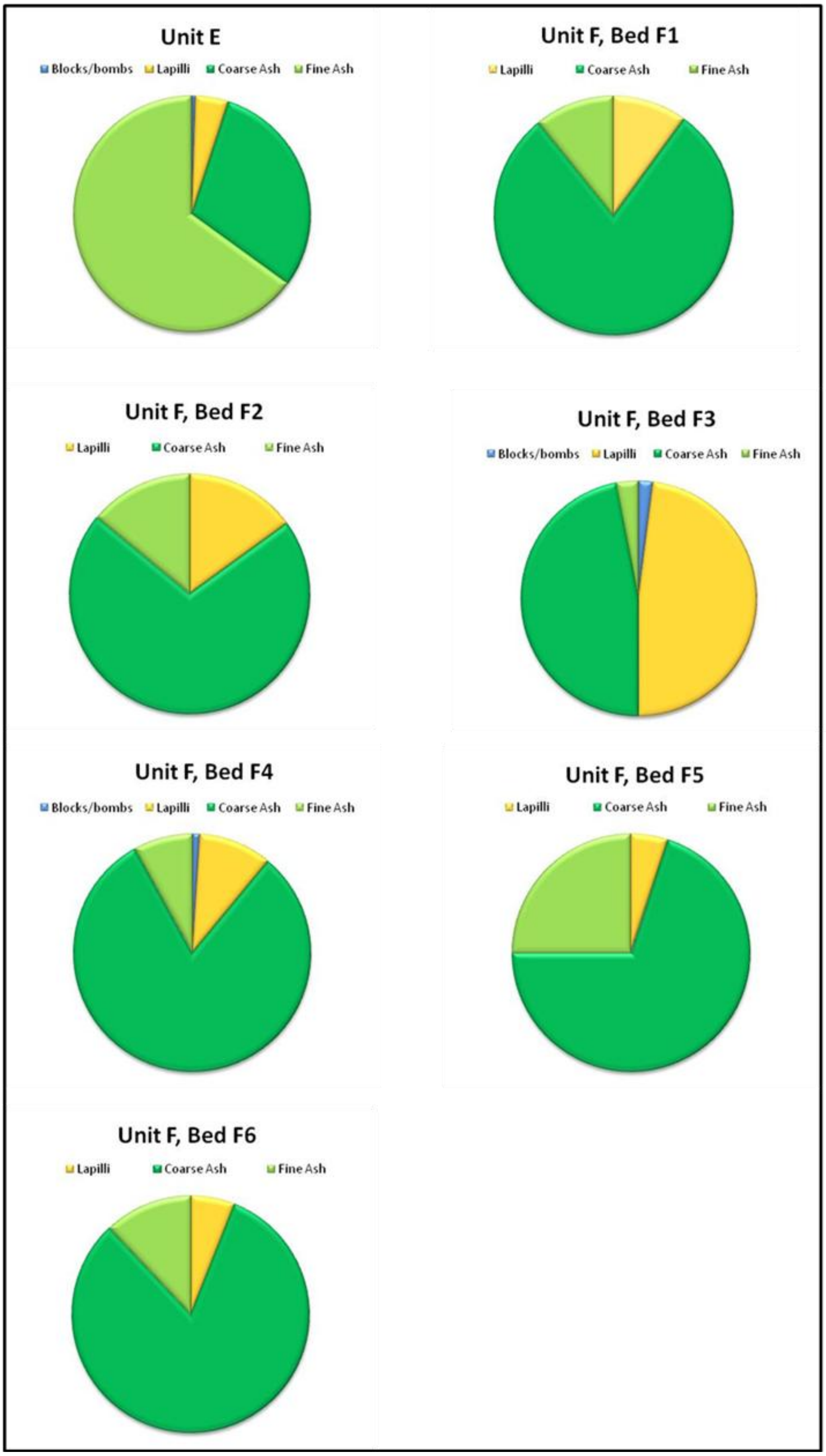

**Figure 3.10:** Grain size componentry graphs of vulcanian ash units E and F. Blocks and bombs, and lapilli refer to both scoriaceous juvenile, and dense basaltic andesite clasts. Block and bomb, lapilli, and ash proportions were obtained through sieving in the laboratory, while coarse and fine ash proportions were acquired through laser sizer analyses. The graphs clearly demonstrate the relatively large fine ash proportion in Unit E, and the relatively large lapilli proportion in bed F3. Grain size proportions are relatively similar in beds F1, F2, F4, and F6.

**Figure 3.11:** Dense, angular block and lapilli from Unit E, scale in mm.

SEM-scale observations show sub-rounded to sub-angular ash clast morphologies containing low vesicularities, with surfaces ranging from smooth and glassy, to irregular (Figure 3.12a-c). A higher magnification (5-50 µm) view shows some adhesion of fine ash and crystals to the clast surfaces (Figure 3.12c-d). The ash particles are separate and show no cohesion, accretionary, or quenching textures that might be expected in a vulcanian ash deposit resulting from magma-water interaction.

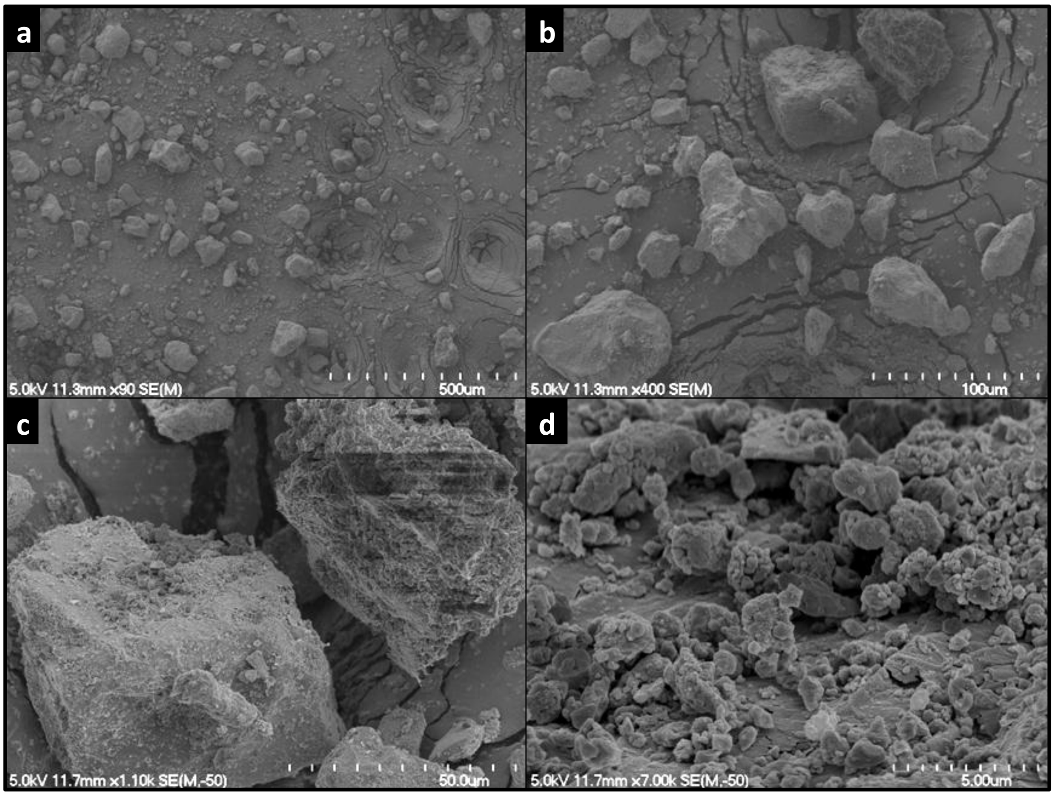

**Figure 3.12:** SEM images of a Unit E fine ash sample. (a) Sub-rounded to sub-angular fine ash particles. (b) Poorly vesicular ash clasts. (c) Magnified view of fine ash particles showing irregular surfaces, elongate holes along the blade-like ridges running up the side of the clast, and abundant cryptocrystalline and basaltic andesite material adhered to the surface. (d) Further close-up of fine ash particles showing clustered cryptocrystalline material adhered to the surface.

### *3.3.6 Unit F*

Unit F is a series of basaltic andesite vulcanian ash and lapilli beds. They are predominantly composed of coarse ash (Figure 3.10) with smaller proportions of fine ash and vesicular to dense lapilli and blocks. No fluidal bombs are present within the deposit. The six Unit F ash beds have been classified on the basis of grain size componentry, colour, and bed contacts.

Bed F1 is predominantly composed of coarse ash and lapilli (c. 90% ash component made up of 88% coarse ash, 12% fine ash) ranging from dark to light brown in colour. It contains approximately 10% basaltic andesite, sub-rounded to angular (< 30% angular) lapilli, ranging from pink to dark grey in colour, with c. 95% poorly-vesicular clasts. Vesicular lapilli are scarce. The smaller clasts (≤ 2 cm in diameter) are sub-rounded to rounded and brown to grey in colour, while the majority of larger clasts are sub-angular and dark grey.

Bed F2 has a higher lapilli content than F1 with c. 15% abundance. F2 is predominantly composed of light brown coarse ash (c. 85% ash component composed of 84% coarse ash and 16% fine ash). The dense basaltic andesite lapilli are sub-rounded to sub-angular, and are medium to dark grey in colour. The lapilli clasts average 1.5 cm in diameter, with larger clasts reaching 3 cm in diameter. Lapilli vesicularities range from moderately vesicular, to poorly-vesicular (c. 90% of clasts are poorly vesicular).

Bed F3 is a coarse ash and lapilli bed (c. 50% ash fraction comprising 95% coarse ash and 5% fine ash) containing the highest lapilli and block content of the ash beds, with a total abundance of c. 48% lapilli, and c. 2% block-sized clasts reaching 8 cm in diameter. The lapilli and block clasts range from sub-rounded to sub-angular with the majority, especially the clasts larger than 1.5 cm, being sub-angular. The colour of the lapilli and blocks varies from light pink to dark grey. Lapilli and blocks range from moderately vesicular scoriaceous, to poorly vesicular dense clasts, with the poorly-vesicular type accounting for c. 95% of the lapilli and block fraction.

Bed F4 is predominantly composed of coarse ash (c. 89% ash component made up of 91% coarse ash and 9% fine ash), with c. 10% dense basaltic andesite lapilli, and block-sized clasts up to 9 cm in diameter that account for 1% of the componentry. Approximately 5% of the lapilli are highly vesicular, and sub-rounded to sub-angular, while the remaining clasts are poorly vesicular, and sub-angular to angular.

Bed F5 is a coarse ash bed that is finer, and lighter in colour than the rest of the Unit F ash beds, comprising c. 95% ash (74% coarse ash and 26% fine ash) and c. 5% lapilli (Figure 3.13a). Some of the larger, more rounded clasts have a c. 2 mm thick layer of fine ash adhered to the surface (Figure 3.13b). Bed F5 contains a higher proportion of vesicular lapilli, reaching c. 40% of total lapilli component. Vesicular lapilli clasts range from pink, brown, and black in colour, and the dense clasts are all dark grey. Vesicles within scoriaceous lapilli are irregular due to coalescence, with a minor occurrence of elongate vesicles.

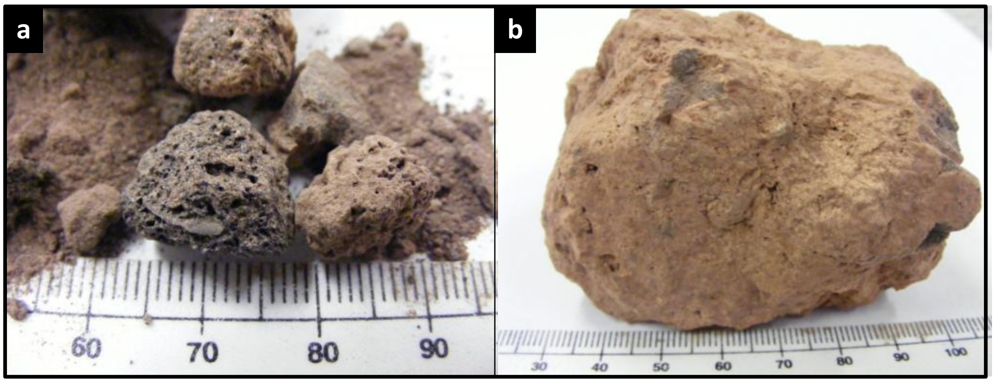

**Figure 3.13:** (a) Moderately vesicular, sub-rounded lapilli from bed F5, and (b) sub-rounded, poorly vesicular block with a thin layer of fine ash adhered to the surface.

F6 is a coarse ash bed (c. 94% ash component containing 87% coarse ash and 13% fine ash) containing c. 6% lapilli. Lapilli clasts are predominantly dark grey, dense (< 1% vesicular clasts), sub-angular to angular, reaching 3 cm in diameter. SEM images (Figure 3.14) of the ash fraction of bed F6 show variations in clast morphology and texture. Ash morphologies range from sub-rounded blocky clasts, to angular elongate shards (Figure 3.14a). Very few clasts (< 3%) contain vesicles visible in hand specimen. Clast types include: sub-angular blocks with coalesced vesicles filled with fine irregular particulate ash and crystals (Figure 3.14b-c); angular clasts with smooth, flat planes displaying step-like fractures (Figure 3.14d); glassy ash clasts containing elongate fractures with moderate fine ash and crystals adhered to the clast surface; and cusp-shaped clasts with fine ash and crystals adhered to the surface of the depression (Figure 3.14f).

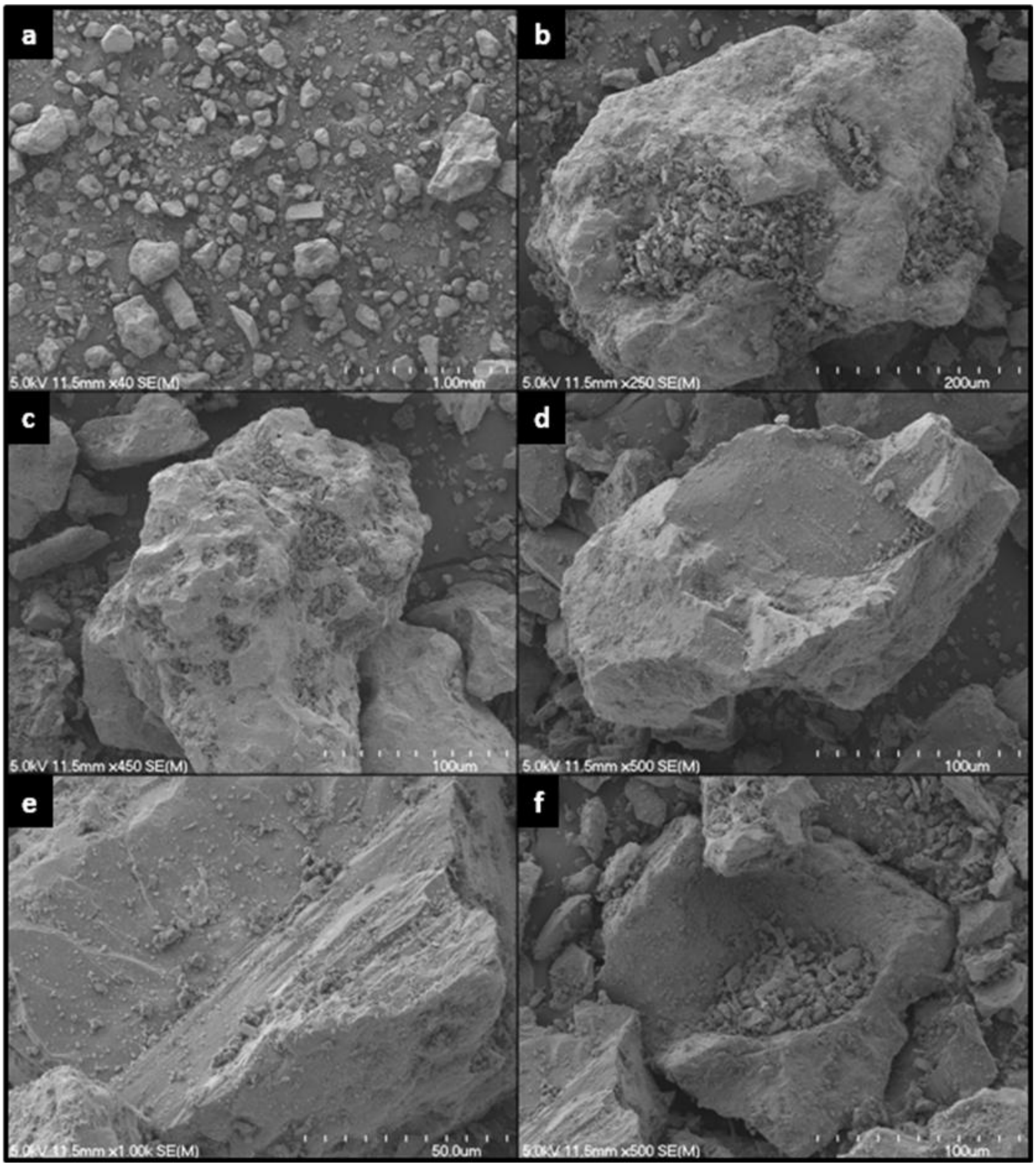

**Figure 3.14:** SEM images of ash clasts from bed F6. (a) Range of ash morphologies from sub-rounded to sub-angular, all poorly-vesicular. (b) Sub-rounded ash particle with an irregular surface and very-fine ash adhered to the surface. (c) Sub-angular clast with an irregular surface and very-fine ash adhered to the surface depressions. (d) Sub-angular ash particle with a flat fractured surface. (e) Sub-angular block-shaped ash particle. (f) Very-fine ash within a rounded depression in an ash particle.

### *3.3.7 Unit G*

Unit G is a densely agglutinated, basaltic andesite to andesite, strombolian to fire fountain spatter deposit largely composed of red flattened, deformed, dense basaltic andesite to andesite bombs displaying irregular and spindle bomb morphologies within a red ash matrix (Figure 3.15a-c). The deposit consists of densely agglutinated spatter, with clear block and bomb clast outlines in the base and top of the deposit. The bombs are coarsely porphyritic, sub-rounded to angular, and flattened from deposition and overlying loading pressures. Vesicles have irregular morphologies and some are elongate, with lengths up to 2 cm (Figure 3.15a) due to bubble coalescence and flattening of the clast.

Clast outlines are more apparent in the lower portion of the deposit, with an upper zone (c. 70% of deposit) composed of irregular and rubbly, sharp, very angular, poorly vesicular spatter. Local agglutination has occurred around the spatter clasts in the base and top of the deposit, containing contrasting dark grey deformed clasts that results in a higher degree of agglutination than the surrounding deposit (Figure 3.15c). A higher proportion of both granular and non-granular quartzofeldspathic xenoliths occur as inclusions within the dense deformed clasts, with the smaller proportion (< 20%) loose within the deposit.

Unit G has a ratio of vesicular to dense material about 50:50. The vesicular bombs have irregular and elongate vesicles due to bubble coalescence and flattening of the spatter upon deposition and through overlying loading pressures (Figure 3.15a). The coalesced vesicles contain ruptured vesicle walls on the clast surfaces and within vesicle cavities (Figure 3.16b). Some clasts are relatively smooth and glassy (Figure 3.16 c-d), with adhered cryptocrystalline material on the surface and within vesicle cavities (Figure 3.16e-f). Magnified views of cryptocrystalline material indicate the presence of spear-head shaped crystals, possibly quartz polymorphs within vesicles (Figure 3.16f).

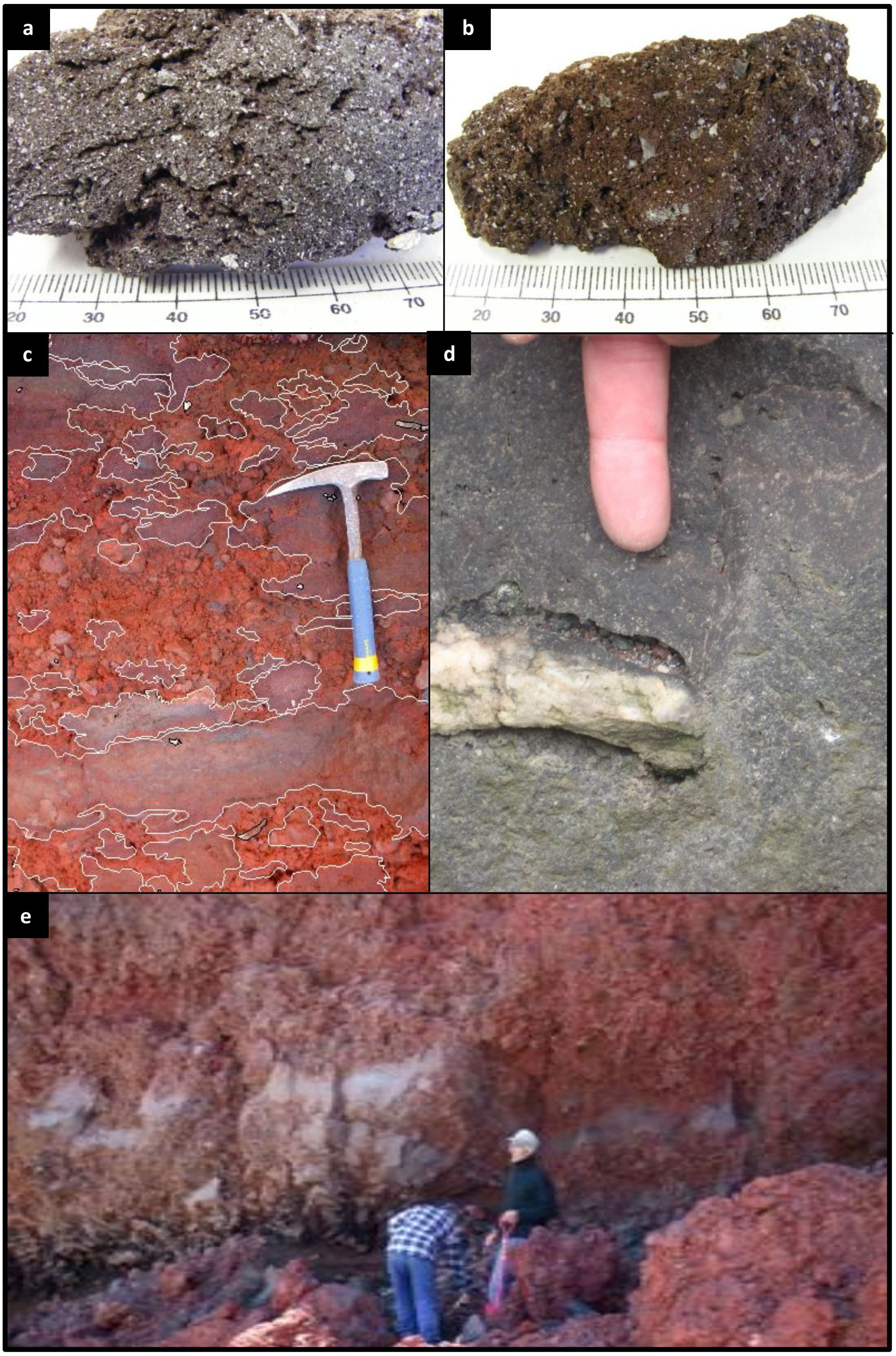

**Figure 3.15:** Clast morphologies and vesicularities from Unit G. (a) Very angular scoria clast with coalesced, elongate vesicles. (b) Porphyritic bomb containing phenocrysts up to 6 mm in length, scale in mm. (c) Bomb outlines (in white) at the base of the western outcrop of Unit G, with xenolith outlines in black. (d) Exposed interior of a blocky clastogenic lava flow on the northern rim of the inner crater (photo courtesy of S. Cooke). (e) Large elongate bombs and surrounding zones of local agglutination at the base of Unit G.

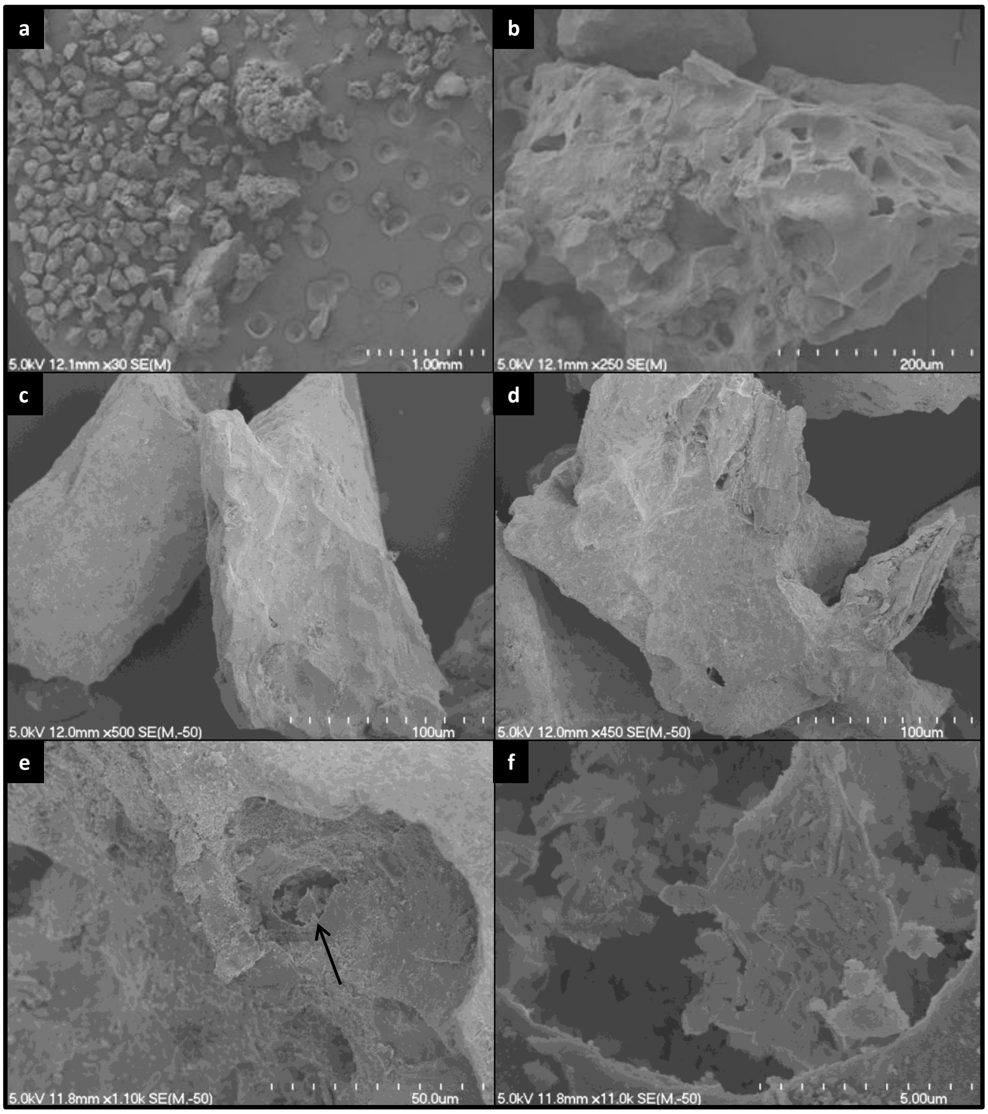

**Figure 3.16:** SEM images of irregular ash-sized particles of Unit G. (a) Sub-angular to angular ash-sized particles displaying low to moderate vesicularities. (b) Sub-angular, vesicular ash-sized particle showing ruptured vesicle walls. (c) Sub-angular, non-vesicular ash clasts with irregular fractured surfaces. (d) Sub-angular, poorly vesicular ash clast with two ruptured vesicle walls. (e) Coalesced vesicle within an ash-sized clast. (f) A magnified view of the vesicle indicated by the arrow in (e), with quartz-polymorph growth within.

### *3.4 Quartzose Xenoliths*

Within the stratigraphic units of the inner crater, quartzofeldspathic xenolith abundances average approximately 3% across the deposit. Xenoliths are much more abundant within the lava flows on the NW flanks of Ngauruhoe, and larger xenoliths could be obtained for thin section and hand specimen descriptions. Mineralogical compositions of the xenoliths are described in Chapter Four.

Quartzose xenoliths (both quartzofeldspathic and quartz-wollastonite-diopside) found in the inner crater and 1954 lava flows have two end types: type (1) clear granular quartzose xenoliths with a 'sugary' texture that are often fragile, with quartz grains often breaking off during handling (Figure 3.17a-b), and type (2) white dense, massive quartzose xenoliths that are less fragile (Figure 3.17c). There is an array of xenoliths between these two end types, with some clasts containing distinct zones with characteristics of both xenolith types (Figure 3.17d).

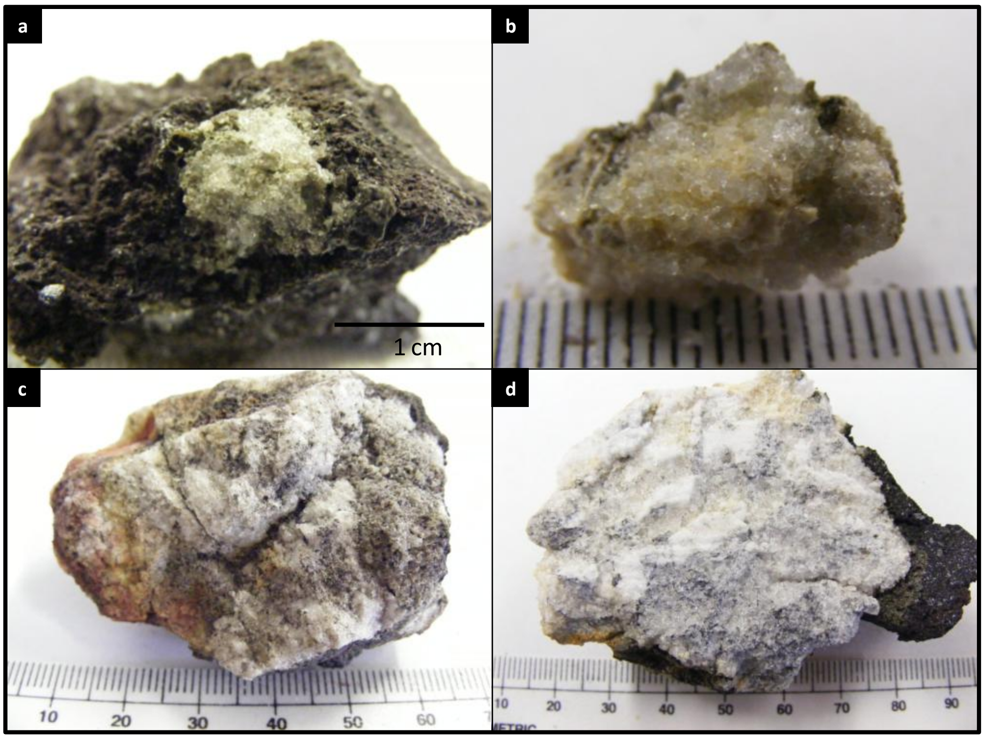

**Figure 3.17:** (a) Type 1 granular quartzofeldspathic xenolith within scoriaceous lapilli from Unit B. (b) Loose type 1 granular quartzofeldspathic xenolith from Unit B. (c) Type 2 quartzofeldspathic xenolith from Unit B. (d) Granular quartz-wollastonite-diopside xenolith from the June 30, 1954 lava flow on the NW flanks of Ngauruhoe, the majority of which contains type 1 xenolith textures with zones of type 2 xenolith characteristics.

Dark grey zones are present near the edges of some xenoliths that are interpreted to represent melt zones from interaction with the surrounding host lava. Type 1 xenoliths (Figure 3.17a) are the most common variety present throughout the inner crater deposits, occurring both loose within the deposit and as inclusions within scoriaceous lapilli and bombs. It is common for the two types of xenoliths to have undergone alteration, causing a yellow to red discolouration (Figure 3.17c). SEM images of a large 15 x 15 cm xenolith sampled from the June 30, 1954 lava flow (Figure 3.18) show the grains to be smooth, equigranular, blocky clasts with conchoidal fracturing.

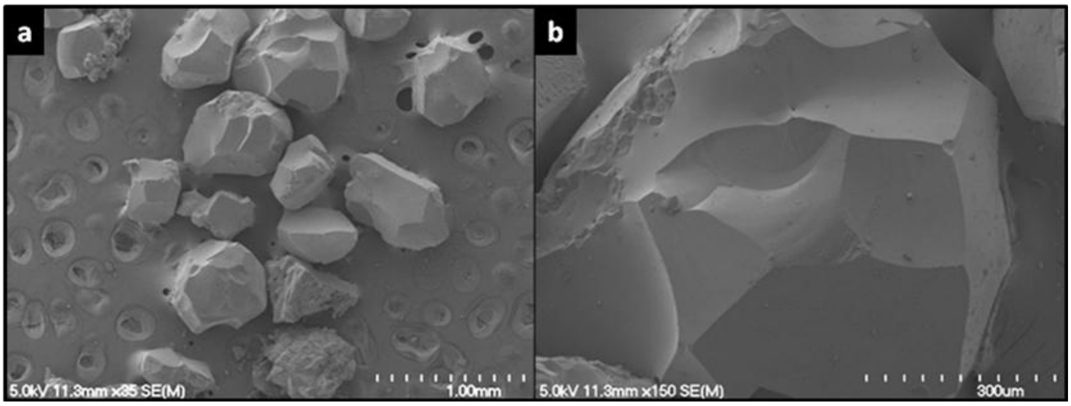

**Figure 3.18:** SEM images of loose quartz grains from granular quartzite xenolith in Figure 3.17d, with conchoidal fracturing on the surface. Pits in the background of (a) are within the carbon paper that adhere the ash clasts to the SEM stage.

## 3.5 Summary

Ash, scoriaceous lapilli and bombs, dense basaltic andesite lapilli and blocks, and quartzose xenoliths have been described through grain size analyses, SEM image analysis, and clast morphology descriptions. Within the clasts the vesicles and surface textures have been described in hand specimen and µm scales, to determine eruptive and depositional processes in Chapter Five. Units A (northern outcrop) and C have undergone coalescence to form clastogenic lava flows that have partially flown down into the inner crater. Units A (southern outcrop) and D have undergone poor to moderate agglutination, leaving clast outlines intact. Units B and G contain abundant deformed bombs from deposition and overlying loading pressures. Units E and F are fine to coarse ash and lapilli beds with varying proportions of scoriaceous and dense lapilli and blocks.

# Chapter Four

# Petrography, Mineralogy and Geochemistry

# PART 1: PETROGRAPHY AND MINERALOGY

## 4.1 Introduction

Petrographic investigations have been carried out on samples representing vertical and horizontal variations in the inner crater, from stratigraphic Units A to G (erupted between 1954 and 1975), and one xenolith sample from a 1954 lava flow. The phenocryst assemblages and textures represent early pre-eruption magmatic conditions, while microlites and glass content within the groundmass provide an insight into later conditions during the eruption and cooling.

The Ngauruhoe inner crater 1954-55 eruption deposits (Units A to E) are hypocrystalline, medium grained, porphyritic (13-32% phenocrysts), basaltic andesites to andesites ($SiO_2$ 54.88 – 57.37 wt. %), with one sample, A3, having an elevated $SiO_2$ content (68.81 wt. %), that falls into the dacite field. The high $SiO_2$ content in the Unit A northern deposit is due to hydrothermal alteration. The 1974-75 deposits (Units F and G) are hypocrystalline, medium grained, porphyritic basaltic andesite to andesite ($SiO_2$ 55.46 – 58.85 wt. %), although the higher $SiO_2$ content found in Unit G may be due to contamination from quartzose xenoliths that could not be removed for analysis. Plagioclase and orthopyroxene are the dominant phenocrysts with lesser amounts of clinopyroxene and minor olivine. Quartzofeldspathic xenoliths are common, with minor metagreywacke xenoliths, and most originate from the underlying Torlesse metagreywacke that is exposed to the west of the TVZ (Cole, 1978).

## 4.2 Methodology

### *Thin Section Petrography*

Representative samples of each major clast type were selected from each stratigraphic unit within the inner crater (Table 4.1; Appendix Three). Bulk ash and lapilli samples were also selected. Thin sections were made of each sample using standard petrographic techniques, and covered with a glass cover slip. Those samples selected for microprobe analysis were polished and left uncovered. Phenocryst, groundmass, and vesicle modal data were collected by standard point-counting, with 400 counts per thin section (Table 4.2; Figure 4.1).

**Table 4.1:** Unit and location of each thin section and sample.

| Unit | Thin Section | Location |
|---|---|---|
| A | A1c | Base of southern deposit |
| | A3 | Base of northern deposit |
| B | B1a | 1.5 m above the base of Unit B, at the southern end of deposit |
| | B1b | 3 m above the base of Unit B, at the northern end of deposit |
| | B5 | 2 m above the base of Unit B, at the northern end of deposit |
| C | C1a | Base of Unit C block fallen to crater floor |
| | C1b | Middle of first Unit C block fallen to crater floor |
| | C1c | Top of first Unit C block fallen to crater floor |
| | C2a | Base of second Unit C block fallen to crater floor |
| D | D1 | 2 m from the top of the eastern side of Unit D |
| | D2 | Very top of the eastern side of the deposit |
| E | E | Eastern side of deposit directly above D2 |
| F | F1 | Eastern side of deposit directly above E |
| | F2 | Eastern side of deposit directly above F1 |
| | F3 | Eastern side of deposit directly above F2 |
| | F4 | Eastern side of deposit directly above F3 |
| | F5 | Eastern side of deposit directly above F4 |
| | F6 | Eastern side of deposit directly above F5 |
| G | G1a | 1.8 m from the base of the NW side of deposit |
| | G1b | 5 m from the base of the NW side of deposit |
| | G1c | 8 m from the base of the NW side of deposit |
| | G2 | Middle of northern lava flow (into crater) |
| | G3 | Upper portion of northern lava flow (into crater) |
| | G4 | Base of northern lava flow (into crater) |

### *Electron Microprobe Analysis (EMP)*

After the polished thin sections were prepared, a map and photomicrograph of each analysis point was made to help identification under the microprobe. Phenocrysts of plagioclase, orthopyroxene, clinopyroxene, and olivine were analysed by EMP for geochemical composition. Analyses were focused on the phenocryst rims to measure the final stage compositions, but some core analyses were also done to determine zoning. EMP data is given in Appendix Four.

Electron microprobe analyses were carried out in the School of Geography, Geology and Environmental Science at the University of Auckland using a JEOL JXA-840A EMPA using an eumeX EDS detector supported by Moran Scientific, with a Beam current of 800 pA, analysis live-time 100 seconds, analytical spot of approximately 2 microns, and standardised by a suite of Astimex mineral standards.

## 4.3 Petrography and Mineralogy

**Table 4.2:** Modal analysis data for selected Ngauruhoe inner crater units. (Plag.) plagioclase, (opx) orthopyroxene, (cpx) clinopyroxene, (GW) metagreywacke xenolith, (qtz) quatzofeldspathic xenolith, (GM) groundmass.

| | Plag. | Opx | Cpx | Olivine | Vesicle | Opaque | GW | Qtz. | GM |
|---|---|---|---|---|---|---|---|---|---|
| A1c | 16.3% | 5.0% | 1.8% | 0.3% | 15.0% | 1.3% | 0.3% | 1.0% | 59.0% |
| A3 | 21.3% | 7.5% | 0.5% | - | 11.5% | - | - | 0.3% | 58.9% |
| B1a | 10.5% | 6.0% | 0.5% | - | 50.0% | - | - | - | 33.0% |
| B1am | 6.0% | 6.8% | - | 1.0% | 43.0% | - | 1.3% | - | 41.9% |
| B5 | 7.4% | 7.2% | 0.3% | - | 12.3% | - | - | 39.9% | 32.9% |
| C1a | 7.0% | 3.8% | 2.0% | - | 42.0% | 0.5% | 0.3% | 0.3% | 44.2% |
| C1b | 13.1% | 16.1% | 2.0% | - | 9.3% | - | - | 14.8% | 44.7% |
| C1c | 10.5% | 2.3% | 0.5% | - | 53.3% | - | - | - | 33.4% |
| C2a | 12.3% | 9.3% | 1.3% | 0.8% | 35.8% | - | - | - | 40.5% |
| D1 | 20.3% | 7.3% | 1.3% | - | 6.8% | - | - | 1.3% | 63.0% |
| D1a | 23.1% | 16.3% | 2.8% | - | - | - | - | 6.8% | 51.0% |
| D1b | 18.5% | 8.5% | 2.5% | 0.5% | - | - | - | 1.5% | 68.4% |
| D1c | 20.3% | 12.3% | 0.8% | 3.5% | - | - | - | 5.0% | 58.2% |
| E | 18.3% | 5.0% | 1.5% | - | - | - | - | 4.5% | 70.7% |
| F1 | 13.0% | 6.0% | 0.5% | 0.3% | - | - | - | - | 80.2% |
| F2 | 20.0% | 6.0% | 0.8% | 0.5% | - | - | 1.5% | 0.8% | 70.4% |
| F3 | 19.0% | 8.5% | 0.5% | 0.8% | - | - | 0.3% | 1.5% | 69.4% |
| F4 | 23.5% | 8.5% | 0.8% | 0.3% | - | - | 0.5% | 3.8% | 62.6% |
| F5 | 21.3% | 10.0% | 1.3% | 0.3% | - | - | - | - | 67.1% |
| F6 | 13.8% | 6.5% | 2.8% | - | - | - | - | 1.5% | 75.4% |
| G1a | 15.5% | 3.8% | - | - | 26.0% | - | - | - | 54.7% |
| G1b | 11.3% | 4.8% | 1.0% | - | 23.3% | - | 1.3% | 3.0% | 55.3% |
| G1ciii | 7.8% | 7.5% | 0.8% | - | 35.0% | - | 1.0% | 0.3% | 47.6% |
| GA | 12.0% | 5.8% | 1.0% | - | 47.0% | - | - | - | 34.2% |
| GB | 13.4% | 3.0% | 0.5% | - | 6.3% | - | 1.5% | 1.0% | 74.3% |
| GC | 14.3% | 6.0% | - | - | 28.0% | - | - | 1.3% | 50.4% |

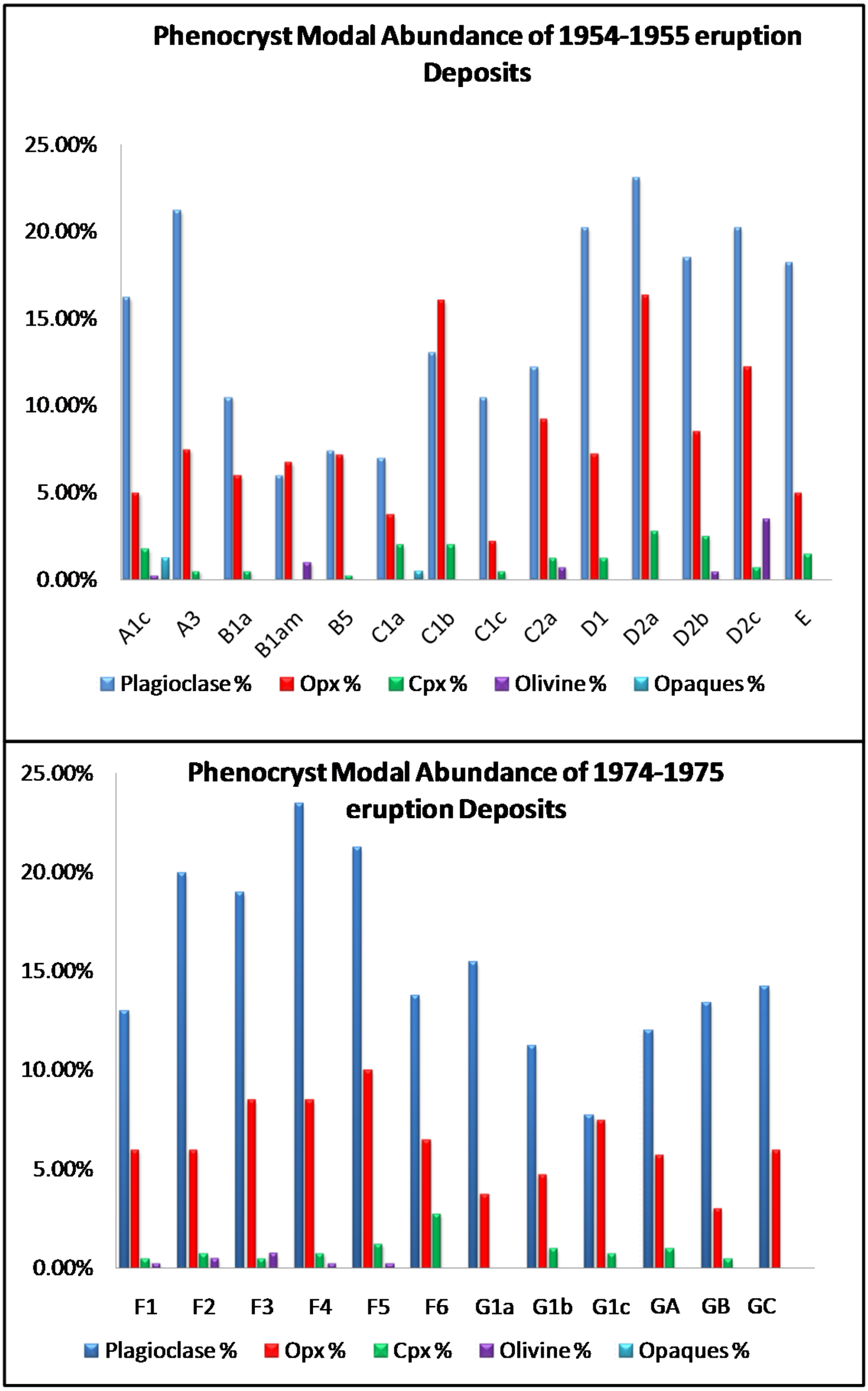

**Figure 4.6:** Phenocryst modal abundances in the 1954-55 (top) and 1974-75 (below) deposit thin sections. Modal abundances determined from 400 point counts per thin section.

### *4.3.1 Plagioclase*

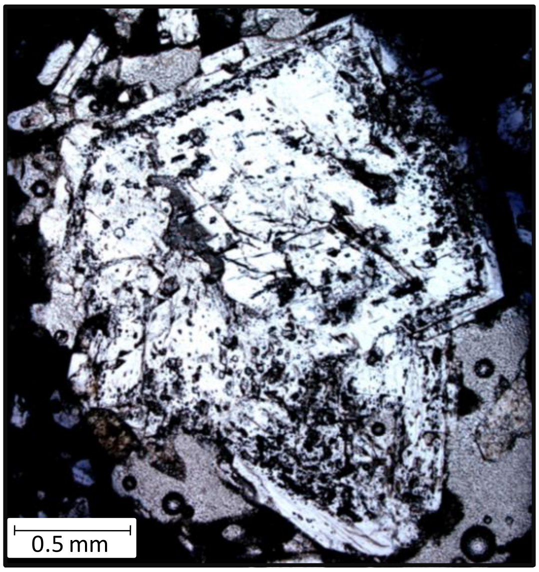

**Figure 4.2:** Irregular, fractured plagioclase phenocryst in thin section C1b under plane polarised light showing oscillatory zoning, sieve textures, and a plagioclase phenocryst grown into the base.

Plagioclase feldspar is the dominant phenocryst phase within juvenile clasts throughout the inner crater deposits, with a modal abundance of 6-22% (Table 4.2; Figure 4.1). The dominant morphology is subhedral with minor euhedral crystals, and the majority of phenocrysts are lath-shaped. Complex phenocrysts are common, where multiple crystals have intergrown with each other, and display oscillatory zoning patterns, intricate disequilibrium sieve textures, and irregular, embayed rims (Figure 4.2). Polysynthetic twinning and oscillatory zoning occurs in most phenocrysts (Figure 4.3). Phenocrysts average

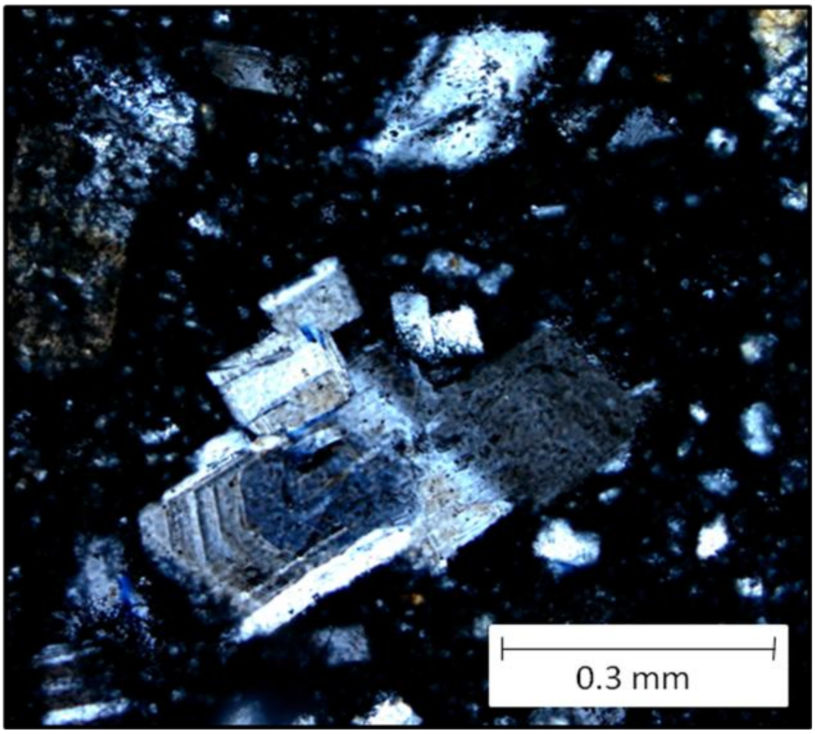

**Figure 4.3:** Plagioclase phenocryst within thin section D1 under crossed polarised light displaying oscillatory zoning and slight sieve texture.

0.5 mm in length, but some large crystals reach 6 mm. The majority of plagioclase phenocrysts occur as discrete grains, although plagioclase phenocrysts are present in glomerocrysts containing orthopyroxene and clinopyroxene. Many larger plagioclase crystals > 0.5 mm in length have been fractured and broken, most commonly in Units B, D, and F. Phenocrysts with no fracturing and/or disequilibrium textures are rare in the inner crater deposits and are generally smaller than 0.4 mm long. Inclusions of Fe-Ti oxides, glass, epidote, apatite, and clinopyroxene are common.

Most plagioclase phenocrysts which are greater than 0.2 mm long have experienced some degree of resorption, indicated by sieve textures, while smaller phenocrysts (< 0.2 mm) are generally not resorbed. There are no compositional differences between plagioclase phenocrysts with and without sieve textures. Four main disequilibrium sieve texture patterns are present throughout the inner

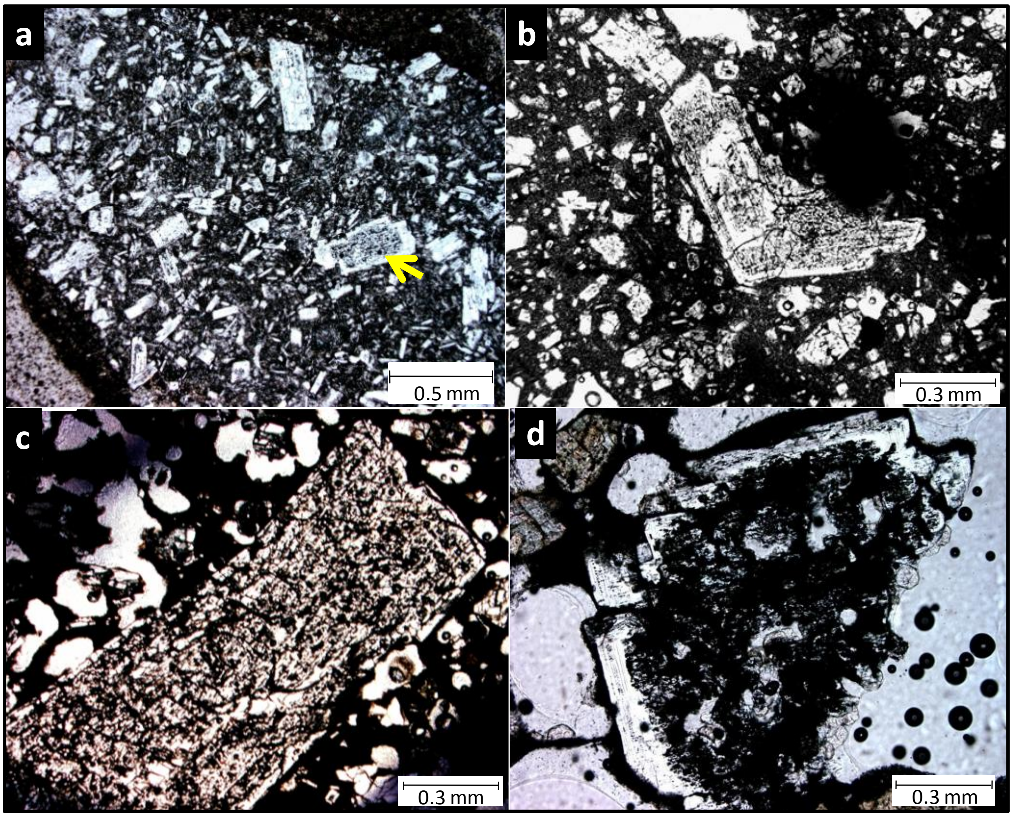

**Figure 4.4:** (a) Type 1 plagioclase disequilibrium sieve texture with a sieved core and pristine rim. (b) Type 2 plagioclase disequilibrium sieve texture with multiple concentric sieved and clear zones, with a clear rim. (c) Type 3 disequilibrium sieve texture, no concentric sieve patterns. (d) Type 4 disequilibrium sieve texture with the remains of a heavily resorbed plagioclase phenocryst.

crater deposits (in order of occurrence from highest to lowest abundance): (1) phenocrysts with a sieve textured centre, and a clear subhedral plagioclase overgrowth rim (Figure 4.4a); (2) multiple concentric zones of disequilibrium sieve textured plagioclase, separated by concentric clear zones with an outermost overgrowth rim of clear plagioclase (Figure 4.4b); (3) no pattern in disequilibrium sieve textures (Figure 4.4c), and (4) skeletal phenocryst remains after almost entire phenocryst has been resorbed (Figure 4.4d).

Sieve textures are often infilled with glass or opaque minerals. Inclusions are generally sub-rounded in shape, but lath-shaped inclusions are also present (Figure 4.5). Sieve textures within plagioclase phenocrysts are widespread across the TgVC, and like the inner crater deposits, the sieve textures often occur in multiple oscillatory zones and rare reversely zoned crystals containing An enriched rims (Hobden, 1997).

Plagioclase compositions range from labradorite to bytownite ($An_{53-87}$ Figure 4.6a). A selection of EMP results are given in Table 4.3. Plots of plagioclase

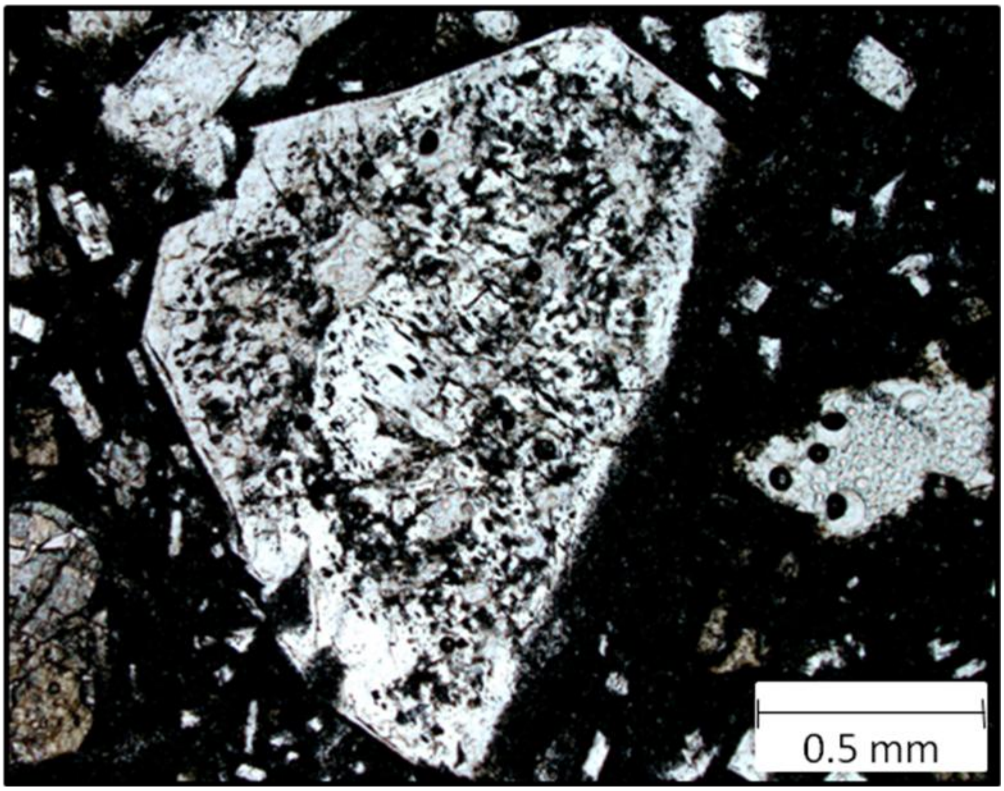

**Figure 4.5:** Broken plagioclase phenocryst from thin section A1c displaying both irregular and lath shaped glass inclusions.

**Table 4.3:** Selected EMP plagioclase analysis from the Ngauruhoe Inner Crater. All units measured in wt. %. (plag) plagioclase, (c) core, (r) rim.

| | ID | $SiO_2$ | $TiO_2$ | $Al_2O_3$ | FeO | MnO | MgO | CaO | $Na_2O$ | $K_2O$ | $P_2O_5$ | $SO_3$ | Cl | $Cr_2O_3$ | NiO | TOTAL |
|---|---|---|---|---|---|---|---|---|---|---|---|---|---|---|---|---|
| A1c2 Plag c | 5203 | 47.55 | -0.03 | 32.33 | 0.49 | 0.11 | 0 | 16.68 | 1.89 | 0.19 | -0.05 | -0.1 | 0.02 | 0 | -0.06 | 99.02 |
| B1a12 plag c | 5216 | 47.68 | 0 | 32.79 | 0.45 | -0.01 | 0.11 | 16.66 | 1.95 | 0.2 | 0 | 0.06 | 0.01 | 0.18 | -0.1 | 99.99 |
| C1b9 plag c | 5272 | 52.93 | 0.15 | 28.45 | 0.53 | -0.05 | 0.06 | 12.19 | 4.18 | 0.34 | -0.11 | 0.14 | 0 | 0.01 | 0.15 | 98.97 |
| C15 plag c | 5245 | 46.7 | 0.01 | 33.07 | 0.45 | -0.09 | 0.01 | 16.86 | 1.59 | 0.2 | 0 | -0.07 | 0.07 | 0.02 | 0.25 | 99.08 |
| D15 plag r | 5246 | 46.94 | -0.02 | 32.68 | 0.56 | 0.05 | 0.05 | 16.98 | 1.67 | 0.2 | -0.09 | -0.14 | 0.05 | 0.05 | -0.05 | 98.93 |
| E52 plag c | 5299 | 48.43 | -0.02 | 31.62 | 0.61 | -0.11 | 0.05 | 15.8 | 2.25 | 0.17 | -0.16 | -0.01 | 0.03 | 0.07 | 0.09 | 98.84 |
| F1b7 plag c | 5289 | 50.82 | 0.07 | 30.14 | 0.77 | 0 | -0.02 | 14.1 | 3.36 | 0.24 | -0.02 | -0.07 | -0.04 | 0.09 | 0.02 | 99.45 |

**Table 4.4:** Selected EMP clinopyroxene, orthopyroxene, and olivine analysis from the Ngauruhoe Inner Crater. All units measured in wt. %. (cpx) clinopyroxene, (opx) orthopyroxene, (ol) olivine, (c) core, (r) rim.

| | ID | $SiO_2$ | $TiO_2$ | $Al_2O_3$ | FeO | MnO | MgO | CaO | $Na_2O$ | $K_2O$ | $P_2O_5$ | $SO_3$ | Cl | $Cr_2O_3$ | NiO | TOTAL |
|---|---|---|---|---|---|---|---|---|---|---|---|---|---|---|---|---|
| A1c1a cpx c | 5223 | 51.15 | 0.38 | 3.02 | 7.09 | 0.13 | 15.99 | 19.42 | 0.27 | 0.15 | 0.19 | 0 | 0.06 | 0.26 | 0.06 | 98.16 |
| B1a4 cpx c | 5207 | 51.73 | 0.62 | 2.2 | 11.28 | 0.11 | 15.12 | 17.94 | 0.3 | 0.04 | 0.01 | 0.11 | 0.07 | 0.17 | 0.01 | 99.7 |
| C1b11b cpx c | 5275 | 53.08 | 0.12 | 28.8 | 0.63 | 0.04 | 0.1 | 12.47 | 4.34 | 0.32 | -0.01 | 0.1 | -0.02 | 0.03 | -0.07 | 99.93 |
| D13 cpx c | 5243 | 53.01 | 0.21 | 2.72 | 4.7 | 0.12 | 18.31 | 19.33 | 0.13 | 0.11 | 0.1 | -0.04 | 0 | 1.21 | 0.01 | 99.92 |
| E53 cpx c | 5300 | 52.33 | 0.32 | 3.49 | 6.54 | 0.2 | 16.54 | 20.28 | 0.14 | 0.08 | 0.11 | 0.07 | 0.01 | 0.4 | 0.1 | 100.6 |
| F1b13 cpx c | 5296 | 50.56 | 0.39 | 3.6 | 7.36 | 0.16 | 15.83 | 20.1 | 0.15 | 0.15 | 0.01 | -0.03 | 0.03 | 0.34 | 0.01 | 98.64 |
| A1c6 opx c | 5227 | 53.57 | 0.43 | 1.09 | 20.14 | 0.44 | 23.14 | 2.05 | 0 | 0.04 | 0 | 0 | 0.02 | 0 | 0 | 100.9 |
| B1a11 opx c | 5215 | 53.61 | 0.33 | 1.76 | 17.8 | 0.37 | 24.57 | 1.8 | -0.04 | 0.06 | 0.04 | 0.05 | -0.02 | 0.02 | 0.03 | 100.4 |
| C1b13 opx c | 5277 | 54.41 | 0.29 | 0.85 | 17.84 | 0.48 | 24.78 | 1.97 | -0.07 | 0.07 | 0.02 | -0.01 | -0.01 | -0.05 | 0.1 | 100.7 |
| D110 opx c | 5251 | 53.84 | 0.18 | 1.44 | 18.13 | 0.46 | 25.01 | 1.54 | -0.07 | 0.04 | -0.04 | 0.14 | -0.03 | 0 | -0.01 | 100.6 |
| E54 opx c | 5301 | 53.78 | 0.34 | 1.13 | 18.82 | 0.44 | 23.83 | 2.14 | -0.1 | 0.07 | 0.11 | -0.03 | 0.02 | 0.1 | -0.05 | 100.6 |
| F1b10 opx c | 5292 | 53.15 | 0.34 | 1.12 | 20.39 | 0.62 | 22.3 | 1.93 | -0.03 | 0.02 | 0.02 | -0.01 | 0.02 | -0.05 | 0.01 | 99.82 |
| D115 ol c | 5256 | 37.28 | 0 | 0.04 | 31.36 | 0.53 | 31.44 | 0.11 | 0 | 0 | 0.2 | 0.1 | 0.06 | -0.1 | -0.05 | 101 |
| E56 ol c | 5303 | 40.8 | -0.01 | 0.11 | 15.05 | 0.27 | 45.02 | 0.25 | -0.05 | 0.01 | -0.02 | 0.04 | 0 | 0.06 | 0.15 | 101.7 |

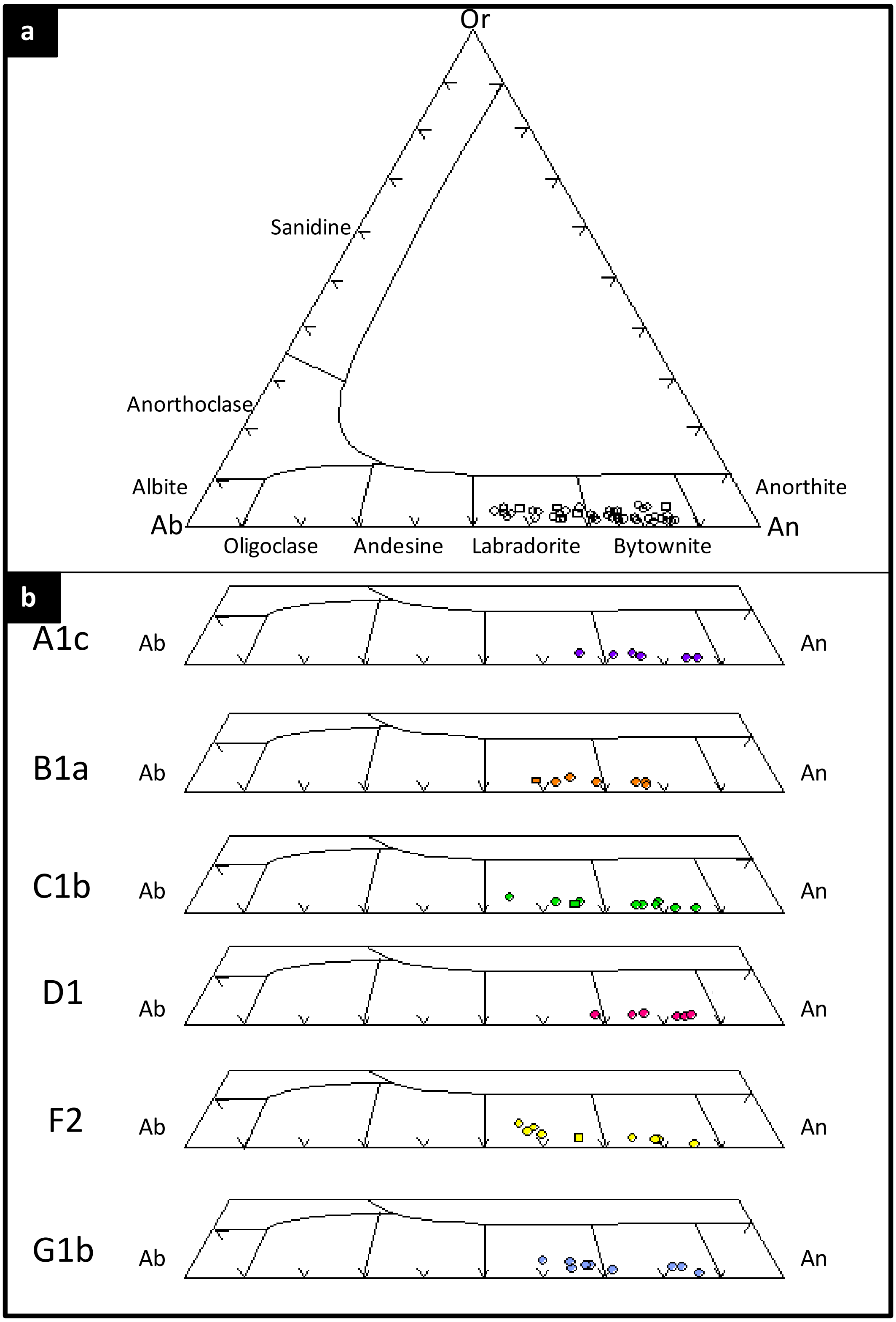

**Figure 4.6:** (a) Ternary diagram plot for plagioclase compositions for Ngauruhoe inner crater eruptives, labradorite and bytownite. (b) Plagioclase composition plots based on stratigraphic units. No data for Unit E.

compositions on An-Ab-Or ternary classification diagrams (Figure 4.6b) show little variation of the two crystal types throughout the stratigraphic section, although plagioclase in A1c and D1 are mainly bytownite. Analysis of oscillatory zoning was conducted on three zones from selected samples containing clear zoning patterns. Results show differing An contents with a decrease from the rim, and sharp increase towards the core (Figure 4.7a,c). Normal zoning is observed in some phenocrysts with sodic rims and calcic cores (Figure 4.7b). Plagioclase compositions across the TgVC range from $An_{45-90}$, with a slightly wider range from andesine to bytownite (Hobden, 1997).

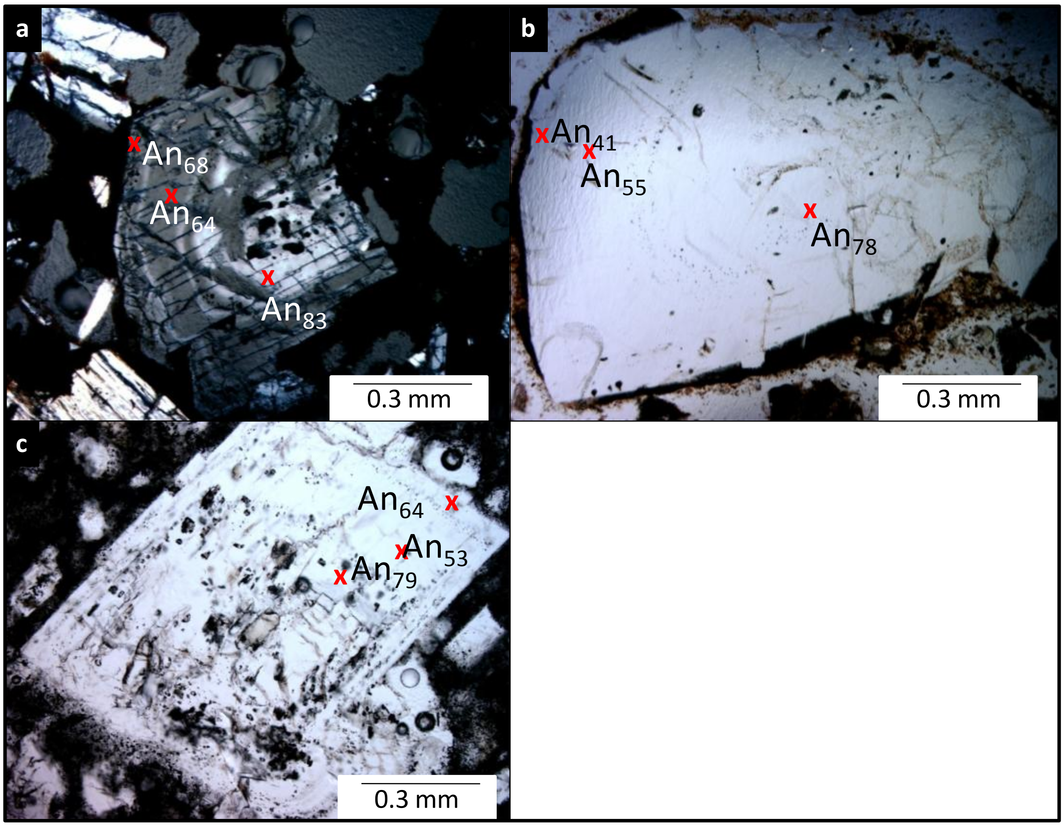

**Figure 4.7:** Anorthite compositions in (a) oscillatory zoned plagioclase phenocrysts (b) normally zoned plagioclase phenocryst, (c) oscillatory zoned plagioclase phenocryst.

### *4.3.2 Pyroxene*

Orthopyroxene is the second most abundant phenocryst in the inner crater deposits. Modal abundances are 2.25-16.08% (Table 4.2; Figure 4.1) and phenocrysts occur as discrete grains, with < 5% occurring within glomerocrysts alongside plagioclase and clinopyroxene. Phenocrysts are largely subhedral with minor euhedral and anhedral morphologies, and reach lengths of 3 mm. Many orthopyroxene phenocrysts throughout the deposits are fractured and broken, and minor phenocrysts contain Fe-Ti oxides, glass and clinopyroxene inclusions. Some phenocrysts larger than 0.4 mm have undergone resorption. Orthopyroxene is rarely twinned, and is sometimes rimmed by clinopyroxene (Figure 4.8).

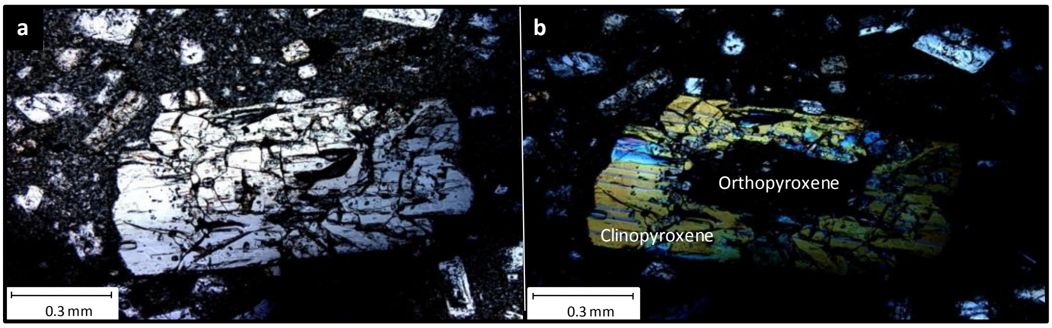

**Figure 4.8:** Orthopyroxene with a thick overgrowth of clinopyroxene in plane (a) and crossed polarised (b) light. Phenocryst from Unit A.

Clinopyroxene phenocrysts are the third most common phenocryst in the inner crater eruption sequence with a modal abundance up to 2.7% and are not present in all thin sections. Clinopyroxene phenocrysts are often found in glomeroporphyritic clusters with orthopyroxene and plagioclase (Figure 4.9), with less than half of the crystals occurring as discrete grains. Phenocrysts reach lengths of 1.8 mm, rarely display twinning, and are all dominantly subhedral with rare euhedral morphologies. A number of phenocrysts display disequilibrium sieve textures.

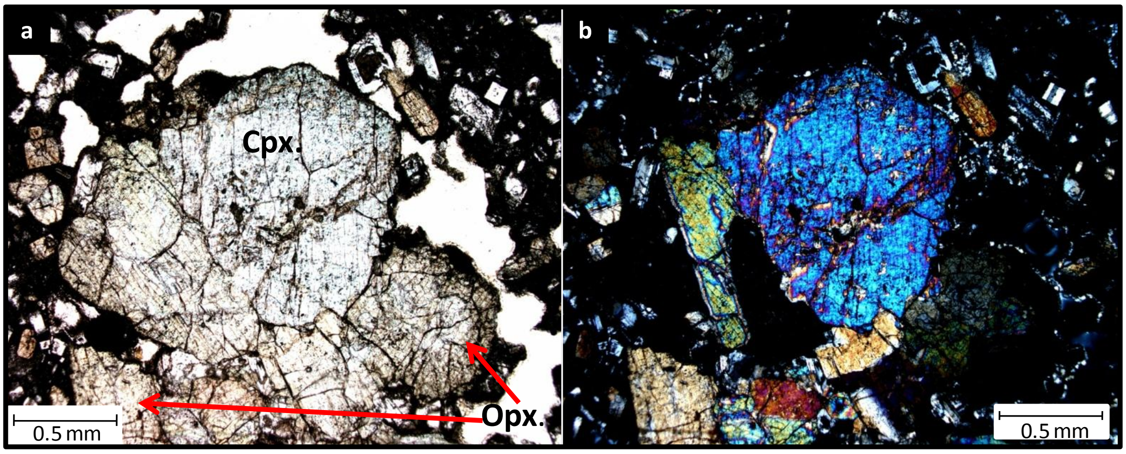

**Figure 4.9:** Plane polarised (a), and crossed polarised (b) view of a clinopyroxene-orthopyroxene glomerocryst (Unit A).

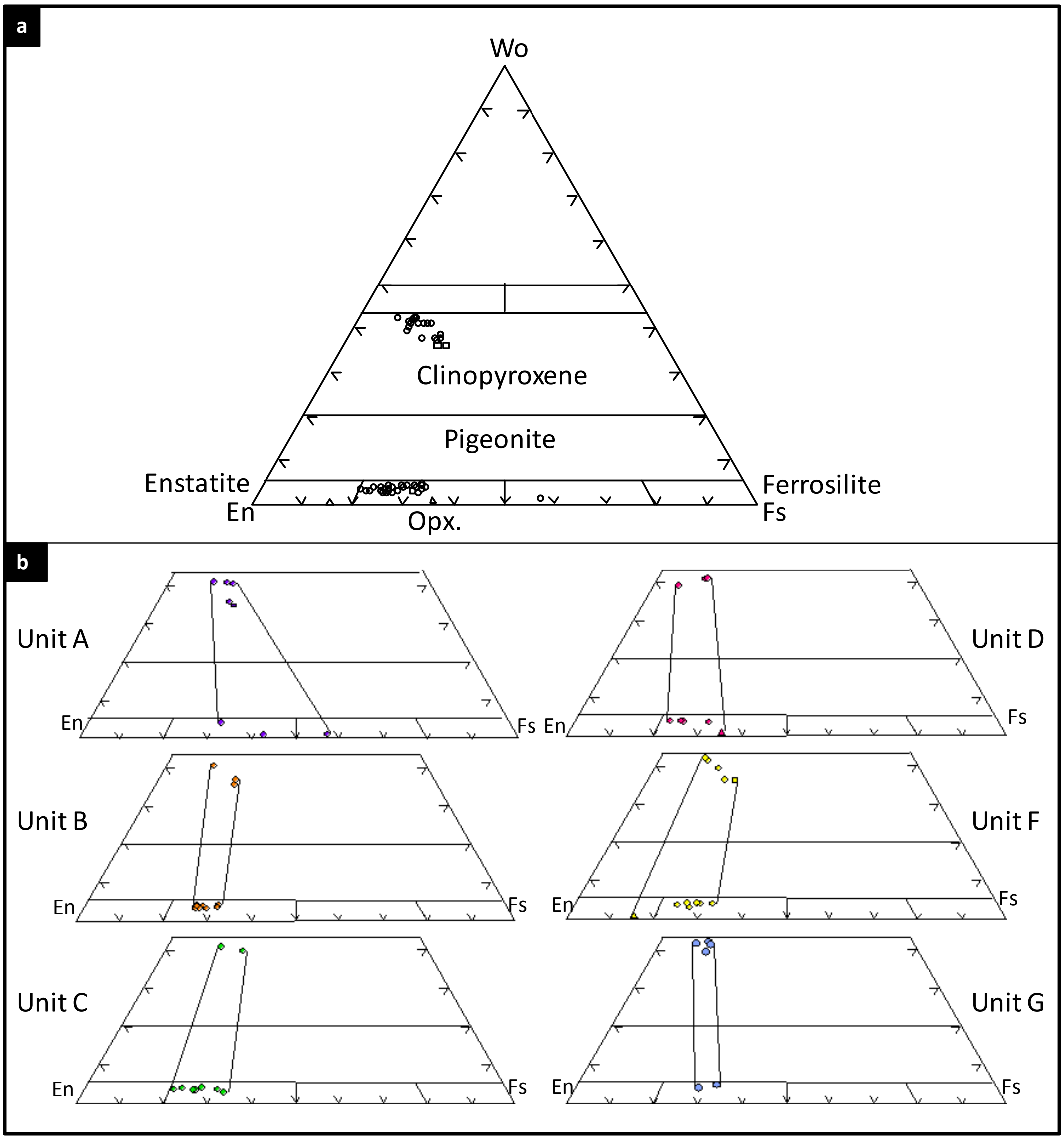

**Figure 4.10:** (a) Ternary diagram orthopyroxene (opx.) and clinopyroxene compositions. (b) Pyroxene composition plots in stratigraphic units indicating disequilibrium. No data for Unit E.

Orthopyroxene and clinopyroxene compositions range from $Wo_{0.5}En_{42}Fs_{58}$ to $Wo_3En_{-76}Fs_{20}$ and $Wo_{39}En_{41}Fs_{19}$ to $Wo_{40}En_{53}Fs_8$ respectively, with the two compositional groups forming relatively tight clusters (Figure 4.10a). When the pyroxene compositional data are plotted on ternary diagrams based on their stratigraphic unit, outlying tie lines are not parallel indicating disequilibrium between the two pyroxenes (Best and Christiansen, 2001), although Units C and F have values close to equilibrium (Figure 4.10b). A sample of pyroxene EMP data is shown in Table 4.4.

### *4.3.3 Olivine*

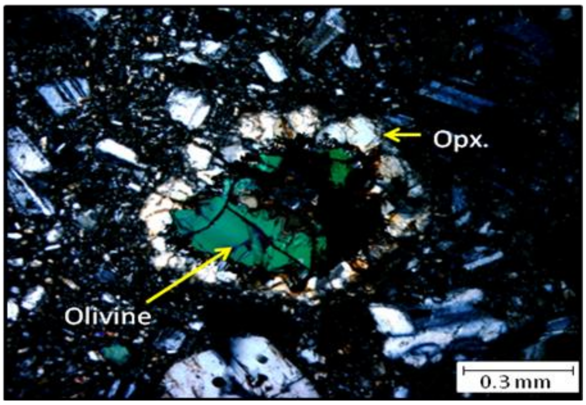

**Figure 4.11:** Olivine phenocryst with an orthopyroxene rim under crossed polarised light, Unit D.

Olivine is a subordinate phenocryst within the Ngauruhoe inner crater samples and is not present in all thin sections. Olivine phenocrysts average 0.3 mm in length and usually have thin, fine-grained rims of orthopyroxene (Figure 4.11). Two olivine crystals were analysed by EMP, giving compositions of $Fo_{84}$ and $Fo_{64}$. One olivine crystal has an orthopyroxene rim with a composition of $En_{66}$. Throughout the TgVC eruptives olivine is a minor phenocryst phase with a modal abundance of < 2 % in approximately 30 % of lavas sampled by Hobden (1997). The TgVC olivines range from $Fo_{67-96}$, with the Ngauruhoe lavas containing the most Fo-poor olivines. Within 1954 lava flows on the NW flanks of Ngauruhoe olivine phenocrysts are commonly enclosed by rims of orthopyroxene and clinopyroxene (pers. comm. F. Sanders). Griffin (2007) also noted rims of orthopyroxene and clinopyroxene around olivine phenocrysts within the Tongariro North Crater deposits.

### 4.3.4 Fe-Ti oxides

Fe-Ti oxide grains are abundant in the groundmass, but there are no Fe-Ti oxide phenocrysts in any samples from the inner crater. Titanomagnetite is the dominant variety and scattered crystals contain thatched ilmenite lamellae parallel to (111) octahedral directions. Rare haematite and minor discrete ilmenite are present, and inclusions of pyrite and titanomagnetite are present in some pyroxenes. Approximately 90% of TgVC eruptives contain Fe-Ti oxides (mainly magnetite with minor ilmenite) as microphenocrysts, within pyroxene glomerocrysts, and as inclusions in pyroxene, plagioclase, and amphibole (Hobden, 1997).

Fe-Ti oxide geothermometry was successfully used by Hobden (1997) and Griffin (2007) to obtain magma temperatures for Ngauruhoe and other Tongariro crater eruptives through co-existing ilmenite and titanomagnetite pairs (Table 4.5). No coexisting ilmenite and titanomagnetite pairs were found in this study. Temperatures calculated for Ngauruhoe and Tongariro craters range from 741-1175°C, with the Ngauruhoe group 4 ranging from 820-862°C (Hobden, 1997; Griffin, 2007).

**Table 4.5:** Fe-Ti oxide geothermometry temperatures from Ngauruhoe and Tongariro craters from [1]Hobden (1997) and [2]Griffin (2007).

| | Ngauruhoe group 4[1] | Red Crater[1] | North Crater[1] | North Crater[2] |
|---|---|---|---|---|
| Temperature °C | 820-862 | 861-951 | 861-1116 | 898 |
| Mean temperature °C | 846 ± 32 | 904 ± 53 | 945 ± 186 | |
| | Pukeonaki[1] | SW Oturere 1[1] | SW Oturere 2[1] | SW Oturere 3[1] |
| Temperature °C | 1055 | 741-842 | 846-918 | 791-1175 |
| Mean temperature °C | | 802 ± 87 | 879 ± 48 | 910 ± 233 |

[1] Hobden, 1999

[2] Griffin, 2007

### 4.3.5 Xenoliths

Country rock quartzose xenoliths are commonly found throughout the lavas and pyroclasts ejected during the 1954-55 and 1974-75 Ngauruhoe eruptions. While these xenoliths are not abundant within the inner crater exposures in hand specimen, smaller (c. 0.5 mm) xenoliths are seen in thin section. The xenoliths are metamorphosed quartzites, quartzofeldspathic buchites, and rare metagreywacke. Within the inner crater, the highest abundance of quartzofeldspathic xenoliths occurs in Unit G where they comprise c. 5% of the rock mass.

Figure 4.12a-c is a thin section of a 15 x 15 cm granular quartz-wollastonite-diopside xenolith collected from the 30th June, 1954 lava flow on the NW flanks of Ngauruhoe. The majority of the xenolith is composed of recrystallised quartz intergrown with Fe-Ti oxide minerals. Acicular elongate splays of wollastonite crystals (up to 3.5 mm in length) and minor stubby, irregular diopside crystals occur between the quartz grains. Secondary veins cross-cut the recrystallised textures (Figure 4.12c).

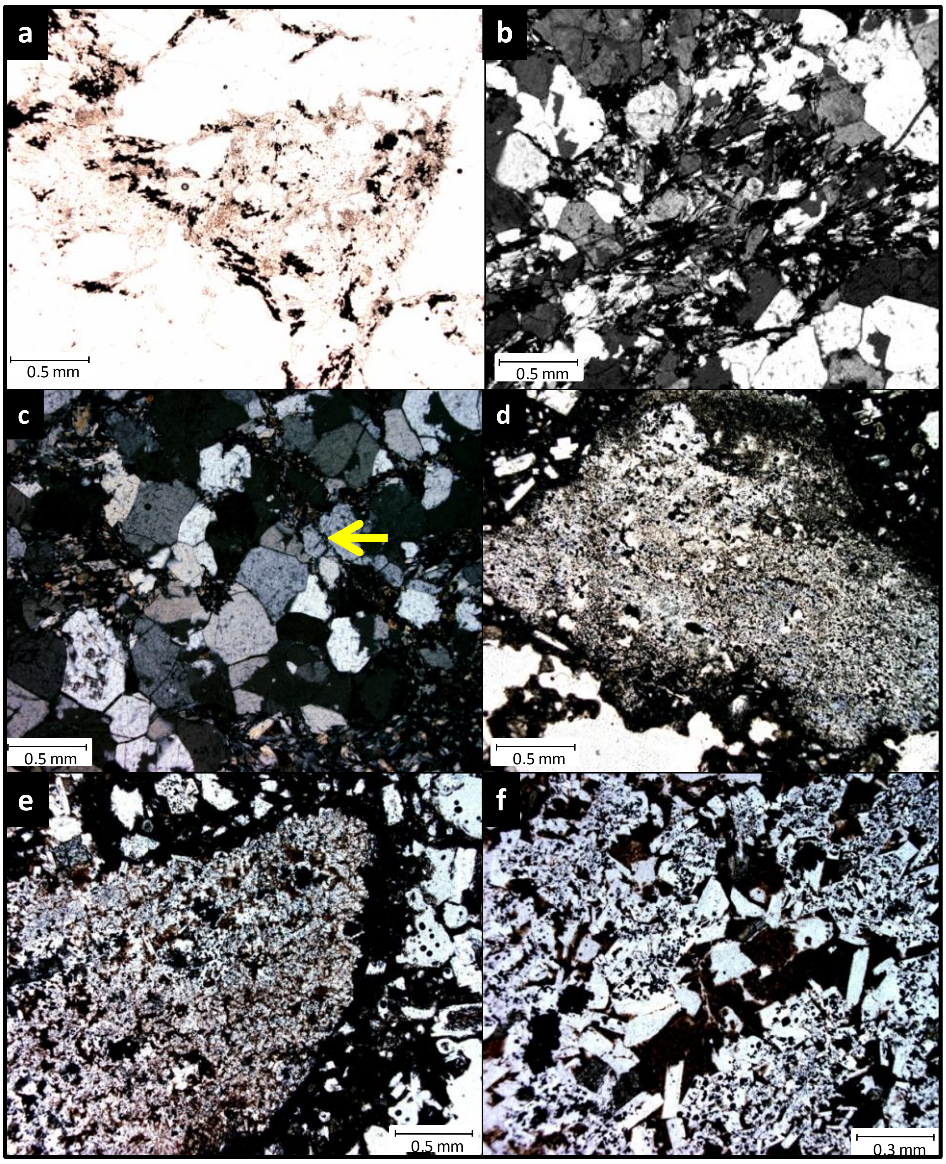

**Figure 4.12:** (a) Plane polarised light image of the quartz-wollastonite-diopside xenolith from the June 30, 1954 lava flow. (b) Crossed polarised view of (a) with wollastonite crystals splaying out between quartz crystals. (c) The same quartzite xenolith showing secondary veins indicated by yellow arrow, cross-cutting quartz crystals. (d) Fine-grained quartzofeldspathic xenolith containing Fe-Ti oxides from Unit A. (e) Quartzofeldspathic xenolith containing plagioclase, brown glass, and abundant opaque minerals from Unit B. (f) Magnified view of (e) showing plagioclase laths infilled with abundant Fe-Ti oxide crystals, with dark brown glass between laths.

Smaller accidental quartzofeldspathic xenoliths, averaging 0.5 mm in diameter, have been described in most thin sections throughout the stratigraphic units, and have the same recrystallised quartz textures as the larger quartz-wollastonite-diopside xenolith, with plagioclase and pyroxenes present in differing proportions.

Fe-Ti oxides are abundant throughout most xenoliths, and some contain small proportions of glass and epidote crystals. Resorption is evident in rims around the xenoliths (Figure 4.12d-e) and through sieve textured plagioclase that has then been infilled with glass and Fe-Ti oxides (Figure 4.12 e-f). Xenolith inclusions within juvenile scoriaceous bombs have resulted in some surrounding vesicle deformation patterns (Figure 4.13).

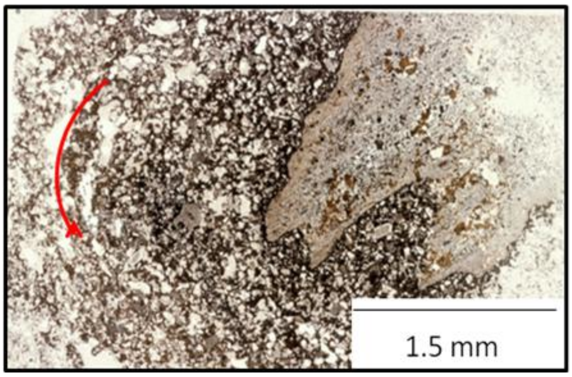

**Figure 4.13:** Quartzofeldspathic xenolith within a juvenile scoria clast from Unit B. Vesicles are coalesced and elongate, and have curved around the xenolith, indicated by the red arrow.

Fine-grained metagreywacke xenoliths are visible in thin sections of Units A, B and G (up to 3 mm in length) but were not observed in hand specimen. They are smaller and less common than quartzofeldspathic xenoliths, and display granular, recrystallisation textures with abundant plagioclase and Fe-Ti oxides, with rare orthopyroxene and clinopyroxene.

### *4.3.6 Groundmass*

The groundmass is hyalopilitic and interstertial in places, and is dominantly composed of subhedral laths of plagioclase and pyroxenes, with abundant Fe-Ti oxides (titanomagnetite) and glass. Glass ranges from colourless, to brown, to black, with microlites generally larger within the lighter-coloured glass (up to 0.25 mm with rare 0.5 mm crystals). Within the vulcanian ash deposits (Units E and F) ash particles contain the same variation in glass colours within beds, with the same microlite size to glass colour correlation. Fe-Ti oxide crystals grow to 0.25 mm but are predominantly < 0.125 mm throughout the samples.

Three main groundmass varieties have been recognised throughout the inner crater deposits: (1) groundmass appearing black in hand specimen with small

Abundant microlites of Fe-Ti oxides inset in glass (Figure 4.14a); (2) groundmass appearing grey in hand specimen with abundant larger microlite laths, and larger, less abundant Fe-Ti oxides set in glass (Figure 4.14b); and (3) dark brown near-opaque glass groundmass that largely obscures microlite content. In the darker glasses it is difficult to see Fe-Ti oxide crystals, but around the edges of phenocrysts or ash clasts it is apparent that there is a lower abundance than in the clear to light coloured glass (Figure 4.14c). The brown glass groundmass is mainly present in ash clasts, with the first two groundmass types dominant in strombolian deposits, and in several thin sections (A1c, A3, C1b and D1) types 1 and 2 occur as banding in individual clasts (Figure 4.14d).

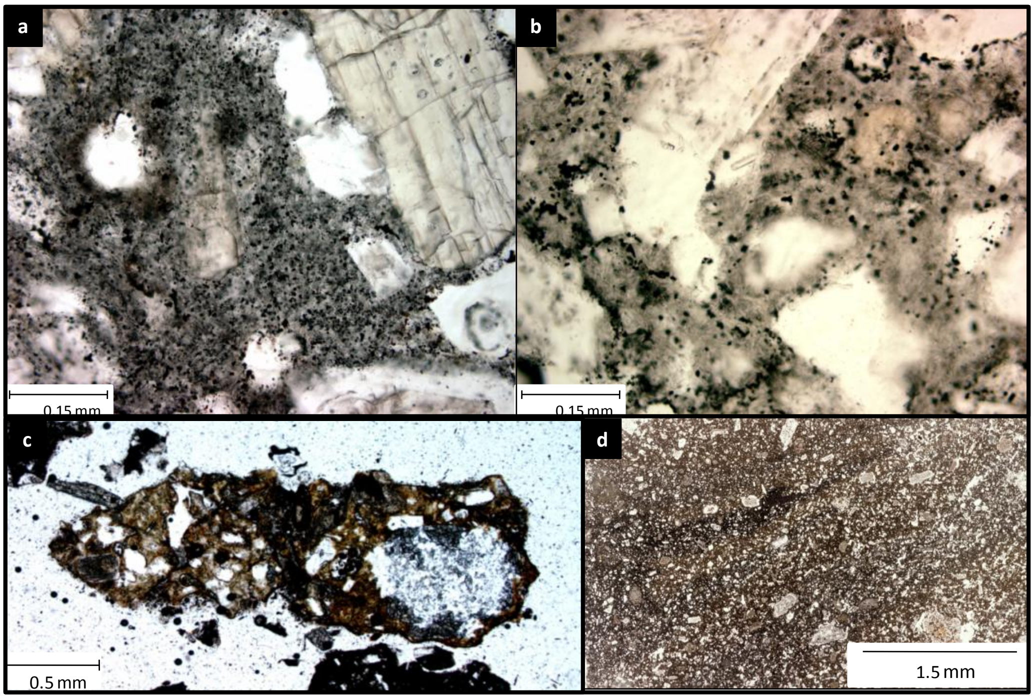

**Figure 4.14:** (a) Plane polarised view of type 1 groundmass (Unit C) with small microlites and abundant opaque minerals and abundant glass. (b) Type 2 groundmass also within Unit C (both types present as bands) with larger microlites and fewer, larger opaque minerals and abundant glass. (c) Type 3 brown glass groundmass within an ash fragment in Unit E. (d) Slide scan of a basaltic andesite juvenile clast illustrating groundmass types (1) (black) and (2) (brown) banded within Unit D.

There are no correlations of groundmass crystallisation with stratigraphic succession. Crystal sizes vary from small (< 0.0625 mm), medium (≤ 0.25 mm) and large (≤ 0.5 mm with rare crystals up to 1 mm in length).

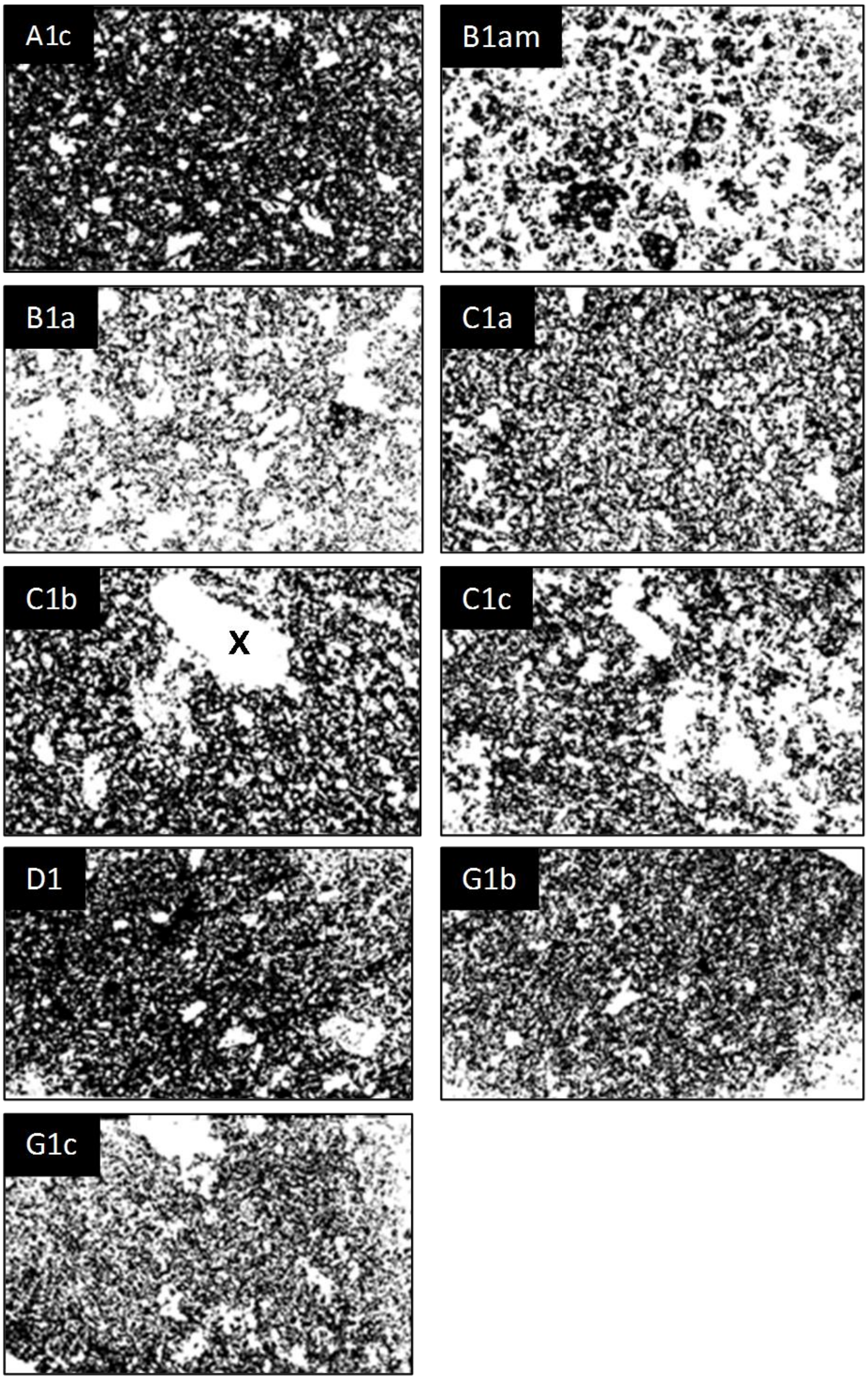

**Figure 4.15:** Differing degrees of vesiculation and coalescence throughout the inner crater stratigraphic succession. A1c has a modal vesicularity of 15%, B1am and B1a have modal vesicularities of 43-50%, Unit C samples have modal vesicularities ranging from 9-53%, D1 has a modal vesicularity of 7%, and Unit G sample vesicularities range from 6-47%. The highest degrees of vesicle coalescence are in Units B and C. Degree of coalescence varies within units. The large cavity in C1b marked by the ‘x’ is a quartzofeldspathic xenolith, rectangular cavities are phenocrysts.

### *4.3.7 Vesicularity and vesicle wall crystallisation*

Modal data displays no linear patterns in vesicularity with stratigraphic succession (Table 4.2). Vesicularity and degree of coalescence varies within and between units. Slide scans of thin sections (Figure 4.15) illustrate the varying degree of coalescence throughout the stratigraphic succession. Units B, C and G contain the highest degrees of coalescence, with modal vesicularities ranging from 6 – 53%. Unit B has a bulk vesicularity range of 22 – 82%, and the connected vesicularity almost equivalent to this range, with up to 99% of vesicles connected (vesicularity data for Unit B scoria samples calculated using a pycnometer, see Appendix Five). Vesicle cross-sections reveal irregular outlines, with rare rounded vesicle cavities. There is no pattern in modal vesicularity data within the inner crater scoria and spatter deposits with stratigraphic succession (Figure 4.16).

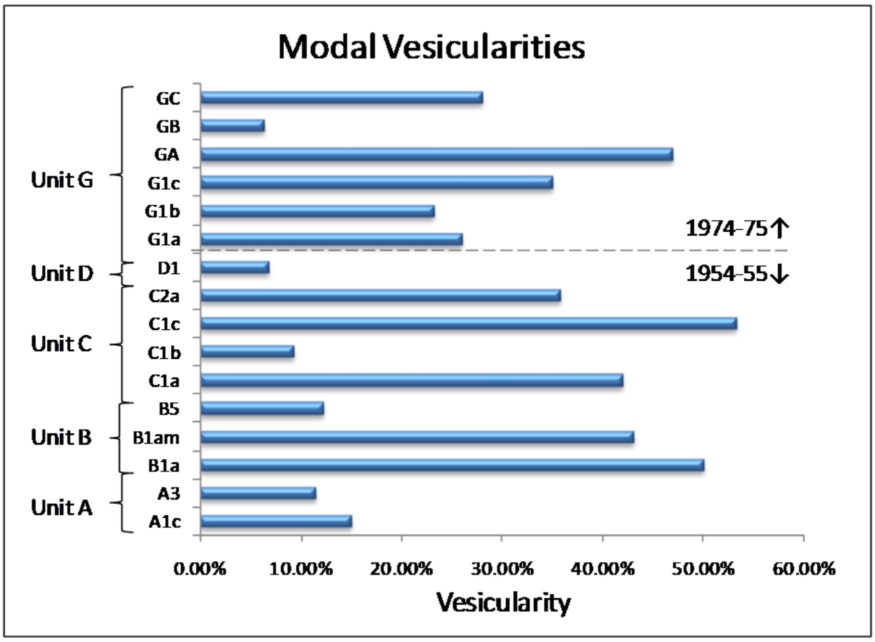

**Figure 4.16:** Modal vesicularity data for the Ngauruhoe inner crater spatter deposits.

Through SEM imaging, secondary mineral cryptocrystalline growth has been identified within some vesicle cavities. As discussed in Chapter 3, crystals of gypsum and quartz polymorphs, including cristobalite and opaline quartz, have crystallised within vesicle cavities. In most thin sections this cryptocrystalline growth is not visible, however, in thin section A3 (from the Unit A northern deposit) fine-grained crystalline silica growth is visible on the inner vesicle walls (Figure 4.17).

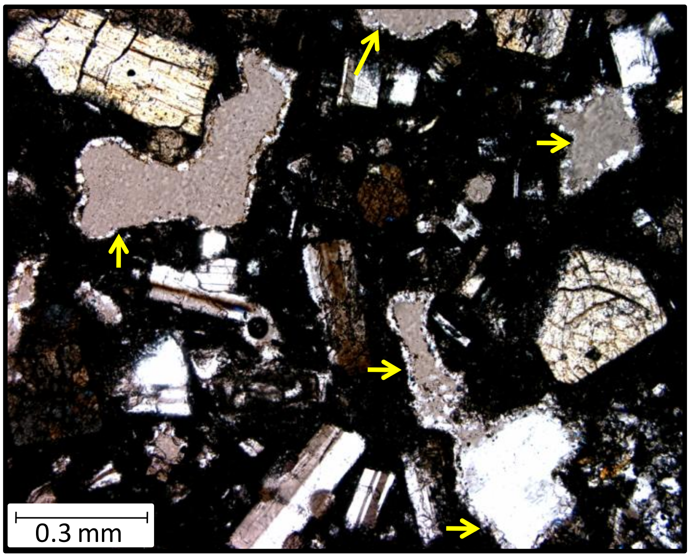

**Figure 4.17:** Crossed polarised view of crystalline silica growth on the inside of vesicle cavity walls in Unit A, indicated by yellow arrows, with phenocrysts of plagioclase, orthopyroxene, and clinopyroxene, set in a groundmass of glass.

## 4.4 Ash Morphology and Mineralogy

Vulcanian ash clasts average 1.5 mm in length (coarse ash) with a matrix composed of subhedral crystals (plagioclase, pyroxenes, and opaques) and glass. Some ash clasts are surrounded by a fine-grained glassy rim (Figure 4.18a). The very fine ash matrix is composed of crystals and basaltic andesite ash particles (Figure 4.18b). The majority of ash clasts are sub-rounded, with lesser amounts

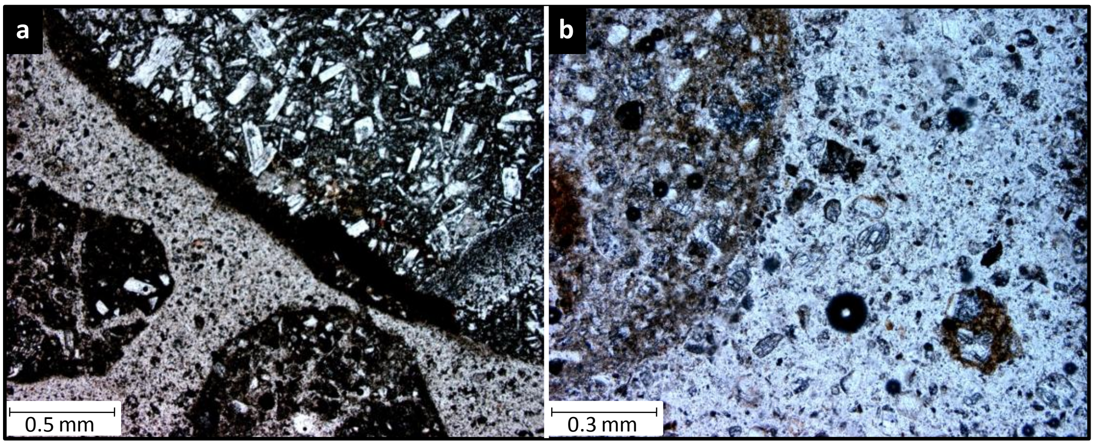

**Figure 4.18:** Ash clasts under plane polarised light in thin section E. (a) Fine ash matrix surrounding the ash clasts and a dark brown fine-grained glassy rim around the large ash clast in the top-right. (b) Fine ash matrix in composed of broken crystals and basaltic andesite ash clasts.

of sub-angular clasts.

Ash clasts in Unit E are very similar to ash clasts of Unit F, but Unit E has a finer surrounding matrix (Figure 4.18a). Thin sections reveal the ratio of poorly to non-vesicular (Figure 4.19a), to moderately to highly-vesicular ash clasts (Figure 4.19b) to be approximately 60:40, respectively. Under plane polarised light ash clast colours vary from light grey, to brown, to black, with differing degrees of brown to black glass in each ash bed (Figure 4.19c). The glass content within the vulcanian ash clasts in Units E and F is significantly higher than within the strombolian derived ash clasts (Units B and D). Crystal to groundmass ratios vary widely between ash clasts (Figure 4.19d). Groundmass abundances vary between ash clasts, from ≥ 99% (ash clast contains little to no visible crystals, possibly due to fragmentation) to c. 20% (ash clast contains few large phenocrysts or abundant smaller crystals) (Figure 4.20a). The groundmass within Unit F contains abundant Fe-Ti oxides, but there is less than 1% Fe-Ti oxide content within the Unit E groundmass.

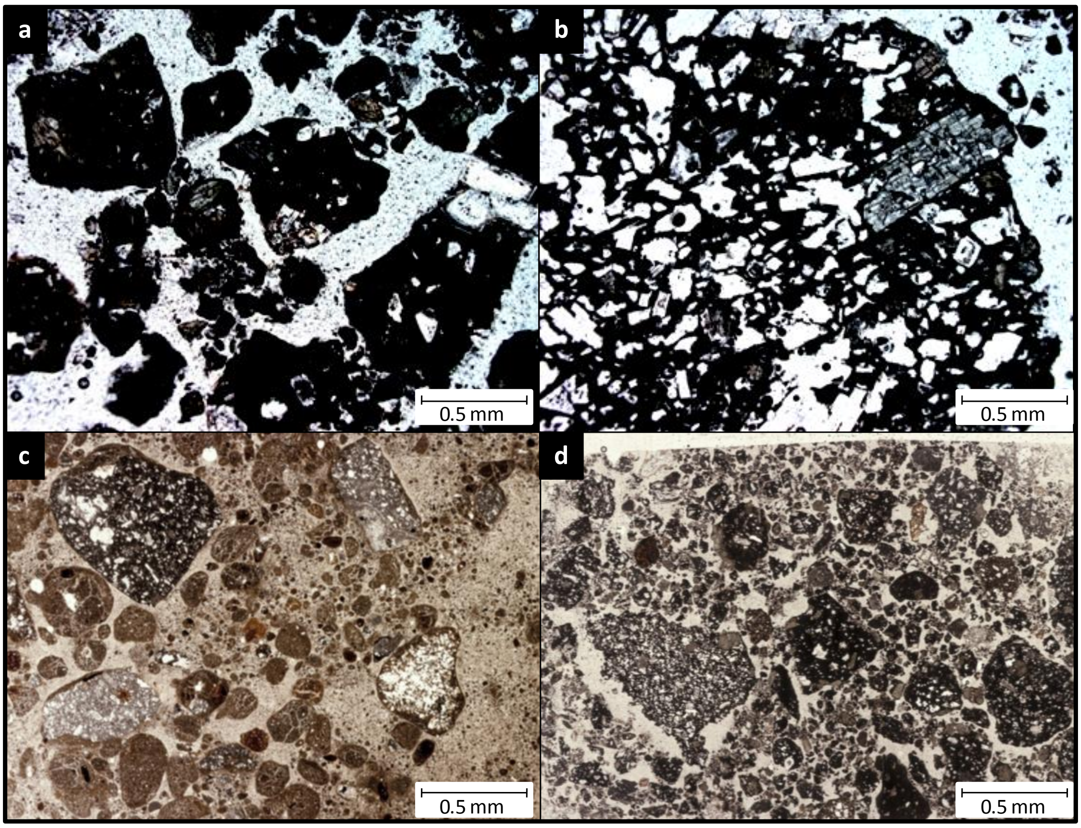

**Figure 4.19:** (a) Plane polarised view of sub-angular to angular, non-vesicular ash clasts (Unit F). (b) Plane polarised view of a large vesicular ash clast (Unit F). (c) Slide scan of thin section E showing sub-rounded to rounded ash clasts. (d) Slide scan of thin section F6 showing ash clasts with a range of crystal to groundmass proportions.

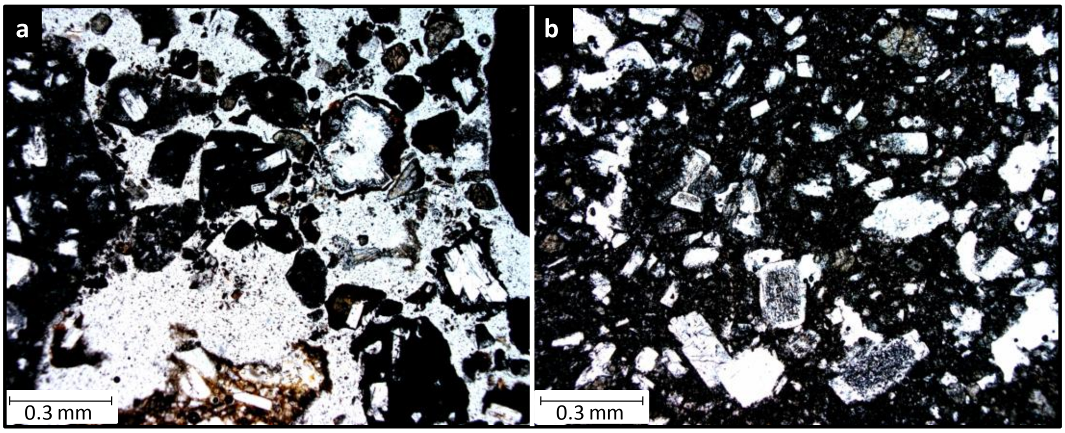

**Figure 4.20:** (a) Ash clasts vary in crystal content from a large phenocryst with a rim of host rock, to ash clasts containing little to no visible crystals. (b) Larger phenocrysts of plagioclase and two pyroxenes contained within the ash clasts; plagioclase phenocrysts contain the same disequilibrium sieve textures as the strombolian deposits.

The phenocryst assemblages within the ash clasts have the same characteristics as the phenocrysts described in Section 4.3. Phenocrysts of plagioclase, orthopyroxene, and clinopyroxene reach lengths of 1 mm. Plagioclase crystals display the same disequilibrium sieve textures contained in the larger strombolian units (Figure 4.20b).

## 4.5 Secondary Alteration Minerals

Two samples were analysed using X-Ray Diffraction (XRD) to identify secondary surface minerals in Unit D, and to determine the presence or absence of clay minerals within the finer-grained Unit E. The results showed no clay minerals, and the surface crystals on the Unit D lapilli and blocks are gypsum (Appendix Six).

# PART 2: GEOCHEMISTRY

## 4.6 Introduction

Representative pyroclasts from the Ngauruhoe inner crater were analysed for whole rock major and trace elements by XRF. Their compositions are compared to older Ngauruhoe eruptives, and eruptives from various TgVC craters.

## 4.7 Methodology

### *X-Ray Fluorescence*

Major and trace elements for 22 samples have been measured using a Spectro X-Lab 2000 X-Ray Fluorescence (XRF) at the University of Waikato. 21 trace elements (S, Cl, V, Cr, Co, Ni, Cu, Zn, Ga, As, Rb, Sr, Y, Zr, Nb, Ba, La, Ce, Pb, Th, U) have been analysed, and are presented here along with major element ($SiO_2$, $TiO_2$, $Al_2O_3$, FeO, CaO, MgO, MnO, $Na_2O$, $K_2O$, $P_2O_5$ ) data. Major and trace elements have been measured to see if any distinguishing patterns occur between units, which would then provide the possibility of matching the stratigraphic units with the 1954-55 lava flows.

### *Major element analysis*

Samples chosen for XRF analysis were dried in an oven overnight at 80˚C before powdering in a tungsten carbide mill until the sample had the texture of talcum powder. This high degree of crushing is required to homogenise the porphyritic samples. The powdered rock is used to make fused discs for major element analysis by XRF. 0.35 g of sample was added to 2.50 - 2.55 g of type 1.2:2.2 flux (35% Li-tetraborate, 65% Li-metaborate generally used for basaltic andesites) and mixed in a platinum crucible. The samples are step heated (to appropriately break the $SiO_2$ bonds) with 15 minute intervals in a Bradway Fusion Furnace at 700˚C, 800˚C, then 1040˚C with the furnace shaker on. Once the 45 minutes of heating is complete, a pinch of ammonium iodide is added to the sample to prevent sticking to the crucible while the sample is poured onto a graphite disc on a press (the press is situated on a 230˚C hot plate). The molten samples are pressed into glass discs, then step-cooled for annealment and prevention of cracking. Once cooled, the samples are labelled and the edges trimmed ready for analysis.

***Trace element analysis***

The same powdered rock samples are used for trace element analysis. The pressed pellets were prepared in aluminium cups with 5 g of powdered sample and 13-15 drops of PVA binder. The powder and binder were mixed with a wooden spatula in a paper cup to ensure no contamination took place. The samples were dried at 70°C to evaporate the PVA binder before analysis.

***Loss on ignition***

The final step of the XRF analysis is determination of Loss on Ignition (LOI), using a sample of the same powdered rock used for the first two analyses. 2 g of powdered sample is added to silica crucibles and are heated in the furnace at 1000°C for one hour. The samples are then cooled before recording the weights. For all three methods, three samples were re-run to ensure reproducibility of the analyses.

## 4.8 Rock Classification

Major element data have been plotted on the $K_2O$ versus $SiO_2$ graph (Figure 4.21) to determine rock classification. The data points fall into the lower zone of the medium-K calc-alkaline series in a near-linear trend, and are basaltic-andesite (52-57% $SiO_2$ wt. %) to andesite (57-63 $SiO_2$ wt. %). The high dacite $SiO_2$ value of the Unit A northern deposit, A3 ($SiO_2$ 68.81 wt. %), is due to secondary silica growth on vesicle cavity walls, while the higher $SiO_2$ andesite composition of Unit G (reaching $SiO_2$ 58.85 wt. %) could be due to contamination from quartzofeldspathic xenoliths, or the high xenolith content altering the magma composition.

**Table 4.6:** Major and trace element data for the Ngauruhoe inner crater stratigraphic sequence. Major elements presented in wt. % and trace elements in ppm.

| | A1c | A3 | B1a | B5 | C1a | C1b | C1c | D1 | D2 | E | F1 | F2 | F3 | F4 | F5 | F6 | G1b | GA | GB1 | GC |
|---|---|---|---|---|---|---|---|---|---|---|---|---|---|---|---|---|---|---|---|---|
| SiO2 | 54.88 | 68.81 | 56.13 | 55.46 | 56.72 | 57.37 | 55.70 | 55.58 | 56.07 | 56.99 | 55.95 | 56.21 | 55.36 | 55.67 | 55.75 | 55.44 | 57.55 | 57.03 | 58.85 | 55.88 |
| TiO2 | 0.80 | 0.9 | 0.77 | 0.75 | 0.80 | 0.82 | 0.77 | 0.75 | 0.74 | 0.78 | 0.77 | 0.76 | 0.75 | 0.76 | 0.77 | 0.79 | 0.86 | 0.79 | 0.87 | 0.82 |
| Al2O3 | 17.54 | 12.9 | 16.92 | 17.05 | 15.97 | 15.47 | 16.88 | 16.91 | 16.14 | 16.35 | 16.48 | 16.66 | 16.99 | 16.74 | 17.08 | 16.84 | 16.24 | 17.48 | 15.28 | 17.56 |
| FeO* | 8.07 | 5.87 | 7.99 | 8.55 | 8.25 | 8.54 | 8.48 | 8.19 | 8.74 | 8.76 | 9.08 | 8.80 | 8.57 | 8.77 | 8.74 | 9.00 | 8.97 | 7.86 | 9.23 | 8.64 |
| MnO | 0.14 | 0.09 | 0.14 | 0.15 | 0.14 | 0.15 | 0.15 | 0.14 | 0.15 | 0.14 | 0.15 | 0.14 | 0.15 | 0.15 | 0.15 | 0.15 | 0.15 | 0.14 | 0.16 | 0.14 |
| MgO | 4.39 | 3.19 | 5.27 | 5.37 | 5.40 | 5.42 | 5.43 | 5.29 | 5.98 | 5.13 | 5.53 | 5.49 | 5.47 | 5.47 | 5.19 | 5.36 | 4.52 | 4.63 | 4.51 | 4.48 |
| CaO | 7.31 | 4.71 | 8.14 | 8.33 | 7.34 | 7.35 | 8.14 | 8.17 | 8.06 | 7.36 | 7.59 | 7.63 | 8.17 | 7.84 | 7.88 | 8.06 | 6.94 | 7.54 | 6.67 | 7.95 |
| Na2O | 3.02 | 2.1 | 3.07 | 2.95 | 2.92 | 2.99 | 3.04 | 2.96 | 2.85 | 3.08 | 2.78 | 2.83 | 2.99 | 3.37 | 3.15 | 3.12 | 3.17 | 3.09 | 3.04 | 3.32 |
| K2O | 1.12 | 1.27 | 1.12 | 1.11 | 1.26 | 1.24 | 1.11 | 1.13 | 1.10 | 1.20 | 1.08 | 1.07 | 1.09 | 1.09 | 1.07 | 1.09 | 1.14 | 1.27 | 1.23 | 1.15 |
| P2O5 | 0.18 | 0.15 | 0.15 | 0.17 | 0.26 | 0.12 | 0.14 | 0.16 | 0.15 | 0.14 | 0.14 | 0.14 | 0.14 | 0.13 | 0.14 | 0.12 | 0.15 | 0.18 | 0.15 | 0.14 |
| LOI | 2.56 | 4.75 | 0.29 | 0.12 | 0.93 | 0.53 | 0.17 | 0.73 | 0.02 | 0.07 | 0.46 | 0.27 | 0.34 | 0.02 | 0.09 | 0.04 | 0.32 | 2.27 | 0.29 | -0.09 |
| Total | 100 | 100 | 100 | 100 | 100 | 100 | 100 | 100 | 100 | 100 | 100 | 100 | 100 | 100 | 100 | 100 | 100 | 100 | 100 | 100 |
| | | | | | | | | | | | | | | | | | | | | |
| S | 10800 | 10800 | 1267 | 366 | 2656 | 709 | 776 | 2851 | 392 | 494 | 1356 | 749 | 1107 | 326 | 363 | 352 | 643 | 9535 | 787 | 459 |
| Cl | 189 | 189 | - | 383 | - | - | - | 350 | 174 | 47 | 267 | 204 | 160 | 94 | 92 | 117 | 283 | 332 | 393 | 406 |
| V | 246 | 246 | 247 | 257 | 282 | 263 | 254 | 244 | 240 | 244 | 253 | 244 | 246 | 246 | 252 | 257 | 297 | 230 | 272 | 252 |
| Cr | 56 | 56 | 94 | 99 | 97 | 97 | 100 | 107 | 155 | 92 | 104 | 98 | 103 | 91 | 81 | 85 | 157 | 72 | 58 | 61 |
| Co | 98 | 98 | 38 | 68 | 38 | 46 | 35 | 30 | 36 | 19.4 | 41 | 30 | 35 | 38 | 30 | 37 | 33 | 38 | 44 | 38 |
| Ni | 21 | 21 | 30 | 30 | 29 | 33 | 31 | 29 | 40 | 26 | 32 | 29 | 29 | 28 | 26 | 28 | 19.9 | 22 | 18.7 | 19.6 |
| Cu | 28 | 28 | 38 | 32 | 29 | 26 | 27 | 42 | 38 | 33 | 39 | 42 | 40 | 44 | 44 | 43 | 31 | 43 | 40 | 45 |
| Zn | 88 | 88 | 81 | 87 | 100 | 96 | 87 | 86 | 88 | 91 | 89 | 87 | 88 | 91 | 88 | 88 | 93 | 87 | 97 | 88 |
| Ga | 18.4 | 18.4 | 18.4 | 19.4 | 17.4 | 18 | 18.3 | 18.8 | 17.8 | 18.1 | 17 | 19 | 18.5 | 19 | 18.5 | 18.9 | 19.9 | 17.9 | 17.5 | 19 |
| As | 1.2 | 1.2 | 0.7 | 1.2 | 9.8 | 8.5 | 2.2 | 0.3 | 5.8 | 10.1 | 3.3 | 3 | - | 1.8 | 2.5 | 2.1 | 4.8 | 0.8 | 3.3 | 2 |
| Rb | 37 | 37 | 38 | 35 | 42 | 42 | 33 | 37 | 36 | 40 | 35 | 36 | 35 | 36 | 34 | 35 | 38 | 42 | 41 | 36 |
| Sr | 235 | 235 | 255 | 235 | 228 | 214 | 238 | 232 | 219 | 223 | 226 | 228 | 238 | 219 | 222 | 226 | 206 | 225 | 195 | 229 |
| Y | 25 | 25 | 22 | 21 | 19.4 | 20 | 19.4 | 21 | 19.4 | 19.3 | 20 | 21 | 21 | 21 | 20 | 22 | 23 | 21 | 24 | 23 |
| Zr | 101 | 101 | 96 | 95 | 104 | 103 | 97 | 98 | 96 | 105 | 96 | 97 | 96 | 94 | 96 | 97 | 106 | 105 | 108 | 104 |
| Nb | 6.4 | 6.4 | 4.6 | 4.8 | 4.8 | 5 | 4.9 | 4.8 | 4.7 | 5.1 | 4.5 | 4.1 | 4.7 | 4.4 | 4.4 | 4.8 | 5.1 | 4.9 | 5.2 | 5.1 |
| Ba | 207 | 207 | 222 | 218 | 227 | 229 | 228 | 228 | 222 | 249 | 217 | 228 | 219 | 215 | 223 | 226 | 227 | 251 | 243 | 232 |
| La | 8.1 | 8.1 | 6.5 | 8.2 | 5.9 | 5.4 | 6.7 | 9.2 | 6.5 | 7.5 | 8 | 6.3 | 6.6 | 6.9 | 6.4 | 6.8 | 7.5 | 7.1 | 6.6 | 8.5 |
| Ce | 24 | 24 | 21 | 23 | 18.7 | 20 | 19.8 | 22 | 20 | 16.6 | 21 | 19.5 | 21 | 21 | 17.4 | 22 | 22 | 24 | 24 | 22 |
| Pb | 13.5 | 13.5 | 5.8 | 7 | 7.4 | 6.1 | 6.5 | 6.8 | 7.7 | 9.2 | 7.3 | 7.3 | 6.3 | 7 | 6.8 | 6.8 | 9.3 | 8.8 | 9.2 | 7.4 |
| Th | 14 | 14 | 3.1 | 3.7 | 4.4 | 3.2 | 3.3 | 4.7 | 3.6 | 5.6 | 3.5 | 4 | 4.2 | 3.5 | 3.3 | 4 | 4.7 | 0.4 | 4.4 | 4.8 |
| U | 13.7 | 13.7 | 1.2 | 0.9 | 1.9 | - | - | 2.3 | - | 1.4 | - | 1.3 | 1.9 | 1.5 | 1.2 | 1.2 | 2.1 | 1.5 | 1.7 | - |

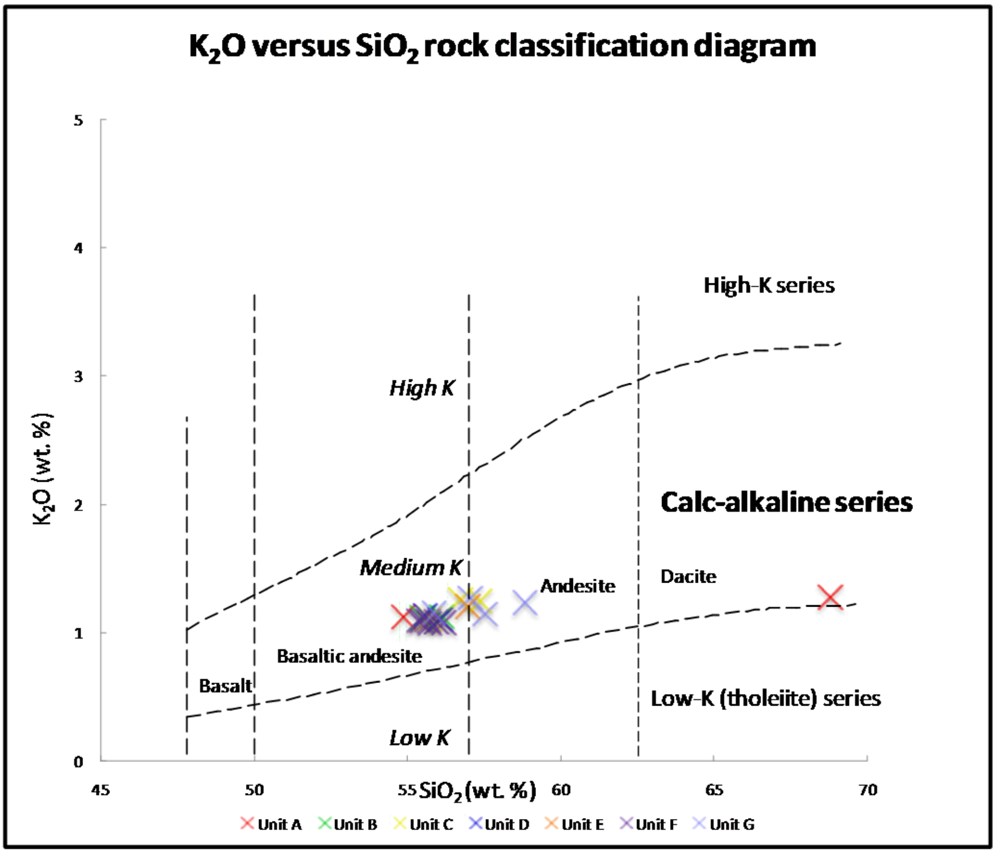

**Figure 4.21:** $K_2O$ versus $SiO_2$ whole rock classification diagram with the plotted compositions of the Ngauruhoe inner crater units A to G, total alkali versus silica composition boundaries (vertical lines) after Rollinson, 1993.

## 4.9 Major Oxide Compositions

Major oxide and trace element data for the inner crater stratigraphic units are given in Table 4.6. $SiO_2$ varies from 54.98  68.81 wt. %, and other than the peak in Unit A (due to secondary hydrothermal alteration), the $SiO_2$ trend is very consistent throughout the stratigraphic succession, with an increase in the 1974-75 eruption deposits. $SiO_2$ content coincides with an increase in explosivity between the two eruptions. The 1954-55 Units A to D have an $SiO_2$ range of 54.88 – 57.37 wt. % with only one value over $SiO_2$ 57 wt. % (excluding sample A3), and the more explosive vulcanian phase Unit E has a higher range $SiO_2$ content of 56.99 wt. %. The 1974-75 deposits have higher $SiO_2$ contents ranging from 55.36 – 56.21 wt. % in Unit F, and 57.03 – 58.85 wt. % in Unit G. The 1974-75 eruption was more explosive than the 1954-55 strombolian eruption and $SiO_2$ contents generally increased with time, however, the vulcanian ash unit has a lower $SiO_2$ content than the intense 1974-75 strombolian spatter-producing deposit. Higher

$SiO_2$ values are also measured within Unit G samples, which could be a result of the high abundance of quartzofeldspathic xenoliths increasing $SiO_2$ content of the magma.

CaO varies from 6-9 wt. %, with a trough in Unit A that coincides with the peak in $SiO_2$, troughs in other major elements and Sr, and a peak in Ni. $Al_2O_3$ content varies between 15-19 wt. %, with troughs coinciding with peaks in $SiO_2$ (Figure 4.22). FeO experiences a large variation between 5-10%, with a slight gradual increase from Unit A to G. MgO is relatively constant, with decreases in Units A and G corresponding to increases in $SiO_2$ values. A peak in MgO in Unit D coincides with a peak in Ni, and an increase in modal olivine (up to 3.5 % olivine content Table 4.2). The significant increase of $SiO_2$ content in sample A3 has resulted in a constant sum effect, lowering the proportions of other major oxides (Figure 4.22).

## 4.10 Whole Rock Trace Element Analysis

Trace elements plotted on a multi-element diagram, normalised against primordial mantle, display generally consistent magmatic trends (Figure 4.23). Elevated Pb levels are consistent with previous studies on Tongariro and Ruapehu eruptives (Cole, 1978; Patterson and Graham, 1988; Price et al., 2005, 2007).

Selected trace elements (Ba, Zr, Rb, Ni, Sr, La, Y, V, Cr, and Th) have been plotted against silica in Harker variation diagrams in Figure 4.24. S and Cl have elevated values in most units due to extensive post-depositional hydrothermal alteration, especially in the Unit A northern deposit. A decrease in Sr, and a slight increase in incompatible elements Ba, Zr, and Rb, is consistent with a very slight crystal fractionation of plagioclase. Rare earth elements La, Ce, and Y show constant trends with increasing $SiO_2$. Th has a relatively constant trend throughout the inner crater stratigraphic succession with the exception of two values from Unit A showing elevated levels up to 14 ppm. Ni has a wide scatter likely due to variations in olivine content, and has a general decreasing trend from

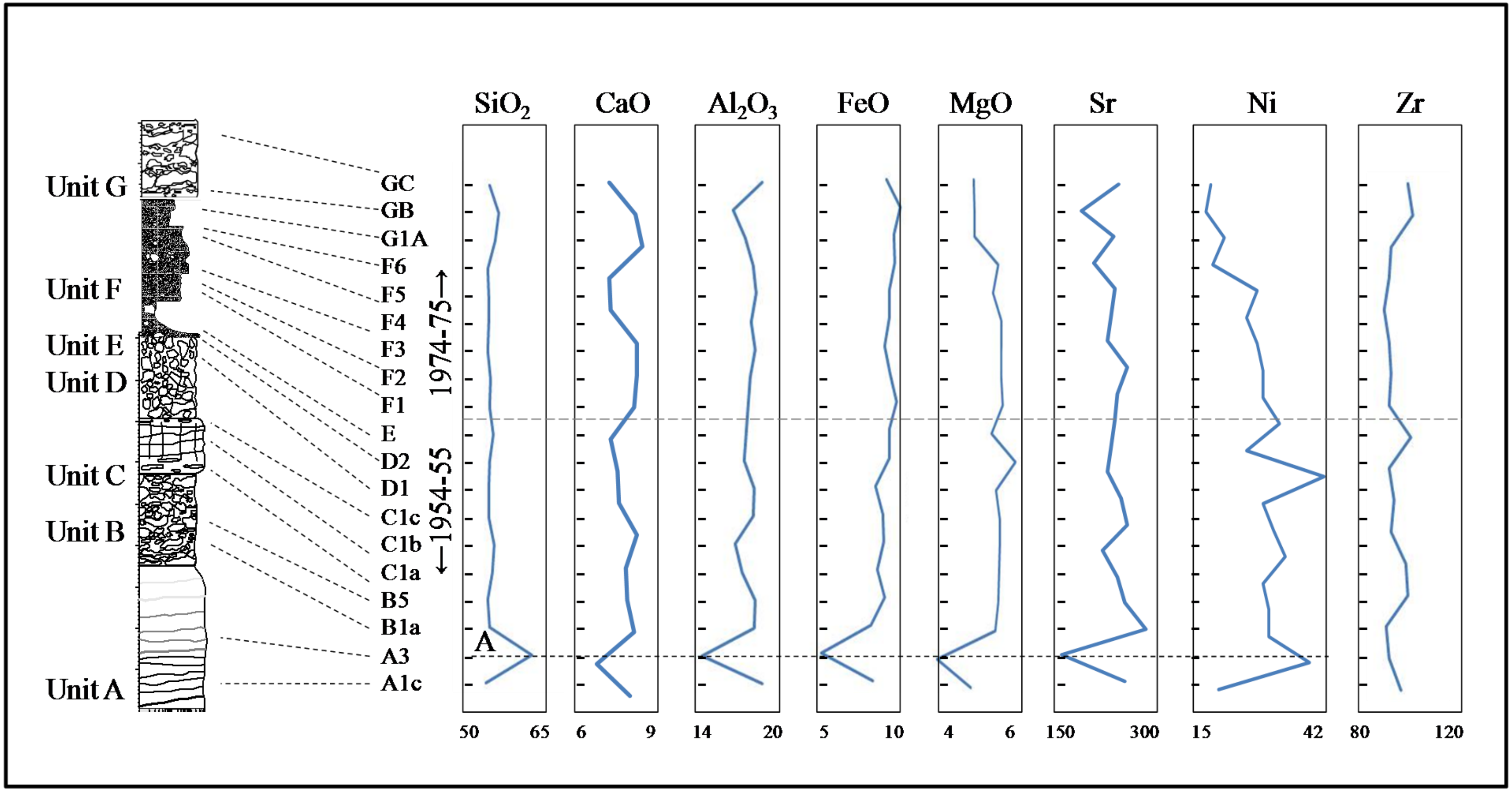

**Figure 4.22:** Selected major and trace element plots against the inner crater stratigraphic succession (not to scale) indicating the relatively minor trends. Line A indicates a strong correlation of major and trace element troughs with a peak in $SiO_2$ and Ni. Units below the major element plots are in wt. %, and units below the trace element plots are in ppm.

Unit A through to F, with Unit G containing higher Ni content. Cr and V both display a high degree of scatter, with a general increasing trend in Cr, and a constant trend in V, indicating little or no crystal fractionation of pyroxene or Fe-Ti oxide. No trace element geochemical trends are apparent between the 1954-55 and 1974-75 eruptions.

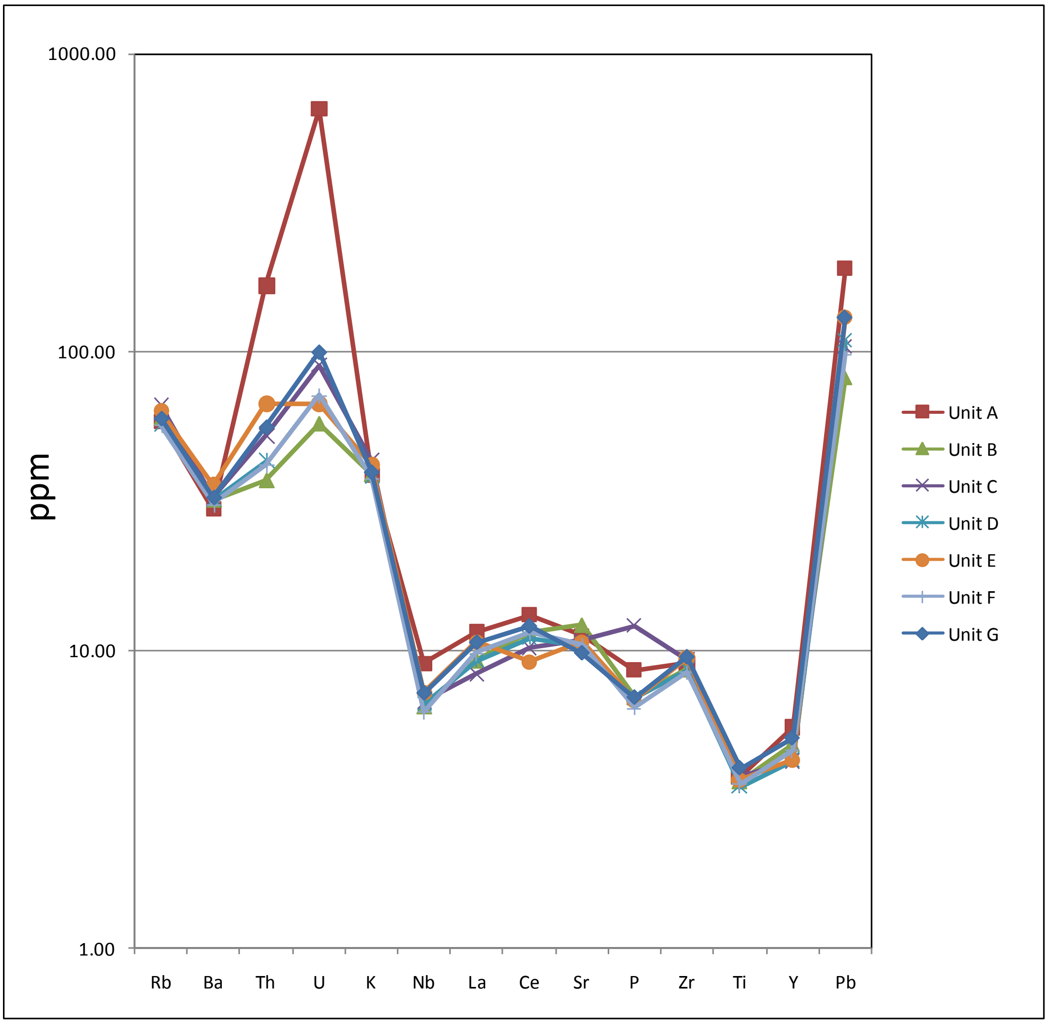

**Figure 4.23:** Multi-element diagrams for the Ngauruhoe inner crater stratigraphic units. Primordial mantle normalising values used are those of McDonough et al. (1992) cited in Rollinson (1993).

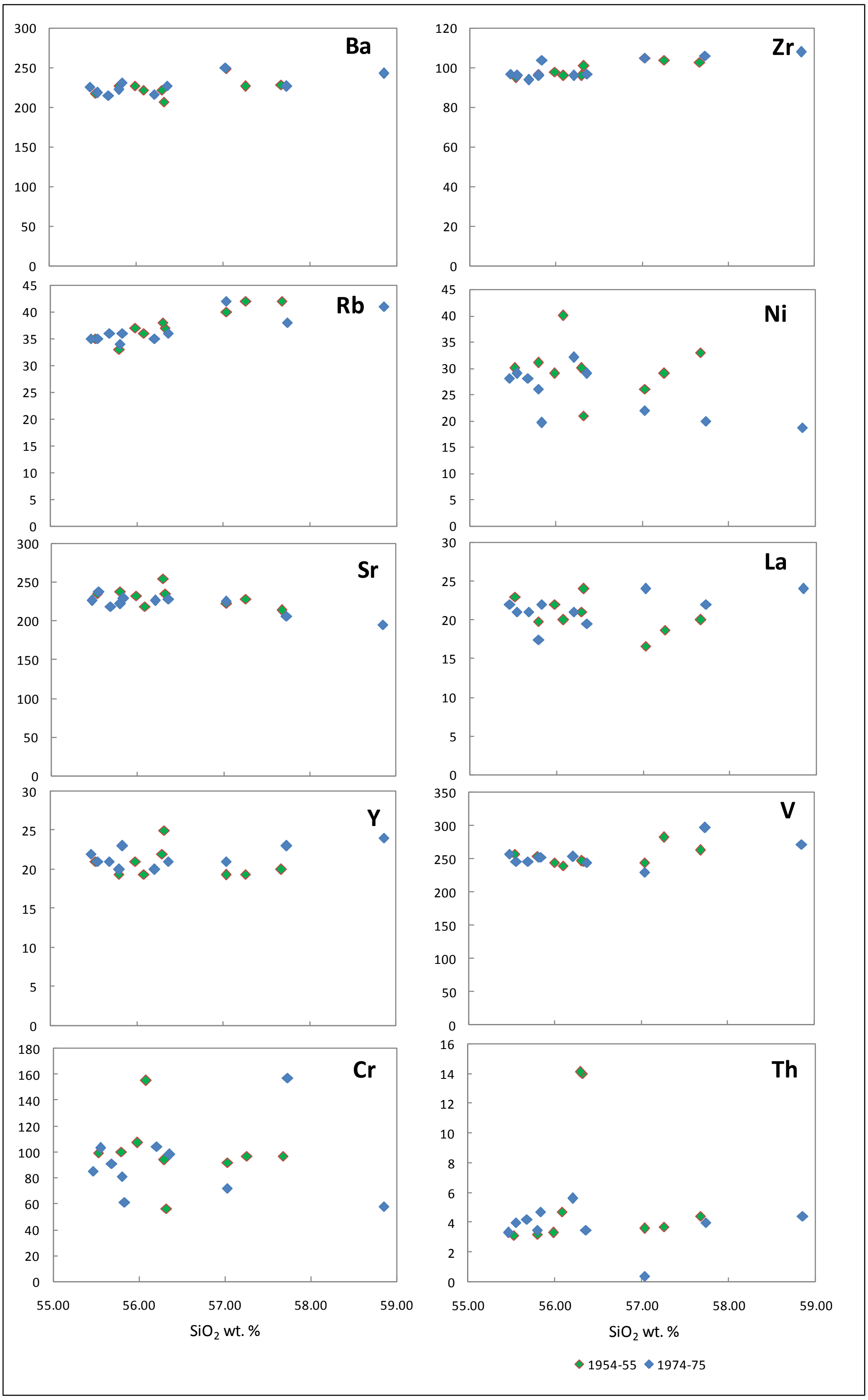

**Figure 4.24:** Harker variation diagrams for selected trace elements for the Ngauruhoe inner crater eruptives, all trace elements measured in ppm.

## 4.11 Whole Rock Geochemical Comparison with Other TgVC data

### *4.11.1 Evolution of Ngauruhoe eruptives*

The geochemical evolution of Ngauruhoe is indicated by inner crater data from this study and four earlier chronological groups of Ngauruhoe lavas (Table 4.5). Ngauruhoe groups 1 through to 5 are chronological lava flow groups defined by Hobden (1997), that were erupted from 2.5 ka through to 1974-75. Group 5 includes both 1954-55 and 1974-75 data. From 2.5 ka through to the most recent eruptives, $SiO_2$ content began as relatively mafic in groups 1 and 2 and moved to more felsic compositions in groups 3 and 4. Group 5 returned to a more mafic composition that is consistent with the inner crater values obtained in this study. MgO contents generally decrease with increasing $SiO_2$ content, with the exception of group 4 that has a high MgO content relative to $SiO_2$ compared to other Ngauruhoe data sets. Cr values decrease from groups 1 to 2, and increase in groups 3 and 4, before decreasing again in group 5 to values consistent with inner crater data. Ni values are relatively constant throughout the groups, with the exception of an increase in group 4 that coincides with the elevated MgO values suggesting an increase in olivine content. MgO values are constant in 1949, ranging from 4.5 – 4.6 wt. % (Hobden et al., 1999), and rises to 4.4 - 6 wt. % in 1954. Sr values experience an overall decline through magma evolution, with the lowest values in group 5 matching the low inner crater values. Rb/Zr ratios increase from group 1 to 4 with increasing $SiO_2$, then decline in the more mafic group 5, consistent with inner crater values. $SiO_2$ values have a slight increase between the 1954-55 and 1974-75 eruptions. This study obtained $SiO_2$ contents for the 1954-55 eruptives ranging from 54.88 – 57.37 wt. % (excluding sample A3), and the 1974-75 eruptives ranging from 55.34 – 58.85 wt. %. This rise in $SiO_2$ content is consistent with Hobden et al. (2002), with values of $SiO_2$ 54.80 – 56.25 wt. % for 1954-55 deposits, $SiO_2$ 55.71 – 55.81 wt. % for 1974, and $SiO_2$ 55.93 – 56.93 wt. % for the 1975 deposits.

### *4.11.2 Ngauruhoe and TgVC geochemical data*

The Ngauruhoe inner crater eruptives are the more mafic end members within the TgVC. Representative geochemical data for various TgVC vents (Red Crater, Tama Lakes, Te Maari Craters, North Crater, NE Oturere, and Pukekaikiore) range from basaltic andesite to andesite, with major and trace element ranges generally larger and more diverse than the inner crater values (Table 4.7), ranging from $SiO_2$ 53 - 64.2 wt. %. MgO values throughout the TgVC are relative to $SiO_2$ contents, as with the Ngauruhoe eruptives, with a larger range from 1.1 – 7.7 wt. %. Ni contents range from 4 – 260 ppm, a much larger range than the Ngauruhoe eruptives that have an overall range of 7-57 ppm. Sr compositions are relatively similar to those of the inner crater (195 – 255 ppm) and other Ngauruhoe eruptives (220 – 408 ppm), and total Ngauruhoe values of 194 – 408 ppm. Rb/Zr ratios are similar, with a wider range, to the inner crater values, ranging from 0.20 – 0.44. The major and trace element range data (Figure 4.25) show relatively small ranges for the Ngauruhoe groups 1-5, and wider ranges towards the more recent eruptions represented by groups 4 and 5, indicating wider major and trace element ranges with magma evolution. The Tongariro craters have much wider ranges than the Ngauruhoe inner crater and groups data.

**Table 4.7:** Geochemical characteristics of Ngauruhoe inner crater, major Ngauruhoe group, and other TgVC group eruptives. Ngauruhoe group lavas range from group 1: 2.5 – 1.85 ka, to group 5: 1870 – 1975, with locations indicated in Figure 1.3. Major elements measured in wt. % and trace elements in ppm.

| | Ng. inner crater[1] | Ng. Group 1[2] | Ng. Group 2[2] | Ng. Group 3[2] | Ng. Group 4[2] | Ng. Group 5[2] |
|---|---|---|---|---|---|---|
| SiO2 wt% | 54.9-57.6 | 54.2-55.5 | 55.2-55.9 | 57.9-58.3 | 57.2-58.6 | 54.8-58.2 |
| MgO wt% | 6-4.4 | 4.5-4.9 | 3.6-4.0 | 2.2-3.2 | 4.4-5.4 | 3.8-5.6 |
| Cr ppm | 56-157 | 28-36 | 5-35 | 17-33 | 108-193 | 32-147 |
| Ni ppm | 18.7-40 | 13-17 | 9-13 | 7-13 | 34-57 | 9-36 |
| Sr ppm | 195-255 | 316-359 | 200-334 | 266-284 | 219-225 | 194-284 |
| Rb/Zr | 0.35-0.39 | 0.20-0.25 | 0.25-0.32 | 0.33-0.39 | 0.40-0.44 | 0.29-0.39 |
| | Red Crater[2] | Tama Lakes[2] | Te Maari Craters[2] | North Crater[2] | NE Oturere[2] | Pukekaikiore[2] |
| SiO2 wt% | 53-61.1 | 56.1-64.2 | 57.5-60.2 | 56.3-60.1 | 55.4-62.2 | 59.8-61.8 |
| MgO wt% | 3.8-7.7 | 1.1-4.5 | 3.1-4.4 | 3.3-6.2 | 3.5-7.1 | 3.6-4.3 |
| Cr ppm | 56-267 | 3-32 | 24-65 | 33-314 | 21-260 | 20-53 |
| Ni ppm | 18-60 | 4-16 | 1-22 | 10-79 | 7-33 | 9-18 |
| Sr ppm | 269-295 | 264-331 | 253-375 | 249-309 | 225-408 | 220-294 |
| Rb/Zr | 0.23-0.5 | 0.35-0.47 | 0.35-0.49 | 0.38-0.5 | 0.26-0.50 | 0.25-0.47 |

[1] This Study

[2] Hobden, 1997

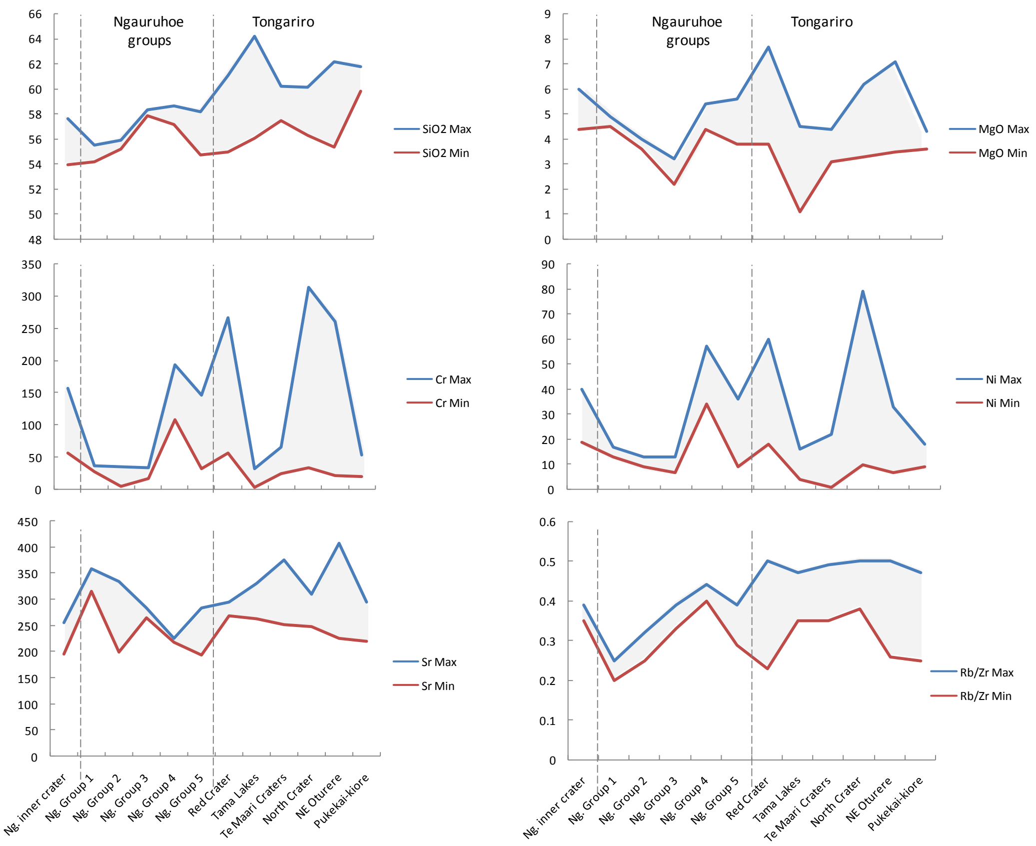

**Figure 4.25:** Major and trace element characteristics for Ngauruhoe and Tongariro craters. Maximum values are displayed by the blue lines, minimum by the red lines, and ranges are shaded in grey. Data used are presented in Table 4.5.

# Chapter Five

# Discussion

## 5.1 Introduction

This chapter discusses the development of the seven stratigraphic units within the Ngauruhoe inner crater, through magma genesis, ascent dynamics, eruption chronology, depositional mechanisms, and post-depositional processes. Global case studies provide a comparison and contrast to the local processes and deposits seen at Ngauruhoe.

## 5.2 Correlations Between the Inner Crater Stratigraphy and Eye Witness Eruption Accounts

The inner crater 1954-55 eruption deposits are divided into five units that represent five main eruption phases. An overview of the 1954-55 eruption has been given in Chapter One. From June to December 1954 strombolian and fire fountaining were the dominant eruption styles, the deposits of which are now preserved within the inner crater. The later phases of the eruption were marked by more explosive, vulcanian-style ash events that deposited ash beyond the inner and outer crater rims. Correlation of the stratigraphic units, defined in this study, to the eye witness eruption chronology (summarised from Gregg, 1956) is based on the assumption that the spatter deposits are products of strombolian or fire fountaining activity, with lower degrees of agglutination in the former, and higher in the latter.

The 1954-55 eruption likely began with vent-clearing explosions, before strombolian/fire fountaining eruptions produced the Unit A spatter deposit, with deposition concentrated towards the north. Toward the end of the first phase deposition occurred on the southern portion of the cone where spatter was deposited on the poorly to moderately agglutinated pre-existing Unit A. This could be the result of the lava fountaining seen in early June that resulted in the first lava flows down the cone flanks.

The second phase of the eruption produced Unit B, with a high abundance of fluidal and scoriaceous lapilli and bombs likely produced by pulsatory strombolian explosions. The largest lava producing period was from June 20 to 30, which may correlate with the large Unit B scoria and spatter deposit.

The third phase of the eruption produced an increased deposition rate represented by the central clastogenic lava that makes up the bulk of Unit C. The high deposition rate allowed sufficient heat to be retained in the clasts to produce extensive welding and coalescence throughout the deposit. This was most likely a result of a change in eruption style from strombolian to fire fountaining due to an increase in gas content or magma ascent rate. Toward the end of the third eruption phase the rate of deposition decreased, represented by a gradual change to the overlying agglutinated scoriaceous material. Based on the high degree of agglutination and stratigraphic position of Unit C, it was most likely deposited during the end of June when lava emission was at its greatest, or during the two weeks following the 14th of July where assumed fire fountaining occurred.

Phase four of the eruption experienced fluctuations in eruption intensity and/or deposition rate, indicated by coarse beds of alternating highly and poorly agglutinated scoria. The alternating beds in Unit D, based on variations in agglutination, indicate changes in explosion duration from shorter strombolian bursts to more sustained fire fountaining due to gas bubbles moving toward an annular flow regime (Section 5.6.2). The coarsely bedded structure of the Unit D scoria deposit can be attributed to variations in eruption style from late July to December 1954 when the eruption alternated between lava fountaining to strombolian activity.

The final phase of the 1954-55 eruption was marked by an increase in explosivity, producing vulcanian ash eruptions that led to the deposition of the fine grained Unit E ash bed. The very fine nature of ash particles that comprise Unit E suggests the interaction with meteoric water possibly from snow melt, or the pressurisation of magma under a cap rock, however the absence of quenching textures and accretionary ash indicates a dry eruption. Unit E is considered to represent 1955 activity where the eruption style moved to vulcanian, and ash was the dominant product.

A twenty year period of relative quiescence followed (with minor explosive activity) before Ngauruhoe began its next major eruption in January 1974 that was dominantly vulcanian in nature, producing Units F and G. The 1974-75 eruption deposit contains two units representing two different eruption style phases. Unit F is a series of six ash beds with alternating grain size, and dense, basaltic andesite lapilli and block content that likely represent the vent-clearing and vulcanian phase of the eruption. The alternations in grain size and dense basaltic andesite clast content suggest changes in eruption intensity due to interaction with external water, changes in gas content, magma ascent rate, crystallinity, viscosity, or a combination of these.

The second phase of the 1974-75 eruption is represented by Unit G. The large c. 10 m thick deposit is highly agglutinated and welded with abundant deformed bombs that represent an intense strombolian eruption phase. Deposition rate was sufficient to form a clastogenic lava that flowed down the inner walls of the inner crater, overlapping the underlying deposits, suggesting the progression to fire fountaining. The inward slump of the NW crater rim occurred after the deposition of Unit G, once it had significantly cooled to fracture in a brittle manner, producing the angular blocks of the slump deposit. The final stage of the eruption ejected large blocks and bombs that are scattered on the inner crater rim and in the Ngauruhoe summit fosse. During January 1974 the existing inner crater rim was blanketed with incandescent material (Nairn et al., 1976) that likely formed the agglutinated scoria of Unit G, although there are no reports of strombolian or fire fountaining activity. Additional molten ejecta were produced during March 1974 (Nairn et al., 1976) that may have added to this deposit but there is no evidence of two separate events forming Unit G. No further ash deposits have been preserved on the cone.

## 5.3 Ngauruhoe Magma Genesis

Arc magmas are generated by the convergence of tectonic plates and subduction of the oceanic lithosphere (Ulmer, 2000), resulting in subduction zone volcanism, one of the most abundant sources of volcanism on Earth (Reubi et al., 2002). Ngauruhoe is situated within the Taupo Volcanic Zone (TVZ), a typical continental margin setting through the subduction of the oceanic Pacific Plate under the continental Australian Plate, forming the Taupo-Hikurangi Arc system (Patterson and Graham, 1988). Continental arc magmas are primarily calc-alkaline in composition, displaying an enrichment in large iron lithophile elements (LILE) and light Rare Earth Elements (REE), and are depleted in High Field Strength Elements (HFSE) (Ulmer, 2000).

The geochemical classification of Ngauruhoe inner crater rocks have been determined by plotting whole rock major element data on a $K_2O$ versus $SiO_2$ diagram (Figure 4.21). Units A through G are basaltic andesite to andesite in composition, which is consistent with previous geochemical work on Ngauruhoe eruptives (Nairn et al., 1976; Nairn and Self, 1978; Hobden, 1997; Hobden et al., 2000, 2002). There is an increase in silica content from 1954-55 to 1974-75, consistent with the increase in explosivity.

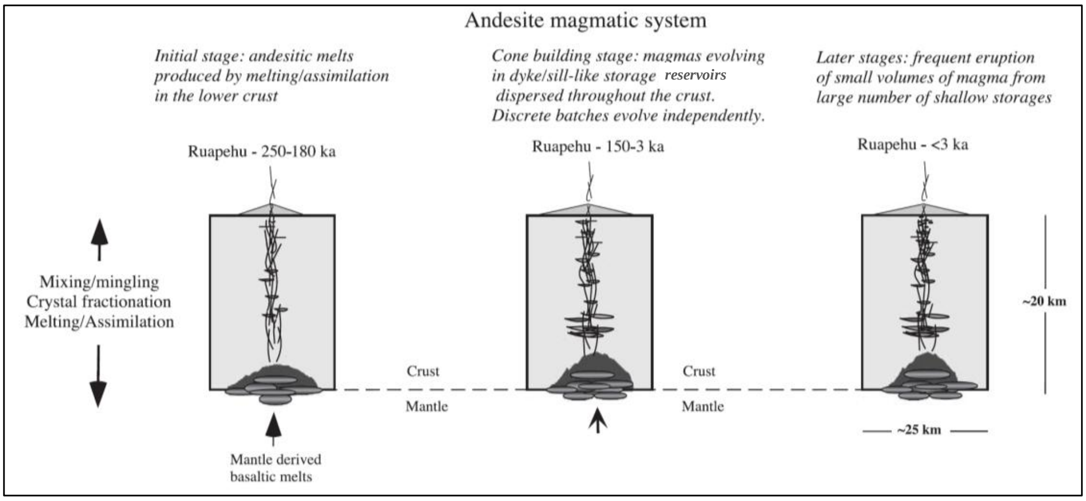

**Figure 5.7:** Diagrams illustrating the progressive development of andesitic magmas of Ruapehu Volcano within the Taupo Volcanic Zone. The primary basaltic magmas originate from the mantle where they undergo fractional crystallisation, partial melting, and mixing and mingling. The incorporation of crustal material results in a basaltic andesite magma, and further fractionation produces basaltic andesites and andesites like those of Ngauruhoe. The magma batches rise through the crust and temporarily reside in shallow reservoirs (Price et al., 2005) before finally erupting.

The two main arc magma-producing andesite centres within the Taupo Volcanic Zone are the Tongariro Volcanic Centre (TgVC), representing over 95% of the TVZ andesite, and the Bay of Plenty (Cole, 1981; Graham et al., 1995; Rowland and Sibson, 2001). The TgVC encompasses two large, currently active composite volcanoes: Ruapehu and Tongariro (including Ngauruhoe). The basaltic andesite to andesite magma below the TgVC originate from the mantle, from where they filter through the lower crust, undergoing crystal fractionation, crustal assimilation, and magma mixing and mingling (Price et al., 2005 in Fig. 5.1).

The incorporation of the crust into the fractionating mantle basalt can result in the evolution to basaltic andesite. The magma rises into the complex plumbing systems below the TgVC where they are stored in shallow sill and dyke reservoirs (Gamble et al., 1990; Price et al., 2007). Evidence for crustal contamination is provided by the presence of xenoliths throughout the stratigraphic succession, and evidence for magma mixing is shown by phenocryst disequilibrium textures and pyroxene compositions showing disequilibrium tie-lines. Quartzite and quartzofeldspathic xenoliths are abundant throughout the Tongariro lavas, with the quartzose xenoliths mainly confined to Ngauruhoe and other younger eruptives, with schists in some Tongariro eruptives (Hobden, 1997).

## 5.4 Magma Residence Times Below Ngauruhoe Volcano

Complex magma genesis processes that occur throughout the magma conduit system and within the magma chamber are in part affected by magma residence times. Hildreth and Moorbath (1988) outlined a process of crustal Melting and Assimilation concurrent with magma Storage and Homogenisation (MASH), produced for the Andean volcanic arc subduction setting. Magma filters through to crust, until it reaches neutral buoyancy and accumulates in shallow zones where crustal anatexis occurs. The enrichment of crust increases the magma buoyancy to the point where the magma recommences ascent and finally erupts. Magma evolution through the MASH model incorporates three of the main processes occurring below Ngauruhoe: magma storage, assimilation and homogenisation occurring in a series of shallow chambers, supported by data obtained in this study, and work done by previous authors (e.g. Hobden, 1997; Hobden et al., 1999).

The frequency of eruptive events at Ngauruhoe and surrounding TgVC vents gives a chronology of magma evolution throughout the underlying magma system. Geochemical data representing the evolution of Ngauruhoe from 2.5 ka to the present suggests that magma recharge and mixing occurred between the relatively frequent eruptions (Hobden et al., 2002). The magma batches that feed the TgVC eruptions are relatively small (< 0.1 km$^3$) and short-lived (≥ 1 ka) (Hobden et al., 1999, 2002), with a lack of significant linear time-compositional trends (Figure 5.2).

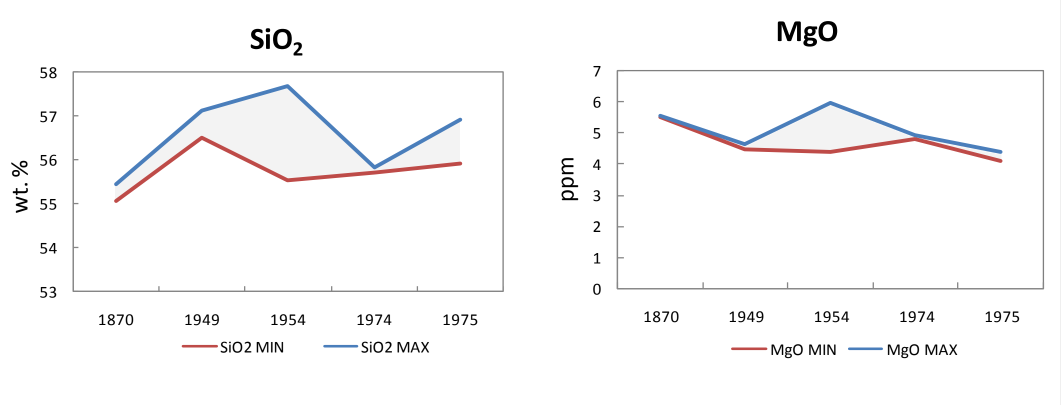

**Figure 5.8:** $SiO_2$ and MgO contents for Ngauruhoe eruptives from 1870 to 1975. 1870, 1949, 1974, and 1975 data from Hobden et al. (2002). Both graphs display data measured in wt. %.

This lack in significant compositional trends throughout the wide range of Ngauruhoe eruption styles and intensities, from effusive lava production to sub-plinian explosions indicates the change in eruption style to largely be a function of physical processes, not magma evolution. For example, within the inner crater eruptives there is very little variation in $SiO_2$ values across the 1954-55 and 1974-75 eruptions, through effusive magma discharge, strombolian blasts, and vulcanian explosions. There is however, evidence for magma recharge events, indicated by peaks in MgO and Ni, prior to the 1954-55 eruption, and within the 1954-55 Unit D deposit, and a slight increase in the $SiO_2$ content within the 1974-

75 eruptives. Magma storage is indicated by the porphyritic texture of juvenile clasts that suggests a magma body that has risen slowly and/or stagnated in shallow crust, allowing phenocrysts to grow to lengths up to 6 mm. Disequilibrium textures, and crossing tie-lines in orthopyroxene and clinopyroxene throughout the inner crater stratigraphic succession suggests the incorporation of new material through magma recharge. The presence of crustal xenoliths indicates crustal assimilation.

The Ngauruhoe MASH scenario is supported by studies carried out at the nearby Ruapehu volcano. Ruapehu eruptions of the past 60 years are thought to originate from at least two clusters of small magma pockets with some pockets mixing to trigger an eruption (Nakagawa et al., 1999; Price et al., 2005). Changes in geochemical trends correlate to magma mixing in association with assimilation and fractional crystallisation (AFC) processes. In Ngauruhoe eruptives there is evidence for fractional crystallisation, consistent with findings of Hobden et al. (2002). Geochemical data shows decreasing Sr and Ni with increasing $SiO_2$, indicating minor crystal fractionation of plagioclase and olivine, respectively.

The small volume and intermittent nature of the Ruapehu eruptions are further evidence of the eruptions originating from small, short lived magma batches (Gamble et al., 1999; Nakagawa et al., 1999) similar to the eruptions at Ngauruhoe and Tongariro, assuming erupted magma volume relates to magma batch size. Both the Ruapehu and Ngauruhoe eruptives suggest an open, steady-state magma system where magma recharge, mixing, assimilation of crust, and magma homogenisation are continual processes feeding the relatively frequent eruptions. An increase in MgO from 4.5 – 4.6 wt. % in 1949 (Hobden et al., 1999) to 4.4 - 6 wt. % in 1954, and erupted lava volume in 1954, suggests the incorporation of a small (< 0.1 $km^3$) batch of less evolved magma that mixed with remaining 1949 lava (Hobden et al., 1999). Relatively consistent geochemical trends between the 1954-55 and 1974-75 eruptions and the suggested incorporation of a more primitive melt, gives a time span of 20 years for the magma body that produced the two recent eruptions.

## 5.5 Magmatic Evolution Processes

### 5.5.1 *Crystallisation within the melt*

Crystallisation is a process ubiquitous with magma evolution, and in the 1954-55 and 1974-75 Ngauruhoe eruptives, crystallisation occurred right through the magma evolution to point of, and possibly during, eruption and cooling of the deposits. This ongoing crystallisation is indicated by: (1) high microlite abundance in the groundmass; (2) the presence of different phenocryst phases (plagioclase, orthopyroxene, clinopyroxene, and olivine); and (3) the majority of small phenocrysts (< 0.2 mm in length) showing little or no disequilibrium sieve textures or resorption throughout the stratigraphy. It is evident that plagioclase was forming throughout the evolution of the melt, as seen by the different zonation types and disequilibrium sieve textures, suggesting periods of growth and partial melting of plagioclase in a complex plumbing system. In the strombolian pyroclasts the groundmass contains abundant plagioclase, pyroxene, and Fe-Ti oxide microlites, set within glass. Crystallisation occurred even after deposition due to high temperatures suggested by the degree of welding, and high microlite content.

Welding is dependent on the lava clasts retaining high temperatures. These high temperatures allow the crystallisation process to continue, producing the high microlite contents seen throughout the Ngauruhoe inner crater eruptives. Higher glass contents (up to 80%) relative to microlite content in the vulcanian ash Units E and F indicate rapid quenching by air (due to the high eruption rate) or water, ceasing the crystallisation process. This could also be affected by differences in cooling rates and/or viscosity.

### 5.5.2 *Crystal fractionation*

Crystal fractionation is the process of crystals settling out of the melt, removing compatible elements and leading to changes in magma composition. Crystal fractionation rates depend on the relative density of the crystals in the melt, magma viscosity, crystal size, crystal distribution (within the melt or adhered to chamber walls), and the active dynamics of the magma chamber (Hawkesworth et al., 2000). Crystal fractionation is considered to be one of the most important magmatic processes that give rise to the wide variations in magma composition. As a group of crystals (such as plagioclase) gravitationally settle out of the melt, the major and trace elements that compose these minerals are depleted.

Gamble et al. (1990) has suggested that the diversity in major element compositions throughout the TgVC eruptives could be due to crystal fractionation and accumulation processes. There is evidence for limited crystal fractionation in the Ngauruhoe inner crater deposits, with a slight decrease in Sr coupled with an increase in the incompatible elements Ba, Rb, and Zr, indicating crystal fractionation of plagioclase, and a decrease in Ni and MgO indicating some crystal fractionation of olivine. There is little evidence for crystal fractionation of pyroxene and Fe-Ti oxides.

### *5.5.3 Assimilation of the Crust*

Assimilation is the process of incorporating wall-rock material into the magma, and extracting thermal energy to heat and melt the newly assimilated material (Grove, 2000).

Contamination and assimilation is one of the more apparent magmatic processes in the Ngauruhoe inner crater rocks due to the presence of crustal xenoliths, and is an important step in the MASH process. One quartzofeldspathic xenolith analysed using the electron microprobe showed a $SiO_2$ content of 98.6%. Even minor contributions from a xenolith would have a significant effect on magma composition by increasing the $SiO_2$ content. This effect can be seen in Unit G, with a high abundance of xenoliths and an andesite composition, with $SiO_2$ contents up to 58.85%.

Evidence of the interaction between the xenoliths and host magma is shown in thin section (Figure 4.12) where a reaction rim is present around a large quartzite-plagioclase xenolith with a finer grained, darker appearance towards the rim. Evidence of crustal contamination includes the presence of xenoliths, raised and correlated radiogenic and stable isotopes ratios, and relatively enriched LILE contents that are significantly higher than contents predicted solely by crystal fractionation processes (Graham and Hackett, 1987; Graham et al., 1988, 1995). This process is confirmed by $^{87}Sr/^{86}Sr$ values obtained by Hobden et al. (2002) of 0.704910 - 0.706133 that indicate the involvement of crustal contamination and assimilation. It was also noted by Hobden et al. (2002) that quartzite xenoliths within Ngauruhoe lavas display characteristics of partial melting and disaggregation. High Pb values throughout the inner crater stratigraphic succession is possibly further evidence of crustal assimilation, also seen in Ruapehu and other TgVC eruptives (Cole, 1978; Patterson and Graham, 1988; Price et al., 2005, 2007).

### *5.5.4 Magma mixing and homogenisation of the melt*

Magma mixing often occurs due to the episodic nature of volcanic systems with a new magma being introduced to the system, modifying the current geochemistry and magma composition to form a hybrid magma (Grove, 2000). Mixing can also occur with the main batch of magma interacting with remnants of an older crystal mush, as seen at Slamet Volcano in Java, Indonesia (Reubi et al., 2002), or within a single temperature-zoned magma chamber (Couch et al., 2001). Figure 5.3 illustrates how a temperature-zoned magma chamber undergoes mixing, with heating occurring at the bottom from a source such as a new uprising magma batch, causing the resorption of crystals back into the melt, then followed by convective mixing with the cooler, more crystallised magma. These changing magma compositions can be tracked through glass inclusions and compositional changes with sequential phenocryst zoning from core to rim, especially when magma mixing affects the bulk rock composition (Gioncada, 2005).

Within the Ngauruhoe inner crater eruptives there are abundant phenocryst resorption textures (embayments and sieve textures), along with orthopyroxene and clinopyroxene showing disequilibrium compositions. These features are evidence for the mixing of two chemically distinct magma batches (Couch et al., 2001). Humphreys et al. (2006) state that the cause of zoning in crystals could be due to several changes in the magma including temperature, pressure, water content, and oxygen fugacity. The presence of oscillatory zoning within plagioclase crystals is attributed to pulsatory changes in water content and/or temperature during magma ascent. The presence of sieve textures is sequential to changes in temperature in a complex plumbing system, such as through rising and

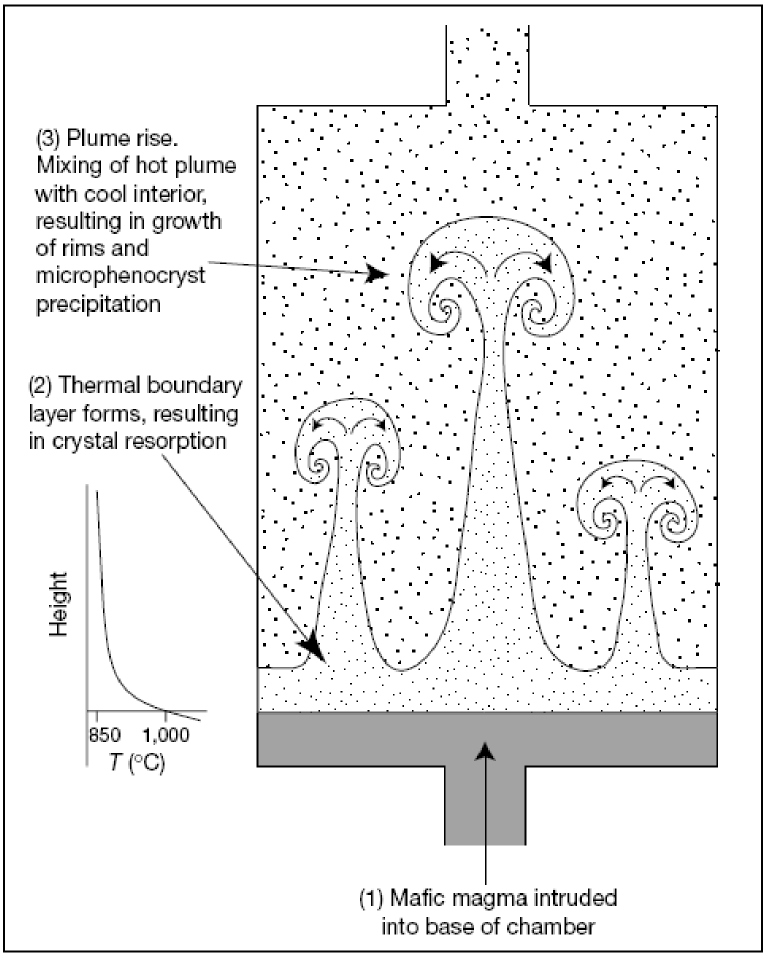

**Figure 5.3:** Thermal convectional mixing of a magma chamber with a hotter, less crystallised recharge magma (Couch et al., 2001).

falling in a conduit, or magma mixing with a more mafic melt.

Anorthite proportions in zoned plagioclase phenocrysts generally decrease with a more evolved melt, or increase with higher temperatures and/or higher water content (Andrews et al., 2008). Microprobe data for Ngauruhoe inner crater deposits show that in one phenocryst there is a reduction, then sharp increase in An contents from plagioclase core to rim, with the highest values residing in the core (Figure 4.7). The sharp decrease in An could be due to reduction in water content and temperature, as seen in El Chichon magmas (Andrews et al., 2008). The more calcic rims could be a result of mixing or recharge with a less evolved magma. These changes in An content however, could also be due to magma convection in a temperature-zoned chamber or conduit, with the crystals reaching a higher/cooler point in the chamber or conduit. Individual phenocrysts have differing complex growth histories consistent with a complex magma chamber.

The majority of plagioclase phenocrysts along with some pyroxenes display sieve textures that are characteristic of magma mixing (Gill, 1981; Couch et al., 2001). The sieve textures are displayed in varying patterns from a sieved core with a clear rim, to oscillatory zoned sieve textures, coexisting within the same samples. As the phenocrysts grew, it is likely they came into contact with a magma in which they were out of equilibrium with, then re-equilibrated with the magma. Samples across the stratigraphic succession contain phenocrysts both with and without sieve textures, suggesting the mixing of two partially crystallised magma batches (Nakagawa et al., 2002).

Further evidence of disequilibrium occurring within the magma is shown by the two pyroxene phases. When clinopyroxene and orthopyroxene data are plotted on En-Wo-Fs ternary diagrams, they indicate mineral phase disequilibrium, as seen by the outer tie-lines not being parallel to each other in most units (Figure 4.10). This signifies the introduction of a new melt into the host magma that was either more compositionally evolved and/or lower temperature or water content, then a return toward more original compositions (Andrews et al., 2008). These changes

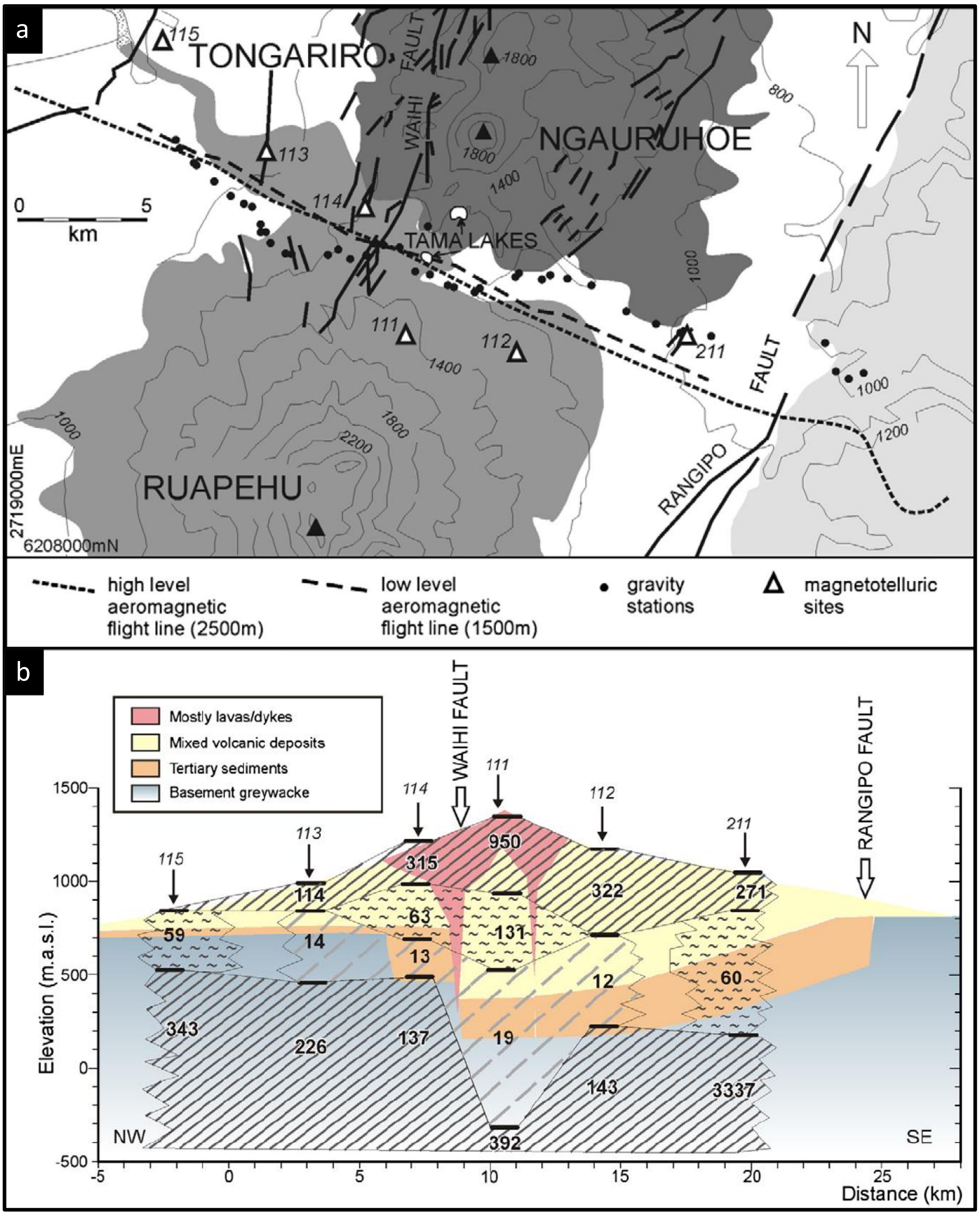

**Figure 5.4:** (a) The axis of the gravity surveys taken to produce (b), a cross section of the volcanic terrain, sediments, and greywacke basement underlying the TgVC (Cassidy et al., 2009).

in equilibrium require convection patterns within the feeder dyke system or magma chamber, resulting in a change in magma composition as compositionally dissimilar magma enters the system and is gradually homogenised with the melt. Hobden (1997) interpreted the ubiquitous sieve-textured plagioclase crystals to be a result of both magma mixing and rapid decompression.

Magma homogenisation is a result of significant mixing within the magma chamber and conduit. Ngauruhoe inner crater deposit trace element data displays relatively consistent trends across the 1954-55 Ngauruhoe inner crater units (excluding the hydrothermally altered Unit A northern deposit). Major element data is more diverse, with basaltic andesite to andesite compositions, and an increase in $SiO_2$ in the 1974-75 eruptives. Mixing occurs in the dyke system, homogenising the old magma batch with any incoming recharge magma and resulting in a range of compositions.

## 5.6 Recent Eruption Processes at Ngauruhoe Volcano

### *5.6.1 Vesiculation, coalescence, and fragmentation*

The primary physical control on eruptive styles, from quiet degassing to violent explosions, is volatile exsolution and transport within the volcanic conduit (Polacci et al. 2008). The common occurrence of broken and fractured phenocrysts throughout the stratigraphy, especially in Units B, E, and F, give an indication of the rapid vesicle growth and explosive magma fragmentation during the Ngauruhoe eruptions. Herd and Pinkerton (1997) describe two simplified paths for degassing in low-viscosity magmas. Low magma ascent rates result in an effective ‘bubble ascent/bursting’ mechanism, causing slight disruption to the surrounding melt. Higher magma ascent rates result in minor interaction between bubbles until a high-vesicularity foam is formed at the top of the magma body, and either coalescence, or violent fragmentation of the foam occurs when bubble volume within the melt reaches approximately 70-80% (Cashman et al., 2000). Through these ascent paths bubble growth is constrained by the proximity of other bubbles, the rate of magma decompression, and the rate of volatile diffusion (Cashman et al., 2000).

At vesicularities greater than 18%, bubble coalescence takes place concurrently with bubble expansion (Bai et al., 2008), as would have been the case in the high vesicularity Ngauruhoe lavas with a vesicularity range of 6 to 82% (range from modal and pycnometer vesicularity data), with the lower vesicularities most likely due to degassing. Bubble coalescence occurs when two or more bubbles merge through the fracture or collapse of the intercepting walls. Once this has occurred, and if the melt does not solidify, the walls retract to leave one larger bubble with little or no evidence of the two or more initially individual bubbles (Herd and Pinkerton, 1997). There is abundant evidence of bubble coalescence in the Ngauruhoe inner crater pyroclasts in hand specimen, SEM images, and in thin section, with partially collapsed bubble walls between the main vesicle cavities and only minor spherical vesicles present. This indicates that bubble coalescence occurred very close to the eruption of the pyroclasts, leaving insufficient time for the bubble wall retraction to form spherical vesicles. Near-ejection coalescence in Unit B produced a bulk vesicularity range of 22-82% (obtained by gas pycnometry analyses, Appendix Five), with c. 99% interconnectedness, indicating that although the bubbles did not have time to relax into spheres, coalescence was extensive.

If the source of xenoliths that have been incorporated into a magma is known, magma fragmentation depth can be approximated, assuming that high xenolith contents relate to the fracturing of wall rock by magmatic fragmentation. Cassidy et al. (2009) have developed a sub-structure model for the TgVC, with an axis across the Tama Lakes region (Figure 5.4). This model places the Mesozoic greywacke basement, the source of the xenoliths, at greater than 800 – 1600 m below the surface. This value is consequently an approximate fragmentation depth for the magmas with high xenolith concentrations, the 1954 lavas and 1974-75 Unit G. The vulcanian eruptions likely fragmented at shallow levels, supported by the absence of xenoliths within the ash deposits, although the lack of xenoliths could be due to significant fragmentation. Another possible cause for differing xenolith abundances is changes in magma ascent rate. Magma ascent has to be greater than the settling velocity of the xenolith (Rutherford and Gardner, 2000), therefore, the magmas with higher xenolith populations would have to ascend at a greater rate than the lower xenolith population lavas. These two parameters could both have influenced the differing xenolith populations.

### *5.6.2 Strombolian eruptions*

Strombolian eruptions are pulsatory, rhythmic, dry magmatic explosions occurring at the top of a basaltic to basaltic-andesite magma column, where large gas bubbles burst at the surface as a result of a two-phase flow regime (Vergniolle and Mangan, 2000; Parfitt, 2004; Houghton and Gonnermann, 2008). As the gas bubbles burst, a shower of incandescent spatter is thrown out of the vent that can eventually lead to the build up of a scoria and spatter cone, such as the inner crater of Ngauruhoe. The molten, fluidal spatter clasts undergo deformation upon impact and under the weight of continued deposition (depending on the heat retained in the lava clasts) can result in a semi-stratified deposit. This is the case for Units B, C (the portion containing lower levels of agglutination to the north), and G of the inner crater of Ngauruhoe, where large scoriaceous bombs up to 2 m in length have been flattened, and fluidal clasts drape over underlying scoria, resulting in a horizontal alignment. Flattened spatter clasts also have elongated vesicles.

Two major clast types were produced during the Ngauruhoe 1954-55 eruption: scoriaceous juvenile clasts, and dense basaltic andesite sub-rounded to sub-angular blocks. The dense blocks may originate from degassed solidified lavas from previous eruptions, or could be fragmented clasts from a cooled, degassed crust of a lava lake or other solidified lava clasts. The sub-rounded clasts may have been fluidal on eruption, or recycled clasts that have fallen back into a lava lake residing in the crater to be blasted out again. The high proportion of dense angular clasts within the base of Unit G could be remnants of the fragmented cap rock from the preceding vulcanian eruption phase.

Large gas bubbles are the result of low viscosity magma allowing the easy dissolution and coalescence of volatiles in the melt, growing to the width of the volcanic conduit, and in the case of Stromboli Volcano, around lengths of 82 ± 11 m, or up to 20 times the width (Vergniolle and Mangan, 2000; Vergniolle et al., 2004). They form during the growth and coalescence of smaller rising bubbles through diffusion and decompressional expansion, with the former being more important during early formation, and the latter more dominant as the gas moves towards the volcanic vent (Jaupart and Vergniolle, 1988; Vergniolle and Mangan, 2000).

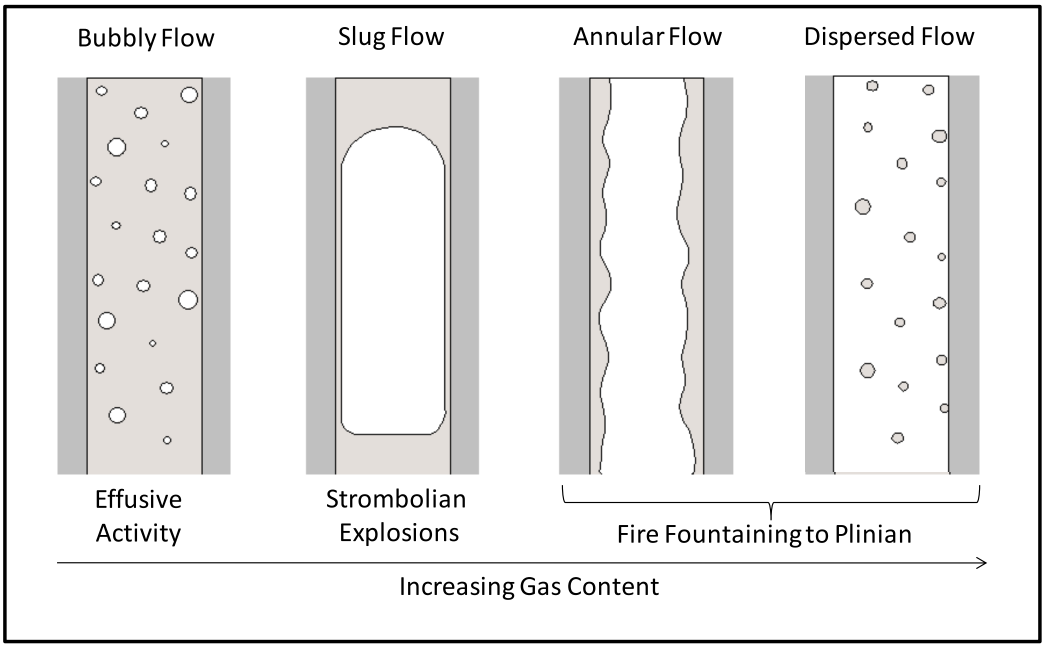

**Figure 5.5:** The four two-phase flow regimes, bubbly flow, slug flow, annular flow, and dispersed flow, with increasing gas content. Modified from Vergniolle and Mangan, (2000).

Two-phase flow models have been developed to describe the relationship between gas content and gas flow regimes (Figure 5.5). This two-phase flow model illustrates, in order from lowest to highest gas content: (1) a bubbly flow that produces effusive lava emission, as an outcome of a gas content below 30% forming small randomly dispersed, isolated bubbles within the melt; (2) a slug flow resulting from a gas content of around 70% causing the discrete gas bubbles to coalesce into the large gas pocket amounting to strombolian eruptions; (3) a gas content > 70% results in the slug flow evolving into an annular flow, a channel of gas surrounded by a relatively thin envelope of melt, that leads to a fire-fountaining eruption when the build up of magmatic foam at the top of the column collapses; and (4) with a significant increase of gas above 70%, the annular flow advances to a dispersed flow where globules of melt are suspended within a stream of gas that can lead to a plinian eruption (Vergniolle, 1996; Vergniolle and Mangan, 2000). During the strombolian and fire fountaining eruptions of Ngauruhoe, gas flow types two and three would have occurred during the strombolian and fire fountaining episodes respectively.

Slug flow gas pockets rise at 30-60 m $s^{-1}$ (Vergniolle et al., 2004) to the top of the magma column, and create a swelling on the surface before bursting and releasing acoustic energy that lasts from 1 to 10 seconds. At Stromboli Volcano these episodic explosions occur on average 100 to 300 times a day, with rare cycles producing 100 to 1000 explosions an hour (Ripepe et al., 1993; Vergniolle and Mangan, 2000; Parfitt, 2004). Similar acoustic bursting occurs at Karymsky Volcano in Kamchatka, where strombolian explosions average 5 to 20 times an hour (Johnson and Aster, 2005) producing average mass effusion rates of 0.1 to 0.6 m $s^{-1}$, with the higher effusion rates due to an increased supply of magma and/or gas into the shallow magma system (Landi et al., 2006). Strombolian (and vulcanian) explosions at Ngauruhoe produced sharp, loud detonations and visible shock waves. Visible shock waves are usually associated with vulcanian explosions as a result of the erupting material being over-pressured relative to the surrounding atmosphere, moving at speeds greater than that of sound, at 340 m $s^{-1}$. The shock wave is visible due to the condensation of atmospheric moisture as it moves through the air above the eruption, behind the shock front in the rarefaction wave (Morrissey and Mastin, 2000). Visible shock waves at Ngauruhoe were reported to accompany strombolian explosions on June, 29 and September, 17, 1954, and during vulcanian activity in 1974-75.

### 5.6.3 *Fire fountaining eruptions*

During the Ngauruhoe inner crater eruptions, fire fountaining and intense strombolian activity produced clastogenic lava flows and welded spatter deposits within the crater. Fire fountaining episodes are generally products of Hawaiian eruptions and are due to annular and dispersed flow regimes (where magma ascent rate is adequate to prevent bubble accumulation at the top of the magma column) most commonly seen at Kilauea Volcano, Hawaii (Vergniolle and Mangan, 2000; Wolff and Sumner, 2000). The height and structure of fire fountains are controlled by the gas content of the magma and magma effusion rate. Higher gas contents result in higher fire fountains, smaller spatter clasts, and high effusion rates (300-500 m $s^{-1}$) produce high accumulation rates around the vent (Wolff and Sumner, 2000; Capaccioni and Cuccoli, 2005).

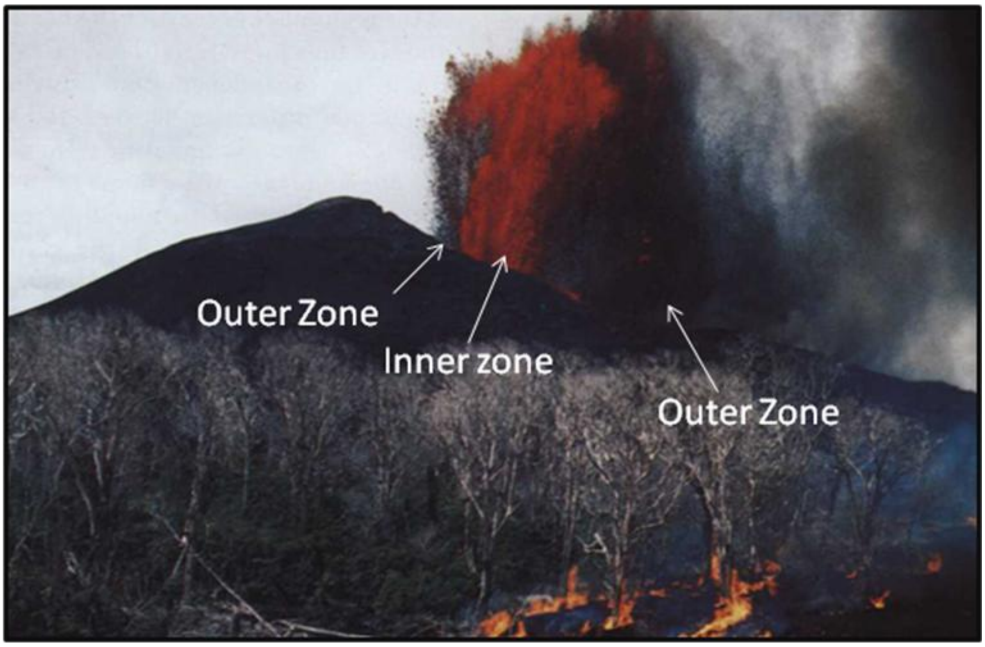

**Figure 5.6:** The inner hot zone (red) that produces lava flows such as the 1954 flows, and outer chilled zone (black) that forms spatter deposits, such as Units A to D and G. Pu'u 'O'o Hawaiian fire fountain (Head and Wilson, 1989).

Fire fountaining (at a singular vent) is usually more energetic and sustained at the early stages of the fountain, then decreases in energy due to the development of a lava pond at the base, where the new magma mixes with the degassed magma reducing the overall effective gas content (Wolff and Sumner, 2000). Lava fountains contain two zones, an inner, hot zone, and an outer, chilled zone (Figure 5.6). With increased mass eruption rates a larger inner zone is formed, and with increased gas content, the fire fountain would have a larger chilled outer zone (Sumner et al., 2005). Lava clots from the inner hot zone may fall back into the lava pond at the base of the fountain, causing a steady growth in the lava pond that may lead to lava flow formation and sustainment (Wolff and Sumner, 2000), or they may be deposited in the cone to form agglutinated spatter (Head and Wilson, 1989). The former was likely the cause of the 1954 Ngauruhoe lava flows that advanced down the northwestern flanks of Ngauruhoe at velocities up to 300 m $h^{-1}$ (Gregg, 1956) leading to a total lava flow volume for 1954 of c. 3,030,750 $m^3$ (Sanders, Unpublished data). The outer, cooler zone likely produced chilled scoriaceous spatter that produced Units A-D and G within the Ngauruhoe inner crater, with partial lava flow in Units A, G, and possibly C. A range of spatter products resulting from accumulation rate and degree of cooling is given in Figure 5.7. The partial flow of Unit G is likely due to the over-steepening of the rapidly-formed spatter deposit, as seen in the 1986 eruption of Izu-Oshima Volcano, eastern Japan (Sumner et al., 2005).

Fire fountaining during the 1954-55 eruption at Ngauruhoe was largely directional and changed focus as the eruption progressed. This resulted in Units A and C, where portions of the deposits greatly vary in agglutination. The northern deposit of Unit A is highly agglutinated and partially flowed into the crater, indicated by rounded lobe-like structures at the base and surface that appears to be flow related.

The Unit A southern outcrop is weakly to highly agglutinated with a cap of fluidal lava draping over the deposit. This is interpreted to be the result of a higher deposition rate from a northerly direction of fountaining for the majority of the initial Unit A-producing eruption phase, shifting only at the end of the fire fountain eruption sequence to the south, depositing fluidal lava on top of the already-deposited Unit A.

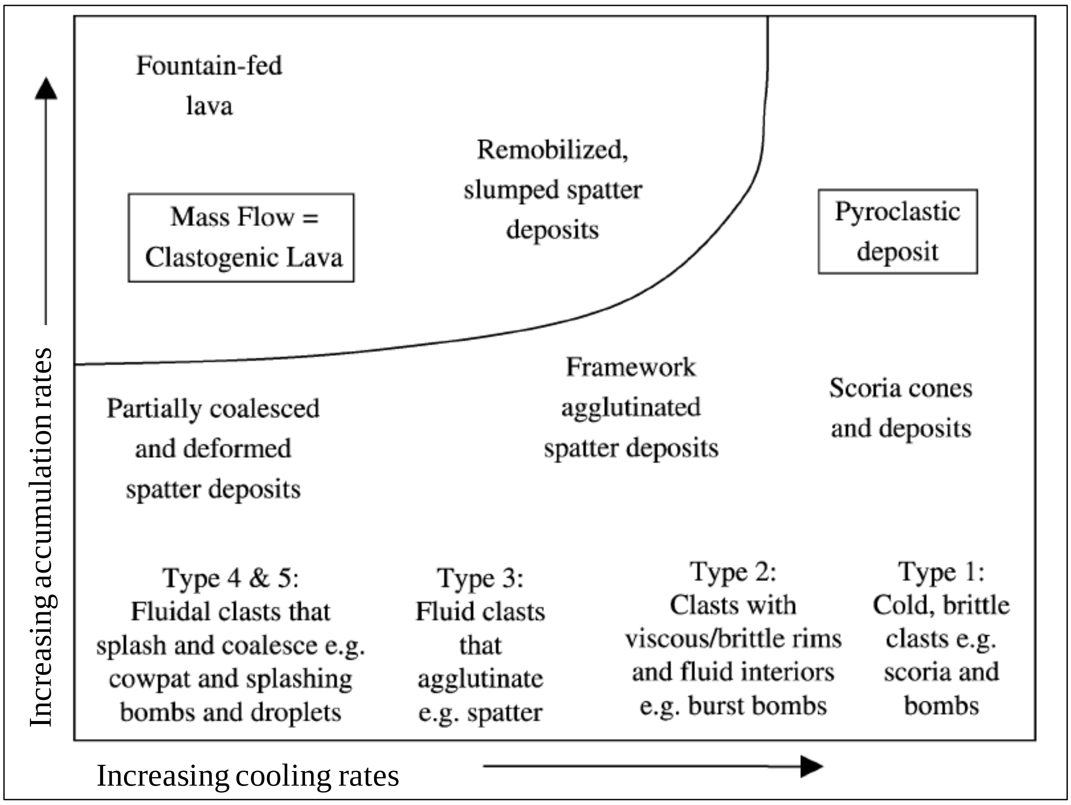

**Figure 5.7:** Accumulation rate and degree of cooling are important controlling factors in the deposits resulting from fire fountaining. The Ngauruhoe inner crater displays a range of these deposits from clastogenic lava flows and remobilised slumped spatter deposits to cold, brittle scoriaceous clasts, indicating fluctuations in accumulation rate and degree of cooling upon deposition (modified from Sumner et al., 2005).

During the 1954-55 eruption the dominant eruption style was strombolian, alternating with fire fountaining episodes. The alternation from discrete strombolian explosions to fire fountaining is a relatively common occurrence and can be quite abrupt due to increasing magma ascent rates (Houghton et al., 1999; Vergniolle and Mangan, 2000; Parfitt, 2004).

Scandone et al. (2008) found that more energetic strombolian eruptions at Vesuvius during the 1631 and 1944 eruptions were due to the close arrival of multiple, discrete batches of magma with higher ascent rates preventing degassing, resulting in up to 1 km high lava fountains. This faster gas ascent rate could have been the cause of the fire-fountaining episodes at Ngauruhoe, with fire fountains reaching heights of 300 m above the crater rim in 1954-55.

### *5.6.4 Vulcanian eruptions*

Morrissey and Mastin (2000) define vulcanian eruptions as small to moderate-sized volcanic outbursts that eject pyroclasts to heights > 20 m and last on the order of seconds to minutes. These eruptions are characterised by discrete, violent explosions, ballistic ejection of blocks and bombs, atmospheric shock waves, and emission of tephra deposits that range widely in the percentage of juvenile versus nonjuvenile components. The Ngauruhoe eruption of 1974-75 (Figure 5.8) is an example of vulcanian eruption style, and has strong similarities to the eruption of Vulcano in the Aeolian Islands, Irazu Volcano in Costa Rica (1963-1966), Sakurajima (1988-1989) and Tokachidake (since 1955) in Japan (Morrissey and Mastin, 2000; Landi et al., 2006).

Vulcanian eruptions produce discrete explosions much more violent than the strombolian style. They can last up to several minutes and can produce shock waves that have been known to shatter windows up to 7 km away from source (Vulcano, 1888-1890), with high eruption velocities from 200 to 400 m $s^{-1}$ (Morrissey and Mastin, 2000).

Vulcanian deposits are produced through: (1) ballistic block expulsion, (2) pyroclastic avalanches, (3) pyroclastic flows, and (4) ash fall (Morrissey and Mastin, 2000). The 1974-75 eruption of Ngauruhoe produced all four of these deposit types: (1) ballistic blocks deposited on the inner crater rim and in the fosse between the inner and outer crater; (2) block and ash flows down the northern and western flanks of Ngauruhoe resulting from ballistic blocks accumulating in the fosse before collapsing down the cone (Gregg, 1960; Nairn and Self, 1978); (3) pyroclastic flows down the NW flanks; and (4) ash fall preserved within the inner crater. An interesting feature of the 1974-75 deposits is the abrupt change from vulcanian ash deposits (Unit F) to the overlying strombolian spatter deposits (Unit G) marked by a sharp boundary. This may have been the result of a change in viscosity, as marked by the increase in $SiO_2$ wt. %.

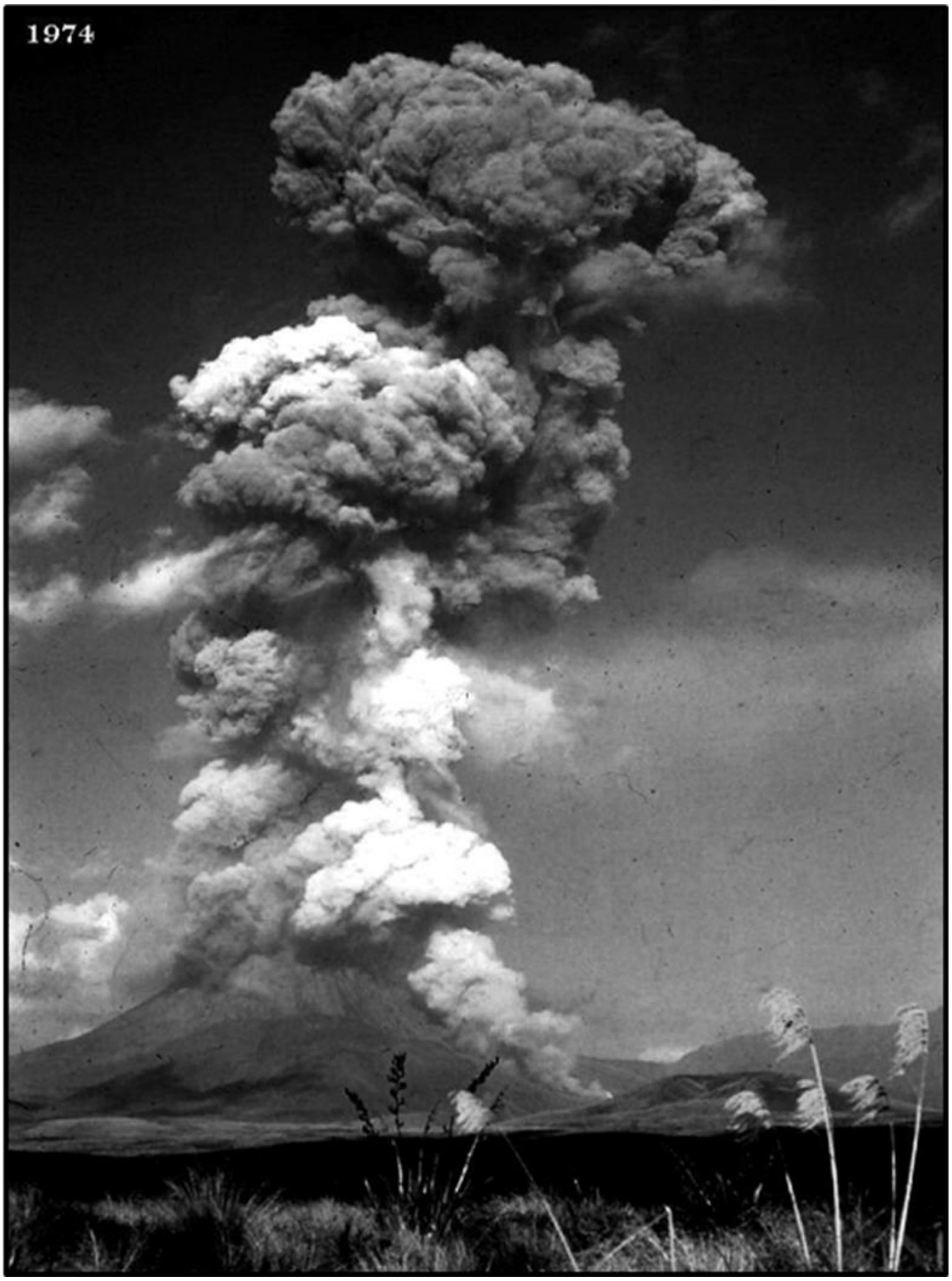

**Figure 5.8:** Vulcanian ash column rising from the 1974 eruption with partial collapse producing pyroclastic flows down the northern flanks of Ngauruhoe with Pukeonaki and Pukekaikiore to the far right (photo courtesy of John A. Krippner).

The explosivity of the vulcanian eruption style is due to two common mechanisms: the brittle fracturing of a cap rock above a magmatic conduit, under which magma may interact with external water, and/or magmatic gasses that have accumulated due to volatile exsolution and coalescence. These two scenarios are investigated in models by Woods (1995) and Platz et al. (2007), respectively.

The model by Woods (1995) is based on the build up of pressure underneath cap rock due to interaction of magma with external water (Figure 5.9). This model entails the buoyant ascent of volatiles, through both magmatic, and magma-water interaction processes, where it builds up in a two-phase magma-volatile foam below the hardened cap rock. Disruption of the cap rock causes rapid decompression and expansion of the foam, resulting in a vulcanian eruption, erupting material at speeds of 50-400 m $s^{-1}$ (Woods, 1995).

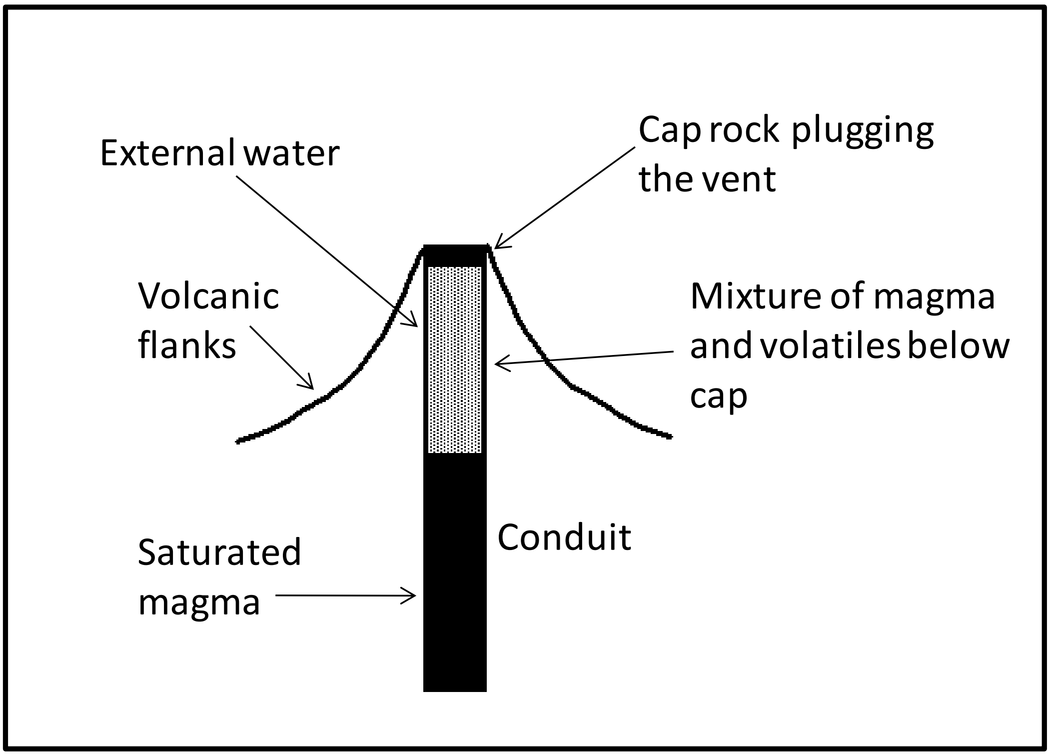

**Figure 5.9:** The factors contributing to the onset of a vulcanian eruption, through the interaction of magma with external water building pressure below a cap rock (modified from Woods, 1995).

The model proposed by Platz et al. (2007) begins with a build-up of degassed lava forming a cap rock and blocking the volcanic vent (Figure 5.10). Underneath the cap rock, volatile exsolution and bubble coalescence cause overpressure in the conduit, resulting in a violent eruption upon the disruption of the dome or cap rock (Platz et al., 2007). This model was developed to explain the change from effusive to explosive activity during the AD1655 eruption of Taranaki, where a period of dome growth was interrupted by an explosive sub-plinian eruption (Platz et al., 2007). If the lava dome is substituted for cap rock, this model offers a second explanation for the change from strombolian to vulcanian eruption style in the 1954-55 eruption, and the vulcanian eruption phase at the commencement of the 1974-75 eruption.

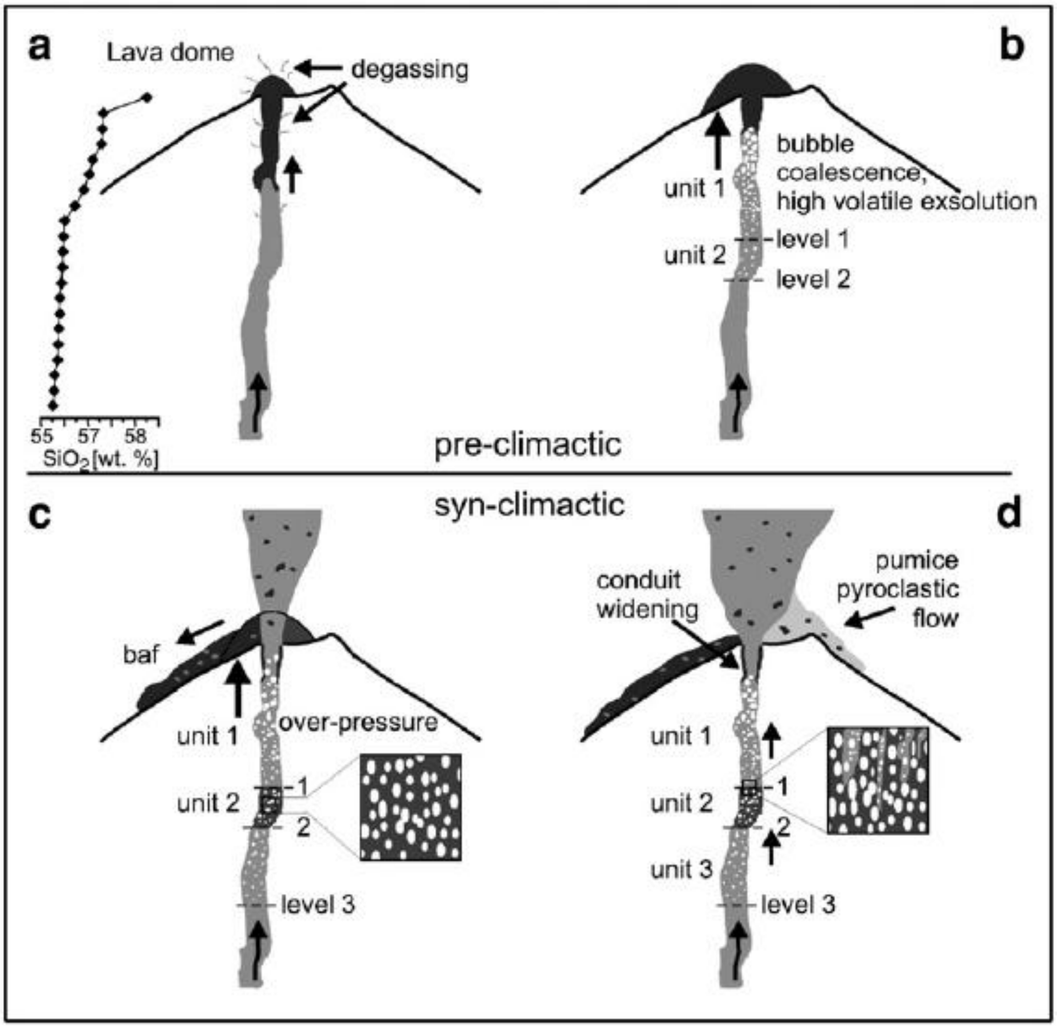

**Figure 5.10:** Processes leading to the onset of a vulcanian eruption excluding interaction with external water, through (a) degassing and solidifying of a plug or cap rock; (b) build up of pressure through volatile exsolution and bubble coalescence; (c) overpressure leading to fracturing of the cap rock; and (d) the resulting vulcanian eruption plume and pyroclastic flow (Platz et al., 2007).

The vulcanian-style eruption at Ngauruhoe in 1955 occurred after a period of relative quiescence from the 1954 phase of the eruption that was dominated by strombolian activity. This relative quiescence, from late December 1954 to late January 1955 may have allowed the cooling of degassed lava originating from fire fountaining episodes to form a hardened cap rock, causing the build up of pressure from volatile exsolution and bubble coalescence. The ash deposits contain a ratio of 60:40 for poorly to non-vesicular ash, to moderately to highly vesicular ash. The ash clasts that contain little to no vesicles may represent the degassed cap rock, and the ash clasts containing moderate to high vesicularities could represent the accumulating magma below the cap rock.

It is unlikely that the increase in explosivity from strombolian to vulcanian eruption style was due to magma-water interactions. It is possible that snow melt percolated down through the permeable scoriaceous material to interact with the magma, but snow build up at the summit was unlikely due to ongoing activity. There is no field evidence, such as accretionary lapilli or quenching textures, to suggest the involvement of water in the final stages of the 1954-55 eruption.

The 1974-75 eruption commenced with violent vulcanian explosions after a 20 year lull in volcanic activity. Nairn and Self (1978) proposed a similar scenario for the vulcanian eruption of 1974-75 to the Woods (1995) model. They proposed that fresh magma interacted with meteoric water below a cap rock, causing explosive vaporisation of the water, before erupting through the cap rock at the onset of the eruption. This suggestion of involvement of water was based on the recording of a steam column during the eruption, lasting 1.5 hours, and the ejection of dense, andesitic blocks that are regarded to be fragmented cap rock that formed at the end of the 1954-55 eruption (Nairn and Self, 1978). The inner crater deposits show little sign of water involvement other than in bed 5 of Unit F, which contains dense basaltic andesite clasts with a thin layer (up to 2 mm) of fine ash cemented to the surface. No accretionary lapilli or quenching textures were recorded in Unit F. The lack of field evidence to support phreatomagmatic activity suggests that the model prepared by Platz et al. (2007) is a more likely cause for the explosive activity during 1974-75, although some water involvement may have occurred, resulting in the steam reported in the ash column. There is no progressive increase in microlite crystallisation in Units E and F that may have led to an increase in viscosity to cause the increase in explosivity.

The 1954-55 Ngauruhoe eruption experienced an increase in explosivity from strombolian and fire-fountaining style eruptions, to more explosive, ash-producing vulcanian-style eruption. This increase in explosivity is not uncommon, also occurring at Taranaki, and yearly at Stromboli Volcano in Italy where typical activity is similar to that of the strombolian stage of the 1954-55 eruption at Ngauruhoe (Harris et al., 2008). The April 2003 paroxysmal event at Stromboli was vulcanian, the eruption style seen in the final stages of the Ngauruhoe 1954-55 eruption, and the beginning of the 1974-75 Ngauruhoe eruption.

## 5.7 Depositional Processes and Products

### *5.7.1 Composite cones*

Tongariro is a large composite cone comprising smaller temporary pyroclastic cones that undergo periods of construction and erosion, and are constructed from alternating scoria, spatter, lava, and ash strata. The main Ngauruhoe composite cone is a result of intermittent eruptions since c. 3.47 ka, with the two recent 1954-55 and 1974-75 eruptions building the spatter and scoria pyroclastic cone at the summit.

Pyroclastic cones consist of poorly bedded, very coarse-grained and sometimes red (oxidised) scoria and spatter, with metre-sized ballistic bombs and blocks (Cas and Wright, 1987; Vespermann and Schmincke, 2000). The main depositional edifice produced during the 1954-55 and 1974-75 Ngauruhoe eruptions is the c. 65 m high (from northern-most base of the cone) inner pyroclastic composite cone and 1954 aá lava flows that travelled down the northwestern flanks of the main composite cone of Ngauruhoe. The inner crater pyroclastic composite cone grew c. 60 m during the 14 months of the 1954-55 eruption, with the majority of cone growth occurring during the first four months when strombolian and fire fountaining activity was dominant.

### *5.7.2 Spatter deposition, agglutination, and welding*

Spatter clasts flung out of a volcanic vent can be hot enough to agglutinate (the kinetic deformation of a pyroclast upon deposition resulting in near-instantaneous adhesion) or weld (post-depositional plastic deformation of pyroclasts due to load pressure) to form a deposit containing fused clasts up to a few kilometres from the vent (Wolff and Sumner, 2000; Capaccioni and Cuccoli, 2005; Sumner et al., 2005; Carey et al., 2008a,b).

The degree of agglutination or welding depends on several factors: 1) spatter accumulation rate, 2) spatter temperature, 3) shape of the individual spatter clots, 4) density of the lava, 5) duration of deposition, and 6) size of the spatter clots (Capaccioni and Cuccoli, 2005). The Unit A northern deposit and Unit C have undergone the highest degrees of agglutination within the Ngauruhoe inner crater, to the point of eliminating clast boundaries. The surface of the Unit A northern deposit is smooth with lobate structures that suggest the lava partially flowed into the crater, requiring extensive agglutination and welding. Unit C contains columnar jointing that spans almost the entire height of the deposit, indicating that the deposit cooled as a coherent lava. The clast outlines at the base and top of Unit C, and the 15 m zone of decreased agglutination to the north, indicate that the lava formed by intense agglutination and welding of spatter and was not erupted as a coherent lava, or formed at the top of a cooling lava lake. A controlling factor of the agglutination of Unit C and G is the large spatter clast sizes reaching 2 m lengths, such large clast sizes are not present in other inner crater units. This likely coupled with high accumulation rates and/or higher temperatures to produce the extensive agglutination and welding. A minimum accumulation rate of 0.5 m $h^{-1}$ (Capaccioni and Cuccoli, 2005) must have been exceeded to provide such a high degree of agglutination and welding.

Units A and C were formed by directional fire fountaining, similar to interpretation of lateral variation of welding in proximal Askja 1987 deposits (Carey et al., 2008a). Carey et al. (2008b) concluded that the Askja 1987 deposit cooling as a single unit was an effect of the significant thickness of the deposit, which allowed the welding pyroclasts to undergo thermal equilibration to maintain the higher temperature for a longer period. This is likely the cause for Unit C cooling as a single, coherent unit, leading to the development of columnar jointing.

The grain size of the Unit A northern deposit is much smaller than Unit C (determined through the smaller grain size apparent in the Unit A southern outcrop), so factors other than grain size, such as accumulation rate due to lava fountain direction, would have been dominant controls on degree of agglutination. Unit B as a whole has the lowest degree of agglutination of the strombolian deposits, with the exception of the coarse banding (that appears to be due to change in agglutination) present throughout Unit D, with even lower agglutination towards the top of the deposit. These alternations in agglutination may have been due to fluctuations in spatter accumulation rates. Unfortunately the inaccessibility of Unit D prevented a closer inspection of the bands containing higher degrees of agglutination to describe grain size and shape. The clasts at the top of Unit D that have experienced little to no agglutination overall have a higher density than Unit B, ruling out lower lava density as a controlling factor of agglutination, suggested by Capaccioni and Cuccoli (2005).

### *5.7.3 Ash fallout and surge*

There are two main recognised means of producing ash fallout deposits, firstly by short-lived intermittent eruption plumes (vulcanian), and secondly through long-lived, sustained eruption columns (sub-plinian, plinian, phreatoplinian) (Morrissey and Mastin, 2000). Units E and F were produced through the first mechanism that produces small proximal deposits with volumes < $10^{-1}$ $km^3$ (Morrissey and Mastin, 2000).

Pyroclastic surges are the result of collapsing ash columns during explosive eruptions (Valentine and Fisher, 2000). Pyroclastic surge deposits characteristically contain low angle cross beds of centimetre to decimetre thicknesses (Valentine and Fisher, 2000). These characteristics are present in a discontinuous, thin (< 4 cm) deposit at the top of Unit F that contains fine (< 5 mm) cross-bedded laminae. The surge deposit at the top of Unit F likely represents the collapse of the explosive vulcanian phase, before the eruption changed to a strombolian style, producing the overlying Unit G. Similar deposits were produced at Vulcano during the 1888 to 1890 vulcanian eruption, containing discontinuous, near-parallel, gently undulating medium to fine ash (De Rossa et al., 1991) that resulted from phreatomagmatic explosions. The 1975 Pyroclastic flows travelled down the northern slopes of Ngauruhoe, while smaller surges surrounded the vent, most likely forming the surge deposits.

### *5.7.4 Post-depositional processes*

On February 19, 1975 the northwestern sector of Unit G and some underlying crater rim deposit collapsed inwards into the inner crater, resulting in a chaotic slump deposit obscuring the underlying 1954-55 stratigraphy, and lowering the NW crater rim by c. 15 m. The broken blocks average 60 – 80 cm in length and many have been hydrothermally altered to a light grey colour.

The Unit G spatter deposit experienced sufficient deposition rates to agglutinate and partially flow down the northern, southern, and western inner walls of the inner crater, with a thickness of ≥ 10 m to the south, and almost reaching the crater floor on the western wall. The low viscosity of the flow is evident through flow structures including flow lobes, and an impact crater where a large (1.7 m diameter) rounded bomb impacted 1 m into the lava.

In the early stages of the 1974-1975 eruption the inner crater was c. 180 m deep and near-vertical, with a secondary crater at the bottom (Nairn et al., 1976). Since then, eruptives from the 1974-75 eruption and erosion of the inner crater walls have infilled the crater to its current depth of c. 80 m. The upper portion of infill is lapilli and block scree from overlying units, and the slump deposit to the NW. The depth of the crater directly after the 1974-75 eruption was not recorded.

Small steam-producing geothermal vents are scattered around the inner crater, currently concentrated on the northern to western walls. It is very likely that vents were active in other areas of the crater, as the vent locations changed within the two months of visiting the crater in 2007 to 2008.

Secondary hydrothermal alteration has been an active process throughout the inner crater, especially on the northern face of Unit A where there has been deposition of silica within vesicle cavities. The present concentration of geothermal vents is on the N-W face where the inward slump occurred, with some vents actively steaming on the outer crater rim. Secondary hydrothermal alteration has largely affected Units A (northern deposit), C, and D. This is apparent through colour alteration to a yellow/brown to red on the surfaces of Units A and C, while the subsurface rock remains medium to dark grey, and both have a significantly smoother surface than the non-altered units. High loss on ignition values for the Unit A (both northern and southern deposits) are explained by the presence of hydrothermal clays, and sulfur crystals that are visible to the naked eye in both outcrops. Unit D has a high degree of gypsum growth, with crystals reaching 7 mm in diameter, with less significant quantities of sulfur crystals reaching 2 mm in length. Secondary mineral growth is common throughout the stratigraphic succession, indicated by cryptocrystalline quartz growth on ash clast surfaces and within vesicle cavities, visible in SEM images.

# *Chapter Six*

# *Conclusions*

## 6.1 Conclusions and Summary

Ngauruhoe is a young (3.47 ka) composite cone, and is the most recent and active cone of the Tongariro Volcanic Centre. Ngauruhoe last erupted in 1954-55 and 1974-75 to produce a pyroclastic scoria and spatter cone with a c. 220 m diameter crater, within an older crater at the summit of the young composite cone volcano. The 1954-55 eruption produced at least 11 fire fountain derived lava flows that travelled down the NW flanks of Ngauruhoe. The inner crater stratigraphic succession exposed on the southern crater wall has been divided into seven units from A to G. Units A to E are attributed to the 1954-55 eruption, and the overlying Units F and G to the 1974-75 eruption. The 1954-55 eruption was dominantly strombolian, with alternating fire fountaining episodes producing Units A-D, and a final vulcanian phase depositing Unit E. The commencement of the 1974-75 eruption was vulcanian depositing Unit F, then changed to strombolian, depositing the Unit G spatter deposit.

The emplacement origins of the inner crater stratigraphic units are based on deposit characteristics and eye witness accounts. The 1954-55 eruption sequence contains:

- Unit A that varies from an agglutinated spatter deposit to a clastogenic lava formed from a directional fire fountain;
- Unit B, a strombolian scoria lapilli and spatter bomb deposit;
- Unit C, a clastogenic lava from a more intense fire fountaining episode;
- Unit D, composed of coarsely bedded scoria lapilli and blocks with variations in agglutination resulting from alternating intensity in strombolian activity; and
- Unit E, a fine ash fallout bed from the final vulcanian phase.

The 1974-75 eruption experienced alternations in explosivity during the vulcanian phase that was initiated by pressurised magma underneath a hardened cap rock with possible interaction with external water. The eruption produced:

- Unit F, composed of six ash and lapilli beds that vary in grain size and dense basaltic andesite lapilli and block content; and

- Unit G, a highly agglutinated spatter bomb deposit that caps the inner crater stratigraphy, formed during intense strombolian activity.

The juvenile basaltic andesite to andesite clasts in all units are porphyritic, containing plagioclase, orthopyroxene, clinopyroxene, and olivine phenocrysts, and a microlite-rich, glassy groundmass containing plagioclase, pyroxene, and Fe-Ti oxides. Quartzose xenoliths are common in all units except Units E and F, and are derived from the underlying Mesozoic greywacke argillite basement and quartz veins. Plagioclase and some pyroxene phenocrysts display complex disequilibrium textures, including resorption features (sieve textures and embayments), and complex oscillatory zoning, indicative of magma mixing and recharge in a complex plumbing system. Vesicularities throughout the inner crater stratigraphic succession range from 6-82%, with up to 99% interconnectedness. This is consistent with annular and dispersed two-phase flow regimes that produce strombolian, fire fountaining, and vulcanian eruptions.

The eruptive products of Ngauruhoe have continental arc medium-K calc-alkaline basaltic andesite to andesite compositions. The magma body ascended to shallow levels in the crust, assimilated quartzose and metagreywacke basement xenoliths, and underwent crystal fractionation as it filtered through the crust. The magma stagnated in the shallow crust, assimilated further country rock and suffered minor crystal fractionation of plagioclase and olivine, with repeated magma mixing and homogenisation throughout the process. Prior to 1954 a more primitive melt entered the chamber and mixed with the remnant magma from the previous 1949 eruption. This new magma batch fed both the 1954-55 and 1974-75 eruptions, with a span of at least 20 years, depositing the basaltic andesite to andesite products of the inner crater. Another possible recharge event occurred prior to the deposition of Unit D, marked by an increase in MgO content. Post-deposition hydrothermal processes have altered the pyroclastic deposits, resulting in colour change and mineralisation of silica, gypsum, and sulfur.

## 6.2 Further Work

Further work on the Ngauruhoe inner crater deposits includes calculating magma ascent rates using xenolith size and magma viscosity, gaining more accurate pre-eruptive gas contents, and obtaining isotope data for each unit to determine the degrees of crustal contamination.

# *References*

Allen, L.R. 1948. Activity at Ngauruhoe, April-May 1948. *New Zealand Journal of Science and Technology*, 30: 187-193.

Allen, L.R. 1949. The eruption of Ngauruhoe, February-March, 1949. *New Zealand Science Review*, 7(10): 180-183.

Allan, A.S.R., Baker, J.A., Carter, L., Wysoczanski, R.J. 2008. Reconstructing the Quaternary evolution of the world's most active silicic volcanic system: insights from a ~1.65 Ma deep ocean tephra record sourced from Taupo Volcanic Zone, New Zealand. *Quaternary Science Reviews*, 27: 2341-2360.

Andrews, B.J., Gardener, J.E., Housh, T.B. 2008. Repeated recharge, assimilation, and hybridization in magmas erupted from El Chichon as recorded by plagioclase and amphibole phenocrysts. *Journal of Volcanology and Geothermal Research*, 175: 415-426.

Bai, L., Baker, D.R., Rivers, M. 2008. Experimental study of bubble growth in Stromboli basalt melts at 1 atm. *Earth and Planetary Science Letters*, 267: 533-547.

Ballance, P. F., Ablaev, A.G., Pushchin, I.K., Pletnev, S.P., Birylina, M.G., Itaya, T., Follas, H.A., Gibson, G.W. 1999. Morphology and history of the Kermadec trench-arc-backarc basin-remnant arc system at 30 to 32ºS: geophysical profile, microfossil and K-Ar data. *Marine Geology*, 159: 35-62.

Bardsley, C.J. 2004. Physical volcanology of Red Crater, Tongariro. MSc Thesis, University of Waikato, Hamilton.

Basher, R. 2005. Physical volcanology and future volcanic risk from Te Maari Craters, Tongariro. MSc Thesis, University of Waikato, Hamilton

Bebbington, M.S. and Lai, C.D. 1996. Statistical analysis of New Zealand volcanic occurrence data. *Journal of Volcanology and Geothermal Research*, 74: 101-110.

Best, M.G., and Christiansen, E.H. 2001. *Igneous Petrology*. Blackwell Science, Massachusetts.

Bibby, H. M., Caldwell, T. G., Davey, F.J., Webb, T.H. 1995. Geophysical evidence on the structure of the Taupo Volcanic Zone and its hydrothermal circulation. *Journal of Volcanology and Geothermal*

*Research*, 68: 29-58.

Bibby, H. M., Risk, G. F., Caldwell, T.G., Davey, F.J., Webb, T.H. 2002. Long offset tensor apparent resistivity surveys of the Taupo Volcanic Zone, New Zealand. *Journal of Applied Geophysics*, 49: 17-32.

Bidwill, J.C. 1841. *Rambles in New Zealand*. 1st ed. Orr, London. p49-52.

Capaccioni, B. and Cuccoli, T.F. 2005. Spatter and welded air fall deposits generated by fire-fountaining eruptions: Cooling of pyroclasts during transport and deposition. *Journal of Volcanology and Geothermal Research*, 145: 263-280.

Carey, R.J., Houghton, B.F., Thordarson, T. 2008a. Contrasting styles of welding observed in the proximal Askja 1875 eruption deposits I: Regional welding. *Journal of Volcanology and Geothermal Research,* 171: 1-19.

Carey, R.J., Houghton, B.F., Thordarson, T. 2008b. Contrasting styles of welding observed in the proximal Askja 1875 eruption deposits II: Local welding. *Journal of Volcanology and Geothermal Research,* 171: 20-44.

Cas, R.A.F. and Wright, J.V. 1987. *Volcanic successions modern and ancient*. Allen and Unwin Ltd. London.

Cashman, K.V., Sturtevant, B., Papale, P., Navon, O. Magmatic fragmentation. In: *Encyclopedia of Volcanoes*, H. Sigurdsson (Ed.). Academic Press, New York, 2000.

Cassidy, J., Ingham, M., Locke, C.A., Bibby, H. 2009. Subsurface structure along the axis of the Tongariro Volcanic Centre, New Zealand. *Journal of Volcanology and Geothermal Research*, 179: 233-240.

Chizmar, J.M. 2003. The nature and dynamics of explosive eruptions and associated crater formation at Tama Lakes, Tongariro Volcano. MSc Thesis, University of Waikato, Hamilton.

Cloud, P.E. 1951. The 1949 eruption of Ngauruhoe. *The Scientific Monthly,* 72(4): 241-251.

Cole, J.W. 1978. Andesites of the Tongariro Volcanic Centre, North Island, New Zealand. *Journal of Volcanology and Geothermal Research,* 3: 121-153.

Cole, J.W. 1981. Genesis of lavas of the Taupo Volcanic Zone, North Island, New Zealand. *Journal of Volcanology and Geothermal Research*, 10: 317-337.

Cole, J.W. and Nairn, I.A. 1975. *Catalogue of active volcanoes of the world including Solfatara fields. Part 22: New Zealand*. International Association of Volcanology and Chemistry of the Earth's Interior, Rome, Italy.

Collie, W. 1880. Remarks of volcanoes and geysers from New Zealand. *Transactions and Proceedings of the New Zealand Institute*, 12: 418-420.

Couch, S., Sparks, R.S.J., Carroll, M.R. 2001. Mineral disequilibrium in lavas explained by convective self-mixing in open magma chambers. *Nature*, 411: 1037-1039.

Davy, B. W. and Caldwell T. G. 1998. Gravity, magnetic and seismic surveys of the caldera complex, Lake Taupo, North Island, New Zealand. *Journal of Volcanology and Geothermal Research*, 81: 69-89.

De Rosa, R., Frazzetta, G., La Volpe, L. 1992. An approach for investigating the depositional mechanism of fine-grained surge deposits. The example of the dry surge deposits at "La Fossa di Vulcano". *Journal of Volcanology and Geothermal Research*, 51: 305-321.

Duncan, R. 1918. *Early walks in New Zealand*. Napier. 135pp.

Gamble, J.A., Smith, I.E.M., Graham, I.J., Kokelaar, B.P., Cole, J.W., Houghton, B.F., Wilson, C.J.N. 1990. The petrology, phase relations, and tectonic setting of basalts from the Taupo Volcanic Zone, New Zealand and the Kermadec Island Arc – Havre Trough, SW Pacific. *Journal of Volcanology and Geothermal Research*, 43: 235-270.

Gamble, J.A., Wood, C.P., Price, R.C., Smith, I.E.M., Stewart, R.B., Waight, T. 1999. A fifty year perspective of magmatic evolution of Ruapehu volcano, New Zealand: verification of open-system behaviour in an arc volcano. *Earth and Planetary Science Letters*, 170: 310-314.

Gill, J.B. 1981. *Orogenic andesites and plate tectonics*. Springer-Verlag, Berlin.

Gioncada, A., Mazzuoli, R., Milton, A.J. 2005. Magma mixing at Lipari (Aeolian Islands, Italy): Insights from textural and compositional features of phenocrysts. *Journal of Volcanology and Geothermal Research*, 145: 97-118.

Girdlestone, H.E. 1909. The mountains of the Tongariro National Park. *Appendices to the Journals of the House of Representatives*. Session II, C-1: 41-45.

Google Maps New Zealand, 2008. *Mount Ngauruhoe* (Volcano/New Zealand), viewed 3 December 2008, http://maps.google.co.nz/maps?hl=en&tab=wl.

Graham, I.J. and Hackett, W.R. 1987. Petrology of calc-alkaline lavas from Ruapehu Volcano and related vents, Taupo Volcanic Zone, New Zealand. *Journal of Petrology*, 28: 531-567.

Graham, I.J., Grapes, R.H., Kilfe, K. 1988. Buchitic metagreywacke xenoliths from Mount Ngauruhoe, Taupo Volcanic Zone, New Zealand. *Journal of Volcanology and Geothermal Research*, 35: 205-216.

Graham, I. J., Cole, J.W., Briggs, R.M., Gamble, J.A., Smith, I.E.M., 1995. Petrology and petrogenesis of volcanic rocks from the Taupo Volcanic Zone: A review. *Journal of Volcanology and Geothermal Research*, 68: 59-87.

Gregg, D.R. 1956. Eruption of Ngauruhoe 1954-1955. *New Zealand Journal of Science and Technology*, B37: 675-688.

Gregg, D.R. 1960. *The Geology of the Tongariro Subdivision*. New Zealand Geological Survey Bulletin 40.

Griffin, A.G. 2007. Products and processes of cone-building eruptions from North Crater, Tongariro. MSc Thesis, University of Waikato, Hamilton.

Grove, T.L. Origin of Magmas. In: *Encyclopedia of Volcanoes*, H. Sigurdsson (Ed.). Academic Press, New York, 2000.

Hagerty, M. and Benites, R. 2003. Tornillos beneath Tongariro Volcano, New Zealand. *Journal of Volcanology and Geothermal Research*, 125: 151-169.

Harris, H., Ripepe, M., Calvari, S., Lodato, L., Spampinato, L. The 5 April 2003 explosion of Stromboli: Timing of eruption dynamics using thermal data. In: Calvari, S., Inguaggiato, S., Puglisi, G., Ripepe, M., Rosi, M. (Eds.) *The Stromboli Volcano: An integrated study of the 2002-2003 Eruption*. American Geophysical Union, Italy, 2008.

Hawkesworth, C.J., Blake, S., Evans, P., Hughes, R., MacDonald, R., Thomas, L.E., Turner, S.P., Zellmer, G. 2000. Time scales of crystal fractionation in magma chambers – integrating physical, isotopic, and geochemical processes. *Journal of Petrology*, 41: 991-1006.

Head, J.W. and Wilson, L. 1989. Basaltic pyroclastic eruptions: influence of gas-release patterns and volume fluxes on fountain structure, and the formation of cinder cones, spatter cones, rootless flows, lava ponds, and lava flows. *Journal of Volcanology and Geothermal Research,* 37: 261-271.

Hector, 1887. Presidential Address. *Transactions and Proceedings of the New Zealand Institute*, 19: 461-470

Herd, R.A. and Pinkerton, H. 1997. Bubble coalescence in basaltic lava: Its impact on the evolution of bubble populations. *Journal of Volcanology and Geothermal Research,* 75: 137-157.

Hildreth, W. and Moorbath, S. 1988. Crustal contributions to arc magmatism in the Andes of Central Chile. *Contributions to Mineralogy and Petrology*, 98: 455-489.

Hitchcock, D.W. and Cole, J.W. 2007. Potential impacts of a widespread subplinian andesitic eruption from Tongariro Volcano, based on a study of the Poutu Lapilli. *New Zealand Journal of Geology and Geophysics,* 50: 53-66.

Hobden, B.J., Houghton, D.F., Lanphere, M.A., Nairn, I.A. 1996. Growth of the Tongariro volcanic complex: new evidence from K-Ar age determinations. *New Zealand Journal of Geology and Geophysics*, 39: 151-154.

Hobden, B.J. 1997. Modelling magmatic trends in time and space: eruptive and magmatic history of Tongariro volcanic complex, New Zealand. PhD Thesis, University of Canterbury, Christchurch.

Hobden, B.J., Houghton, B.F., Davidson, J.P., Weaver, S.D. 1999. Small and short-lived magma batches at composite volcanoes: Time windows at Tongariro volcano, New Zealand. *Journal of the Geological Society*, 159: 865-868.

Hobden, B.J. and Houghton, B.F. 2000. Geology of the Tongariro Volcano traverse. In Price, R.C., Gamble, J.A., and Hobden, B.J. (eds) 2000. *State of the Arc 2000; Guidebook for field excursions on Ruapehu and Tongariro Volcanoes*. The Royal Society of New Zealand, Wellington, New Zealand.

Hobden, B.J., Price, R., Gamble, J., Stewart, R. Growth and magmatic evolution of Tongariro and Ruapehu Volcanoes, New Zealand. In: *Geological Society of New Zealand Annual Conference – Advances in Geoscience Fieldtip Guides*. R. Smith (Ed), University of Waikato, Geological Society of New Zealand misc. Publication 110A, 2001.

Hobden, B.J., Houghton, B.F., Nairn, I.A. 2002. Growth of a frequently active composite cone: Ngauruhoe Volcano, New Zealand. *Bulletin of Volcanology*, 64: 392-409.

Houghton, B.F., Wilson, C.J.N., Smith, I.E.M. 1999. Shallow-seated controls of explosive basaltic volcanism: a case study from New Zealand. *Journal of Volcanology and Geothermal Research*, 91: 97-120.

Houghton, B.F. and Gonnermann, H.M. 2008. Basaltic explosive volcanism: Constraints from deposits and models. *Chemie der Erde*, 68: 117-140.

Humphreys, M.C.S., Blundy, J.D., Sparks, R.S.J. 2006. Magma evolution and open-system processes at Shiveluch Volcano: Insights from phenocryst zoning. *Journal of Petrology*, 47: 2303-2334.

Jaupart, C. and Vergniolle, S. 1988. The flow of gas and lava: A review of dynamic models for volcanic eruptions. *Chemical Geology*, 70: 38.

Johnson, J.B. and Aster, R.C. 2005. Relative partitioning of acoustic and seismic energy during Strombolian eruptions. *Journal of Volcanology and Geothermal Research,* 148: 334-354.

Landi, P., Francalanci, L., Pompilio, M., Rosi, M,. Corsaro, R.A., Petrone, C.M., Nardini, I., Miraglia, L. 2006. The December 2002 – July 2003 effusive event at Stromboli Volcano, Italy: Insights into the shallow plumbing system by petrochemical studies. *Journal of Volcanology and Geothermal Research*, 155: 263-284.

Lube, G., Cronin, S.J., Platz, T., Freundt, A., Procter, J.N., Henderson, C., Seridan, M.F. 2007. Flow and deposition of pyroclastic granular flows: A type example from the 1975 Ngauruhoe eruption, New Zealand. *Journal of Volcanology and Geothermal research*, 161: 165-186.

McDonough, W.F., Sun, S., Ringwood, A.E., Jagoutz, E., Hofmann, A.W. 1992. Potassium, rubidium, and cesium in the Earth and Moon and the evolution of the mantle of the Earth. *Geochemica et Cosmochimica Acta*, 56: 1001-1012.

Marshall, P. 1909. Crater of Ngauruhoe. *Transactions and Proceedings of the New Zealand Institute*, 41: 102-105.

Morrissey, M.M. and Mastin, L.G. Vulcanian eruptions. In: *Encyclopedia of Volcanoes*, H. Sigurdsson (Ed.). Academic Press, New York, 2000.

Nairn, I.A., Hewson, C.A.Y., Latter, J.H., Wood, C.P. 1976. Pyroclastic eruptions of Ngauruhoe Volcano, central North Island, New Zealand, 1974 January and March. In: R.W. Johnson (Editor) *Volcanism in Australasia*. Elsevier, Amsterdam, pp 385-405.

Nairn, I.A. and Self, S. 1978. Explosive eruptions and pyroclastic avalanches from Ngauruhoe in February 1975. *Journal of Volcanology and Geothermal Research*, 3: 39-60.

Nairn, I.A., Kobayashi, T., Nakagawa, M. 1998. The ~10 ka multiple vent pyroclastic eruption sequence at Tongariro Volcanic Centre, Taupo Volcanic Zone, New Zealand. Part 1. Eruptive processes during regional extension. *Journal of Volcanology and Geothermal Research*, 86: 19-44.

Nakagawa, M., Wada, K., Thordarson, T., Wood, C.P., Gamble, J.A. 1999. Petrologic investigations of the 1995 and 1996 eruptions of Ruapehu Volcano, New Zealand: Formation of discrete and small magma pockets and their intermittent discharge. *Bulletin of Volcanology*, 61: 15-31.

Nakagawa, M., Wada, K., Wood. C.P. 2002. Mixed magmas, mush chambers and eruption triggers: Evidence from zoned clinopyroxene phenocrysts in andesitic scoria from the 1995 eruptions of Ruapehu Volcano, New Zealand. *Journal of Petrology*, 43: 2279-2303.

Parfitt, E.A. 2004. A discussion of the mechanisms of explosive basaltic eruptions. *Journal of Volcanology and Geothermal Research*, 134: 77-107.

Patterson, D.B. and Graham, I.J. 1988. Petrogenesis of andesitic lavas from Mangatepopo Valley and Upper Tama Lake, Tongariro Volcanic Centre, New Zealand. *Journal of Volcanology and Geothermal Research*, 35: 17-29.

Platz, T., Cronin, S.J., Cashman, K.V., Stewart, R.B., Smith, I.E.M. 2007. Transition from effusive to explosive phases in andesite eruptions – A case-study from the AD1655 eruption of Mt. Taranaki, New Zealand. *Journal of Volcanology and Geothermal Research*, 161: 15-34.

Polacci, M., Burton, M.R., La Spina, A., Muré, F., Fravetto, S., Zanini, F. 2008. The role of syn-eruptive vesiculation on explosive basaltic activity at Mt Etna, Italy. *Journal of Volcanology and Geothermal Research*, doi:10.1016/j.jvolgeores.2008.11.026.

Price, R. C., Gamble J. A., Smith, I.E.M., Stewart, R.B., Eggins, S., Wright, I.C. 2005. An integrated model for the temporal evolution of andesites and rhyolites and crustal development in New Zealand's North Island. *Journal of Volcanology and Geothermal Research*, 140: 1-24.

Price, R.C., George, R., Gamble, J.A., Turner, S., Smith, I.E.M., Cook, C., Hobden, B., Dosseto, A. 2007. U-Th-Ra fractionation during crustal-level andesite formation at Ruapehu volcano, New Zealand. *Chemical Geology*, 244: 437-451.

Reubi, O., Nicholls, I.A., Kamenetsky, V.S. 2002. Early mixing and mingling in the evolution of basaltic magmas: Evidence from phenocryst assemblages, Slamet Volcano, Java, Indonesia. *Journal of Volcanology and Geothermal Research*, 119: 225-274.

Ripepe, M., Rossi, M., Saccorotti, G. 1993. Image processing of explosive activity at Stromboli. *Journal of Volcanology and Geothermal Research*, 54: 335-351.

Rollinson, H.R. 1993. *Using geochemical data: Evaluation, presentation, interpretation*. Longman Scientific and Technical, New York.

Ross, M. 1898. The Northern Alps of New Zealand. *Weekly Press*, Christchurch. Christmas Number, 29 October 1898, pp. 1-6.

Rowland, J.V. and Sibson, R.H. 2001. Extensional fault kinematics within the Taupo Volcanic Zone, New Zealand: Soft-linked segmentation of a continental rift system. *New Zealand Journal of Geology and Geophysics* 44: 271-283.

Rowlands, D.P., White, R.S., Haines, A.J. 2005. Seismic tomography of the Tongariro Volcanic Centre, New Zealand. *Geophysical Journal International*, 163: 1180-1194.

Rutherford, M.J. and Gardner, J.E. Rates of magma ascent. In: *Encyclopedia of Volcanoes*, H. Sigurdsson (Ed.). Academic Press, New York, 2000.

Scandone, R., Giacomelli, L., Speranza, F.F. 2008. Persistent activity and violent strombolian eruptions at Vesuvius between 1631 and 1944. *Journal of Volcanology and Geothermal Research*, 170: 167-180.

Self, S. 1975. Explosive activity of Ngauruhoe, 27-30 March 1974 (Note). *New Zealand Journal of Geology and Geophysics*, 18: 189-195.

Steiner, A. 1958. Petrogenic implications of the 1954 Ngauruhoe lava and its xenoliths. *New Zealand Journal of Geology and Geophysics*, 1: 325-363.

Sumner, J.M. 1998. Formation of clastogenic lava flows during fissure eruption and scoria cone collapse: The 1986 eruption of Izu-Oshima Volcano, Eastern Japan. *Bulletin of Volcanology*, 60: 195-212.

Sumner, J.M., Blake, S., Matela, R.J., Wolff, J.A. 2005. Spatter. *Journal of Volcanology and Geothermal research*, 142: 49-65.

Topping, W.W. 1973. Tephrostratigraphy and chronology of late Quaternary eruptives from the Tongariro Volcanic Centre, New Zealand. *New Zealand Journal of Geology and Geophysics*, 16: 397-423.

Ulmer, P. 2000. Partial melting in the mantle wedge – the role of $H_2O$ in the genesis of mantle-derived 'arc-related' magmas. *Physics of the Earth and Planetary Interiors*, 127: 215-232.

Valentine, G.A. and Fisher, R.V. Pyroclastic surges and blasts. In: *Encyclopedia of Volcanoes*, H. Sigurdsson (Ed.). Academic Press, New York, 2000.

Vergniolle, S., Mangan, M., Hawaiian and Strombolian eruptions. In: *Encyclopedia of Volcanoes,* H. Sigurdsson (Ed.). Academic Press, New York, 2000.

Vergniolle, S. 1996. Bubble size distribution in magma chambers and dynamics of basaltic eruptions. *Earth and Planetary Science Letters*, 140: 269-279.

Vergniolle, S., Boichu, M., Caplan-Auerbach, J. 2004. Acoustic measurements of the 1999 basaltic eruption of Shishaldin Volcano, Alaska 1. Origin of Strombolian activity. *Journal of Volcanology and Geothermal Research*, 137: 109-134.

Vespermann, D. and Schmincke, H.-U. Scoria cones and tuff rings. In: *Encyclopedia of Volcanoes*, H. Sigurdsson (Ed.). Academic Press, New York, 2000.

Williams, K. 1989. *Volcanoes from the South Wind: a field guide to the volcanoes and landscape of Tongariro National Park*. Tongariro National History Society, Wellington.

Wilson, C. J. N., Houghton, B. F., McWilliams, M.O., Lanphere, M.A.Weaver, S.D., Briggs, R.M., 1995. Volcanic and structural evolution of Taupo Volcanic Zone, New Zealand: A review. *Journal of Volcanology and Geothermal Research,* 68: 1-28.

Wolff, J.A. and Sumner, J.M. Lava fountains and their products. In: *Encyclopedia of Volcanoes*, H. Sigurdsson (Ed.). Academic Press, New York, 2000.

Woods, A.W. 1995. A model of vulcanian explosions. *Nuclear Engineering and Design*, 155: 345-357.

# Appendix One:

# Sieving Data

| SAMPLE B1a | |
|---|---|
| Phi | Weight (g) |
| -6 | 0 |
| -5 | 229.7 |
| -4 | 268.4 |
| -3 | 228.7 |
| -2 | 165.6 |
| -1 | 157.05 |
| 0 | 135.58 |
| 1 | 131.2 |
| <1 | 241.8 |
| Total | 1558.03 |

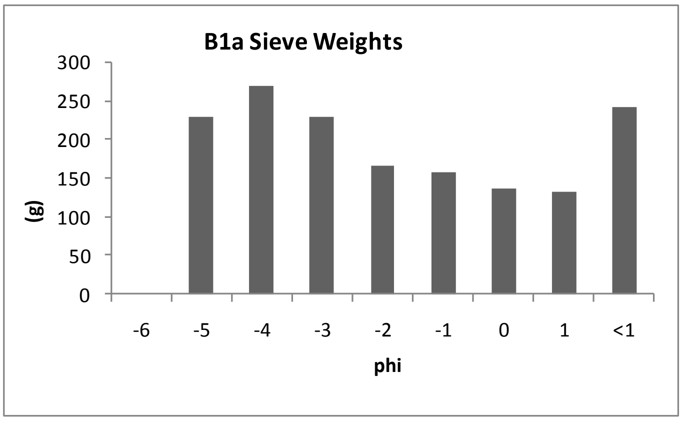

| SAMPLE F3 | |
|---|---|
| Phi | Weight (g) |
| -6 | 0 |
| -5 | 0 |
| -4 | 781.7 |
| -3 | 520.3 |
| -2 | 171.6 |
| -1 | 128.26 |
| 0 | 165.25 |
| 1 | 187.98 |
| <1 | 552.8 |
| Total | 2507.89 |

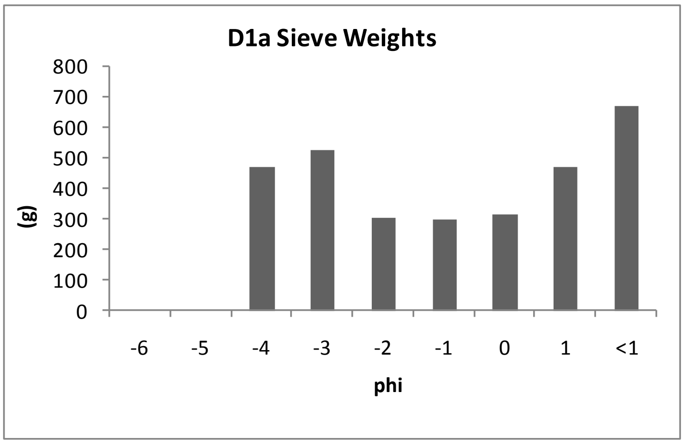

| SAMPLE D1a | |
|---|---|
| Phi | Weight (g) |
| -6 | 0 |
| -5 | 0 |
| -4 | 468.6 |
| -3 | 521.7 |
| -2 | 304.9 |
| -1 | 296.9 |
| 0 | 314.2 |
| 1 | 469 |
| <1 | 667.1 |
| Total | 3042.4 |

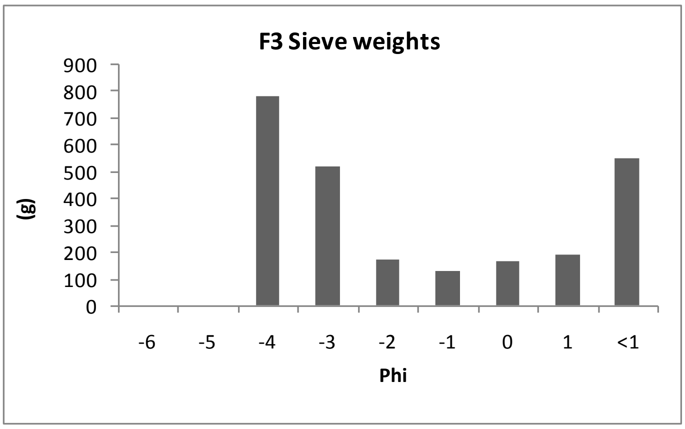

# Appendix Two:

# Ash Grain Size Analyses by Laser Sizer

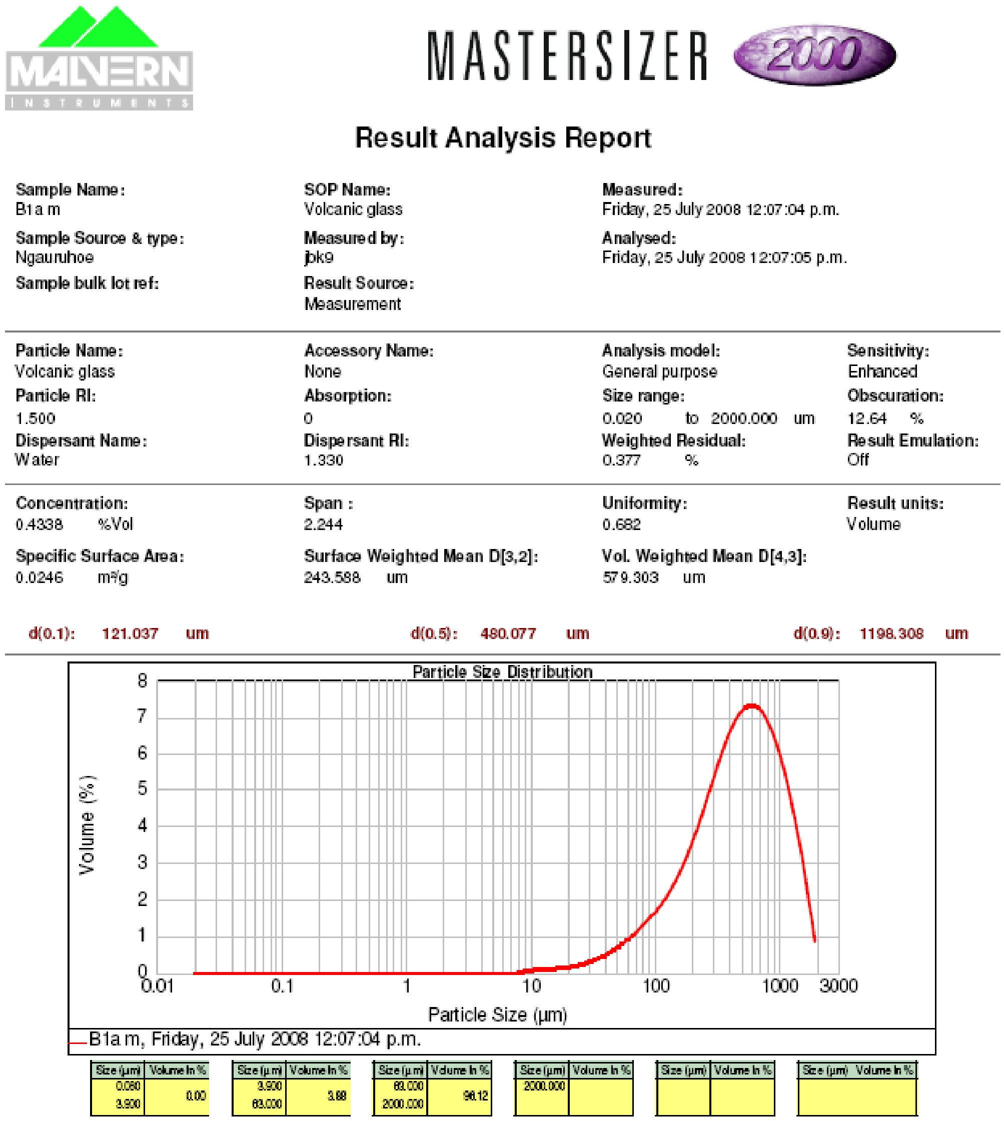

MASTERSIZER 2000

Result Analysis Report

| | | |
|---|---|---|
| **Sample Name:**<br>B1a m | **SOP Name:**<br>Volcanic glass | **Measured:**<br>Friday, 25 July 2008 12:07:04 p.m. |
| **Sample Source & type:**<br>Ngauruhoe | **Measured by:**<br>jbk9 | **Analysed:**<br>Friday, 25 July 2008 12:07:05 p.m. |
| **Sample bulk lot ref:** | **Result Source:**<br>Measurement | |

| | | | |
|---|---|---|---|
| **Particle Name:**<br>Volcanic glass | **Accessory Name:**<br>None | **Analysis model:**<br>General purpose | **Sensitivity:**<br>Enhanced |
| **Particle RI:**<br>1.500 | **Absorption:**<br>0 | **Size range:**<br>0.020 to 2000.000 um | **Obscuration:**<br>12.64 % |
| **Dispersant Name:**<br>Water | **Dispersant RI:**<br>1.330 | **Weighted Residual:**<br>0.377 % | **Result Emulation:**<br>Off |

| | | | |
|---|---|---|---|
| **Concentration:**<br>0.4338 %Vol | **Span :**<br>2.244 | **Uniformity:**<br>0.682 | **Result units:**<br>Volume |
| **Specific Surface Area:**<br>0.0246 m²/g | **Surface Weighted Mean D[3,2]:**<br>243.588 um | **Vol. Weighted Mean D[4,3]:**<br>579.303 um | |

**d(0.1): 121.037 um** **d(0.5): 480.077 um** **d(0.9): 1198.308 um**

| Size (µm) | Volume In % |
|---|---|
| 0.060<br>3.900 | 0.00 |

| Size (µm) | Volume In % |
|---|---|
| 3.900<br>63.000 | 3.88 |

| Size (µm) | Volume In % |
|---|---|
| 63.000<br>2000.000 | 96.12 |

| Size (µm) | Volume In % |
|---|---|
| 2000.000 | |

| Size (µm) | Volume In % |
|---|---|
| | |

| Size (µm) | Volume In % |
|---|---|
| | |

**Figure A2.9:** Laser sizer results for B1amid

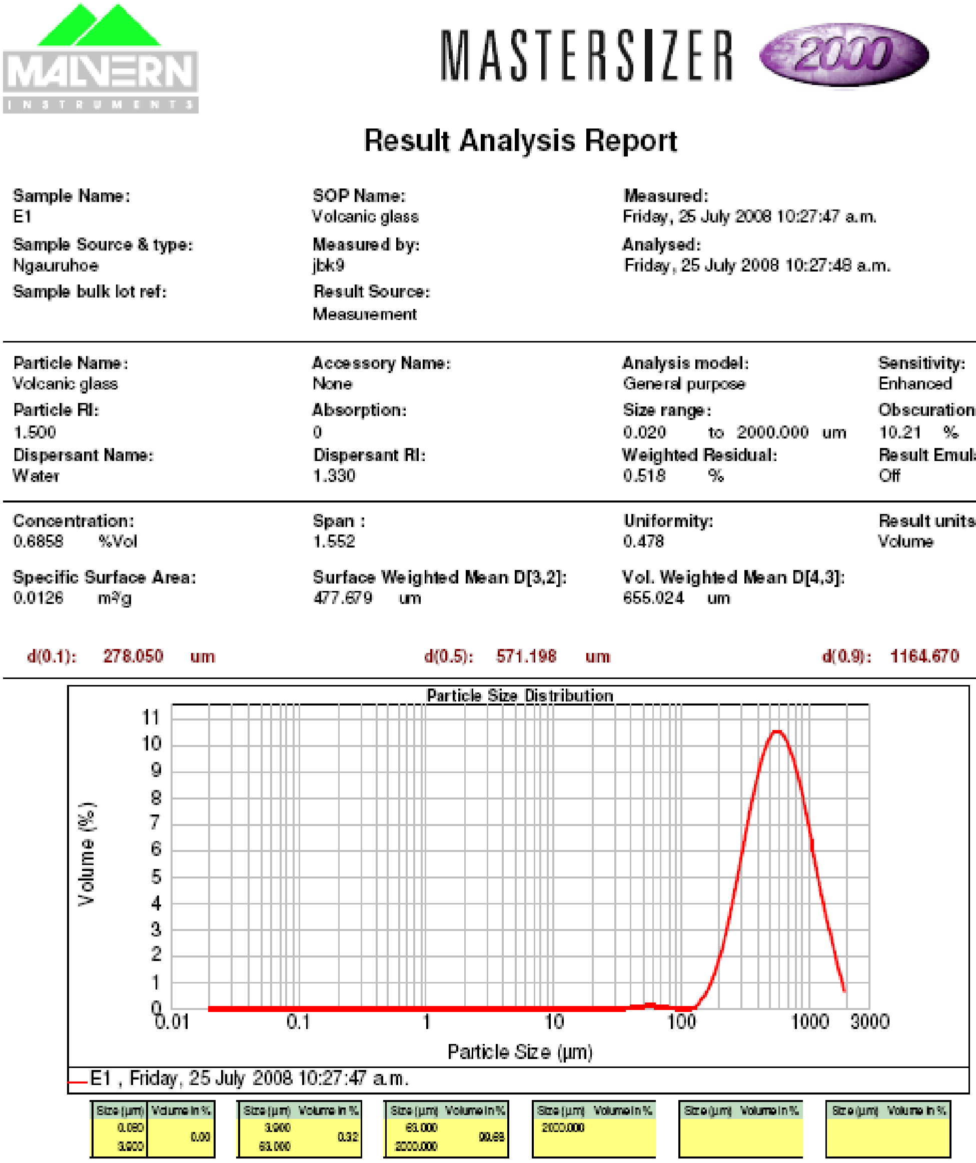

## Result Analysis Report

**Sample Name:**
E1

**Sample Source & type:**
Ngauruhoe

**Sample bulk lot ref:**

**SOP Name:**
Volcanic glass

**Measured by:**
jbk9

**Result Source:**
Measurement

**Measured:**
Friday, 25 July 2008 10:27:47 a.m.

**Analysed:**
Friday, 25 July 2008 10:27:48 a.m.

**Particle Name:**
Volcanic glass

**Particle RI:**
1.500

**Dispersant Name:**
Water

**Accessory Name:**
None

**Absorption:**
0

**Dispersant RI:**
1.330

**Analysis model:**
General purpose

**Size range:**
0.020 to 2000.000 um

**Weighted Residual:**
0.518 %

**Sensitivity:**
Enhanced

**Obscuration:**
10.21 %

**Result Emulation:**
Off

**Concentration:**
0.6858 %Vol

**Specific Surface Area:**
0.0126 m²/g

**Span :**
1.552

**Surface Weighted Mean D[3,2]:**
477.679 um

**Uniformity:**
0.478

**Vol. Weighted Mean D[4,3]:**
655.024 um

**Result units:**
Volume

d(0.1): 278.050 um d(0.5): 571.198 um d(0.9): 1164.670 um

| Size (μm) | Volume In % | Size (μm) | Volume In % | Size (μm) | Volume In % | Size (μm) | Volume In % | Size (μm) | Volume In % | Size (μm) | Volume In % |
|---|---|---|---|---|---|---|---|---|---|---|---|
| 0.020 | 0.00 | 3.900 | 0.32 | 63.000 | 99.68 | 2000.000 | | | | | |
| 3.900 | | 63.000 | | 2000.000 | | | | | | | |

**Figure A2.2:** Laser sizer results for D2a

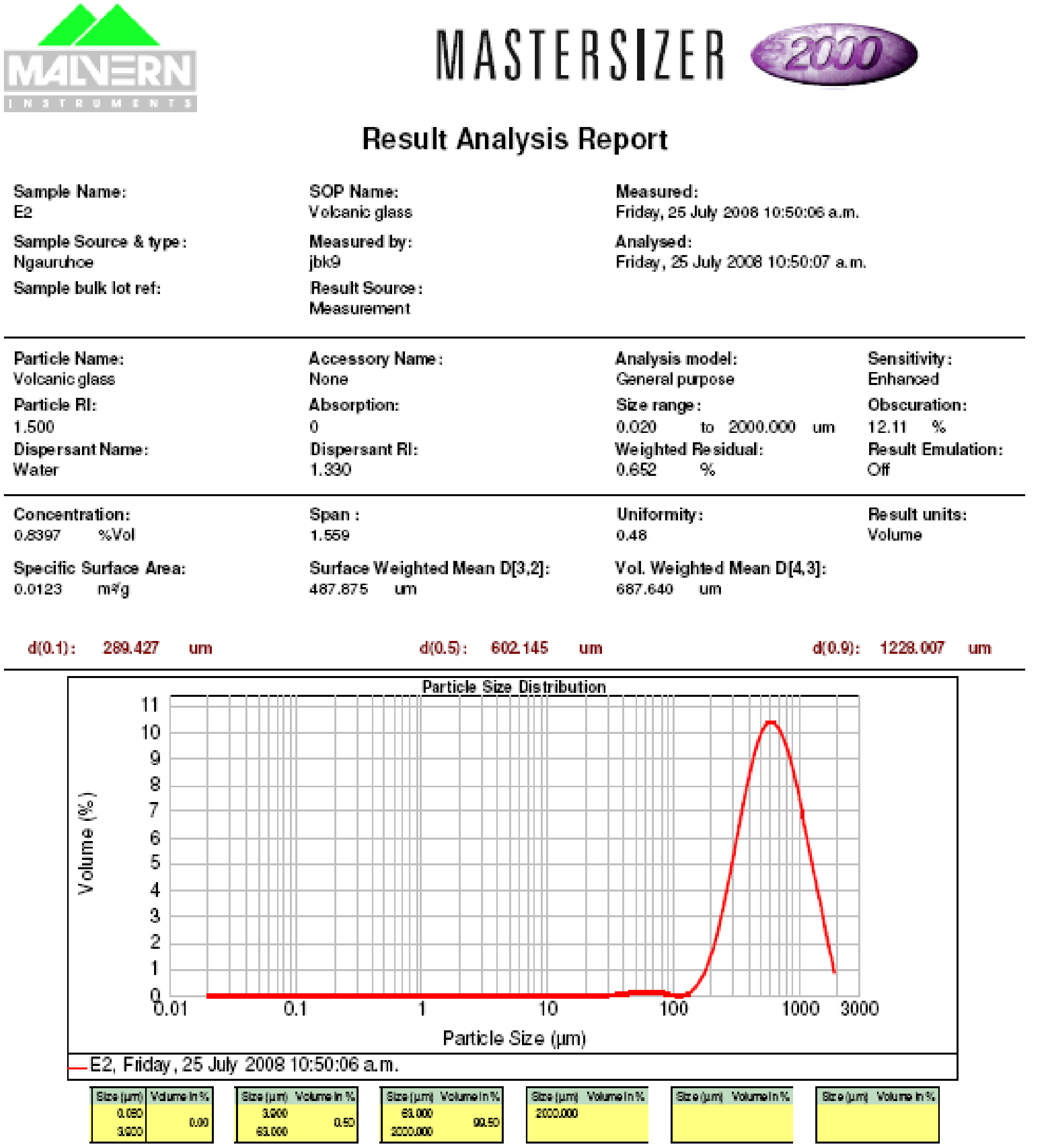

MALVERN INSTRUMENTS MASTERSIZER 2000

Result Analysis Report

**Sample Name:**
E2

**Sample Source & type:**
Ngauruhoe

**Sample bulk lot ref:**

**SOP Name:**
Volcanic glass

**Measured by:**
jbk9

**Result Source:**
Measurement

**Measured:**
Friday, 25 July 2008 10:50:06 a.m.

**Analysed:**
Friday, 25 July 2008 10:50:07 a.m.

**Particle Name:**
Volcanic glass

**Particle RI:**
1.500

**Dispersant Name:**
Water

**Accessory Name:**
None

**Absorption:**
0

**Dispersant RI:**
1.330

**Analysis model:**
General purpose

**Size range:**
0.020 to 2000.000 um

**Weighted Residual:**
0.652 %

**Sensitivity:**
Enhanced

**Obscuration:**
12.11 %

**Result Emulation:**
Off

**Concentration:**
0.8397 %Vol

**Specific Surface Area:**
0.0123 m²/g

**Span :**
1.559

**Surface Weighted Mean D[3,2]:**
487.875 um

**Uniformity:**
0.48

**Vol. Weighted Mean D[4,3]:**
687.640 um

**Result units:**
Volume

d(0.1): 289.427 um d(0.5): 602.145 um d(0.9): 1228.007 um

Particle Size Distribution

| Size (µm) | Volume In % |
|---|---|
| 0.020<br>3.900 | 0.00 |

| Size (µm) | Volume In % |
|---|---|
| 3.900<br>63.000 | 0.50 |

| Size (µm) | Volume In % |
|---|---|
| 63.000<br>2000.000 | 99.50 |

| Size (µm) | Volume In % |
|---|---|
| 2000.000 | |

| Size (µm) | Volume In % |
|---|---|
| | |

| Size (µm) | Volume In % |
|---|---|
| | |

**Figure A2.3:** Laser sizer results for D2b

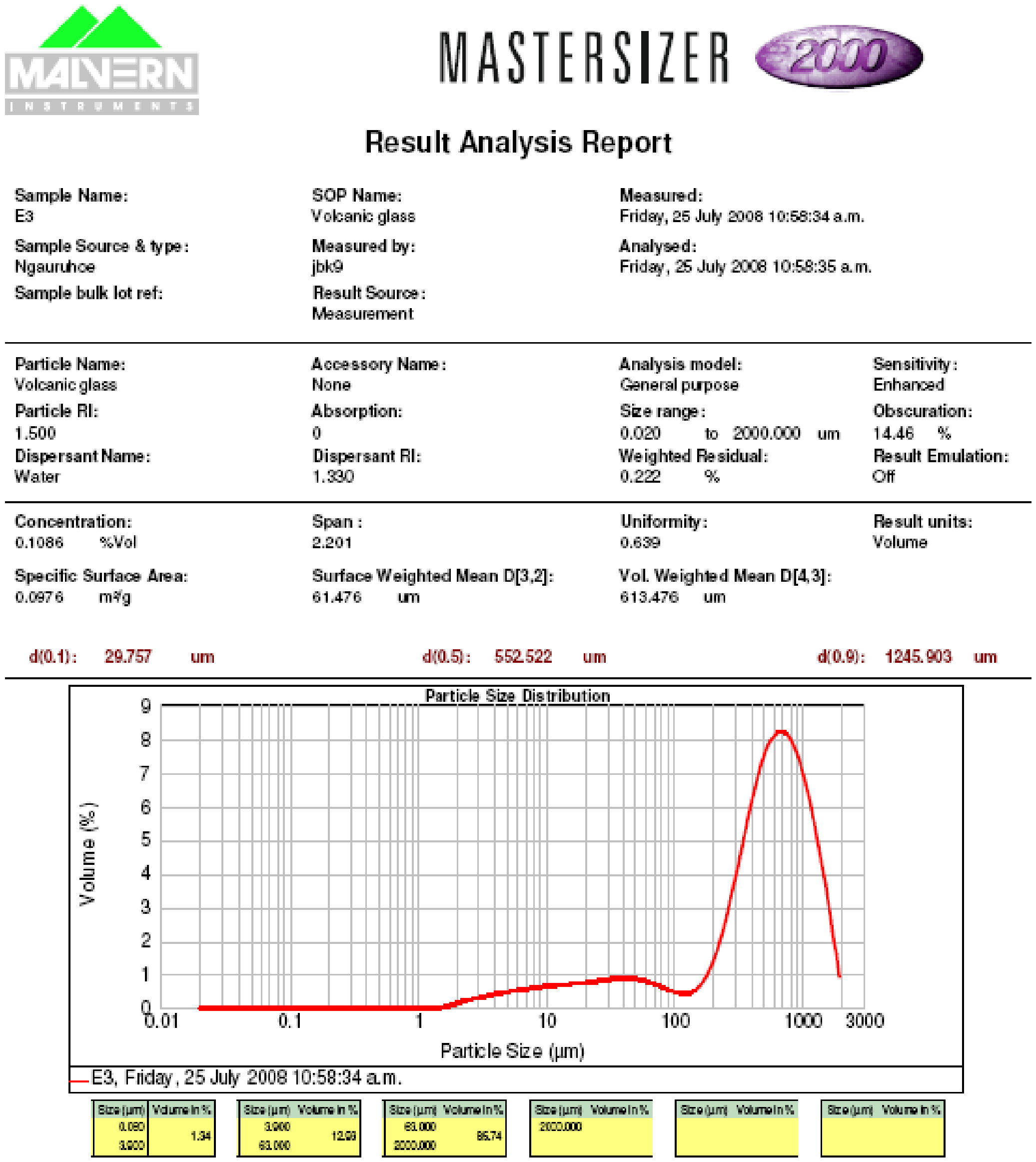

MALVERN INSTRUMENTS

MASTERSIZER 2000

Result Analysis Report

| | | |
|---|---|---|
| **Sample Name:**<br>E3 | **SOP Name:**<br>Volcanic glass | **Measured:**<br>Friday, 25 July 2008 10:58:34 a.m. |
| **Sample Source & type:**<br>Ngauruhoe | **Measured by:**<br>jbk9 | **Analysed:**<br>Friday, 25 July 2008 10:58:35 a.m. |
| **Sample bulk lot ref:** | **Result Source:**<br>Measurement | |

| | | | |
|---|---|---|---|
| **Particle Name:**<br>Volcanic glass | **Accessory Name:**<br>None | **Analysis model:**<br>General purpose | **Sensitivity:**<br>Enhanced |
| **Particle RI:**<br>1.500 | **Absorption:**<br>0 | **Size range:**<br>0.020 to 2000.000 um | **Obscuration:**<br>14.46 % |
| **Dispersant Name:**<br>Water | **Dispersant RI:**<br>1.330 | **Weighted Residual:**<br>0.222 % | **Result Emulation:**<br>Off |

| | | | |
|---|---|---|---|
| **Concentration:**<br>0.1086 %Vol | **Span :**<br>2.201 | **Uniformity:**<br>0.639 | **Result units:**<br>Volume |
| **Specific Surface Area:**<br>0.0976 m²/g | **Surface Weighted Mean D[3,2]:**<br>61.476 um | **Vol. Weighted Mean D[4,3]:**<br>613.476 um | |

d(0.1): 29.757 um d(0.5): 552.522 um d(0.9): 1245.903 um

| Size (μm) | Volume In % |
|---|---|
| 0.020<br>3.900 | 1.34 |

| Size (μm) | Volume In % |
|---|---|
| 3.900<br>63.000 | 12.92 |

| Size (μm) | Volume In % |
|---|---|
| 63.000<br>2000.000 | 85.74 |

| Size (μm) | Volume In % |
|---|---|
| 2000.000 | |

| Size (μm) | Volume In % |
|---|---|
| | |

| Size (μm) | Volume In % |
|---|---|
| | |

**Figure A2.4:** Laser sizer results for D2c

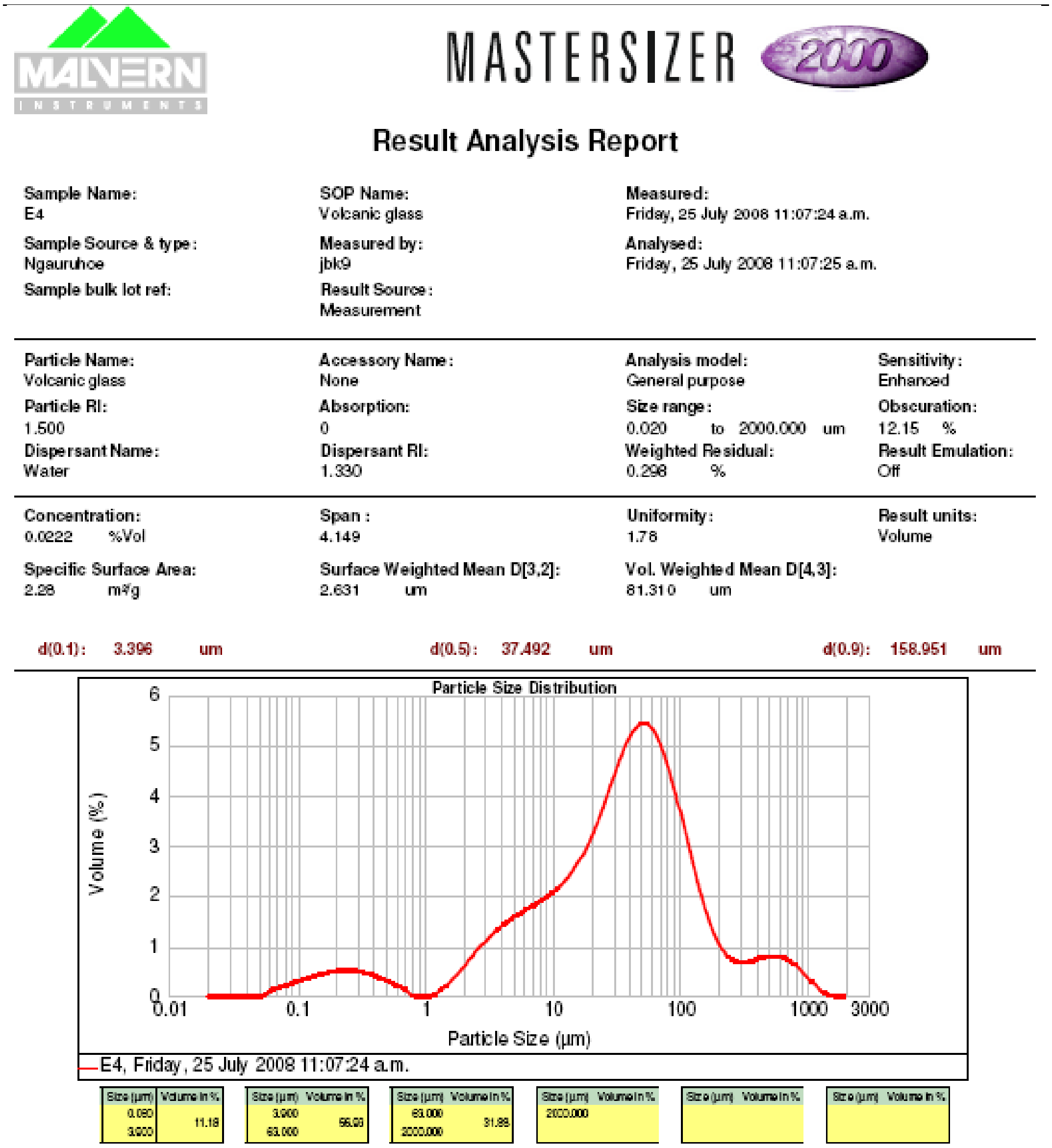

MALVERN INSTRUMENTS

MASTERSIZER 2000

## Result Analysis Report

| | | |
|---|---|---|
| **Sample Name:**<br>E4 | **SOP Name:**<br>Volcanic glass | **Measured:**<br>Friday, 25 July 2008 11:07:24 a.m. |
| **Sample Source & type:**<br>Ngauruhoe | **Measured by:**<br>jbk9 | **Analysed:**<br>Friday, 25 July 2008 11:07:25 a.m. |
| **Sample bulk lot ref:** | **Result Source:**<br>Measurement | |

| | | | |
|---|---|---|---|
| **Particle Name:**<br>Volcanic glass | **Accessory Name:**<br>None | **Analysis model:**<br>General purpose | **Sensitivity:**<br>Enhanced |
| **Particle RI:**<br>1.500 | **Absorption:**<br>0 | **Size range:**<br>0.020 to 2000.000 um | **Obscuration:**<br>12.15 % |
| **Dispersant Name:**<br>Water | **Dispersant RI:**<br>1.330 | **Weighted Residual:**<br>0.298 % | **Result Emulation:**<br>Off |

| | | | |
|---|---|---|---|
| **Concentration:**<br>0.0222 %Vol | **Span :**<br>4.149 | **Uniformity:**<br>1.78 | **Result units:**<br>Volume |
| **Specific Surface Area:**<br>2.28 m²/g | **Surface Weighted Mean D[3,2]:**<br>2.631 um | **Vol. Weighted Mean D[4,3]:**<br>81.310 um | |

d(0.1): 3.396 um d(0.5): 37.492 um d(0.9): 158.951 um

| Size (µm) | Volume In % |
|---|---|
| 0.020<br>3.900 | 11.18 |

| Size (µm) | Volume In % |
|---|---|
| 3.900<br>63.000 | 56.93 |

| Size (µm) | Volume In % |
|---|---|
| 63.000<br>2000.000 | 31.89 |

| Size (µm) | Volume In % |
|---|---|
| 2000.000 | |

| Size (µm) | Volume In % |
|---|---|
| | |

| Size (µm) | Volume In % |
|---|---|
| | |

**Figure A2.5:** Laser sizer results for E

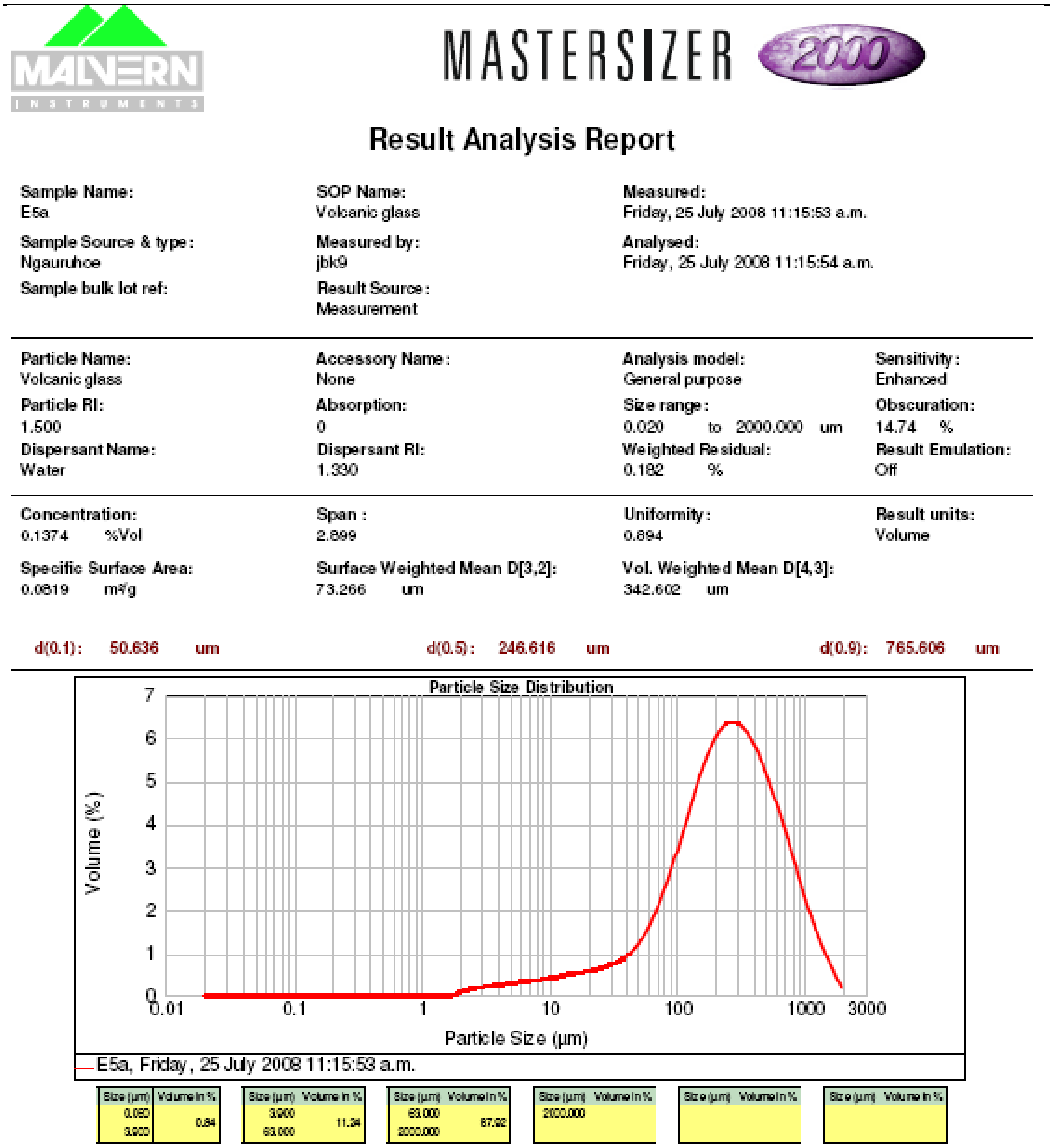

MALVERN INSTRUMENTS MASTERSIZER 2000

## Result Analysis Report

|  |  |  |  |
|---|---|---|---|
| **Sample Name:**<br>E5a | **SOP Name:**<br>Volcanic glass | **Measured:**<br>Friday, 25 July 2008 11:15:53 a.m. |  |
| **Sample Source & type:**<br>Ngauruhoe | **Measured by:**<br>jbk9 | **Analysed:**<br>Friday, 25 July 2008 11:15:54 a.m. |  |
| **Sample bulk lot ref:** | **Result Source:**<br>Measurement |  |  |
| **Particle Name:**<br>Volcanic glass | **Accessory Name:**<br>None | **Analysis model:**<br>General purpose | **Sensitivity:**<br>Enhanced |
| **Particle RI:**<br>1.500 | **Absorption:**<br>0 | **Size range:**<br>0.020 to 2000.000 um | **Obscuration:**<br>14.74 % |
| **Dispersant Name:**<br>Water | **Dispersant RI:**<br>1.330 | **Weighted Residual:**<br>0.182 % | **Result Emulation:**<br>Off |
| **Concentration:**<br>0.1374 %Vol | **Span :**<br>2.899 | **Uniformity:**<br>0.894 | **Result units:**<br>Volume |
| **Specific Surface Area:**<br>0.0819 m²/g | **Surface Weighted Mean D[3,2]:**<br>73.266 um | **Vol. Weighted Mean D[4,3]:**<br>342.602 um |  |

d(0.1): 50.636 um d(0.5): 246.616 um d(0.9): 765.606 um

| Size (µm) | Volume In % | Size (µm) | Volume In % | Size (µm) | Volume In % | Size (µm) | Volume In % | Size (µm) | Volume In % | Size (µm) | Volume In % |
|---|---|---|---|---|---|---|---|---|---|---|---|
| 0.020 | 0.84 | 3.900 | 11.24 | 63.000 | 87.92 | 2000.000 |  |  |  |  |  |
| 3.900 |  | 63.000 |  | 2000.000 |  |  |  |  |  |  |  |

**Figure A2.6:** Laser sizer results for F1

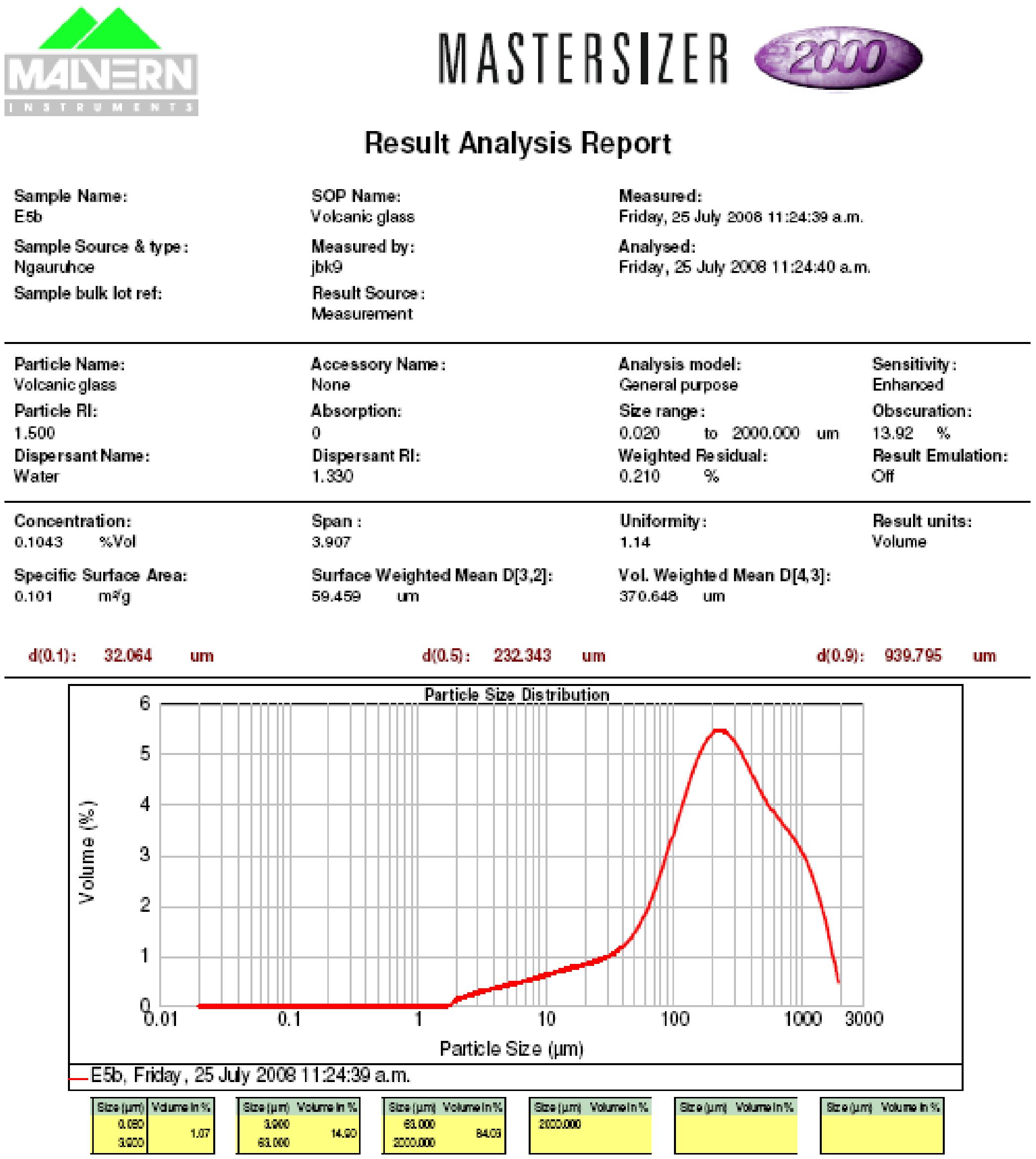

MASTERSIZER 2000

**Result Analysis Report**

| | | |
|---|---|---|
| **Sample Name:**<br>E5b | **SOP Name:**<br>Volcanic glass | **Measured:**<br>Friday, 25 July 2008 11:24:39 a.m. |
| **Sample Source & type:**<br>Ngauruhoe | **Measured by:**<br>jbk9 | **Analysed:**<br>Friday, 25 July 2008 11:24:40 a.m. |
| **Sample bulk lot ref:** | **Result Source:**<br>Measurement | |

| | | | |
|---|---|---|---|
| **Particle Name:**<br>Volcanic glass | **Accessory Name:**<br>None | **Analysis model:**<br>General purpose | **Sensitivity:**<br>Enhanced |
| **Particle RI:**<br>1.500 | **Absorption:**<br>0 | **Size range:**<br>0.020 to 2000.000 um | **Obscuration:**<br>13.92 % |
| **Dispersant Name:**<br>Water | **Dispersant RI:**<br>1.330 | **Weighted Residual:**<br>0.210 % | **Result Emulation:**<br>Off |

| | | | |
|---|---|---|---|
| **Concentration:**<br>0.1043 %Vol | **Span:**<br>3.907 | **Uniformity:**<br>1.14 | **Result units:**<br>Volume |
| **Specific Surface Area:**<br>0.101 m²/g | **Surface Weighted Mean D[3,2]:**<br>59.459 um | **Vol. Weighted Mean D[4,3]:**<br>370.648 um | |

d(0.1): 32.064 um d(0.5): 232.343 um d(0.9): 939.795 um

| Size (μm) | Volume In % |
|---|---|
| 0.020<br>3.900 | 1.07 |

| Size (μm) | Volume In % |
|---|---|
| 3.900<br>63.000 | 14.90 |

| Size (μm) | Volume In % |
|---|---|
| 63.000<br>2000.000 | 84.03 |

| Size (μm) | Volume In % |
|---|---|
| 2000.000 | |

| Size (μm) | Volume In % |
|---|---|
| | |

| Size (μm) | Volume In % |
|---|---|
| | |

**Figure A2.7:** Laser sizer results for F2

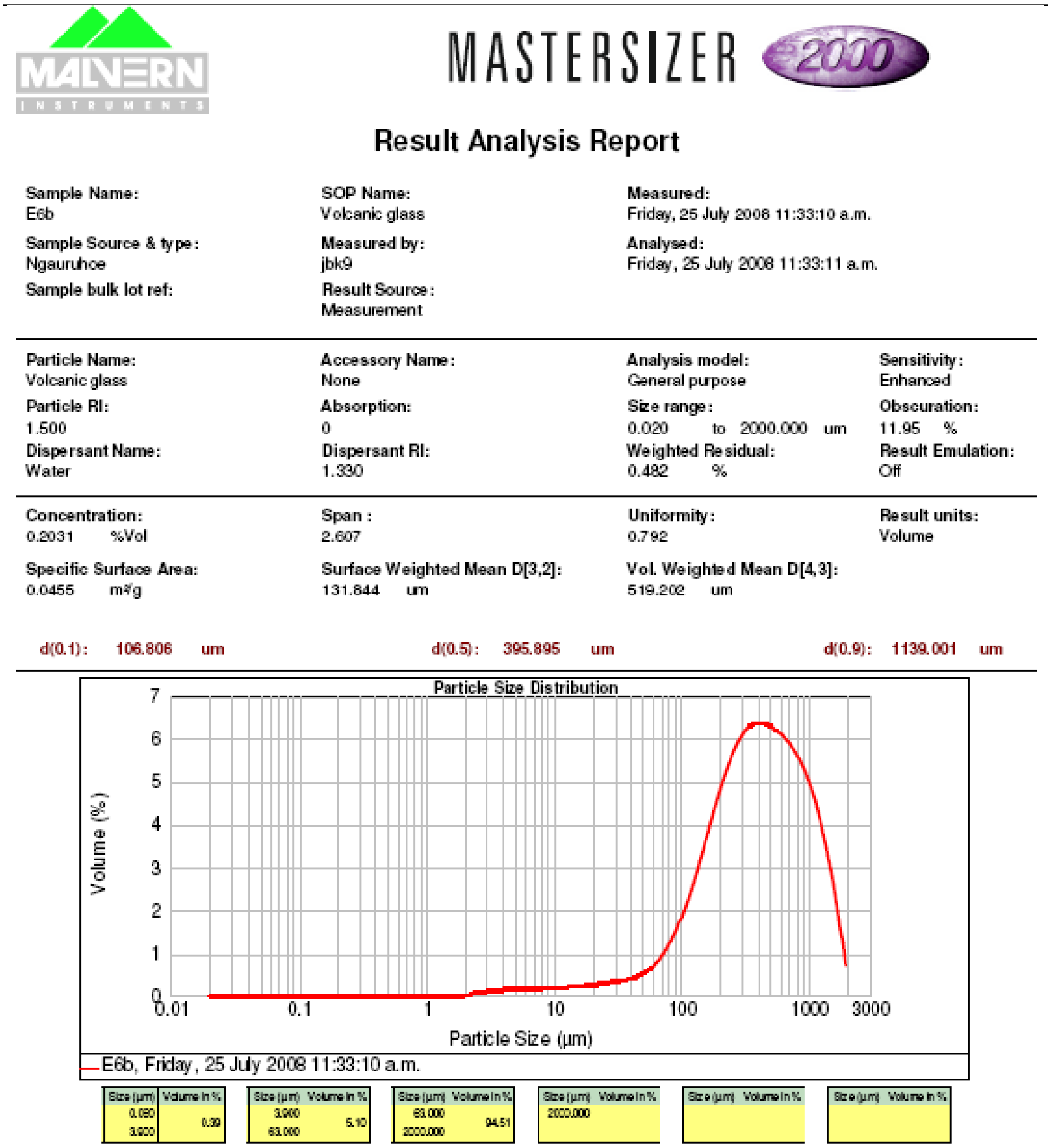

MASTERSIZER 2000

## Result Analysis Report

**Sample Name:**
E6b

**Sample Source & type:**
Ngauruhoe

**Sample bulk lot ref:**

**SOP Name:**
Volcanic glass

**Measured by:**
jbk9

**Result Source:**
Measurement

**Measured:**
Friday, 25 July 2008 11:33:10 a.m.

**Analysed:**
Friday, 25 July 2008 11:33:11 a.m.

**Particle Name:**
Volcanic glass

**Particle RI:**
1.500

**Dispersant Name:**
Water

**Accessory Name:**
None

**Absorption:**
0

**Dispersant RI:**
1.330

**Analysis model:**
General purpose

**Size range:**
0.020 to 2000.000 um

**Weighted Residual:**
0.482 %

**Sensitivity:**
Enhanced

**Obscuration:**
11.95 %

**Result Emulation:**
Off

**Concentration:**
0.2031 %Vol

**Specific Surface Area:**
0.0455 m²/g

**Span :**
2.607

**Surface Weighted Mean D[3,2]:**
131.844 um

**Uniformity:**
0.792

**Vol. Weighted Mean D[4,3]:**
519.202 um

**Result units:**
Volume

d(0.1): 106.806 um d(0.5): 395.895 um d(0.9): 1139.001 um

| Size (µm) | Volume In % |
|---|---|
| 0.020<br>3.900 | 0.39 |

| Size (µm) | Volume In % |
|---|---|
| 3.900<br>63.000 | 5.10 |

| Size (µm) | Volume In % |
|---|---|
| 63.000<br>2000.000 | 94.51 |

| Size (µm) | Volume In % |
|---|---|
| 2000.000 | |

| Size (µm) | Volume In % |
|---|---|
| | |

| Size (µm) | Volume In % |
|---|---|
| | |

**Figure A2.8:** Laser sizer results for F3

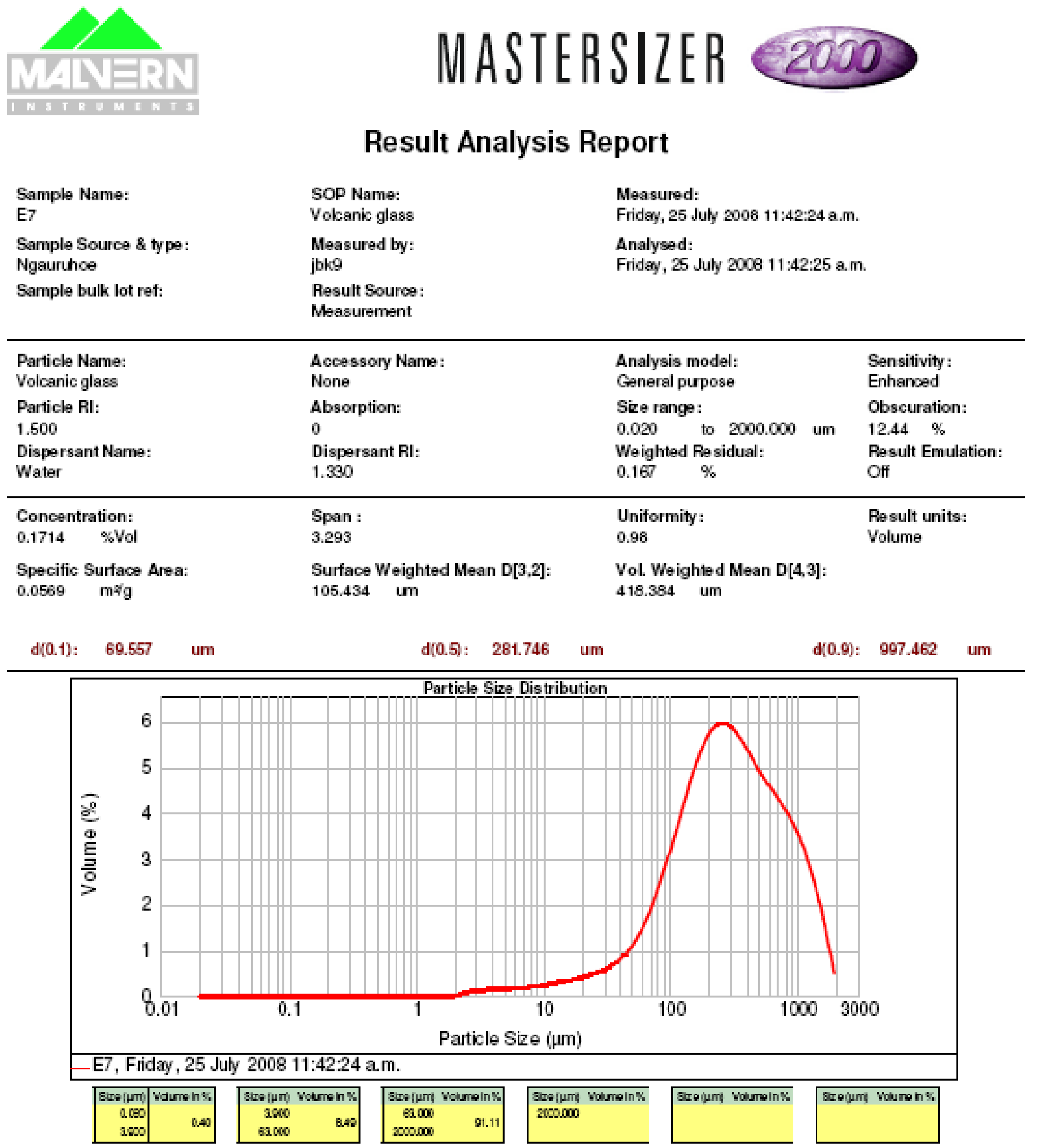

Result Analysis Report

| | | | |
|---|---|---|---|
| **Sample Name:**<br>E7 | **SOP Name:**<br>Volcanic glass | **Measured:**<br>Friday, 25 July 2008 11:42:24 a.m. | |
| **Sample Source & type:**<br>Ngauruhoe | **Measured by:**<br>jbk9 | **Analysed:**<br>Friday, 25 July 2008 11:42:25 a.m. | |
| **Sample bulk lot ref:** | **Result Source:**<br>Measurement | | |
| **Particle Name:**<br>Volcanic glass | **Accessory Name:**<br>None | **Analysis model:**<br>General purpose | **Sensitivity:**<br>Enhanced |
| **Particle RI:**<br>1.500 | **Absorption:**<br>0 | **Size range:**<br>0.020 to 2000.000 um | **Obscuration:**<br>12.44 % |
| **Dispersant Name:**<br>Water | **Dispersant RI:**<br>1.330 | **Weighted Residual:**<br>0.167 % | **Result Emulation:**<br>Off |
| **Concentration:**<br>0.1714 %Vol | **Span :**<br>3.293 | **Uniformity:**<br>0.98 | **Result units:**<br>Volume |
| **Specific Surface Area:**<br>0.0569 m²/g | **Surface Weighted Mean D[3,2]:**<br>105.434 um | **Vol. Weighted Mean D[4,3]:**<br>418.384 um | |

d(0.1): 69.557 um d(0.5): 281.746 um d(0.9): 997.462 um

| Size (µm) | Volume In % |
|---|---|
| 0.020<br>3.900 | 0.40 |

| Size (µm) | Volume In % |
|---|---|
| 3.900<br>63.000 | 8.49 |

| Size (µm) | Volume In % |
|---|---|
| 63.000<br>2000.000 | 91.11 |

| Size (µm) | Volume In % |
|---|---|
| 2000.000 | |

| Size (µm) | Volume In % |
|---|---|
| | |

| Size (µm) | Volume In % |
|---|---|
| | |

**Figure A2.9:** Laser sizer results for F4

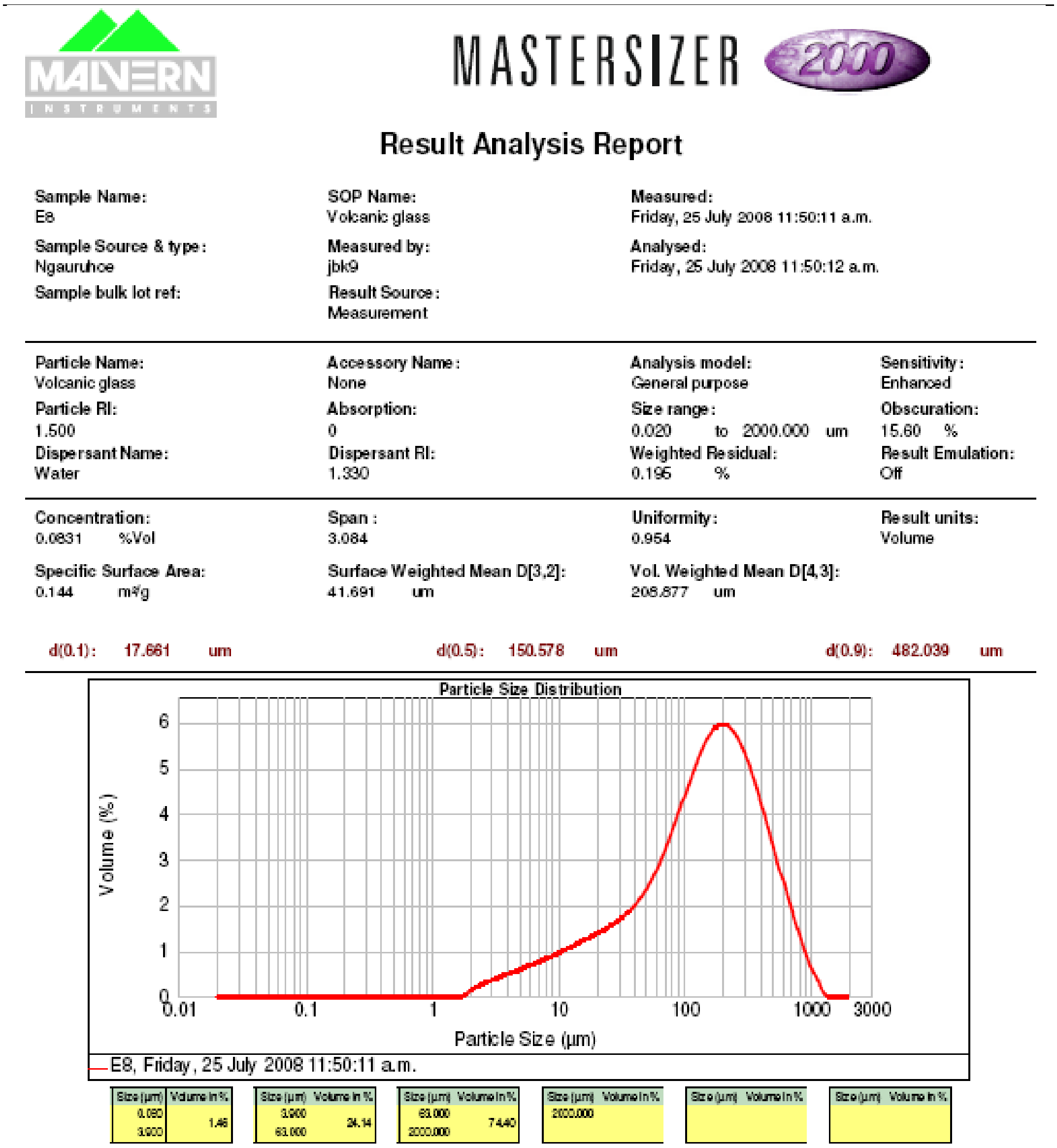

MALVERN INSTRUMENTS

MASTERSIZER 2000

Result Analysis Report

**Sample Name:** E8

**Sample Source & type:** Ngauruhoe

**Sample bulk lot ref:**

**SOP Name:** Volcanic glass

**Measured by:** jbk9

**Result Source:** Measurement

**Measured:** Friday, 25 July 2008 11:50:11 a.m.

**Analysed:** Friday, 25 July 2008 11:50:12 a.m.

**Particle Name:** Volcanic glass

**Particle RI:** 1.500

**Dispersant Name:** Water

**Accessory Name:** None

**Absorption:** 0

**Dispersant RI:** 1.330

**Analysis model:** General purpose

**Size range:** 0.020 to 2000.000 um

**Weighted Residual:** 0.195 %

**Sensitivity:** Enhanced

**Obscuration:** 15.60 %

**Result Emulation:** Off

**Concentration:** 0.0831 %Vol

**Specific Surface Area:** 0.144 m²/g

**Span :** 3.084

**Surface Weighted Mean D[3,2]:** 41.691 um

**Uniformity:** 0.954

**Vol. Weighted Mean D[4,3]:** 208.877 um

**Result units:** Volume

d(0.1): 17.661 um d(0.5): 150.578 um d(0.9): 482.039 um

| Size (µm) | Volume In % | Size (µm) | Volume In % | Size (µm) | Volume In % | Size (µm) | Volume In % | Size (µm) | Volume In % | Size (µm) | Volume In % |
|---|---|---|---|---|---|---|---|---|---|---|---|
| 0.020<br>3.900 | 1.46 | 3.900<br>63.000 | 24.14 | 63.000<br>2000.000 | 74.40 | 2000.000 | | | | | |

**Figure A2.10:** Laser sizer results for F5

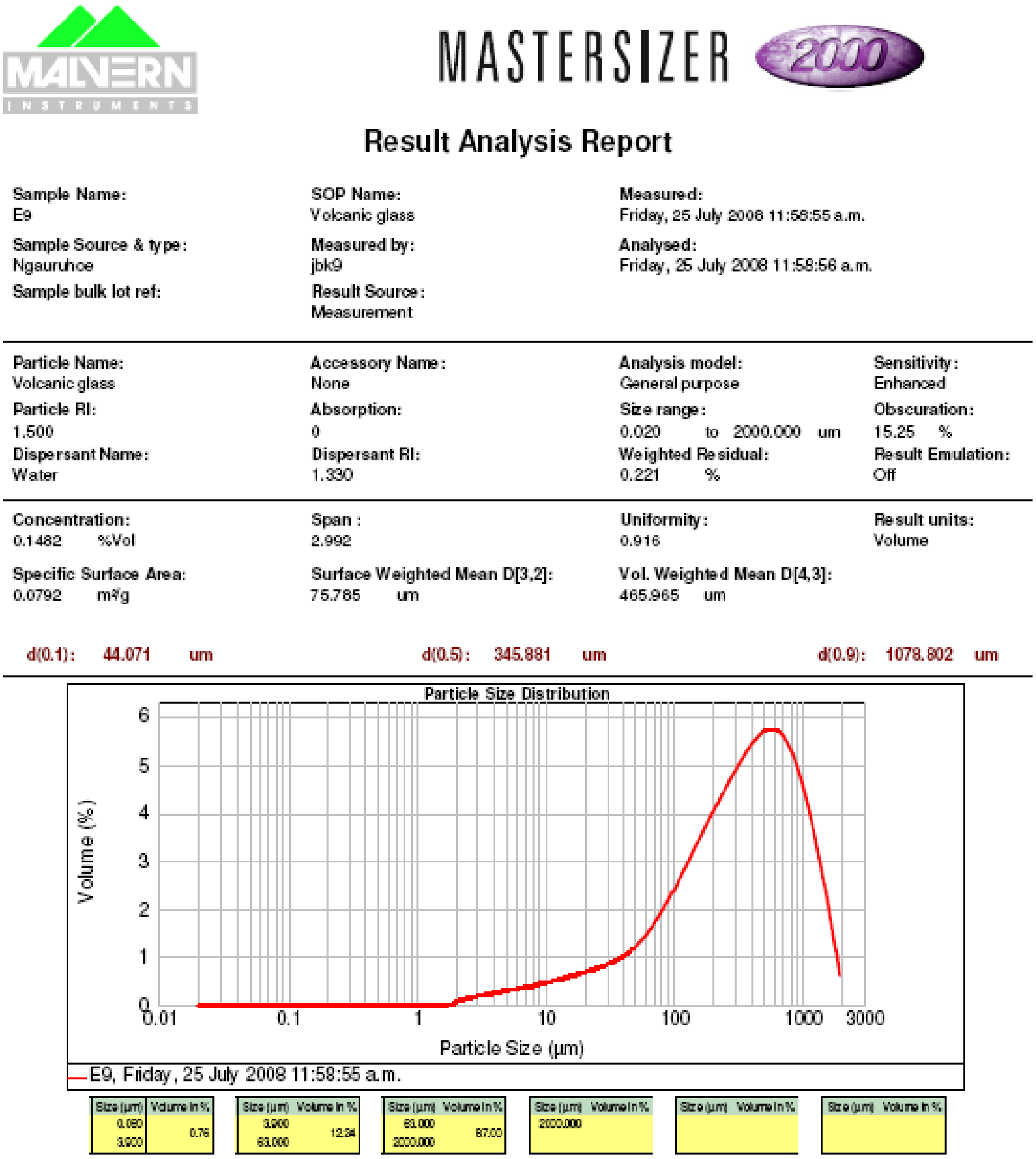

MASTERSIZER 2000

Result Analysis Report

**Sample Name:**
E9

**Sample Source & type:**
Ngauruhoe

**Sample bulk lot ref:**

**SOP Name:**
Volcanic glass

**Measured by:**
jbk9

**Result Source:**
Measurement

**Measured:**
Friday, 25 July 2008 11:58:55 a.m.

**Analysed:**
Friday, 25 July 2008 11:58:56 a.m.

**Particle Name:**
Volcanic glass

**Particle RI:**
1.500

**Dispersant Name:**
Water

**Accessory Name:**
None

**Absorption:**
0

**Dispersant RI:**
1.330

**Analysis model:**
General purpose

**Size range:**
0.020 to 2000.000 um

**Weighted Residual:**
0.221 %

**Sensitivity:**
Enhanced

**Obscuration:**
15.25 %

**Result Emulation:**
Off

**Concentration:**
0.1482 %Vol

**Specific Surface Area:**
0.0792 m²/g

**Span :**
2.992

**Surface Weighted Mean D[3,2]:**
75.765 um

**Uniformity:**
0.916

**Vol. Weighted Mean D[4,3]:**
465.965 um

**Result units:**
Volume

d(0.1): 44.071 um d(0.5): 345.881 um d(0.9): 1078.802 um

| Size (µm) | Volume In % |
|---|---|
| 0.020<br>3.900 | 0.76 |

| Size (µm) | Volume In % |
|---|---|
| 3.900<br>63.000 | 12.24 |

| Size (µm) | Volume In % |
|---|---|
| 63.000<br>2000.000 | 87.00 |

| Size (µm) | Volume In % |
|---|---|
| 2000.000 | |

| Size (µm) | Volume In % |
|---|---|
| | |

| Size (µm) | Volume In % |
|---|---|
| | |

**Figure A2.11:** Laser sizer results for F6

# Appendix Three:

# List of Samples and Analyses

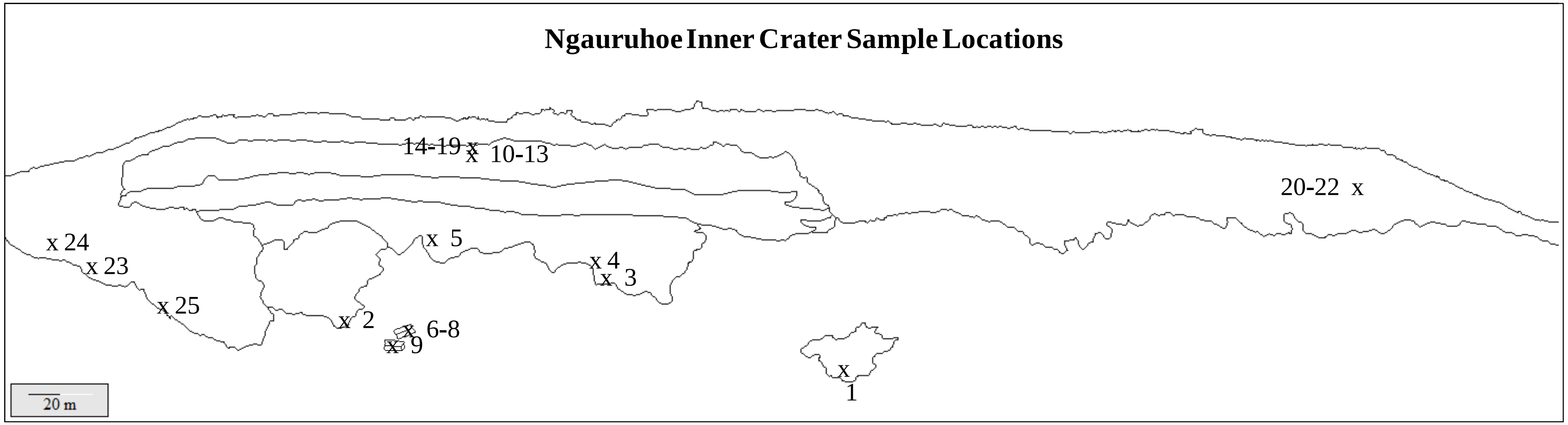

**Table A3.1:** Location and sample data and analysis for each sample used in this study. (TS) Thin Section, (EMP) Electron Microprobe, (XRF) X-Ray Fluorescence, (XRD) X-Ray Diffraction, (SV) Sieve, (LS) Laser Sizer, (P) Pycnometer, (SEM) Scanning Electron Microprobe, (PC) Point Counting.

| | | | | Analysis Undertaken | | | | | | | | | | | |
|---|---|---|---|---|---|---|---|---|---|---|---|---|---|---|---|
| **Sample ID** | **Waikato #** | **Map #** | **Unit** | **TS** | **EMP** | **XRF** | **XRD** | **SV** | **LS** | **P** | **SEM** | **PC** | **Material** | **Height from base (m)** | **Notes** |
| A1c | 20090301 | 1 | A | Y | Y | Y | N | N | N | N | Y | Y | Scoria | 1 | Unit A southern deposit clast |
| A3 | 20090302 | 2 | A | Y | N | Y | Y | N | N | N | N | Y | Lava | 1 | Unit A northern deposit clastogenic lava |
| B1a | 20090303 | 3 | B | Y | Y | Y | N | Y | N | Y | Y | Y | Scoria | 1.5 | Loose scoriaceous clast |
| B1aMid | 20090304 | 4 | B | Y | N | N | N | N | Y | N | N | Y | Scoria | 3 | Loose scoriaceous clast |
| B5 | 20090305 | 5 | B | Y | N | Y | N | N | N | N | Y | Y | Scoria | 3 | Deformed fluidal scoriaceous bomb |
| C1a | 20090306 | 6 | C | Y | N | Y | N | N | N | N | N | Y | Scoria | 0 | Base of detached columnar jointed block |
| C1b | 20090307 | 7 | C | Y | Y | Y | N | N | N | N | N | Y | Lava | 0.6 | Middle of detached columnar jointed block |
| C1c | 20090308 | 8 | C | Y | N | Y | N | N | N | N | Y | Y | Scoria | 1.5 | Top of detached columnar jointed block |
| C2a | 20090309 | 9 | C | Y | N | N | N | N | N | N | N | Y | Scoria | 0 | Base of 2nd detached columnar jointed block |

**Table A3.2:** Location and sample data and analysis for each sample used in this study, continued

| Sample ID | Waikato # | Map # | Unit | TS | EMP | XRF | XRD | SV | LS | P | SEM | PC | Material | Height from base (m) | Notes |
|---|---|---|---|---|---|---|---|---|---|---|---|---|---|---|---|
| D1 | 20090310 | 10 | D | Y | Y | Y | Y | N | N | N | Y | N | Scoria | 2 m (from top) | Clast from gypsum-rich portion of Unit D |
| D2a | 20090311 | 11 | D | Y | N | Y | N | Y | N | N | Y | N | Scoria | 0.6 (from top) | Bedded ash from the top of Unit D |
| D2b | 20090312 | 12 | D | Y | N | N | N | N | N | N | N | N | Scoria | 0.4 (from top) | Bedded ash from the top of Unit D |
| D2c | 20090313 | 13 | D | Y | N | N | N | N | N | N | N | N | Scoria | 0.2 (from top) | Bedded ash from the top of Unit D |
| E | 20090314 | 14 | E | Y | N | Y | N | N | Y | N | Y | N | Ash | 0 | Thin vulcanian ash deposit |
| F1 | 20090315 | 15 | F | Y | N | Y | N | N | Y | N | N | N | Ash | 0 | Vulcanian ash bed |
| F2 | 20090316 | 16 | F | Y | N | Y | N | N | Y | N | N | N | Ash | 0 | Vulcanian ash bed |
| F3 | 20090317 | 17 | F | Y | Y | Y | N | Y | Y | N | N | N | Ash | 0 | Vulcanian ash bed |
| F4 | 20090318 | 18 | F | Y | N | Y | N | N | Y | N | N | N | Ash | 0 | Vulcanian ash bed |
| F5 | 20090319 | 19 | F | Y | N | Y | N | N | Y | N | N | N | Ash | 0 | Vulcanian ash bed |
| F6 | 20090320 | 20 | F | Y | N | Y | N | N | Y | N | Y | N | Ash | 0 | Vulcanian ash bed |
| G1a | 20090321 | 21 | G | Y | N | N | N | N | N | N | N | Y | Spatter | 1.8 | Spatter clast from NW crater rim |
| G1b | 20090322 | 22 | G | Y | Y | Y | N | N | N | N | Y | Y | Spatter | 5 | Spatter clast from NW crater rim |
| G1c | 20090323 | 23 | G | Y | N | N | N | N | N | N | N | Y | Spatter | 8 | Spatter clast from NW crater rim |
| GA | 20090324 | 24 | G | Y | N | Y | N | N | N | N | N | Y | Lava | Mid lava | Unit G clastogenic lava flow |
| GB | 20090325 | 25 | G | Y | N | Y | N | N | N | N | N | Y | Lava | Upper lava | Unit G clastogenic lava flow |
| GC | 20090326 | 26 | G | Y | N | Y | N | N | N | N | N | Y | Lava | Base | Unit G clastogenic lava flow |
| Bb2 | 20090327 | N/A | Lava Flow | Y | N | N | N | N | N | N | Y | N | Xenolith | N/A | From June 30, 1954 aá lava flow on NW flanks |

# Appendix Four:

# Electron Microprobe Analyses of Mineral Compositions

**Table A4.2:** Electron Microprobe analyses of Ngauruhoe inner crater rocks, see Table 4.1 for thin section locations. (plag) plagioclase, (cpx.) clinopyroxene, (opx.) orthopyroxene. (ol) olivine, (qzite) quartzofeldspathic xenolith.

| | EMP ID | $SiO_2$ | $TiO_2$ | Al2O$_3$ | FeO | MnO | MgO | CaO | $Na_2O$ | $K_2O$ | $P_2O_5$ | $SO_3$ | Cl | $Cr_2O_3$ | NiO | TOTAL |
|---|---|---|---|---|---|---|---|---|---|---|---|---|---|---|---|---|
| A1c2 Plag core | 5203 | 47.55 | -0.03 | 32.33 | 0.49 | 0.11 | 0 | 16.68 | 1.89 | 0.19 | -0.05 | -0.1 | 0.02 | 0 | -0.06 | 99.02 |
| A1c3 plag core | 5224 | 48.01 | 0 | 32.61 | 0.59 | 0.04 | 0 | 16.16 | 2.11 | 0.25 | 0.02 | 0.01 | 0.03 | 0.14 | 0 | 99.97 |
| A1c7 plag core | 5228 | 48.75 | 0 | 31.85 | 0.41 | 0.07 | 0 | 15.74 | 2.49 | 0.16 | 0 | 0 | 0 | 0.13 | 0.05 | 99.64 |
| A1c10 plag core | 5236 | 46.65 | -0.09 | 33.33 | 0.43 | 0.07 | 0.12 | 17.51 | 1.56 | 0.1 | -0.02 | 0.07 | 0.02 | 0.04 | -0.02 | 99.77 |
| A1c11 plag core | 5237 | 52.47 | 0.05 | 29.11 | 0.75 | 0.01 | 0 | 13.23 | 3.76 | 0.25 | 0.02 | -0.11 | -0.01 | 0.1 | -0.1 | 99.53 |
| A1c14 plag core | 5240 | 47.55 | 0.04 | 32.85 | 0.61 | 0.04 | -0.05 | 16.86 | 1.68 | 0.06 | 0.1 | -0.01 | 0.02 | 0.18 | 0.16 | 100.1 |
| B1a1 plag core | 5204 | 51.16 | 0.01 | 29.54 | 0.59 | 0 | 0.06 | 13.45 | 3.76 | 0.24 | 0.2 | 0.07 | 0.01 | 0.15 | 0.09 | 99.34 |
| B1a3 plag core | 5206 | 46.83 | -0.02 | 32.69 | 0.69 | 0.03 | 0.01 | 17.04 | 1.74 | 0.14 | 0.08 | 0.07 | 0.08 | 0.06 | -0.03 | 99.42 |
| B1a6 plag core | 5209 | 49.29 | -0.02 | 31.05 | 0.48 | 0 | -0.03 | 14.86 | 2.61 | 0.23 | -0.07 | 0.05 | 0.01 | 0.09 | -0.06 | 98.49 |
| B1a6 plag rim | 5210 | 52.37 | 0.11 | 28.88 | 0.68 | 0.11 | 0 | 12.98 | 3.96 | 0.29 | -0.09 | 0.02 | 0.03 | 0 | 0.1 | 99.44 |
| B1a12 plag core | 5216 | 47.68 | 0 | 32.79 | 0.45 | -0.01 | 0.11 | 16.66 | 1.95 | 0.2 | 0 | 0.06 | 0.01 | 0.18 | -0.1 | 99.99 |
| B1a13 plag core | 5217 | 47.11 | -0.03 | 33.1 | 0.52 | -0.01 | -0.01 | 17.03 | 1.67 | 0.19 | -0.03 | -0.04 | -0.02 | 0.07 | 0.23 | 99.78 |
| B1a17 plag core | 5221 | 50.85 | 0.09 | 30.2 | 0.77 | 0.05 | 0.06 | 14.23 | 3.36 | 0.32 | -0.09 | -0.01 | -0.01 | -0.02 | 0 | 99.79 |
| C1b4 plag core | 5264 | 47.79 | 0.05 | 32.1 | 0.68 | 0.1 | 0.03 | 16.14 | 2.19 | 0.18 | 0.02 | 0.04 | 0.02 | 0 | -0.02 | 99.32 |
| C1b4 plag core2 | 5265 | 55.38 | 0.07 | 27.43 | 0.57 | 0.05 | 0.04 | 10.97 | 5.01 | 0.43 | 0.15 | -0.04 | -0.01 | 0.01 | 0.14 | 100.2 |
| C1b4 plag rim | 5266 | 52.17 | -0.05 | 29.33 | 0.72 | 0.03 | -0.04 | 13.06 | 3.85 | 0.28 | 0.01 | 0.11 | 0 | 0.11 | 0.18 | 99.79 |
| C1b6 plag core | 5268 | 46.46 | -0.1 | 33.36 | 0.41 | 0.05 | -0.06 | 17.38 | 1.46 | 0.13 | -0.13 | -0.03 | 0.01 | 0.01 | -0.02 | 98.94 |
| C1b7 plag core | 5269 | 48.66 | 0.07 | 32.06 | 0.58 | -0.02 | -0.01 | 15.92 | 2.17 | 0.21 | 0 | -0.05 | 0.07 | 0 | 0.09 | 99.73 |
| C1b8 plag core | 5271 | 49.4 | -0.01 | 31.14 | 0.7 | 0.04 | -0.04 | 15.07 | 2.75 | 0.19 | -0.06 | 0 | -0.01 | -0.03 | 0.03 | 99.17 |
| C1b9 plag core | 5272 | 52.93 | 0.15 | 28.45 | 0.53 | -0.05 | 0.06 | 12.19 | 4.18 | 0.34 | -0.11 | 0.14 | 0 | 0.01 | 0.15 | 98.97 |

**Table A4.2:** Electron Microprobe analyses of Ngauruhoe inner crater rocks continued.

|  | EMP ID | $SiO_2$ | $TiO_2$ | $Al_2O_3$ | FeO | MnO | MgO | CaO | $Na_2O$ | K2O | $P_2O_5$ | $SO_3$ | Cl | $Cr_2O_3$ | NiO | TOTAL |
|---|---|---|---|---|---|---|---|---|---|---|---|---|---|---|---|---|
| C1b10 plag core | 5273 | 49.09 | 0.11 | 31.85 | 0.74 | -0.06 | -0.02 | 15.67 | 2.71 | 0.21 | 0.02 | -0.03 | -0.03 | -0.04 | 0.15 | 100.4 |
| C1b15 plag core | 5279 | 47.54 | -0.12 | 32.54 | 0.59 | -0.07 | -0.05 | 16.64 | 1.97 | 0.15 | 0 | -0.04 | -0.01 | 0.07 | 0.17 | 99.37 |
| D12 plag core | 5242 | 55.07 | 0.59 | 4.66 | 11.17 | 0.37 | 10.85 | 15.25 | 0.71 | 0.8 | 0.22 | -0.08 | 0.07 | 0.05 | 0.15 | 99.86 |
| D15 plag core | 5245 | 46.7 | 0.01 | 33.07 | 0.45 | -0.09 | 0.01 | 16.86 | 1.59 | 0.2 | 0 | -0.07 | 0.07 | 0.02 | 0.25 | 99.08 |
| D15 plag rim | 5246 | 46.94 | -0.02 | 32.68 | 0.56 | 0.05 | 0.05 | 16.98 | 1.67 | 0.2 | -0.09 | -0.14 | 0.05 | 0.05 | -0.05 | 98.93 |
| D111 plag core | 5252 | 47.6 | -0.08 | 32.62 | 0.67 | 0.05 | 0.01 | 16.62 | 2 | 0.19 | 0.05 | 0.07 | 0.01 | 0.13 | -0.11 | 99.86 |
| D116 plag core | 5258 | 49.14 | 0.01 | 31.2 | 0.65 | 0.14 | 0.07 | 15.35 | 2.5 | 0.21 | -0.04 | -0.01 | -0.02 | -0.11 | -0.03 | 99.05 |
| D118 plag core | 5260 | 50.58 | 0.08 | 29.72 | 0.8 | -0.04 | -0.03 | 13.96 | 3.33 | 0.27 | -0.07 | -0.06 | 0 | 0.01 | -0.01 | 98.54 |
| D118 plag core | 5260 | 50.58 | 0.08 | 29.72 | 0.8 | -0.04 | -0.03 | 13.96 | 3.33 | 0.27 | -0.07 | -0.06 | 0 | 0.01 | -0.01 | 98.54 |
| D118 plag core | 5260 | 50.58 | 0.08 | 29.72 | 0.8 | -0.04 | -0.03 | 13.96 | 3.33 | 0.27 | -0.07 | -0.06 | 0 | 0.01 | -0.01 | 98.54 |
| D118 plag core | 5260 | 50.58 | 0.08 | 29.72 | 0.8 | -0.04 | -0.03 | 13.96 | 3.33 | 0.27 | -0.07 | -0.06 | 0 | 0.01 | -0.01 | 98.54 |
| E52 plag core | 5299 | 48.43 | -0.02 | 31.62 | 0.61 | -0.11 | 0.05 | 15.8 | 2.25 | 0.17 | -0.16 | -0.01 | 0.03 | 0.07 | 0.09 | 98.84 |
| E58 plag core | 5305 | 46.93 | 0.16 | 33 | 0.69 | 0.08 | 0.04 | 17.11 | 1.59 | 0.1 | 0.08 | 0.03 | 0 | 0.14 | -0.12 | 99.83 |
| E511 plag core | 5309 | 49.57 | 0.03 | 31.23 | 0.58 | 0.02 | 0.08 | 15.12 | 2.8 | 0.23 | -0.15 | -0.04 | -0.03 | 0.04 | 0.2 | 99.67 |
| E511 plag rim | 5310 | 52.34 | -0.06 | 29.1 | 0.67 | -0.02 | 0.06 | 13.07 | 3.83 | 0.27 | -0.02 | 0 | 0.06 | 0.09 | -0.04 | 99.34 |
| E512 plag core | 5311 | 54.46 | 0.05 | 27.99 | 0.55 | 0.1 | 0.08 | 11.28 | 4.63 | 0.26 | 0.06 | 0.08 | 0.02 | 0.01 | -0.01 | 99.57 |
| E514 plag core | 5313 | 53.44 | 0.05 | 29.05 | 0.61 | 0.1 | 0.07 | 12.32 | 4.37 | 0.31 | 0 | -0.02 | 0.01 | 0.03 | 0.17 | 100.5 |
| E516 plag core1 | 5315 | 48.48 | -0.02 | 31.72 | 0.58 | -0.04 | -0.05 | 15.56 | 2.26 | 0.18 | -0.07 | -0.09 | -0.01 | -0.02 | 0.1 | 98.59 |
| E516 plag core2 | 5316 | 54.32 | 0.05 | 27.6 | 0.65 | 0.01 | 0.12 | 11.24 | 4.79 | 0.35 | 0.08 | 0.01 | 0.05 | -0.06 | 0.02 | 99.22 |
| E516 plag rim | 5317 | 54.03 | 0.09 | 28.36 | 0.74 | 0.12 | 0.11 | 11.64 | 4.63 | 0.41 | -0.01 | -0.02 | 0.01 | -0.04 | 0 | 100.1 |
| E518 plag core | 5318 | 54.71 | 0 | 27.72 | 0.59 | -0.02 | 0.06 | 11.16 | 4.88 | 0.42 | -0.06 | 0.01 | -0.02 | 0.05 | -0.14 | 99.35 |

**Table A4.3:** Electron Microprobe analyses of Ngauruhoe inner crater rocks continued.

|  | EMP ID | $SiO_2$ | $TiO_2$ | $Al_2O_3$ | FeO | MnO | MgO | CaO | $Na_2O$ | $K_2O$ | $P_2O_5$ | $SO_3$ | Cl | $Cr_2O_3$ | NiO | TOTAL |
|---|---|---|---|---|---|---|---|---|---|---|---|---|---|---|---|---|
| E518 plag core | 5318 | 54.71 | 0 | 27.72 | 0.59 | -0.02 | 0.06 | 11.16 | 4.88 | 0.42 | -0.06 | 0.01 | -0.02 | 0.05 | -0.14 | 99.35 |
| E518 plag core | 5318 | 54.71 | 0 | 27.72 | 0.59 | -0.02 | 0.06 | 11.16 | 4.88 | 0.42 | -0.06 | 0.01 | -0.02 | 0.05 | -0.14 | 99.35 |
| E518 plag core | 5318 | 54.71 | 0 | 27.72 | 0.59 | -0.02 | 0.06 | 11.16 | 4.88 | 0.42 | -0.06 | 0.01 | -0.02 | 0.05 | -0.14 | 99.35 |
| F1b1 plag core | 5281 | 47.3 | 0.08 | 33.36 | 0.61 | 0.01 | -0.08 | 16.87 | 1.8 | 0.17 | 0.13 | -0.07 | 0.06 | 0.01 | -0.15 | 100.1 |
| F1b1 plag core2 | 5282 | 52.4 | 0.04 | 28.9 | 0.86 | -0.06 | 0 | 12.84 | 3.83 | 0.32 | 0.06 | -0.01 | 0 | 0.07 | 0.23 | 99.5 |
| F1b1 plag rim | 5283 | 51.22 | 0.06 | 29.72 | 0.68 | 0.05 | 0.13 | 13.63 | 3.39 | 0.28 | -0.02 | 0.04 | 0.06 | 0.09 | -0.07 | 99.26 |
| F1b1 plag core | 5284 | 53.42 | 0.01 | 28.54 | 0.69 | 0.08 | 0.01 | 11.93 | 4.28 | 0.32 | 0.01 | -0.09 | -0.01 | 0.03 | 0.02 | 99.26 |
| F1b7 plag core | 5289 | 50.82 | 0.07 | 30.14 | 0.77 | 0 | -0.02 | 14.1 | 3.36 | 0.24 | -0.02 | -0.07 | -0.04 | 0.09 | 0.02 | 99.45 |
| F1b8 plag core | 5290 | 51.75 | 0.12 | 29.3 | 0.68 | -0.06 | 0.08 | 13.27 | 3.89 | 0.24 | -0.08 | -0.13 | 0.05 | 0 | -0.04 | 99.08 |
| F1b11 plag core | 5293 | 46.77 | -0.02 | 32.97 | 0.54 | 0.07 | -0.04 | 17.21 | 1.67 | 0.08 | -0.11 | -0.03 | -0.04 | 0.01 | -0.03 | 99.04 |
| F1b12 plag core | 5294 | 49.34 | 0.19 | 26.07 | 4.9 | 0.21 | 2.47 | 14.69 | 1.86 | 0.25 | 0.14 | 0.05 | 0.06 | 0 | 0.08 | 100.3 |
| F1b12 plag core2 | 5295 | 50.89 | -0.1 | 30.49 | 0.48 | 0.08 | 0.07 | 14.31 | 3.17 | 0.25 | 0.09 | 0.02 | 0.01 | 0.04 | -0.12 | 99.69 |
| A1c5 opx core | 5226 | 49.08 | 0.14 | 2.2 | 33.62 | 0.89 | 13.71 | 0.19 | 0 | 0.01 | 0 | 0 | 0 | 0 | 0 | 99.84 |
| A1c6 opx core | 5227 | 53.57 | 0.43 | 1.09 | 20.14 | 0.44 | 23.14 | 2.05 | 0 | 0.04 | 0 | 0 | 0.02 | 0 | 0 | 100.9 |
| A1c8 opx c in cpx | 5232 | 53.07 | 0.43 | 1.39 | 20.67 | 0.32 | 22.87 | 1.99 | 0 | 0.06 | 0.07 | -0.02 | -0.01 | 0.04 | -0.01 | 100.9 |
| A1c13 opx core | 5239 | 53.65 | 0.37 | 2.38 | 19.17 | 0.46 | 21.58 | 2.05 | 0.19 | 0.16 | 0.04 | 0.02 | -0.02 | 0.04 | -0.19 | 99.89 |
| B1a2 opx core | 5205 | 53.95 | 0.27 | 1.05 | 18.42 | 0.43 | 24.19 | 1.91 | 0.17 | 0.11 | -0.02 | 0.07 | -0.03 | 0.12 | -0.2 | 100.4 |
| B1a5 opx core | 5208 | 52.85 | 0.23 | 2.08 | 20.09 | 0.58 | 22.93 | 1.49 | 0.03 | 0 | -0.06 | 0.06 | 0 | 0.01 | -0.22 | 100.1 |
| B1a7 opx core | 5211 | 53.64 | 0.22 | 2.02 | 16.64 | 0.37 | 25.72 | 1.75 | -0.04 | 0.08 | 0.01 | 0.06 | 0 | -0.04 | 0.05 | 100.5 |
| B1a8 opx core | 5212 | 53.73 | 0.29 | 2.14 | 16.9 | 0.43 | 25.23 | 1.44 | 0.01 | 0.13 | 0.04 | 0.07 | 0.05 | -0.02 | 0.12 | 100.6 |

**Table A4.4:** Electron Microprobe analyses of Ngauruhoe inner crater rocks continued.

| | EMP ID | $SiO_2$ | $TiO_2$ | $Al2O_3$ | FeO | MnO | MgO | CaO | Na2O | K2O | $P_2O_5$ | $SO_3$ | Cl | $Cr_2O_3$ | NiO | TOTAL |
|---|---|---|---|---|---|---|---|---|---|---|---|---|---|---|---|---|
| B1a9 opx core | 5213 | 54.16 | 0.14 | 1.26 | 17.65 | 0.33 | 25.21 | 1.79 | -0.03 | 0.01 | 0 | -0.06 | 0.06 | 0.07 | -0.11 | 100.5 |
| B1a11 opx core | 5215 | 53.61 | 0.33 | 1.76 | 17.8 | 0.37 | 24.57 | 1.8 | -0.04 | 0.06 | 0.04 | 0.05 | -0.02 | 0.02 | 0.03 | 100.4 |
| B1a14 opx core | 5218 | 53.53 | 0.34 | 1.19 | 19.45 | 0.39 | 23.13 | 2 | 0.01 | 0.01 | 0.17 | 0.11 | 0.02 | 0.05 | -0.03 | 100.4 |
| B1a15 opx core | 5219 | 55.22 | 0.27 | 3.06 | 15.8 | 0.51 | 23.39 | 1.73 | 0.46 | 0.33 | 0.19 | 0.11 | 0.07 | -0.01 | 0.09 | 101.2 |
| C1b2 opx core | 5262 | 53.63 | 0.15 | 1.24 | 20.43 | 0.45 | 23.15 | 1.54 | -0.06 | 0.09 | -0.13 | -0.03 | 0 | 0 | -0.18 | 100.3 |
| C1b3 opx core | 5263 | 54.96 | 0.29 | 1.58 | 14.54 | 0.37 | 27.11 | 1.85 | -0.11 | 0.04 | -0.08 | 0.01 | 0.01 | -0.04 | 0.03 | 100.6 |
| C1b5 opx core | 5267 | 53.45 | 0.25 | 1.25 | 19.19 | 0.43 | 23.44 | 1.82 | 0.15 | 0.01 | 0.04 | 0.02 | -0.02 | 0.17 | 0.21 | 100.4 |
| C1b8 opx core | 5270 | 54.16 | 0.22 | 1.87 | 16.43 | 0.27 | 25.74 | 1.71 | 0 | 0 | -0.06 | 0.08 | 0 | 0.15 | -0.01 | 100.5 |
| C1b11a opx core | 5274 | 55.09 | 0.14 | 2.48 | 13.42 | 0.4 | 28.25 | 1.77 | -0.1 | 0.05 | 0 | -0.03 | -0.05 | 0.09 | -0.02 | 101.5 |
| C1b13 opx core | 5277 | 54.41 | 0.29 | 0.85 | 17.84 | 0.48 | 24.78 | 1.97 | -0.07 | 0.07 | 0.02 | -0.01 | -0.01 | -0.05 | 0.1 | 100.7 |
| C1b14 opx core | 5278 | 54.45 | 0.32 | 1.63 | 17.1 | 0.37 | 25.46 | 1.51 | -0.04 | 0.04 | -0.09 | 0.01 | 0.01 | 0.02 | -0.08 | 100.7 |
| D11 opx core | 5241 | 54.15 | 0.22 | 2 | 15.55 | 0.41 | 26.3 | 1.71 | -0.05 | 0.09 | 0.05 | -0.14 | -0.04 | 0.03 | -0.12 | 100.2 |
| D18 opx core | 5249 | 53.25 | 0.37 | 1.68 | 17.69 | 0.46 | 24.13 | 1.9 | -0.06 | 0.03 | 0.12 | -0.02 | 0 | 0.04 | -0.07 | 99.53 |
| D19 opx core | 5250 | 54 | 0.41 | 1.32 | 15.64 | 0.33 | 26.24 | 1.77 | -0.1 | 0.07 | -0.04 | 0.08 | 0.01 | 0.09 | 0.07 | 99.89 |
| D110 opx core | 5251 | 53.84 | 0.18 | 1.44 | 18.13 | 0.46 | 25.01 | 1.54 | -0.07 | 0.04 | -0.04 | 0.14 | -0.03 | 0 | -0.01 | 100.6 |
| D112 opx core | 5253 | 55.37 | 0.03 | 1.79 | 12.47 | 0.29 | 28.72 | 1.72 | -0.11 | 0.13 | 0.09 | -0.04 | 0.03 | 0.23 | -0.01 | 100.7 |
| D115 opx rim | 5257 | 53.54 | 0.11 | 1.19 | 19.63 | 0.49 | 23.53 | 1.49 | 0.05 | 0.09 | 0.07 | -0.02 | 0.05 | -0.03 | 0.07 | 100.3 |
| D117 opx core | 5259 | 54.33 | 0.25 | 2.22 | 14.12 | 0.41 | 27.31 | 1.61 | -0.07 | 0.08 | -0.1 | 0 | -0.01 | 0.03 | -0.01 | 100.2 |
| E54 opx core | 5301 | 53.78 | 0.34 | 1.13 | 18.82 | 0.44 | 23.83 | 2.14 | -0.1 | 0.07 | 0.11 | -0.03 | 0.02 | 0.1 | -0.05 | 100.6 |
| E57 opx core | 5304 | 52.82 | 0.18 | 1.94 | 19.72 | 0.33 | 22.85 | 1.9 | 0.08 | 0.1 | 0.08 | 0.04 | 0.04 | 0.06 | 0.26 | 100.4 |
| E510 opx core | 5307 | 53.18 | 0.26 | 1.76 | 18.69 | 0.47 | 23.84 | 1.63 | -0.12 | 0.07 | -0.04 | -0.05 | -0.04 | 0.23 | -0.01 | 99.88 |

**Table A4.5:** Electron Microprobe analyses of Ngauruhoe inner crater rocks continued.

| | EMP ID | $SiO_2$ | $TiO_2$ | $Al_2O_3$ | FeO | MnO | MgO | CaO | $Na_2O$ | $K_2O$ | $P_2O_5$ | $SO_3$ | Cl | $Cr_2O_3$ | NiO | TOTAL |
|---|---|---|---|---|---|---|---|---|---|---|---|---|---|---|---|---|
| E510 opx core2 | 5308 | 52.86 | 0.22 | 3.13 | 16.97 | 0.29 | 24.7 | 2.03 | 0.05 | 0.12 | 0.07 | -0.03 | 0.02 | 0.11 | -0.04 | 100.5 |
| E513 opx core | 5312 | 53.61 | 0.13 | 2.17 | 14.18 | 0.34 | 26.81 | 1.6 | -0.1 | 0.08 | -0.04 | 0.1 | 0.03 | 0.04 | 0.04 | 99 |
| F1b10 opx core | 5292 | 53.15 | 0.34 | 1.12 | 20.39 | 0.62 | 22.3 | 1.93 | -0.03 | 0.02 | 0.02 | -0.01 | 0.02 | -0.05 | 0.01 | 99.82 |
| A1c1a cpx core | 5223 | 51.15 | 0.38 | 3.02 | 7.09 | 0.13 | 15.99 | 19.42 | 0.27 | 0.15 | 0.19 | 0 | 0.06 | 0.26 | 0.06 | 98.16 |
| A1c4 cpx core | 5225 | 51.35 | 0.35 | 3.09 | 8.71 | 0.21 | 15.66 | 19.72 | 0.31 | 0.07 | 0.06 | 0.01 | 0 | 0.33 | 0.05 | 99.92 |
| A1c8 cpx r on opx | 5233 | 52.14 | 0.53 | 1.64 | 11.47 | 0.36 | 15.64 | 17.77 | 0.04 | 0.07 | -0.05 | 0.06 | 0.01 | 0.09 | 0.23 | 100 |
| A1c9 cpx core | 5234 | 50.78 | 0.58 | 3.51 | 10.14 | 0.3 | 14.67 | 19.08 | 0.21 | 0.09 | -0.1 | 0.01 | 0.06 | 0.25 | 0.02 | 99.59 |
| A1c9 cpx rim | 5235 | 51.8 | 0.69 | 2.2 | 11.93 | 0.3 | 15.4 | 17.67 | 0.08 | 0.04 | -0.04 | -0.06 | -0.02 | 0.11 | 0.1 | 100.2 |
| A1c12 cpx core | 5238 | 51.76 | 0.4 | 2.96 | 9.29 | 0.12 | 15.32 | 19.34 | 0.19 | 0.11 | 0.01 | 0 | 0 | 0.2 | 0.04 | 99.72 |
| B1a4 cpx core | 5207 | 51.73 | 0.62 | 2.2 | 11.28 | 0.11 | 15.12 | 17.94 | 0.3 | 0.04 | 0.01 | 0.11 | 0.07 | 0.17 | 0.01 | 99.7 |
| B1a10 cpx core | 5214 | 51.97 | 0.44 | 3.63 | 6.81 | 0.07 | 16.84 | 19.87 | 0.18 | 0.14 | 0.26 | 0.13 | -0.01 | 0.36 | -0.12 | 100.6 |
| B1a16 cpx core | 5220 | 51.43 | 0.49 | 1.54 | 12.28 | 0.45 | 15.22 | 17.3 | 0.34 | 0.11 | 0.07 | 0.05 | 0.04 | 0.2 | -0.05 | 99.46 |
| C1b1 cpx core | 5261 | 52.17 | 0.35 | 2.88 | 6.61 | 0.13 | 17.24 | 19.67 | 0.16 | 0.09 | 0.1 | -0.01 | -0.01 | 0.44 | 0.09 | 99.93 |
| C1b11b cpx core | 5275 | 53.08 | 0.12 | 28.8 | 0.63 | 0.04 | 0.1 | 12.47 | 4.34 | 0.32 | -0.01 | 0.1 | -0.02 | 0.03 | -0.07 | 99.93 |
| C1b12 cpx core | 5276 | 51.22 | 0.53 | 3.55 | 8.28 | 0.07 | 15.98 | 19.48 | 0.25 | 0.11 | 0.18 | 0.01 | 0.05 | 0.3 | 0.1 | 100.1 |
| C1b16 cpx core | 5280 | 50.55 | 0.71 | 3.24 | 11.8 | 0.28 | 14.24 | 18.94 | 0.24 | 0.04 | -0.01 | -0.03 | -0.01 | 0.49 | 0.1 | 100.6 |
| D13 cpx core | 5243 | 53.01 | 0.21 | 2.72 | 4.7 | 0.12 | 18.31 | 19.33 | 0.13 | 0.11 | 0.1 | -0.04 | 0 | 1.21 | 0.01 | 99.92 |
| D16 cpx core | 5247 | 51.85 | 0.29 | 3.25 | 5.77 | 0.18 | 16.7 | 20.29 | 0.17 | 0.14 | 0.21 | -0.03 | 0.01 | 0.65 | -0.01 | 99.46 |
| D17 cpx core | 5248 | 51.23 | 0.44 | 3.76 | 7.08 | 0.1 | 16.48 | 19.62 | 0.16 | 0.12 | 0.11 | -0.05 | 0.07 | 0.51 | 0.04 | 99.65 |
| D114 cpx core | 5255 | 51.5 | 0.32 | 4.14 | 6.43 | 0.13 | 16.21 | 20.48 | 0.2 | 0.11 | 0.17 | 0.05 | 0.04 | 0.57 | 0 | 100.3 |

**Table A4.6:** Electron Microprobe analyses of Ngauruhoe inner crater rocks continued.

|  | EMP ID | $SiO_2$ | $TiO_2$ | $Al_2O_3$ | FeO | MnO | MgO | CaO | $Na_2O$ | $K_2O$ | $P_2O_5$ | $SO_3$ | Cl | $Cr_2O_3$ | NiO | TOTAL |
|---|---|---|---|---|---|---|---|---|---|---|---|---|---|---|---|---|
| E51 cpx core | 5297 | 52.14 | 0.28 | 3.38 | 6.45 | 0.15 | 16.22 | 20.7 | 0.2 | 0.05 | 0.22 | -0.08 | 0.02 | 0.38 | 0.08 | 100.2 |
| E51 cpx rim | 5298 | 51.15 | 0.64 | 2.05 | 12.72 | 0.36 | 14.66 | 17.64 | 0.23 | 0.02 | 0.24 | -0.03 | 0 | 0.15 | -0.07 | 99.77 |
| E53 cpx core | 5300 | 52.33 | 0.32 | 3.49 | 6.54 | 0.2 | 16.54 | 20.28 | 0.14 | 0.08 | 0.11 | 0.07 | 0.01 | 0.4 | 0.1 | 100.6 |
| E55 cpx core | 5302 | 51.19 | 0.68 | 1.94 | 11.93 | 0.44 | 14.72 | 18.24 | 0.28 | 0.05 | 0.08 | -0.07 | 0 | 0.17 | 0.02 | 99.67 |
| E515 cpx core | 5314 | 52.08 | 0.57 | 2.15 | 9.92 | 0.27 | 15.7 | 18.94 | 0.15 | 0.08 | 0.03 | 0.04 | 0 | 0.22 | -0.08 | 100.1 |
| F1b3 cpx core | 5285 | 52.37 | 0.34 | 3.1 | 5.4 | 0.01 | 17 | 20.51 | 0.08 | 0.07 | 0.07 | -0.05 | 0.02 | 0.39 | 0.09 | 99.39 |
| F1b4 cpx core | 5286 | 53.32 | 0.35 | 1.96 | 18.1 | 0.43 | 24.22 | 1.93 | 0.03 | 0.08 | -0.11 | -0.08 | 0.01 | 0.01 | 0 | 100.3 |
| F1b5 cpx core | 5287 | 51.16 | 0.45 | 3.23 | 7.91 | 0.29 | 15.91 | 20.26 | 0.18 | 0.12 | 0.04 | 0.04 | 0.02 | 0.47 | -0.06 | 100 |
| F1b6 cpx core | 5288 | 52.42 | 0.4 | 2.77 | 7.85 | 0.32 | 16.84 | 19.58 | 0.14 | 0.1 | 0.11 | -0.08 | -0.04 | 0.28 | 0.07 | 100.8 |
| F1b13 cpx core | 5296 | 50.56 | 0.39 | 3.6 | 7.36 | 0.16 | 15.83 | 20.1 | 0.15 | 0.15 | 0.01 | -0.03 | 0.03 | 0.34 | 0.01 | 98.64 |
| A1c1a Qzite core | 5222 | 99.79 | 0 | 0 | 0 | 0 | 0 | 0 | 0 | 0 | 0 | 0 | 0 | 0 | 0 | 99.79 |
| D115 ol core | 5256 | 37.28 | 0 | 0.04 | 31.36 | 0.53 | 31.44 | 0.11 | 0 | 0 | 0.2 | 0.1 | 0.06 | -0.1 | -0.05 | 101 |
| E56 ol core | 5303 | 40.8 | -0.01 | 0.11 | 15.05 | 0.27 | 45.02 | 0.25 | -0.05 | 0.01 | -0.02 | 0.04 | 0 | 0.06 | 0.15 | 101.7 |

# Appendix Five:

# Vesicularity Analyses by Gas Pycnometry

**Table A5.3:** Pycnometer vesicularity data for Unit B, block 1

| **Block 1** | Weight | Standard deviation | Average Volume | Average Density | Bulk Volume | Bulk Density | DRE density | Total Vesicularity | Isolated vesicularity | Connected Vesicularity |
|---|---|---|---|---|---|---|---|---|---|---|
| | 16.8900 | 0.0001 | 5.7376 | 2.9438 | 16.4802 | 1.0249 | 2.9525 | 65.2882 | 64.9935 | 0.2947 |
| **Individual Runs** | | | | | | | | | | |
| Block | Run 1 | Run 2 | Run 3 | Run 4 | Run 5 | Run 6 | Run 7 | Run 8 | | |
| Volume | 5.6363 | 5.6898 | 5.6907 | 5.7111 | 5.7178 | 5.7310 | 5.7355 | 5.7462 | | |
| Weight | 2.9967 | 2.9685 | 2.9680 | 2.9574 | 2.9539 | 2.9471 | 2.9448 | 2.9393 | | |
| Powder | Run 1 | Run 2 | Run 3 | Run 4 | Run 5 | Run 6 | Run 7 | Run 8 | | |
| Volume | 5.8033 | 5.8298 | 5.8525 | 5.8615 | 5.8540 | 5.8680 | 5.8699 | 5.8914 | | |
| Weight | 2.9897 | 2.9761 | 2.9646 | 2.9600 | 2.9638 | 2.9567 | 2.9558 | 2.9450 | | |

DRE = dense rock equivalent, Volume cm³, Density g/cm³

**Table A5.2:** Pycnometer vesicularity data for Unit B, block 2

| **Block 2** | Weight | Standard deviation | Average Volume | Average Density | Bulk Volume | Bulk Density | DRE density | Total Vesicularity | Isolated vesicularity | Connected Vesicularity |
|---|---|---|---|---|---|---|---|---|---|---|
| | 1.9000 | 0.0000 | 0.7695 | 2.4690 | 1.8700 | 1.0160 | 2.5736 | 60.5206 | 56.4562 | 4.0643 |
| **Individual Runs** | | | | | | | | | | |
| Block | Run 1 | Run 2 | Run 3 | Run 4 | Run 5 | Run 6 | Run 7 | Run 8 | | |
| Volume | 0.7574 | 0.7620 | 0.7659 | 0.7662 | 0.7686 | 0.7720 | 0.7682 | 0.7684 | | |
| Weight | 2.5086 | 2.4934 | 2.4808 | 2.4799 | 2.4719 | 2.4612 | 2.4733 | 2.4725 | | |
| Powder | Run 1 | Run 2 | Run 3 | Run 4 | Run 5 | Run 6 | Run 7 | Run 8 | | |
| Volume | 0.6996 | 0.7017 | 0.7023 | 0.7095 | 0.7115 | 0.7154 | 0.7207 | 0.7204 | | |
| Weight | 2.6443 | 2.6366 | 2.6343 | 2.6076 | 2.0030 | 2.5861 | 2.5669 | 2.5679 | | |

DRE = dense rock equivalent, Volume cm³, Density g/cm³

**Table A5.3:** Pycnometer vesicularity data for Unit B, block 3

| **Block 3** | Weight | Standard deviation | Average Volume | Average Density | Bulk Volume | Bulk Density | DRE density | Total Vesicularity | Isolated vesicularity | Connected Vesicularity |
|---|---|---|---|---|---|---|---|---|---|---|
| | 12.6100 | 0.0000 | 4.3650 | 2.8889 | 11.2280 | 1.1231 | 2.6898 | 58.2465 | 65.6486 | -7.4020 |
| **Individual Runs** | | | | | | | | | | |
| Block | Run 1 | Run 2 | Run 3 | Run 4 | Run 5 | Run 6 | | | | |
| Volume | 4.2892 | 4.3272 | 4.3452 | 4.3628 | 4.3655 | 4.3667 | | | | |
| Weight | 2.9399 | 2.9141 | 2.9021 | 2.8903 | 2.8885 | 2.8878 | | | | |
| Powder | Run 1 | Run 2 | Run 3 | Run 4 | Run 5 | Run 6 | Run 7 | Run 8 | | |
| Volume | 4.3577 | 4.3822 | 4.4383 | 4.4458 | 4.4072 | 4.4597 | 4.4649 | 4.4705 | | |
| Weight | 2.7560 | 2.7406 | 2.7015 | 2.7015 | 2.7251 | 2.6930 | 2.6899 | 2.6865 | | |

DRE = dense rock equivalent, Volume cm$^3$, Density g/cm$^3$

**Table A5.4:** Pycnometer vesicularity data for Unit B, block 4

| **Block 4** | Weight | Standard deviation | Average Volume | Average Density | Bulk Volume | Bulk Density | DRE density | Total Vesicularity | Isolated vesicularity | Connected Vesicularity |
|---|---|---|---|---|---|---|---|---|---|---|
| | 15.8900 | 0.0001 | 5.5133 | 2.8821 | 13.2030 | 1.2035 | 2.6843 | 55.1647 | 62.5335 | -7.3688 |
| **Individual Runs** | | | | | | | | | | |
| Block | Run 1 | Run 2 | Run 3 | Run 4 | Run 5 | Run 6 | Run 7 | Run 8 | | |
| Volume | 5.4006 | 5.4442 | 5.4643 | 5.4829 | 5.4927 | 5.5058 | 5.5108 | 5.5233 | | |
| Weight | 2.9423 | 2.9187 | 2.9080 | 2.8981 | 2.8930 | 2.8860 | 2.8834 | 2.8769 | | |
| Powder | Run 1 | Run 2 | Run 3 | Run 4 | Run 5 | Run 6 | Run 7 | Run 8 | | |
| Volume | 5.5403 | 5.7116 | 5.7901 | 6.3136 | 6.0352 | 5.5984 | 5.6097 | 5.9806 | | |
| Weight | 2.7760 | 2.6928 | 2.6563 | 2.4360 | 2.5484 | 2.7472 | 2.7417 | 2.5717 | | |

DRE = dense rock equivalent, Volume cm$^3$, Density g/cm$^3$

**Table A5.5:** Pycnometer vesicularity data for Unit B, block 5

| **Block 5** | Weight | Standard deviation | Average Volume | Average Density | Bulk Volume | Bulk Density | DRE density | Total Vesicularity | Isolated vesicularity | Connected Vesicularity |
|---|---|---|---|---|---|---|---|---|---|---|
| | 6.2900 | 0.0000 | 2.2887 | 2.7483 | 4.5940 | 1.3692 | 2.7841 | 50.8216 | 49.5357 | 1.2859 |
| **Individual Runs** | | | | | | | | | | |
| Block | Run 1 | Run 2 | Run 3 | Run 4 | Run 5 | Run 6 | | | | |
| Volume | 2.2769 | 2.2814 | 2.2833 | 2.2875 | 2.2888 | 2.2899 | | | | |
| Weight | 2.7625 | 2.7571 | 2.7548 | 2.7498 | 2.7482 | 2.7468 | | | | |
| Powder | Run 1 | Run 2 | Run 3 | Run 4 | Run 5 | Run 6 | Run 7 | | | |
| Volume | 2.2456 | 2.2463 | 2.2490 | 2.2513 | 2.2480 | 2.2478 | 2.2496 | | | |
| Weight | 2.7877 | 2.7868 | 2.7835 | 2.7806 | 2.7846 | 2.7850 | 2.7827 | | | |

DRE = dense rock equivalent, Volume cm³, Density g/cm³

**Table A5.6:** Pycnometer vesicularity data for Unit B, block 6

| **Block 6** | Weight | Standard deviation | Average Volume | Average Density | Bulk Volume | Bulk Density | DRE density | Total Vesicularity | Isolated vesicularity | Connected Vesicularity |
|---|---|---|---|---|---|---|---|---|---|---|
| | 25.1800 | 0.0002 | 8.7764 | 2.8690 | 12.3260 | 2.0428 | 2.6240 | 22.1480 | 31.4849 | -9.3369 |
| **Individual Runs** | | | | | | | | | | |
| Block | Run 1 | Run 2 | Run 3 | Run 4 | Run 5 | Run 6 | Run 7 | Run 8 | | |
| Volume | 8.6972 | 8.7276 | 8.7928 | 8.7930 | 8.7595 | 8.7712 | 8.7526 | 8.8055 | | |
| Weight | 2.8952 | 2.8851 | 2.8637 | 2.8636 | 2.8746 | 2.8708 | 2.8768 | 2.0596 | | |
| Powder | Run 1 | Run 2 | Run 3 | Run 4 | Run 5 | Run 6 | Run 7 | | | |
| Volume | 8.5858 | 8.5927 | 8.6134 | 8.9125 | 9.2057 | 9.2098 | 9.2176 | | | |
| Weight | 2.8151 | 2.8128 | 2.8061 | 2.7119 | 2.6255 | 2.6244 | 2.6222 | | | |

DRE = dense rock equivalent, Volume cm³, Density g/cm³

**Table A5.7:** Pycnometer vesicularity data for Unit B, block 7

| **Block 7** | Weight | Standard deviation | Average Volume | Average Density | Bulk Volume | Bulk Density | DRE density | Total Vesicularity | Isolated vesicularity | Connected Vesicularity |
|---|---|---|---|---|---|---|---|---|---|---|
| | 4.1900 | 0.0000 | 1.1944 | 2.8039 | 2.8890 | 1.4503 | 2.7599 | 47.4499 | 49.0442 | -1.5943 |
| **Individual Runs** | | | | | | | | | | |
| Block | Run 1 | Run 2 | Run 3 | Run 4 | Run 5 | Run 6 | Run 7 | Run 8 | | |
| Volume | 1.4628 | 1.4744 | 1.4842 | 1.4825 | 1.4916 | 1.4923 | 1.4952 | 1.4957 | | |
| Weight | 2.8643 | 2.8419 | 2.8230 | 2.8263 | 2.8091 | 2.8078 | 2.8024 | 2.8014 | | |
| Powder | Run 1 | Run 2 | Run 3 | Run 4 | Run 5 | Run 6 | Run 7 | Run 8 | | |
| Volume | 1.4784 | 1.4860 | 1.4791 | 1.4737 | 1.4848 | 1.4840 | 1.4868 | 1.4860 | | |
| Weight | 2.7732 | 2.7591 | 2.7719 | 2.7822 | 2.7614 | 2.7629 | 2.7576 | 2.7591 | | |

DRE = dense rock equivalent, Volume cm³, Density g/cm³

**Table A5.8:** Pycnometer vesicularity data for Unit B, block 8

| **Block 8** | Weight | Standard deviation | Average Volume | Average Density | Bulk Volume | Bulk Density | DRE density | Total Vesicularity | Isolated vesicularity | Connected Vesicularity |
|---|---|---|---|---|---|---|---|---|---|---|
| | 11.5500 | 0.0001 | 3.9933 | 2.8924 | 9.9900 | 1.1562 | 2.6716 | 56.7242 | 64.9889 | -8.2647 |
| **Individual Runs** | | | | | | | | | | |
| Block | Run 1 | Run 2 | Run 3 | Run 4 | Run 5 | Run 6 | Run 7 | Run 8 | | |
| Volume | 3.8982 | 3.9476 | 3.9674 | 3.9778 | 3.9813 | 3.9870 | 3.9936 | 3.9992 | | |
| Weight | 2.9629 | 2.9259 | 2.9112 | 2.9036 | 2.9011 | 2.8969 | 2.8921 | 2.8881 | | |
| Powder | Run 1 | Run 2 | Run 3 | Run 4 | Run 5 | Run 6 | Run 7 | Run 8 | | |
| Volume | 3.8237 | 3.8659 | 3.8764 | 3.9067 | 3.9100 | 3.9202 | 4.1023 | 3.9589 | | |
| Weight | 2.7905 | 2.7600 | 2.7526 | 2.7312 | 2.7289 | 2.7218 | 2.6010 | 2.6952 | | |

DRE = dense rock equivalent, Volume cm³, Density g/cm³

**Table A5.9:** Pycnometer vesicularity data for Unit B, block 9

| **Block 9** | Weight | Standard deviation | Average Volume | Average Density | Bulk Volume | Bulk Density | DRE density | Total Vesicularity | Isolated vesicularity | Connected Vesicularity |
|---|---|---|---|---|---|---|---|---|---|---|
| | 9.0400 | 0.0001 | 3.0890 | 2.9265 | 18.1200 | 0.4989 | 2.6830 | 81.4053 | 90.4809 | -9.0757 |
| **Individual runs** | | | | | | | | | | |
| Block | Run 1 | Run 2 | Run 3 | Run 4 | Run 5 | Run 6 | Run 7 | Run 8 | | |
| Volume | 3.0174 | 3.0335 | 3.0565 | 3.0527 | 3.0734 | 3.0760 | 3.0826 | 3.1085 | | |
| Weight | 2.9959 | 2.9800 | 2.9576 | 2.9613 | 2.9414 | 2.9389 | 2.9326 | 2.9082 | | |
| Powder | Run 1 | Run 2 | Run 3 | Run 4 | Run 5 | Run 6 | Run 7 | Run 8 | | |
| Volume | 3.0652 | 3.0952 | 3.1074 | 3.1541 | 3.1504 | 3.1421 | 3.1771 | 3.1068 | | |
| Weight | 2.7502 | 2.7235 | 2.7129 | 2.6727 | 2.6759 | 2.6829 | 2.6534 | 2.7134 | | |

DRE = dense rock equivalent, Volume cm³, Density g/cm³

**Table A5.40:** Pycnometer vesicularity data for Unit B, block 10

| **Block 10** | Weight | Standard deviation | Average Volume | Average Density | Bulk Volume | Bulk Density | DRE density | Total Vesicularity | Isolated vesicularity | Connected Vesicularity |
|---|---|---|---|---|---|---|---|---|---|---|
| | 8.5800 | 0.0001 | 2.9377 | 2.9206 | 11.7360 | 0.7311 | 2.4570 | 70.2449 | 89.1134 | -18.8685 |
| **Individual Runs** | | | | | | | | | | |
| Block | Run 1 | Run 2 | Run 3 | Run 4 | Run 5 | Run 6 | Run 7 | Run 8 | | |
| Volume | 2.8683 | 2.8999 | 2.9066 | 2.9986 | 2.9396 | 2.9276 | 2.9340 | 2.9515 | | |
| Weight | 2.9914 | 2.9588 | 2.9519 | 2.9601 | 2.9193 | 2.9307 | 2.9244 | 2.9070 | | |
| Powder | Run 1 | Run 2 | Run 3 | Run 4 | Run 5 | Run 6 | Run 7 | Run 8 | | |
| Volume | 3.0825 | 3.1195 | 3.2656 | 3.5286 | 3.6708 | 3.6144 | 3.2621 | 3.4534 | | |
| Weight | 2.7445 | 2.7117 | 2.5907 | 2.3976 | 2.3047 | 2.3407 | 2.5934 | 2.4498 | | |

DRE = dense rock equivalent, Volume cm³, Density g/cm³

**Table A5.15:** Pycnometer vesicularity data for Unit B, block 11

| **Block 11** | Weight | Standard deviation | Average Volume | Average Density | Bulk Volume | Bulk Density | DRE density | Total Vesicularity | Isolated vesicularity | Connected Vesicularity |
|---|---|---|---|---|---|---|---|---|---|---|
| | 14.8200 | 0.0002 | 5.1592 | 2.8726 | 26.9620 | 0.5497 | 2.7508 | 80.0181 | 84.4459 | -4.4278 |

**Individual Runs**

| Block | Run 1 | Run 2 | Run 3 | Run 4 | Run 5 | Run 6 | Run 7 | Run 8 |
|---|---|---|---|---|---|---|---|---|
| Volume | 5.0865 | 5.0586 | 5.1188 | 5.1263 | 5.1706 | 5.1394 | 5.1808 | 5.1574 |
| Weight | 2.9136 | 2.9297 | 2.8952 | 2.8662 | 2.8662 | 2.8806 | 2.8606 | 2.8736 |
| Powder | Run 1 | Run 2 | Run 3 | Run 4 | Run 5 | Run 6 | Run 7 | Run 8 |
| Volume | 5.1451 | 5.1591 | 5.1789 | 5.1927 | 5.1953 | 5.2093 | 5.2213 | 5.2086 |
| Weight | 2.7871 | 2.7795 | 2.7690 | 2.7616 | 2.7602 | 2.7528 | 2.7465 | 2.7531 |

DRE = dense rock equivalent, Volume cm$^3$, Density g/cm$^3$

# *Appendix Six:*

# *XRD Analyses*

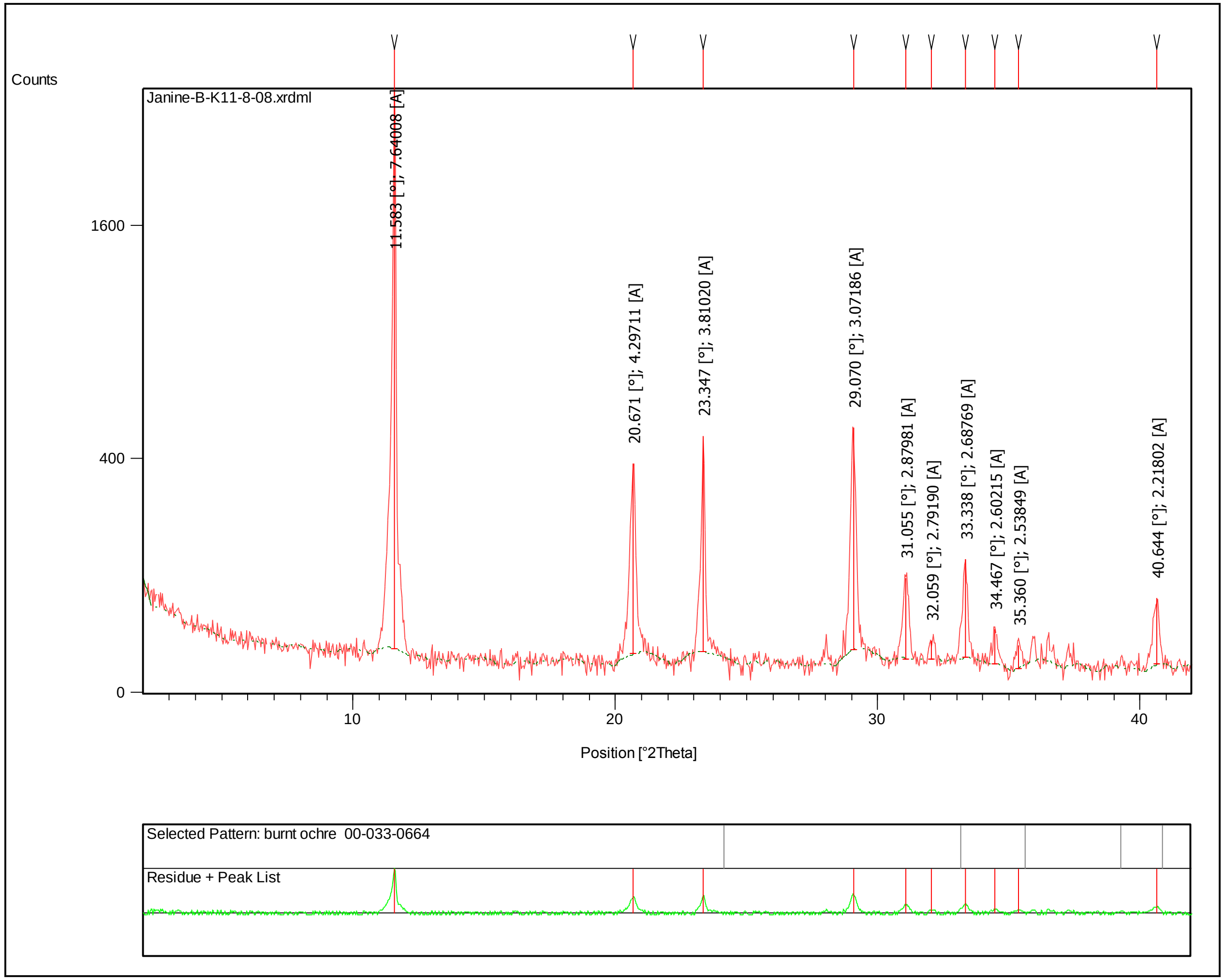

**Figure A6.10:** XRD results for Unit D gypsum mineral identification

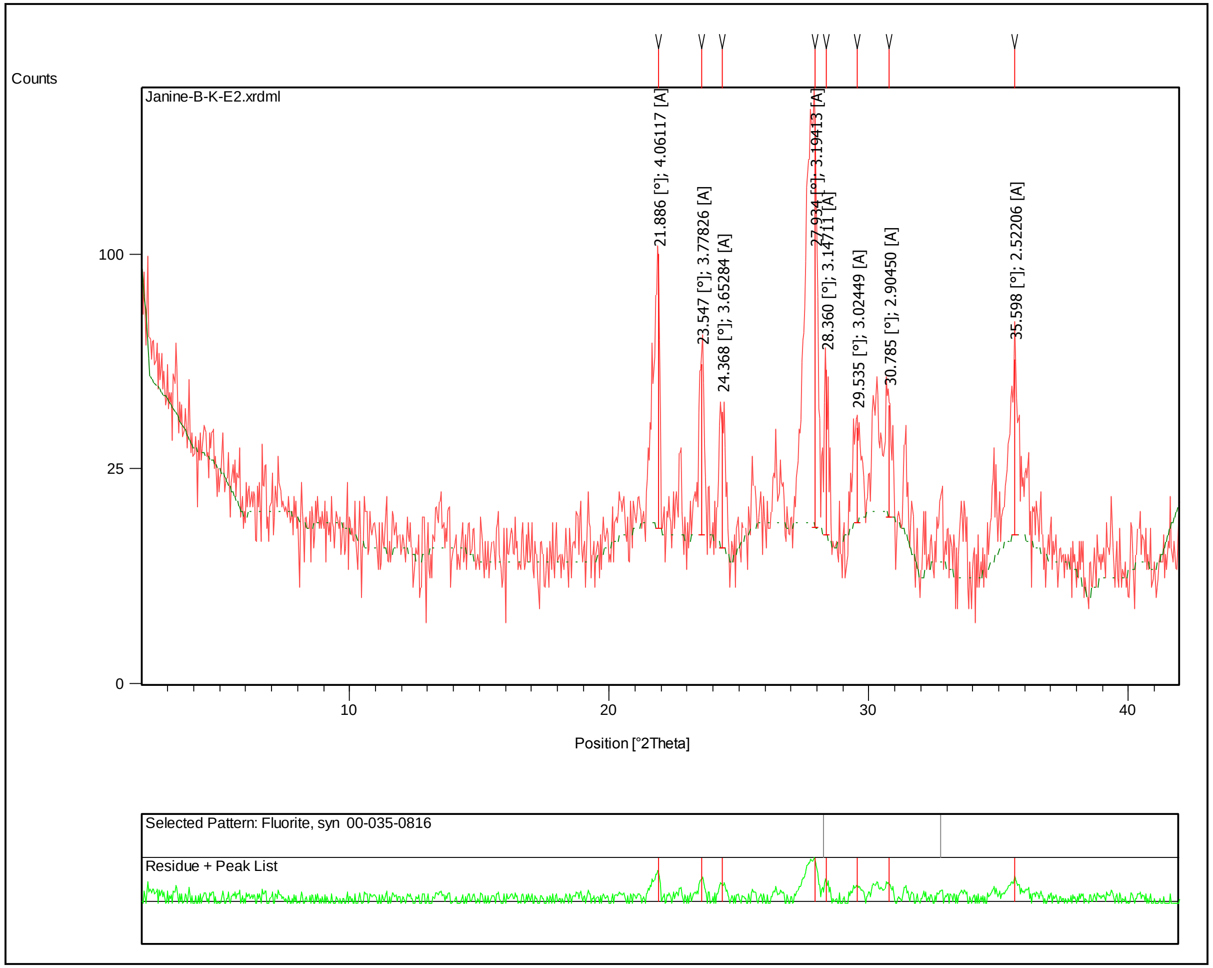

**Figure A6.11:** XRD results for Unit E showing no presence of clay minerals.